# Dynamical Mean-Field Theory Studies on Real Materials

**Nils-Oliver Linden**


München 2019

# Dynamical Mean-Field Theory Studies on Real Materials

**Nils-Oliver Linden**

Dissertation
an der Fakultät der Physik
der Ludwig–Maximilians–Universität
München

vorgelegt von
Nils-Oliver Linden
aus Wilhelmshaven

München, den 11.01.2019

Erstgutachter: Prof. Dr. Ulrich Schollwöck
Zweitgutachter: Prof. Dr. Dieter Vollhardt
Tag der mündlichen Prüfung: 05.04.2019

# Deutschsprachige Zusammenfassung

Numerische Untersuchungen stark korrelierter fermionischer Systeme sind schwierig und beinhalten noch heute essentielle Probleme. Die Hauptgründe dafür sind das exponentielle Wachstum des Hilbertraumes der Quantenzustände mit der Systemgröße und das fermionische Vorzeichenproblem bei Monte-Carlo-Rechnungen. Eine der am häufigsten verwendeten Methoden zur Untersuchung zweidimensionaler Gittersysteme sind Cluster-Erweiterungen der dynamische Molekularfeld Theory (DMFT), wie zum Beispiel die dynamische Cluster Approximation (DCA). Diese Methoden bilden mehrdimensionale Gittersysteme auf eindimensionale Störstellen-Probleme ab. 2015 wurde gezeigt, dass DMFT auf der imaginären Frequenzachse kombiniert mit der Dichtematrix-Renormierungsgruppe (DMFT+DMRG) Mehrband- und Multisite-Systeme schneller lösen kann, als wenn andere Störstellen-Löser verwendet werden.
In dieser Arbeit entwickeln wir diesen Ansatz weiter und wenden ihn auf Modelle realer Materialen an. Am Anfang dieser Arbeit besprechen wir relevante Methoden für DMRG+DMFT, wie zum Beispiel Matrix-Produkt-Zustände, die Dichtematrix-Renormierungsgruppe und mehrere Zeitentwicklungs-Methoden. In diesem Zusammenhang werden wir auch mehrere Verbesserungen besprechen, die von methodischen Anpassungen von Zeitentwicklungen bis hin zur Neuordnung des Tensornetzwerkes basierend auf Verschränkungs-Eigenschaften reichen. Danach werden wir uns detailliert mit den methodologischen und programmiertechnischen Aspekten von DMFT beschäftigen. Dieses Kapitel dient als Grundlage für andere Forscher, die eigene DMRG+DMFT-Codes programmieren wollen. Abschließend werden wir drei verschiedene Modelle besprechen, um das Ausmaß der Systeme zu zeigen, die mit diesem Ansatz gelöst werden können. Wir werden uns im Kontext des Hubbard-Modells detailliert mit Multisite-DCA beschäftigen und zeigen, dass DMRG+DMFT Ergebnisse für Systeme mit mittleren Wechselwirkungsstärken bei niedrigen Temperaturen erzeugen kann. Das ist mit anderen Störstellen-Lösern bisher nicht möglich. Im zweiten Fall beschäftigen wir uns mit Strontiumvanadat $Sr_2VO_4$ und werden die ersten Zweisite-DCA-Ergebnisse für ein realistisches Dreiband-Modell präsentieren. Im Gegensatz zu bisherigen Erwartungen führt die teilweise Wiedereinführung der Impulsabhängigkeit der Selbstenergie nicht zu einer besseren Übereinstimmung von Theorie und Experiment. Das dritte Modell beschreibt Strontiumruthenat $Sr_2RuO_4$. In diesem Fall besprechen wir den Einfluss der Spin-Bahn-Kopplung auf DMFT und wie die damit verbundenen Probleme optimal gelöst werden können. Abschließend zeigen wir die ersten Ergebnisse für dieses Modell bei niedrigen Temperaturen.

# Abstract

Numerical studies on strongly correlated fermionic systems are very complicated and still provide essential problems. The main reason is the exponential growth of the underlying Hilbert state space with the system size and the fermionic sign problem for Monte Carlo studies. Among the most widely employed numerical techniques for studying two-dimensional quantum many-body systems are cluster extensions of the dynamical mean-field theory (DMFT), e.g. dynamical cluster approximation (DCA). They map an infinitely large multi-dimensional lattice problem to a one-dimensional impurity problem. In 2015 it was shown that the density matrix renormalisation group (DMRG) used as an impurity solver for DMFT (DMFT+DMRG) on the imaginary-frequency axis allows to solve multi-site and multi-band problems extremely fast compared to other solvers.
Within this thesis, we further develop this DMRG+DMFT approach to apply the method on real material settings. The step from artificial, completely degenerate multi-band models with simple dispersion relations on a Bethe lattice, studied in 2015, to systems with realistic band structures and lifted degeneracies involves more challenges than originally suspected.
In this thesis, we will first recapitulate relevant methods for our approach like matrix product states, the density matrix renormalisation group and several time evolution methods. In this context we will present several improvements ranging from optimised time evolutions to entanglement based optimisations of tensor networks. Second, we will present a very detailed description of the dynamical mean field theory. We will focus on both methodological aspects and implementation details. This chapter is intended to allow other researcher to implement their own DMFT code using DMRG as an impurity solver. Third, we will discuss three different models to show the extent of problems DMRG+ DMFT is able to solve. We will focus on multi-site DCA calculations in the case of the two-dimensional Hubbard model and show that DMRG allows to tackle systems with intermediate interaction strengths at low temperatures, which are unsolvable with other solvers. In the second case, the real material $Sr_2VO_4$, we will show the first two-site DCA results for a realistic three-band model. In contrast to assumptions, partly reintroducing the momentum dependence of the self-energy does not improve agreement between experimental observations and theoretical results. Finally, we will move on to another realistic three-band model, which describes $Sr_2RuO_4$, to show how to deal with the influence of spin-orbit coupling on DMFT. We will present the first low-temperature results for this material and will confirm previous results of simplified model calculations.

# Contents

# Chapter 1

# Introduction

The aim of Quantum mechanics is to understand and predict the behaviour of electrons, atoms, photons and molecules at atomic scales. In turn, this determines the macroscopic properties of materials such as, for example, electrical and thermal conductivity, and resistance as well as their magnetic behaviour. Condensed matter theory focuses on trying to understand the origin of these properties and determining how they are influenced by the spatial distribution of atoms and orbitals in unit cells, temperature, pressure, doping and other parameters. With this knowledge at hand one can deliberately identify or design compounds that exhibits certain characteristics under clearly defined conditions.
Many of these properties are interesting because they promise to lead to new technical revolutions similar to how the understanding of semi-conductors in the last century led to the development of computers, smartphones and microcontrollers. A comparable understanding of strongly correlated materials could for instance allow to design compounds that are tuned close to phase transitions and react extremely fast to parameter changes like applied currents or pressure. This would decrease the amount of energy needed to control these devices and lower their response times significantly[1,2,3] compared to semi conductors. Another interesting phenomenon is high-temperature superconductivity. Understanding the mechanisms behind this behaviour could allow to design materials that exhibit this property at room temperature, which definitely would change our society dramatically[4,5,6].
However, the wide variety of interaction types and strengths between electrons and between electrons and atoms give rise to an enormous range of different physical phenomena[7,8,9,10,11,12]. Studies of strongly correlated materials are very complicated and demanding. First, it is challenging to determine the important processes and properties of a material to build a reasonable model. For example, it has to be evaluated whether the system can be described by an effective lower-dimensional model or whether the full three-dimensional system has to be considered, whether the geometrical structure of the compound has an important influence on the physics, which orbitals of which atoms are vital for electronic properties, of which type the interactions between the different electrons are and which regimes of dopings, interaction strengths and temperatures are interesting. The description of the system should be as simple as possible and only include

relevant aspects since the difficulty and runtime of computations is affected strongly by the complexity of the model. This leads us to the second step: The model has to be solved. While multiple methods exist that produce results for one-dimensional problems very efficiently such as density matrix renormalisation group [13], exact diagonalisation [14] or continuous time quantum Monte Carlo [15], in general, two-dimensional problems still provide significant problems and three-dimensional models are not solvable at all.
Recent years have seen great interest in two-dimensional quantum many-body systems in both theoretical and experimental physics. On the theoretical side, new non-perturbative approaches are developed [16,17,18] inspired by ideas of different fields. With the help of quantum information theory more efficient tensor networks are invented [19], quantum chemistry provides useful insights on highly correlated models and optimal representations of quantum problems [20,21], while machine learning techniques are used to study quantum many-body states [22,23,24] and to optimise existing numerical techniques [25]. On the experimental side, developments in the field of cold atomic gases and quantum optics allow for the setup and manipulation of quantum lattice systems under controlled and repeatable conditions [26]. This opens completely new possibilities for comparisons and mutual influence between experiment and theory for future research.
These developments are not only interesting from a theoretical point of view but also lead to an increasing amount of research on more and more complex and realistic solid state models. Accordingly, the demand for numerical resources is strongly increasing and many numerical methods that have been very successful so far seem to have reached their limits. Correspondingly, many improvements to these kinds of methods are being developed and are still the main focus of many researchers. However, the most reliable methods to study quantum-mechanical systems so far, exact diagonalisation [27] and Monte Carlo sampling [28], still encounter large difficulties. The former is limited by the exponential growth of the Hilbert state space and fails to tackle relevant systems sizes. The latter is often limited by the so-called sign problem that is encountered in many fermionic systems. If present, it prevents Monte Carlo from determining the behaviour of complex models at low enough temperatures. Among the most widely employed numerical techniques for studying quantum many-body systems are the dynamical mean-field theory [29,30,31] (DMFT) and its cluster extensions, e.g. dynamical cluster approximation [32,33] (DCA). These methods map an infinitely large multi-dimensional lattice problem to an auxiliary problem, consisting of impurity sites coupled to a non-interacting environment. The interaction on and between the impurity sites is similar to the interaction in the original multi-dimensional model. The artificial coupling between impurity sites and environment has to be determined self-consistently in such a way that the physics taking place on the impurity sites is the same as on the lattice sites. This is done, as in all mean-field theories, via a self-consistency equation and an iterative procedure that updates the auxiliary problem until self-consistency is reached. The main physical assumption of dynamical mean-field theory is to approximate the electron self-energy as frequency-dependent but momentum-independent. Cluster extensions such as DCA reintroduce the momentum-dependence of the self-energy partly by creating more complex models that become more

and more similar to the original lattice problem. Unsurprisingly, that causes computation times to increase exponentially.
DMFT is successful because of two main reasons: First, over the time it was shown that many models and materials are well described by DMFT results, despite the fact that self-energies are momentum-independent. Second, the success and failure of DMFT for arbitrary systems depends strongly on the method chosen to solve the auxiliary impurity problem, also called impurity-solver. There exist a wide variety of impurity solvers that make DMFT so flexible and versatile. The most prominent examples are continuous time quantum Monte Carlo [34] (CTQMC), exact diagonalisation [14] (ED), the numerical renormalisation group (NRG) [35] and the density matrix renormalisation group (DMRG) [17,36]
CTQMC is widely and very successfully used as an impurity solver. Unfortunately, computing low-temperature results is computationally highly expensive and limits the use of CTQMC in many cases to unsuitable high temperatures. Since CTQMC solves the impurity problem on the imaginary-frequency axis, calculating real-frequency quantities requires analytical continuations. Unfortunately, they are numerically ill-posed and suffer from severe practical difficulties. Furthermore, the application of CTQMC in some cases is highly limited by the fermionic sign problem, which often occurs for systems with multiple relevant orbitals, non-Hubbard interactions or large cluster DCA calculations at low temperatures.
Exact diagonalisation solves the impurity problem on the imaginary-frequency axis without making any kind of assumptions. It suffers under no general limitations and is only restricted by the size of the Hilbert space of the impurity problem. This restrains the number of correlated impurity sites and associated bath sites that describe the non-interacting environment. In practice, this limits ED to systems with only a couple of relevant orbitals and small cluster DCA calculations, albeit there have been recent developments with restricted Hilbert spaces [37,38] that increase accessible systems sizes slightly.
In contrast to the previous two methods, NRG solves the auxiliary problem on the real-frequency axis and obtains high-quality results for the low-frequency limit especially. Due to its way of solving the impurity problem, NRG is limited strongly by the number of correlated sites, which hardly can exceed one or two impurity sites. Only recently NRG was pushed to solve a three-band problem in the context of DMFT [18] but it remains questionable how far it can be extended.
The density matrix renormalisation group (DMRG) was first used as an impurity solver for DMFT in 2004 [36,39]. In contrast to NRG, the high-quality results obtained on the real-frequency axis are not focused on the low-frequency regime, which makes DMRG more versatile. The impurity problems obtained from DMFT are typically represented as one-dimensional chains. For DMRG this means, that adding additional correlated sites results in creating artificial long-range interactions. They increase entanglement and runtimes dramatically, which was probably the reason why DMRG has not been widely accepted as an impurity solver for DMFT. Originally, only results for a single-band Hubbard model were presented. Recently, in 2017 changes to the topology of the impurity problem, which removed a large portion of artificial long-range interactions, allowed to

solve a three-band model on the real-frequency axis with DMRG[40]. However, it is still in questionable whether DMRG+DMFT is able to solve multi-band models or higher-order DCA calculations of real materials.
Wolf et al. in 2015[17] followed a different road by proposing to solve DMFT on the imaginary-frequency axis with DMRG. While impurity problems on the real-frequency axis consists of 60 to 100 bath sites per correlated site, on the imaginary axis only three to ten are necessary for an excellent description of the non-interacting environments. Wolf et al. showed that these small systems lead to very fast runtimes compared to other solvers and at the same time to remarkable agreements with CTQMC results. Instead of using analytic continuations to obtain real-frequency results after DMFT is converged, they proposed to perform an additional real-frequency calculation based on the converged impurity problem. With this approach they were able to compute the first spectral functions of a completely degenerate three-band Hubbard-Kanamori model at zero temperature with a two-site DCA calculation. The results were not of a high quality but allowed to determine whether a system is an insulator or a metal. Albeit this system was far from being realistic, the remarkably short computations times indicated that more complex and realistic models could be solvable with this ansatz. Thus, they proposed to use DMRG+DMFT on the imaginary axis as an effective low-cost solver for DMFT and DCA problems that were not accessible with other impurity solvers.
Within this thesis, we further develop DMRG+DMFT on the imaginary-frequency axis to be able to apply the method on real material settings. The step from a completely degenerate multi-band problem with a simple dispersion relation on a Bethe lattice to a system with a realistic band structure and lifted degeneracies involved more challenges than originally suspected. The entanglement growth is significant, convergence problems occur due to more complex phases being present and symmetries become more important for the performance and convergence of DMFT. Therefore, to obtain results for real material models, it is necessary to improve methodological aspects such as, for example, a better Krylov method for computing time evolutions or model representations such as the reordering of the lattice sites based on entanglement properties. Additionally, improving implementational details such as optimised parallelisations and determining which symmetry quantum numbers can and should be implemented is also necessary to obtain results for most model calculations.
We will begin this thesis by introducing matrix product states (MPSes) and matrix product operators (MPOs) for lattice problems[41,42] in chapter 2. They form the basis to easily understand tensor networks, DMRG and all MPS-related methods. All necessary operations such as scalar products and operator applications can be performed easily in the MPS language and also be represented graphically. Afterwards, the concept of entanglement, and its relation to MPS will be introduced.
With this fundament we will focus in chapter 3 on discussing the density matrix renormalisation group[43], which can be used to variationally find an optimised representation of the ground state of impurity problems created within DMFT. Furthermore, we will introduce several improvements such as a reordering of lattice sites based on entangle-

ment properties[21], which can improve the runtime of DMRG by up to a factor of ten. We will also discuss different network topologies such as binary tree tensors, minimum-spanning trees or minimum-entangled trees. The former were developed during this thesis and proved in its first and not very refined implementation only to be competetive with one-dimensional reordered MPSes for larger system sizes. The latter are lattice topologies that are determined based on entanglement properties and are used frequently in quantum chemistry[44]. They form a natural next step for improving the network topologies of impurity problems originating from more complex DMFT systems.
In the context of DMFT, impurity solvers are used to compute the self-energy of the auxiliary system. In the case of DMRG, this requires to compute the time-dependent interacting single-particle Green's functions of all impurity sites, which is, in general, the most time-consuming part of each DMFT iteration. Therefore, the choice of the time-evolution method is crucial for the performance of the whole calculation. In chapter 4 we will discuss several time evolution methods such as time evolution with block decimation[45], the time-dependent variational principle[46] and the Krylov subspace method[47]. We will show that the Krylov method can be improved significantly by several adaptations of the standard approach. However, we will argue that time-dependent variational principle is the fastest method available for all models we encountered during this thesis. We will end the chapter by introducing different ansatzes to compute the long-time behaviour of the Green's functions in much cheaper ways by linear prediction or by projecting out the energetically low-lying eigenstates of the Hamiltonian.
After introducing all necessary ingredients to use DMRG as an impurity solver for DMFT, in chapter 5 we will focus on both the theoretical derivation of DMFT and the detailed discussion on the implementation of each step of a DMFT iteration. We will take special care to emphasise on typical parameter and threshold choices and the ideas and experiences behind certain approaches. At the end of this chapter we will introduce multi-site DCA.
The Hubbard model is considered to be the simplest model containing correlated electrons. It is displaying a wide range of different phenomena[48,49,50,51] and is also known to describe high-temperature copper-oxide superconductors relatively well[52]. A key ingredient for the description of high temperature superconductivity is the momentum-dependence of the electrons that form cooper pairs. Since DMFT assumes momentum-independence of the electron self-energy, it is obvious that cluster methods such as DCA are needed to describe the underlying physics of these properties. It is believed that the Hubbard model at intermediate interaction strengths $U \approx 9t$ is especially interesting to understand systems that exhibit high-temperature superconductivity[10,53]. So far multi-site DCA calculations for intermediate interaction strengths and moderately large cluster sizes at low enough temperatures are unfeasible with any kind of impurity solver. In the beginning of chapter 6 we will introduce the two-dimensional Hubbard model Hamiltonian for multi-site DCA calculations. We will put special focus on the implementation of momentum quantum numbers, which describe the conserved total momentum of the impurity problem. They are necessary to reliably obtain the global ground state of multi-site DCA systems with

four or more patches with DMRG. Without them DCA calculations show strong convergence problems. Afterwards, we will show that DMRG+DMFT results are in perfect agreement with CTQMC results for clusters with up to four sites and that eight-site DCA systems are not accessible due to unfeasibly long runtimes. We will close the chapter by presenting the first multi-site DCA results for intermediate interaction strengths $U = 9t$ and $U = 11t$ at temperature $T = 0$. Since the numerical effort is independent of the choice of $U$, DMRG+DMFT is shown to be the method of choice for investigating momentum properties in context of DMFT at low temperatures.
In chapter 7 we will focus on real material calculations of the layered perovskite Strontium Vanadate $Sr_2VO_4$. While experiments show that the $Sr_2VO_4$ is a small gap correlation driven insulator[54], single-site DMFT calculations yield metallic solutions for any reasonable choice of interaction strengths[55]. It is believed that the momentum-independence of the DMFT calculations is the reason for this discrepancy. Unfortunately, to our knowledge no impurity solver was able to combine the three-band model with Hubbard-Kanamori interaction with a multi-site DCA calculation at low temperatures so far. Indeed, the three-band structure and the real material dispersion relation of the Vanadates provide completely different challenges than the single-band multi-site DCA calculations of the Hubbard model. As will be discussed, the most prominent one is the oscillation between two competing solutions due to the degeneracy of two of the three bands. In this context we will also discuss the band parity symmetry of the Hubbard-Kanamori Hamiltonian in much detail and its influence on the convergence properties of DMFT and DCA. We will end the chapter by showing, to our knowledge, the first two-site DCA results for a three-band model with realistic band structure at temperature $T = 0$. A comparison with single-site DMFT reveals that both calculations yield similar results for the layered perovskite $Sr_2VO$. This suggests that the momentum-independence of single-site DMFT is not the reason for the discrepancies between experiment and theory.
In compounds that involve heavier elements, additional interaction types such as spin-orbit coupling are necessary to describe the physics. This is the case for the perovskite oxide compound Strontium Ruthenate $Sr_2RuO_4$. Unfortunately, the spin-orbit coupling introduces single-particle interactions between different orbitals. This results in off-diagonal components in Green's functions and self-energies, which lead to a severe sign-problem for CTQMC. For ED and DMFT they give rise to the not well-understood mathematical problem of fitting matrix-valued functions. In the beginning of chapter 8 we will show how to deal effectively with this problem in the context of the Ruthenates by transforming the problem into a more suitable basis representation. This allows us to calculate the first results for the $Sr_2RuO_4$-model with spin-orbit coupling at low temperatures and without any simplifications of the model. We will confirm previous results of simplified models that show an effective correlation-enhancement of the spin-orbit coupling by approximately a factor of two[56].
Chapter 9 will conclude this thesis and will give an outlook on future research.

# Chapter 2

# Tensor Networks

In this chapter we will define matrix product states and matrix product operators as tensor network representations of states and operators on finite Hilbert spaces. They are the key objects to understand the density matrix renormalisation group (DMRG) and the various time evolution methods, which we will discuss in chapter 3 and 4. Essentially, they are very efficient ways to represent a certain, but very relevant, class of quantum mechanical states and operators that allow for easy approximations. All necessary operations like overlaps, expectation values, applications of operators and simple scalar multiplications as well as additions of matrix product operators can all be easily defined and represented graphically. For further details we refer the interested reader to the extensive literature about this topic[43,57]. In this thesis we will only define the necessary ingredients to follow the discussion in the other chapters.

Originally, matrix product states (MPS) were developed in 1968 in the context of analytical studies on an interesting class of quantum states and proved to be simple and at the same time very useful to describe certain kind of problems[41]. In fact, they can be seen as an example of the simplest useful kind of tensor networks. They can be found in the linear algebra community most commonly as so-called tensor trains[42] but during the last 60 years several other names were used as well[58,59]. After extensive studies on the subclass of translationally invariant MPSes[60], several analytical variational methods based on the MPS language were developed, which for example allowed to work on Heisenberg antiferromagnets[61,62] and ferrimagnets[63].

MPSes got even more attention after they were first connected to infinite-system[64] and finite-system DMRG[65] in the late 90s. But the DMRG community only started to take these developments seriously after Cirac et al. in 2004[66,67] showed the effectiveness of MPSes more systematically. It was an important step when people realised that MPSes were not only conceptually useful but also allow for powerful extensions after reexpressing DMRG completely in MPS language. The most valuable are arguably real-time evolutions at zero[45,68] and finite temperature[69], periodic boundary conditions[70], infinite[71] and continuous[72] systems and the generalisation to higher dimensions[66].

While the precision of DMRG in MPS formulation for one-dimensional problems is essentially limited only by machine precision and quite independent of the detailed nature of

the Hamiltonian, for two-dimensional models the necessary numerical resources for precise results increase exponentially [73]. There exist several ansatzes based on tensor networks to tackle two-dimensional problems ranging from mapping the problem back to long-ranged one-dimensional systems [74] to projected entangled pair states called PEPS [75,76].
To understand all these methods and the strengths and weaknesses of the dynamical mean-field theory with DMRG as an impurity solver, it is necessary to understand the concepts of the MPS language. Therefore, we want to focus in this chapter first on how any quantum state can be written in a very specific form, which is already defining an MPS. In this context we will introduce important canonical forms and their connection to the Schmidt decomposition, which provides a way of measuring entanglement in MPSes. The concept of entanglement and its connection to singular values allows for efficient truncation schemes, which are a key ingredient of MPSes being so useful for describing so many physical systems. We will close this chapter with introducing matrix product operators (MPO) in the same way as MPSes. Additionally, over the whole chapter we will introduce graphical representations of MPSes and MPOs, which allow to describe concepts and methods very efficiently.

## 2.1 Matrix Product States

The discussion of this chapter is based on Schollwöcks review from 2011 [43]. We start with a general quantum many body state described by a wave function $|\psi\rangle$ defined on a lattice. We consider a lattice with $L$ sites and each site $l$ consists of a number of local basis states $|\sigma_l\rangle$. Thus, we can write a general state as

$$|\psi\rangle = \sum_{\sigma_1,\ldots,\sigma_L} c_{\sigma_1,\ldots,\sigma_L} |\sigma_1,\ldots,\sigma_L\rangle. \tag{2.1.1}$$

The coefficients $c_{\sigma_1,\ldots,\sigma_L}$ are complex and describe the weight of each combination of local basis states to the state $|\psi\rangle$. We now want to write the state as a matrix product state. We can consider these coefficients as a multi-dimensional tensor and reshape it to the matrix

$$\Psi_{\sigma_1,(\sigma_2,\ldots,\sigma_L)} = c_{\sigma_1,\ldots,\sigma_L}. \tag{2.1.2}$$

This allows us to perform a singular value decomposition $\Psi = USV^\dagger$ on it, separating the matrix $U$ from the new multi-dimensional tensor $c_{a_1,\sigma_2,\ldots,\sigma_L}$

$$c_{\sigma_1,\ldots,\sigma_L} = \Psi_{\sigma_1,(\sigma_2,\ldots,\sigma_L)} = \sum_{a_1}^{r_1} U_{\sigma_1,a_1} S_{a_1,a_1} (V^\dagger)_{a_1,(\sigma_2,\ldots,\sigma_L)} = \sum_{a_1}^{r_1} U_{\sigma_1,a_1} c_{a_1,\sigma_2,\ldots,\sigma_L}. \tag{2.1.3}$$

At this point we reshape $U_{\sigma_1,a_1}$ back into a tensor with three dimensions $A^{\sigma_1}_{1,a_1}$. The coefficient tensor can again be reshaped into a matrix

$$c_{\sigma_1,\ldots,\sigma_L} = \sum_{a_1}^{r_1} A^{\sigma_1}_{1,a_1} \Psi_{(a_1\sigma_2),(\sigma_3,\ldots,\sigma_L)}. \tag{2.1.4}$$

The index $\sigma_1$ of $A^{\sigma_1}_{1,a_1}$ labels the local basis of site 1 and the index $a_1$ labels the product with the remaining tensor. Since we consider the leftmost tensor in this case, the index on the left of $A^{\sigma_1}_{1,a_1}$ is just 1 because we need to obtain a simple scalar after the contraction of the indices. The 1 is usually omitted.
At this stage we perform a singular value decomposition again similar to Eq. (2.1.3)

$$c_{\sigma_1,\ldots,\sigma_L} = \sum_{a_1}^{r_1}\sum_{a_2}^{r_2} A^{\sigma_1}_{a_1} U_{(a_1\sigma_2),a_2} S_{a_2,a_2} (V^\dagger)_{a_2,(\sigma_3,\ldots,\sigma_L)} = \sum_{a_1}^{r_1}\sum_{a_2}^{r_2} A^{\sigma_1}_{a_1} A^{\sigma_2}_{a_1,a_2} \Psi_{(a_2\sigma_3),(\sigma_4,\ldots,\sigma_L)}. \quad (2.1.5)$$

This time the new tensor $A^{\sigma_2}_{a_1,a_2}$ of site 2, reshaped from the matrix $U_{(a_1\sigma_2),a_2}$, has three indices that are in general not equal to 1. Repeating the procedure to the right end of the system, we can rephrase the multi-dimensional tensor $c_{\sigma_1,\ldots,\sigma_L}$ as a product of three-dimensional tensors

$$c_{\sigma_1,\ldots,\sigma_L} = \sum_{a_1,\ldots,a_L} A^{\sigma_1}_{a_1} A^{\sigma_2}_{a_1,a_2} \cdots A^{\sigma_{L-1}}_{a_{L-2},a_{L-1}} A^{\sigma_L}_{a_{L-1}} = A^{\sigma_1} A^{\sigma_2} \cdots A^{\sigma_{L-1}} A^{\sigma_L}, \quad (2.1.6)$$

which allows us to write the wave function as

$$|\psi\rangle = \sum_{\sigma_1,\ldots,\sigma_L} A^{\sigma_1} A^{\sigma_2} \cdots A^{\sigma_{L-1}} A^{\sigma_L} |\sigma_1,\ldots,\sigma_L\rangle. \quad (2.1.7)$$

Note that this expression is exact since we did not make any assumptions. A graphical representation of this construction can be seen in Fig. 2.1. A tensor is represented as a square with lines connecting tensors, called bonds, indicating the contractions. We ordered the indices on the tensors $A^{\sigma_l}_{a_l,a_l}$ in such a way that they correspond to the positions of the lines, i.e. left, right and top.
The singular value decomposition produces matrices $U$, $S$ and $V^\dagger$ with certain properties. One of the most important property for us is the orthogonality property of $U$ and $V^\dagger$. Since the former matrices are orthogonal when multiplied with $U^\dagger$ from the left, we obtain

$$\delta_{a_l,a'_l} = \sum_{a_{l-1},\sigma_l} (U)^\dagger_{a_l,(a_{l-1}\sigma_l)} U_{(a_{l-1}\sigma_l),a'_l} = \sum_{a_{l-1}\sigma_l} (A^{\sigma_l\dagger})_{a_l,a_{l-1}} A^{\sigma_l}_{a_{l-1},a'_l} = \sum_{\sigma_l} (A^{\sigma_l\dagger} A^{\sigma_l})_{a_l,a'_l}. \quad (2.1.8)$$

We can also write that property as a matrix product of the tensors $A$ of site $l$

$$\sum_{\sigma_l} A^{\sigma_l\dagger} A^{\sigma_l} = I, \quad (2.1.9)$$

where $I$ is the unit matrix. See Fig. 2.2 a) for a graphical representation. A matrix product state where all tensors have this property is called left-canonical and the tensors are called left-normalised. Applying the singular value decompositions from the left to the right of the system was somehow arbitrary. We could also have started on the right site of our system and performed exactly the same steps up to the point where we reach

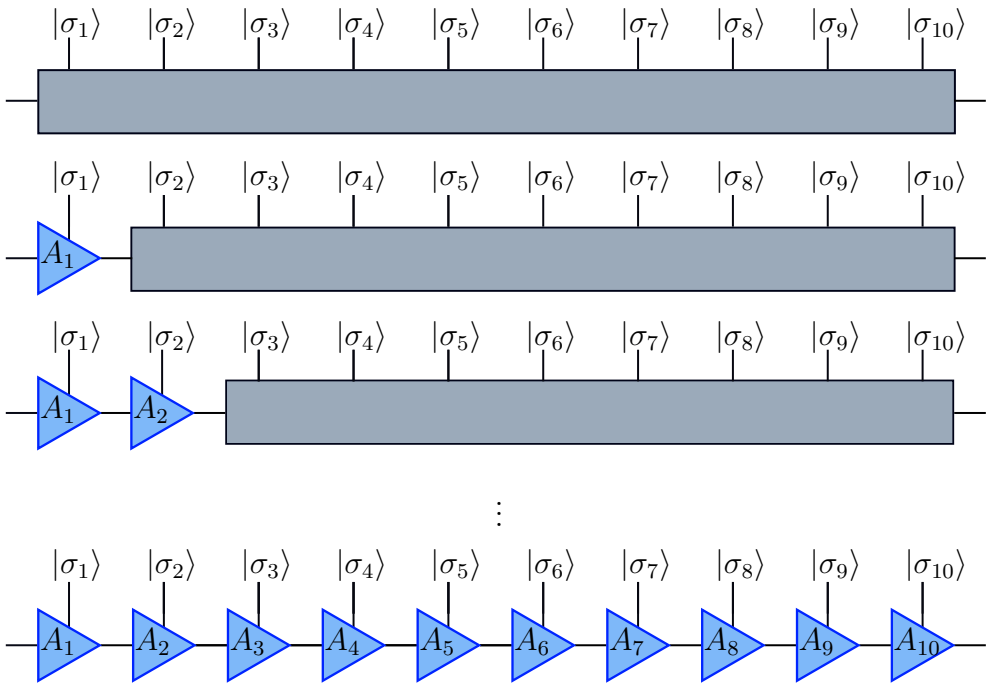


*Figure 2.1: Graphical representation of a construction of a matrix product state. In each step a singular value decomposition is performed and a three-dimensional tensor $A^{\sigma_l}$ is produced, represented by a square. Since we start from the left end of the system, we obtain a left-canonical MPS as indicated by the triangles pointing to the right. The lines connecting the squares symbolise the contractions that have to be summed over, also called bonds. The left- and rightmost line has dimension one, such that after the contraction of all tensors we obtain a simple scalar.*

the left edge of the system

$$\begin{aligned} c_{\sigma_1,\ldots,\sigma_L} &= \Psi_{(\sigma_1,\ldots,\sigma_{L-1}),\sigma_L} = \sum_{a_{L-1}} U_{(\sigma_1,\ldots,\sigma_{L-1}),a_{L-1}} S_{a_{L-1},a_{L-1}} (V^\dagger)_{a_{L-1},\sigma_L} \\ &= \sum_{a_{L-1}} \Psi_{(\sigma_1,\ldots,\sigma_{L-2}),(\sigma_{L-1}a_{L-1})} B^{\sigma_L}_{a_{L-1}} \\ &= \sum_{a_{L-2},a_{L-1}} U_{(\sigma_1,\ldots,\sigma_{L-2}),a_{L-2}} S_{a_{L-2},a_{L-2}} (V^\dagger)_{a_{L-2},(\sigma_{L-1}a_{L-1})} B^{\sigma_L}_{a_{L-1}} \\ &= \sum_{a_{L-2},a_{L-1}} \Psi_{(\sigma_1,\ldots,\sigma_{L-3}),(\sigma_{L-2}a_{L-2})} B^{\sigma_{L-1}}_{a_{L-2},a_{L-1}} B^{\sigma_L}_{a_{L-1}} \\ &= \cdots = \sum_{a_1,\ldots,a_{L-1}} B^{\sigma_1}_{a_1} B^{\sigma_2}_{a_1,a_2} \cdots B^{\sigma_{L-1}}_{a_{L-2},a_{L-1}} B^{\sigma_L}_{a_{L-1}}. \end{aligned} \tag{2.1.10}$$

The tensors we obtain with this approach are in general different from the ones we obtained previously. Thus, we label them as $B$-tensors. A graphical representation can be seen in Fig. 2.3. Of course, we can also write down the matrix product state

$$|\psi\rangle = \sum_{\sigma_1,\ldots,\sigma_L} B^{\sigma_1} B^{\sigma_2} \cdots B^{\sigma_{L-1}} B^{\sigma_L} |\sigma_1,\ldots,\sigma_L\rangle, \tag{2.1.11}$$


*Figure 2.2: Graphical representation of the contraction properties of left a) and right b) normalised tensors obtained from singular value decompositions. We write the complex conjugate tensors $A_l^*$ and $B_l^*$ such that the local index points to the bottom to allow an easy distinction between a ket and a bra state and to connect the local basis indices easily. Since the contraction over the two indices results in an unit matrix, we can write the two matrices as a single line contracting the remaining index.*

but this time we exploit the orthogonality properties of the $V^\dagger$ matrices, leading to a slightly different identity on site $l$

$$\sum_{\sigma_l} B^{\sigma_l} B^{\sigma_l \dagger} = I, \tag{2.1.12}$$

which we depicted in Fig. 2.2 b). States with tensors that all fulfil this property are called right-canonical while the tensors themselves are named right-normalised. Instead of creating the $A$ tensors from the left to the right or the $B$ tensors from the right to the left end of the system, we can also mix the decompositions. Therefore, we first decompose the coefficient tensor $c$ from the left up to site $l$

$$c_{\sigma_1,\ldots,\sigma_L} = \sum_{a_l} (A^{\sigma_1} \cdots A^{\sigma_l})_{a_l} S_{a_l,a_l} (V^\dagger)_{a_l,(\sigma_{l+1},\ldots,\sigma_L)}, \tag{2.1.13}$$

and then we decompose the remaining matrix $(V^\dagger)_{a_l,(\sigma_{l+1},\ldots,\sigma_L)}$ with singular value decompositions from the right end of the system $L$ to site $l$

$$(V^\dagger)_{a_l,(\sigma_{l+1},\ldots,\sigma_L)} = \sum_{a_{l+1},\ldots,a_{L-1}} (B^{\sigma_{l+1}}_{a_{l+1}} \cdots B^{\sigma_L}_{a_{L-1}})_{a_l}. \tag{2.1.14}$$

Thus, we obtain left-normalised $A$ tensors from site 1 to site $l$, right-normalised $B$ tensors on sites $l+1$ to $L$ and a diagonal square matrix $S$ in between, which consists of singular values. We call this representation a mixed-canonical MPS (Fig. 2.4), regardless of the the $S$ matrix being contracted with one of the neighbouring tensors or being kept separated

$$\begin{aligned} |\psi\rangle &= A^{\sigma_1} \cdots A^{\sigma_l} S B^{\sigma_{l+1}} \cdots B^{\sigma_L} |\sigma_1, \ldots, \sigma_L\rangle \\ &= A^{\sigma_1} \cdots A^{\sigma_{l-1}} M^{\sigma_l} B^{\sigma_{l+1}} \cdots B^{\sigma_L} |\sigma_1, \ldots, \sigma_L\rangle \\ &= A^{\sigma_1} \cdots A^{\sigma_l} M^{\sigma_{l+1}} B^{\sigma_{l+2}} \cdots B^{\sigma_L} |\sigma_1, \ldots, \sigma_L\rangle. \end{aligned} \tag{2.1.15}$$

Especially the last two forms in Eq. (2.1.15) are used frequently in the context of multiple methods, which we describe later on such as ground state searches or time evolutions,

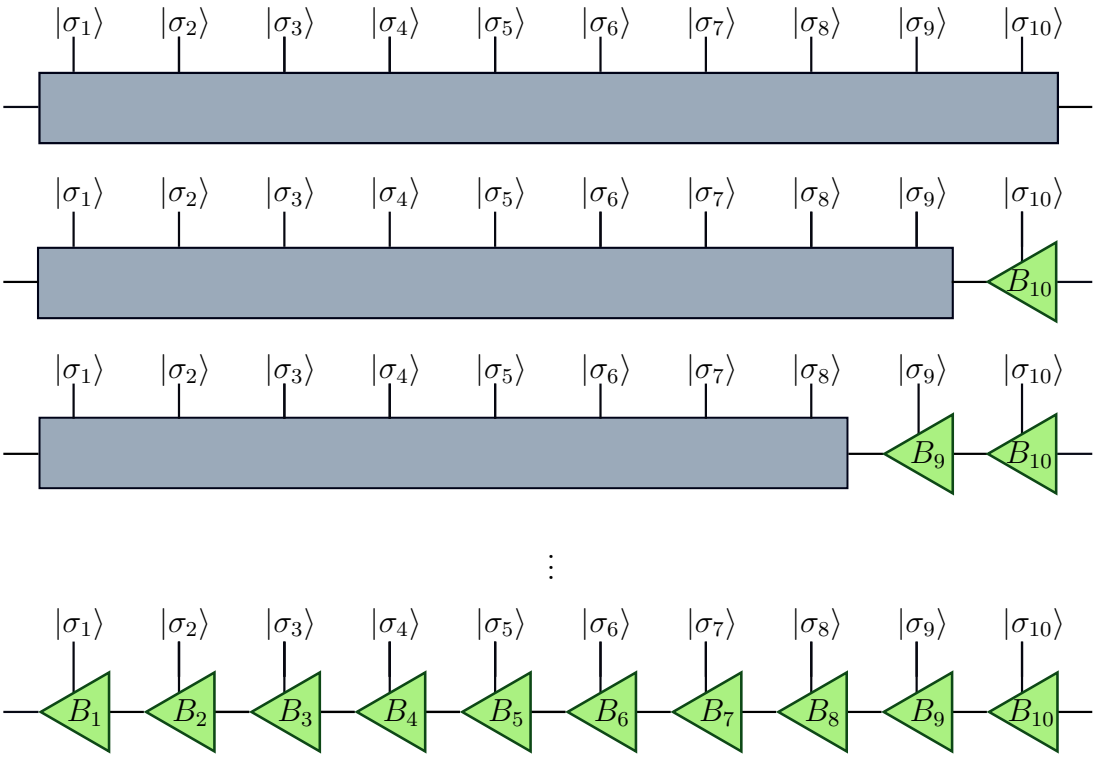


*Figure 2.3: Graphical representation of a construction of a matrix product state. In each step a singular value decomposition is performed and a three-dimensional tensor $B^{\sigma_l}$ is produced, represented by a triangle. Since we start from the right end of the system, we obtain a right-canonical MPS as indicated by the triangles pointing to the left.*

while the first form is used mostly in the context of truncation. We can combine the $A$ and $B$ tensors with the corresponding local bases states to orthonormal basis sets

$$|a_l\rangle_A = \sum_{\sigma_1,\ldots,\sigma_l} (A^{\sigma_1}\cdots A^{\sigma_l})_{1,a_l}|\sigma_1,\ldots,\sigma_l\rangle, \tag{2.1.16}$$

$$|a_l\rangle_B = \sum_{\sigma_{l+1},\ldots,\sigma_L} (B^{\sigma_{l+1}}\cdots B^{\sigma_L})_{a_l,1}|\sigma_{l+1},\ldots,\sigma_L\rangle, \tag{2.1.17}$$

and write the MPS as a Schmidt decomposition of the state $|\psi\rangle$ at the bond between site $l$ and $l+1$.

$$|\psi\rangle = \sum_{a_l} s_a |a_l\rangle_A |a_l\rangle_B. \tag{2.1.18}$$

The singular values obtained from the singular value decompositions iterated through the system are the Schmidt coefficients. They are strictly positive and the squared values sum up to one $\sum_\alpha s_\alpha^2 = 1$ if the state is normalised. They also indicate the amount of entanglement between the two halves of the system described by $|a_l\rangle_A$ and $|a_l\rangle_B$, which can be seen by the von Neumann entropy

$$S = -\sum_\alpha s_\alpha^2 \ln s_\alpha^2. \tag{2.1.19}$$

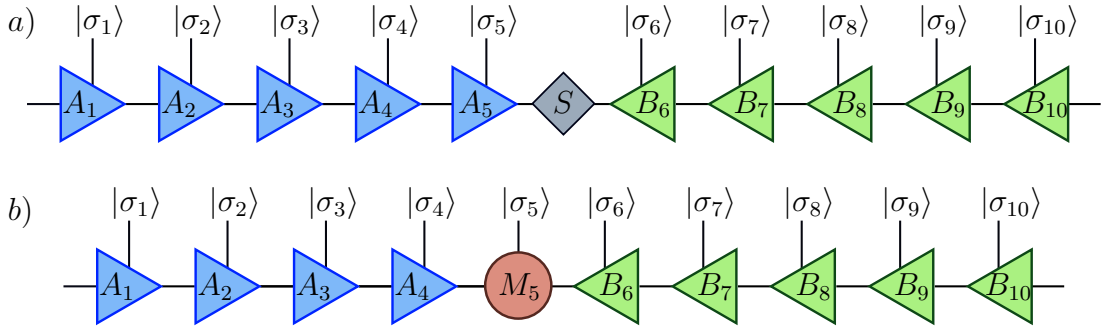


*Figure 2.4: a) Graphical representation of a mixed-canonical matrix product state. All tensors on site* 1 *to* 5 *are left-normalised and all states form site* 6 *to* 10 *are right-normalised. The singular values are collected in the centre bond matrix* $S$*. This representation is used especially for the truncation of MPSes since the tensors to the left of* $S$ *together with their local bases form an orthogonal basis set as well as the tensors to the right combined with their* $|\sigma_l\rangle$*. This results in a Schmidt decomposition. b) The centre bond matrix was contracted with the* $A$ *tensor of site* 5*. This mixed canonical state with respect to site* $l(=5)$ *is the key representation of most MPS methods since in most calculations the orthogonality properties of the* $A$ *and* $B$ *tensors can be used to simplify contractions enormously.*

If only one Schmidt coefficient is non-zero, it must be equal to one. Then, the von Neumann entropy is zero and Eq. (2.1.18) reduces to a simple product state. Thus, the two halves of the system are not entangled and the dimension of the index connecting the tensors on site $l$ and $l+1$, called bond dimension, is $m = 1$. Contrarily, the entropy is maximised by all singular values being equal $s_\alpha^2 = 1/r_l$, where $r_l$ is the bond dimension of the tensor on site $l$ and therefore the number of singular values. The MPS becomes a maximally entangled state. It is obvious that the distribution of the singular values determines the entanglement of the system halves and the actual size of the $s_\alpha$ how important each contribution is to the complete state $|\psi\rangle$.
This provides a natural way to truncate an MPS, i.e. to approximate the state $|\psi\rangle$ with another state $|\psi'\rangle$ that has a smaller bond dimension. This is necessary because, in general, the dimension of the tensors increases exponentially. If the dimension of the local basis $|\sigma\rangle$ is indicated by $d$, the first tensor will have the dimension 1 on the left side, a local dimension $d$ and on the right also the dimension $d$. The next tensor will have the bond dimension $d^2$ on the right hand side. This increases to the middle of the system where the bond dimension is $d^{L/2}$ and decreases in the same manner to the right hand side of the system. Therefore, in any reasonable system the bond dimensions are too large to be feasible and we need to find a better approximation, preferable while monitoring the induced error. So, we note that the the norm of a state written in the mixed-canonical decomposition is given by

$$\text{norm}(|\psi\rangle) = \sum_\alpha s_\alpha^2, \tag{2.1.20}$$

and the overlap of two states $|\psi\rangle$ and $|\psi'\rangle$, if they share the same left- and right-hand Schmidt basis $|a_l\rangle_A$ and $|a_l\rangle_B$ with different coefficients $s_\alpha$ and $s'_\alpha$ by

$$\langle\psi|\psi'\rangle = \sum_\alpha s_\alpha s'_\alpha. \tag{2.1.21}$$

If we now select only the largest $r$ singular values $s'_\alpha = s_\alpha$ if $\alpha \leq r$ and set the remaining values to zero $s'_\alpha = 0$ for $\alpha > r$, we will obtain a state with the norm $\sqrt{R} = \sqrt{\sum_{\alpha\leq r} s_\alpha^2}$. This is called a truncation on a single bond of a matrix product state. Let us now define the discarded weight $D = \sum_{\alpha>r} s_\alpha^2 \in [0,1]$ with the property $D + R = 1$. We can write the error induced by such a truncation of singular values between normalised states $|\psi_N\rangle$ and $|\psi'_N\rangle$ as

$$\begin{aligned} |||\psi'_N\rangle - |\psi_N\rangle|| &= ||R^{-\frac{1}{2}}|\psi'\rangle - |\psi\rangle||^2 \\ &= \frac{1}{R}\langle\psi'|\psi'\rangle - 2R - \frac{1}{2}\langle\psi'|\psi\rangle + \langle\psi|\psi\rangle \\ &= 1 - \sqrt{R} + 1 \\ &= 2 - 2\sqrt{1-D} = 2 - 2\sqrt{1 - \sum_{\alpha>r} s_\alpha^2}. \end{aligned} \tag{2.1.22}$$

In general, we want to truncate the bond dimension on each bond of the MPS. By using the triangle inequality we can find an upper bond to the error between the state $|\psi_N\rangle$ and the state $|\psi''_N\rangle$

$$|||\psi''_N\rangle - |\psi_N\rangle|| \leq |||\psi''_N\rangle - |\psi'_N\rangle|| + |||\psi'_N\rangle - |\psi_N\rangle||, \tag{2.1.23}$$

where $|\psi''_N\rangle$ is the state $|\psi\rangle'_N$ truncated a second time on another bond. Putting this together we can bound the error incurred by a series of SVDs with truncations on each bond by

$$|||\psi'_N\rangle - |\psi_N\rangle|| \leq \sum_{l=1}^{L} \sqrt{2 - 2\sqrt{1 - \sum_{\alpha>r} s_{l,\alpha}^2}}, \tag{2.1.24}$$

where $|\psi'_N\rangle$ is the new normalised state after all the truncations. Thus, the amount of singular values we discard not only reduces the numerical effort dramatically, but it also defines an upper bound for the induced error. Typically in the literature, the degree of truncation is given by the truncation threshold $t$ up to which all singular values are kept $s'_\alpha = s_\alpha$ for $s_\alpha \geq t$ and $s'_a = 0$ for $s_\alpha < t$ or by the truncated weight $w = \sum_{\alpha>r} s_{l,\alpha}^2$. In the latter case the smallest singular values are discarded until their squared sum reaches $w$. The truncated weight is a much better truncation criterium since it directly offers the possibility to calculate the upper bond of the induced error in Eq. (2.1.24) and thus gives a reliable idea of how severe a truncation is independent of the distribution of singular values. In contrast, the same truncation threshold $t$ can induce errors of completely different orders of magnitude depending on the distribution of the singular values. In

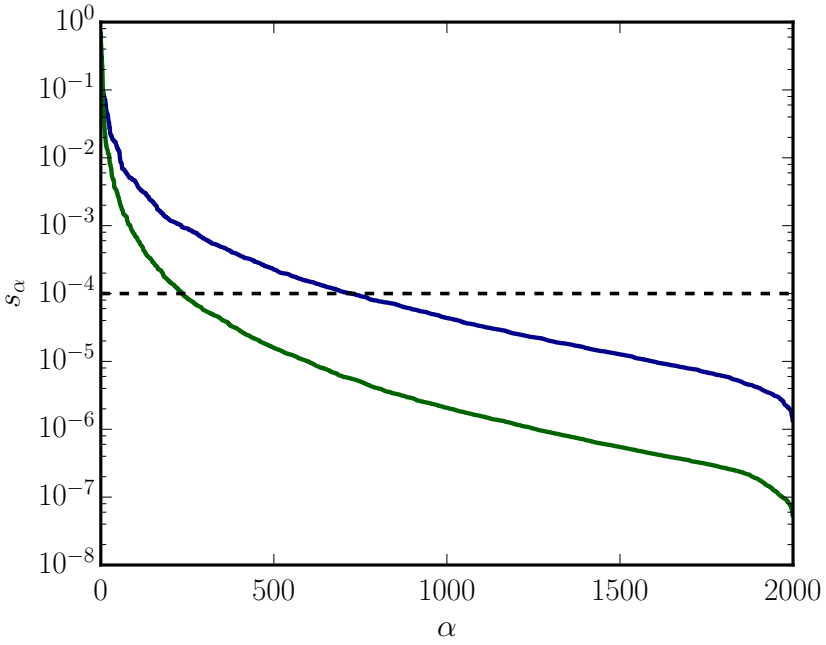


*Figure 2.5: Two singular value distributions (solid lines) and a fictitious truncation threshold $t = 10^{-4}$ (black dashed line). The same value of t results in different errors after the truncation at the bond according to Eq.* (2.1.22) *since the distribution of singular values is different.*

Fig. 2.5 two different distributions of singular values $s_\alpha$ can be seen and a line at a fictitious truncation threshold $t = 10^{-4}$. The corresponding sum of the discarded squared values is very different in both cases and without knowing the distribution of the singular values one can not determine how big the corresponding error is after the truncation. However, in most calculations those two truncation measures can roughly be connected by $w \approx t^2$. For all our calculations we will denote the amount of truncation in terms of a truncated weight.

We want to emphasise again the very important connection between the entanglement of a state and the bond dimension needed to describe the state accurately. The stronger entangled a state is, the more non-zero singular values of approximately the same size exist, which does not allow for an efficient truncation and thus leads to a high bond dimension. Matrix product states are only an efficient description for relatively lowly entangled states. Fortunately, it has been shown that for ground states of systems with size $L$ and a gap between the ground state and excitations the entanglement between two halves of the system goes with $\sim L^{D-1}$, where $D$ denotes the spatial dimension of the system. This is known as the area law[73,77] and states for one-dimensional systems that the entanglement is essentially independent of system size. The vast success of MPSes for one-dimensional and small two-dimensional problems and its failure for larger two-dimensional systems[78,79] can be explained very well by this.

## 2.2 Matrix Product Operators

It is not only possible to decompose any state $|\psi\rangle$ into a product of matrices but also any operator. These so-called matrix product operators (MPOs) can be constructed in the same fashion as MPSes. Given a Hilbert space $\mathcal{H} = \otimes_l^L \mathcal{H}_l$ and corresponding basis states $\{|\sigma_l\rangle\}$ of the Hilbert spaces $\mathcal{H}_l$ we can write any operator $\hat{H} : \mathcal{H} \to \mathcal{H}$ as

$$\hat{H} = \sum_{\sigma_1,\tau_1} \sum_{\sigma_2,\tau_2} \cdots \sum_{\sigma_L,\tau_L} c^{\sigma_1,\sigma_2\cdots\sigma_L}_{\tau_1,\tau_2\cdots\tau_L} |\tau_1\rangle \otimes |\tau_2\rangle \otimes \cdots \otimes |\tau_L\rangle\langle\sigma_1| \otimes \langle\sigma_2| \cdots \langle\sigma_L|. \tag{2.2.1}$$

Analogously to the decomposition of the multi-dimensional coefficient tensor of the matrix product state in the previous section, we can decompose the coefficient tensor $c$ of the operator $\hat{H}$ with size $\Pi_l d_l^2$ into a series of tensors $\{W^{\sigma_l,\tau_l}_{w_{l-1},w_l}\}$ of rank 4

$$c^{\sigma_1,\sigma_2\cdots\sigma_L}_{\tau_1,\tau_2\cdots\tau_L} = \sum_{w_1} \sum_{w_2} \cdots \sum_{w_L} W^{\sigma_1,\tau_1}_{1,w_1} W^{\sigma_2,\tau_2}_{w_1,w_2} \cdots W^{\sigma_L,\tau_L}_{w_{L-1},w_L}. \tag{2.2.2}$$

A graphical representation of an MPO is depicted in Fig. 2.6 as well as an MPO-MPS application in Fig. 2.7. It can be seen that after the contraction of the indices connect-

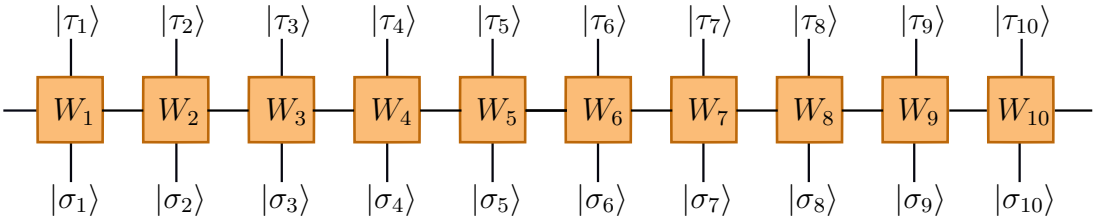


*Figure 2.6: Graphical representation of a matrix product operator. In contrast to an MPS, now we have two local indices, one located on the bottom of each square representing a tensor and one at the top. Again, connecting lines are indicating contractions and are called bonds (as for MPS).*

ing the MPO and MPS we will obtain an MPS again. In general, the bond dimension $m_i^R = w_i^O m_i^\psi$ of the new MPS tensor of site $i$ will be the product of the bond dimension of the MPO $m_i^O$ and MPS $m_i^\psi$, which normally will be truncated immediately to some smaller value $\tilde{w}_i^R \leq m_i^R$. Since this is rather inefficient, other approaches like the zip-up algorithm [80] or a variational approach [43] are recommended. The key idea of the zip-up algorithm is to contract the tensors of MPS and MPO consecutively and truncating each tensor directly before contracting the next site. This approach has proven to be as accurate as the naive contraction of MPS and MPO and significantly faster. The intermediate tensors occurring during the computation only have a bond dimension of $m_i^R \times d_i \times w_i^O m_i^\psi$ with $d_i$ being the bond dimension of the local state space $|\sigma_i\rangle$. In contrast, during the the naive approach tensors with bond dimension $w_i^O m_i^\psi \times d_i \times w_i^O \times m_i^\psi$ occur, which are larger in general.
For very large MPOs even the zip-up algorithm can be very inefficient. Thus, it can be advantageous to use a variational approach. We describe this ansatz in detail in section

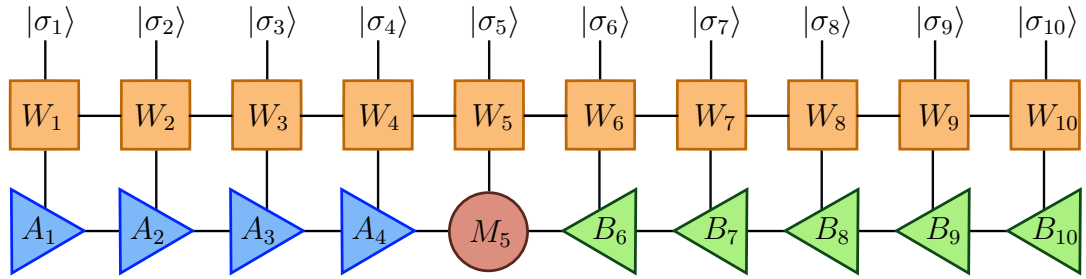


*Figure 2.7: Graphical representation of a multiplication of an MPO to an MPS. After the contraction of the MPO and MPS a new matrix product state is obtained. In general the bond dimension of the new MPS is much higher than of the original MPS.*

4.2.1 in the context of orthogonalisation, except that the environment tensor must be replaced by the contraction of the MPS, MPO and current estimate MPS.
Since we now have MPSes and MPOs defined, we are able to construct overlaps, operators and scalar applications as well as expectation values, which form the building blocks of any MPS method. For further definitions and discussions about runtimes, scalings and implementation details we will refer the reader at this point to more in-depth literature[43,57].

# Chapter 3

# Density Matrix Renormalisation Group

The density matrix renormalisation group (DMRG) was developed by Steve White in 1992[13] for infinite systems and soon became the most powerful numerical method for studying one-dimensional quantum lattices and determining their ground states[81]. The key idea is to consider an increasing number of lattice sites and truncating the number of states describing the system to keep the size of the Hilbert space manageable. For that it is assumed that there exists a reduced state space that describes the essential physics of the system effectively and that DMRG can identify this subspace. Later, because of its great success, DMRG was extended to finite systems and systems with long-range correlations too. This is achieved by building up a one-dimensional lattice with the desired system size with infinite DMRG and afterwards using iterative sweeps over the system to determine a converged ground state description of the system[43,81].
While DMRG was initially only used to compute ground states and static properties of low-energy spectra of strongly correlated Hamiltonians such as the Heisenberg, Hubbard and $t - J$ model, it was extended to study dynamic properties such as frequency dependent conductivities and dynamical structure factors[82,83,84] as well.
As described in the introduction of the previous chapter, in the late 90s the connection between DMRG and matrix product states (MPS) was discovered[64,65], which finally led to the very effective and adaptive MPS-based formulation of DMRG[45,68]. Nevertheless, it is still true that two-dimensional systems can only be solved for very small system sizes, while one-dimensional systems are typically solvable with DMRG up to an accuracy that is only limited by machine precision. There exist several ides how to tackle two-dimensional systems, such as mapping the problem to an one-dimensional system[74] or using projected entangled pair states[75,76], but all methods have in common that the required numerical resources increase drastically.
However, research is still ongoing with the aim of improving the performance of DMRG further. This includes the combination of tensor networks with global symmetries[85,86,87] as well as developments from the field of Quantum Information[88,89] and Quantum Chem-

istry[21]. This is even more important since model Hamiltonians become more and more realistic and consequently more complex. In this context, DMRG is also combined with other methods like dynamical mean-field theory which generates Hamiltonians that include long-range interactions between numerous lattice sites, which give rise to small but at the same time very strongly entangled systems. Thus, ideas and methods from other fields such as Quantum Chemistry can lead to huge performance improvements. Most of these methods has been validated in calculations of highly correlated molecules for decades and still have not found their way into the condensed matter community. Some concepts as reordering of lattice sites based on entanglement information[21,89], variationally obtaining better bases sets for the lattice sites[90] or even changing the topology of the whole lattice system[40,44] are focused on reducing the entanglement in systems and thus can lower bond dimension of MPSes significantly. Other approaches try to systematically find better starting states based on Hartree-Fock orbitals to reduce the convergence times[88,91] compared to using arbitrary random starting states. Overall, improvements based on these concepts can very often lead to performance increases by factors up to ten or higher. Therefore, it is not surprising that DMRG is still considered to be a key method for tackling two-dimensional problems for the future.
In this chapter we want to present the fundamental concept of DMRG based on the MPS formalism and several improvements we find useful for the rest of the thesis, This includes the formulation of strictly single-site DMRG as well as the reordering of lattices based on entanglement information. In the end of this chapter we will shortly focus on binary tree tensors, which were developed by us together with collaborators during this thesis. A first implementation showed that they start to be competitive with usual one-dimensional MPSes for system sizes that were slightly larger than necessary for our models. However, other lattice topologies used in quantum chemistry, such as minimal entangled trees or minimal spanned trees, are a promising route to decrease entanglement in systems further and should be kept in mind for further research. Therefore, we will end this chapter by providing a short introduction to these very interesting concepts.

## 3.1 Single-Site-DMRG

The aim of DMRG is to find the state $|\psi\rangle$ represented by a matrix product state which minimises the energy of a Hamiltonian $\hat{H}$, represented as an MPO,

$$\min_{|\psi\rangle}\left(E=\frac{\langle\psi|\hat{H}|\psi\rangle}{\langle\psi|\psi\rangle}\right). \tag{3.1.1}$$

We can reformulate the problem to the minimisation of $\langle\psi|\hat{H}|\psi\rangle$ under the constraint that $\langle\psi|\psi\rangle=1$. This can be solved using a Lagrangian multiplier[92] $\lambda$, resulting in

$$\min_{|\psi\rangle}\left(\langle\psi|\hat{H}|\psi\rangle-\lambda\langle\psi|\psi\rangle\right). \tag{3.1.2}$$

Optimising the complete MPS corresponds to solving a highly complex non-linear problem which is nearly impossible to do efficiently and reliably. Instead, the key idea of DMRG is to optimise the tensors of the MPS iteratively one after the other while moving through the system using SVDs. This reduces the problem to a multi-linear optimisation problem which can be solved efficiently via the following trick: We assume the the state $|\psi\rangle$ is in the mixed-canonical representation with the tensors on sites 1 to $l-1$ being left-normalised and the tensors on site $l+1$ to $L$ being right-normalised. In the notation of matrix product states we can write the overlap $\langle\psi|\psi\rangle$ as

$$\langle\psi|\psi\rangle = \sum_{\sigma_l} \sum_{a_{l-1} a_l} \sum_{a'_{l-1} a'_l} \Psi^A_{a_{l-1},a'_{l-1}} M^{\sigma_l^\dagger}_{a_{l-1},a_l} M^{\sigma_l}_{a'_{l-1},a'_l} \Psi^B_{a_l,a'_l}, \tag{3.1.3}$$

where we kept the tensor of site $l$ explicitly. The tensors on the left and right hand site of site $l$ we combined as

$$\Psi^A_{a_{l-1},a'_{l-1}} = \sum_{\sigma_1,\ldots,\sigma_{l-1}} (M^{\sigma_{l-1}\dagger} \cdots M^{\sigma_1\dagger} M^{\sigma_1} \cdots M^{\sigma_{l-1}})_{a_{l-1},a'_{l-1}}, \tag{3.1.4}$$

$$\Psi^B_{a_l,a'_l} = \sum_{\sigma_{l+1},\ldots,\sigma_L} (M^{\sigma_{l+1}} \cdots M^{\sigma_L} M^{\sigma_L\dagger} \cdots M^{\sigma_{l+1}\dagger})_{a'_l,a_l}. \tag{3.1.5}$$

Because of the chosen representation and the orthogonality properties of the tensors, particularly clear in the graphical representation (Fig. 3.1), the last two expressions simplify to unit matrices

$$\Psi^A_{a_{l-1},a'_{l-1}} = \delta_{a_{l-1},a'_{l-1}} \quad \text{and} \quad \Psi^B_{a_l,a'_l} = \delta_{a_l,a'_l}. \tag{3.1.6}$$

Let us now consider the term $\langle\psi|\hat{H}|\psi\rangle$, with $\hat{H}$ written in MPO language

$$\langle\psi|\hat{H}|\psi\rangle = \sum_{\sigma_l,\sigma'_l} \sum_{a'_{l-1},a'_l} \sum_{a_{l-1},a_l} \sum_{b_{l-1},b_l} L^{a_{l-1},a'_{l-1}}_{b_{l-1}} W^{\sigma_l,\sigma'_l}_{b_{l-1},b_l} R^{a_l,a'_l}_{b_l} M^{\sigma_l *}_{a_{l-1},a_l} M^{\sigma'_l}_{a'_{l-1},a'_l} \tag{3.1.7}$$

with $L$ being the contraction of all tensors left of site $l$ with the MPO tensors and $R$ equivalently defined for the tensors on the right of site $l$. In Fig. 3.2 a graphical representation of these to operators can be seen. If we now consider the extremum by differentiating with respect to $A^\dagger$ and setting the equation equal to zero, we find

$$\sum_{\sigma'_l} \sum_{a'_{l-1},a'_l} \sum_{b_{l-a},b_l} L^{a_{l-1},a'_{l-1}}_{b_{l-1}} W^{\sigma_l,\sigma'_l}_{b_{l-1},b_l} R^{a_l,a'_l}_{b_l} M^{\sigma'_l}_{a'_{l-1},a'_l} - \lambda M^{\sigma_l}_{a'_{l-1},a'_l} = 0, \tag{3.1.8}$$

which is depicted completely in Fig. 3.2. This is an eigenvalue equation. That can be seen by introducing the matrix $H$ by reshaping $H_{(\sigma_l a_{l-1} a_l),(\sigma'_l a'_{l-1} a'_l)} = \sum_{b_{l-1},b_l} L^{a_{l-1},a'_{l-1}}_{b_{l-1}} W^{\sigma_l,\sigma'_l}_{b_{l-1},b_l} R^{a_l,a'_l}_{b_l}$ as well as the vector $\nu$ with $\nu_{\sigma_l a_{l-1} a_l} = M^{\sigma_l}_{a_{l-1},a_l}$ and arriving at

$$H\nu - \lambda\nu = 0 \tag{3.1.9}$$

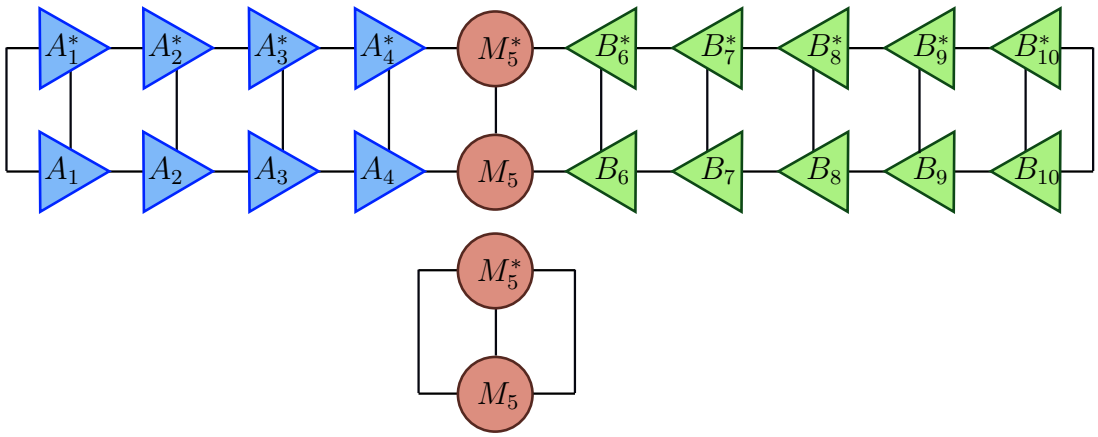


*Figure 3.1: a) Graphical representation of the overlap of a state $|\psi\rangle$ with itself. The ket state is depicted on the bottom while the bra state $\langle\psi|$ is on the top. Since the state is written in the mixed canonical representation with respect to site $l(=5)$, the contractions of the tensors $A$ and $B$ with their complex conjugated counter parts result in unit matrices, leaving only the contraction of the centre tensor $M^{\sigma_l}$ as seen in b).*

with matrix dimension $(dm^2 \times dm^2)$ for $H$. Solving for the lowest eigenvalue $\lambda$ and its eigenvector $\nu$ will result in the locally optimal tensor $M^{\sigma_l}_{a_{l-1},a_l}$ after reshaping $\nu$. A simple SVD lets us move to the next site while staying in the mixed canonical representation. We can then optimise the local tensor on site $l+1$ by solving another eigenvalue problem. This can be done very efficiently when the operators $L$ and $R$ are saved and updated iteratively instead of calculated completely anew. We can sweep back and forth from the left edge to the right edge of the system in this manner, visiting and updating each site for the lowest eigenvalue until we observe convergence. The eigenvalue solver best suited for DMRG is, depending on details, the Lanczos or the Jacobi-Davidson method since, in general, the matrix dimension of $H$ $dD^2$ is too large for an exact diagonalisation. Lanczos only requires the application of $H$ onto the local tensor $A_l$ with costs $O(2m^3dw+m^2d^2w^2)$ and thus equally much as the contraction of the left and right part of the Hamiltonian $L$ and $R$ but significantly more than the SVD $O(m^3d)$. It is therefore not surprising that between 75% and 95% of the total runtime of the single site DMRG algorithm is spent on the eigensolver step. However, the single-site DMRG algorithm is a very easy and cheap way of finding the ground state of a system.
The left and right sweeps are repeated until convergence is achieved which is measured with respect to the energy. Typical values which we want to reach are changes below $\Delta E < 10^{-10}$. A much better test is to consider $\langle\psi|\hat{H}^2|\psi\rangle - (\langle\psi|\hat{H}|\psi\rangle)^2$ to check whether DMRG found an eigenstate. Therefore, the expression should approach 0 as closely as possible. Unfortunately, for large bond dimension of the Hamiltonian ($m_H \approx 16$) the calculation of $\hat{H}^2|\psi\rangle$ becomes too demanding, not allowing us to follow this route.
As for all variational methods the convergence towards the solution of the considered problem can depend on the starting state. At least a part of the randomly generated

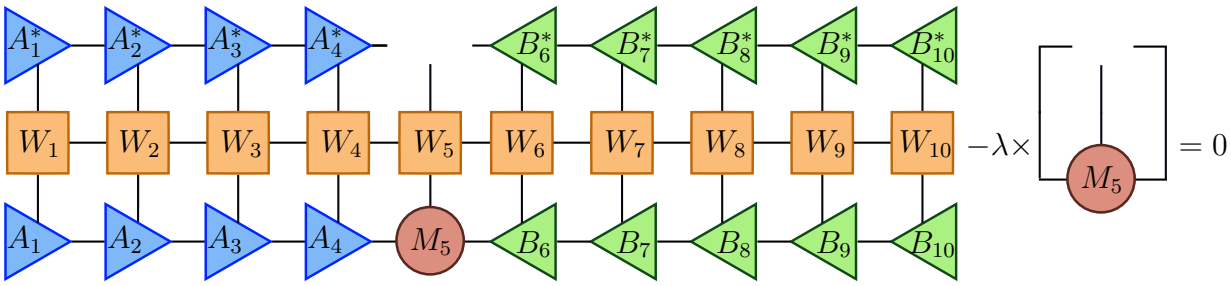


*Figure 3.2: Graphical representation of the eigenvalue equation with the definition of the matrices $L$ and $R$ describing the effective basis of the left and right part of the system.*

starting state $|\psi\rangle$ has to be parallel to the global ground state to allow DMRG to converge to it. A significant drawback of single-site DMRG is that the bond dimension during the optimisation procedure cannot be increased but only decreased during the SVDs. If the ground state $|E_0\rangle$ has a higher amount of entanglement than the initial state $|\psi\rangle$ and therefore needs a larger bond dimension, it is impossible to obtain a good description of $|E_0\rangle$. The usual way of solving this issue is to optimise not only a single site but two adjacent sites at the same time. In the so-called two-site DMRG algorithm, the tensors of site $l$ and $l+1$ are combined before and split up after the solution of the eigenvalue problem. The split up with the SVD allows for an increase of the bond dimension of the tensor $M_l$. However, this increases the size of the effective matrix $H$ and thus slows the algorithm down significantly.

## 3.2 Strictly Single-Site DMRG

In 2015 Hubig et al. developed a version of the single site DMRG which optimises a single site tensor with an additional subspace expansion[93]. The subspace expansion allows an increase of the bond dimension and thus improves the convergence properties substantially. This new approach performs DMRG calculation significantly faster since the scaling of single-site DMRG $\mathcal{O}(m^3dw)$ is better by a factor of $d$ than the scaling of two-site DMRG $\mathcal{O}(m^3d^2w)$. This improvement is scaled down slightly by the fact that the single-site DMRG method needs more sweeps to converge.
The idea of a subspace expansion originates from the numerical lineal algebra community[94,95] and relies on the fact that a matrix product of two matrices $A \in \mathbb{R}^{m\times n}$ and $B \in \mathbb{R}^{n\times p}$ can be expanded with another matrix $P$ in $A$ and zeros in $B$ while keeping their product $A \cdot B \in \mathbb{R}^{m\times p}$ invariant

$$A \cdot B \to \begin{bmatrix} A & P \end{bmatrix} \cdot \begin{bmatrix} B \\ 0 \end{bmatrix} = A \cdot B + P \cdot 0 = A \cdot B. \tag{3.2.1}$$

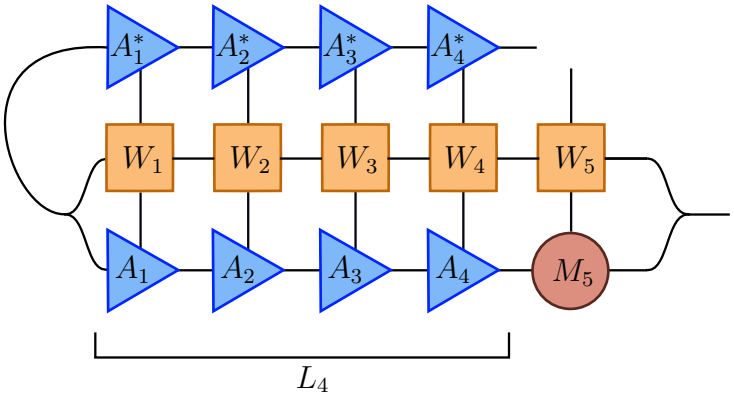


*Figure 3.3: Graphical representation of the expansion term defined in Eq. (3.2.4) for a left-to-right sweep after the optimisation of site 5. The indices on the left of site 1 and the right of site $i$ are fused together.*

This also can be done in the MPS context. The expansion over the bond $m_l$ from the left is written as

$$M_l^{\sigma_l} \to \tilde{M}_l^{\sigma_l} = \begin{bmatrix} M_l^{\sigma_l} & P_l^{\sigma_l} \end{bmatrix}, \tag{3.2.2}$$

$$M_{l+1}^{\sigma_{l+1}} \to \tilde{M}_{l+1}^{\sigma_{l+1}} = \begin{bmatrix} M_{l+1}^{\sigma_{l+1}} \\ 0 \end{bmatrix}. \tag{3.2.3}$$

With this approach single site DMFT can optimise the site $l+1$ with the increased bond dimension $m_l + m_{P_l}$ where $m_l$ is the original bond dimension and $m_{P_l}$ is the dimension of the added rows of site $l$. If the optimisation finds out that elements of the enlarged space are not lowering the energy they are simply discarded by setting the associated factors on site $l+1$ to zero.
It is noteworthy that after the expansion, as in standard DMRG, an SVD is used to move to the next site. During the SVD the most relevant states $m_r$ of the enlarged space $m_l + m_{P_l}$ are selected. This allows to increase the bond dimension adaptively but can also lead to original states of the matrix $M_l^{\sigma_l}$ being discarded. Unless the expansion states are lower in energy, this can increase the energy slightly.
Mathematically, choosing the local components of the exact residual written in MPS notation as the expansion term offers global convergence to the minimum as Dolgov and Kressner showed in their original work [94]. Since this is in general very costly to compute, Hubig et al. [93] proposed an expansion term of the form

$$P_l = \alpha L_{l-1} M_l W_l, \tag{3.2.4}$$

also depicted in Fig. 3.3. The term $M_l W_l$ on the $l$-th site describes the application of the MPO $W_l$ to the current MPS $M_l$, while the left-contraction $L_{l-1}$ is a projection of the left-hand side basis of this new tensor to the basis of the original tensor. Therefore, the whole term describes the states generated by applying the Hamiltonian on the entire left

of the system and thus incorporates some global information. The expansion term when moving from the right to the left of the system is defined accordingly

$$P_l = \alpha M_l W_l R_{l+1}. \tag{3.2.5}$$

$\alpha$ is a scalar controlling the magnitude of the expansion. The choice of $\alpha$ is subtle and depends on multiple observations including the amount of increase or decrease of the energy during an expansion or whether the actual state is an eigenstate or not. For a more detailed discussion of the adaptive choice of $\alpha$ we refer to Hubig et al. [57]. The expansion term has a certain bond dimension depending on the size of the Hamiltonian and the state $|\psi\rangle$. During our DMFT calculation we observed much better convergence properties if the expansion is limited to a maximal bond dimension of 500 allowing a rapid expansion of the bond dimension. This is especially true for so called tunnelling Hamiltonians which have to be introduced artificially to Hamiltonians to break symmetries which have not explicitly been implemented to ensure convergence to the global ground state (see chapter 5.3.2).

## 3.3 Optimal Order of Tensors

During the construction of an MPO, we encountered the Schmidt decomposition Eq. (2.1.18) which describes the amount of entanglement between the left and right part of the system expressed by effective basis sets. The Schmidt coefficients, or singular values, are directly related to the bond dimension by the fact that they also indicate how much weight each basis combination carries to the whole state $|\psi\rangle$. This can be used to approximate the MPS by keeping only the most important states, setting all other singular values to zero while moving successively through the system. At this point truncated weights and truncation threshold are typically introduced. They give a measure on how many states have to be discarded.
However, since the order of the MPS sites is arbitrarily chosen when constructing the system, it seems natural to ask whether better ways to order a system exist in order to achieve an overall decrease of entanglement in the system as well as of the bond dimension of the MPS states. In quantum chemistry this question has been asked for a long time and several methods were developed to determine an optimal ordering of the MPS sites [21]. We want to introduce a very simple and the same time efficient ansatz useable for one-dimensional tensor topologies. We start with the mutual information

$$I_{i,j} = S_i + S_j - S_{i,j}, \tag{3.3.1}$$

between two sites $i$ and $j$. $S_i$ describes the von Neumann entropy of the single site $i$

$$S_i = -\sum_{\alpha} s_{a,i}^2 \ln s_{a,i}^2, \tag{3.3.2}$$

with $s_{a,i}$ being the singular values of site $i$ in the mixed-canonical basis with respect to this site, while $S_{i,j}$ is the von Neumann entropy of a subsystem consisting of site $i$ and $j$

together. We express the overall entanglement encoded in the wave function in form of a cost function

$$I_{\text{system}} = \sum_{i,j} I_{i,j} d_{i,j}^{\eta}. \tag{3.3.3}$$

Since the information about the entanglement between two sites $i$ and $j$ must be carried from one site to the other, it increases the bond dimension of all sites in between. Therefore, it is reasonable to introduce a distance function

$$d_{i,j} = |i - j|, \tag{3.3.4}$$

in the cost function to indicate that strongly entangled sites should be close together. In principle, the exponent $\eta$ has to be chosen in a way that reflects the physical behaviour of the overall entanglement. However, taking $\eta = 2$ over any other choice of $\eta$ allows us to calculate the optimum of Eq. (3.3.3) directly by using spectral graph theory instead of performing an optimisation procedure. More precisely, with this choice the problem can be written in the form

$$F(x) = x^{\dagger} L x = \sum_{i,j} I_{i,j} (x_i - x_j)^2 \tag{3.3.5}$$

by defining the Laplacian

$$L_{i,j} = D_{i,j} - I_{i,j}, \tag{3.3.6}$$

with the diagonal

$$D_{i,j} = \delta_{i,j} \sum_{j'} I_{i,j'}. \tag{3.3.7}$$

This optimisation problem can be solved by using spectral graph theory[96]. Under the constraints

$$\sum_i x_i = 0 \quad \text{and} \quad \sum_i x_i^2 = 1. \tag{3.3.8}$$

the second eigenvector of the Laplacian, the so-called Fiedler vector, is the solution that minimises $F(x)$. Ordering the entries of the Fiedler vector in an increasing or decreasing way provides the optimal ordering of the system. Unfortunately, this approach requires us to have knowledge about the mutual information between all sites of the system. That information can only be obtained from the wave function itself and therefore requires a DMRG calculation to determine $I_{i,j}$. To save computation time we perform the DMRG calculation to determine the mutual information with a low bond dimension, e.g. $m = 500$. That is reasonable since DMRG always keeps the biggest singular values and thus also describes the most important entanglement in the system. In our experience that is enough to obtain a very good approximation of the mutual information and therefore a

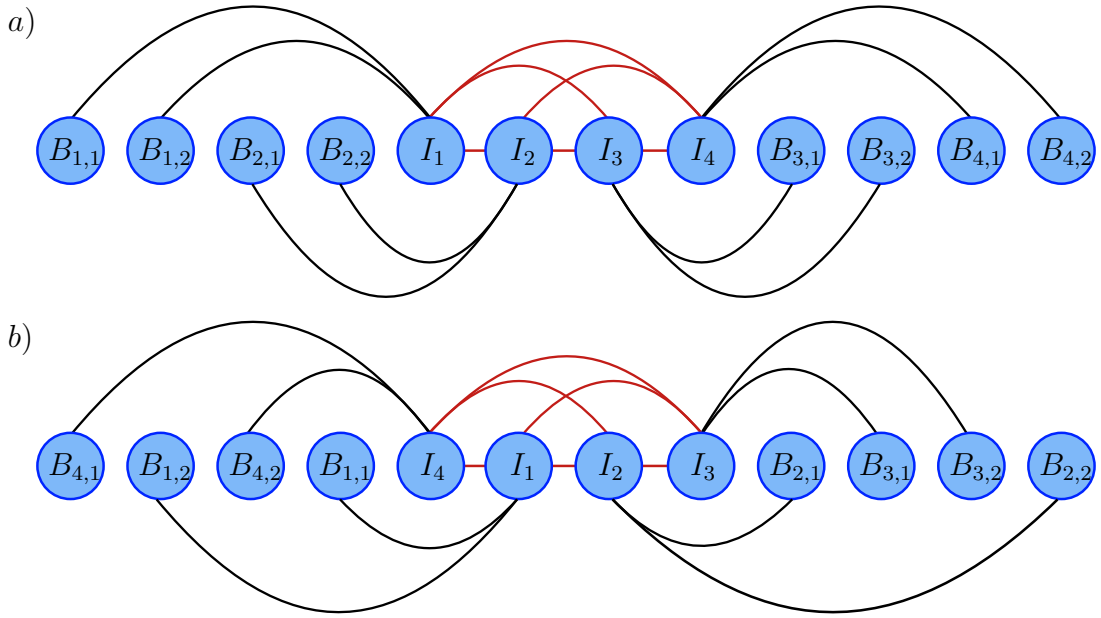


*Figure 3.4: a) The four-site dynamical cluster approximation Hubbard model ordering in our dynamical mean-field theory calculations. We typically place the impurities in the middle of the system and the bath sites symmetrically around it so the distance to the impurity sites is not too large. The bath sites only have an on-site energy and couple via single-particle hopping with only one impurity. The impurities themselves couple with each other in a more complicated way explained in section 6. The second and third impurity as well as their bath sites are completely degenerate. b) New ordering of the same system obtained with the Fiedler vector. Our initial ordering was a good choice since we observe only small changes. The impurity sites are still all located in the middle of the system but it seems that the degenerate sites are sufficiently strongly entangled that the method wants to place them close to each other in the same system half. The data was obtained with an interaction strength $U = 7$, nearest neighbour hopping $t_x = t_y = 1$, next-nearest neighbour hopping $t_p = 1$, chemical potential $\mu = 1.3$ and a bond dimension for the ground state search $m = 2000$.*

good approximation of the optimal ordering of the system for a very cheap extra DMRG run. Subsequent reorderings yield less and less reordering of the sites, supporting our assumption.

Depending on how bad the original ordering of the system with respect to entanglement properties was, we observe reductions of the bond dimension by a factor between 1 and 5 while obtaining the same or a better energy for the ground state. Since the computation time of the SVDs scales with the bond dimension cubed, we were able to observe speedups of a factor 100 in the best cases, but more often around $2 - 10$.

In Fig. 3.4 a) we depicted the typical setup of a DMFT impurity Hamiltonian. In this case it is a Hubbard model with four-site dynamical cluster approximation in momentum space. That means we have four impurities $I_1, I_2, I_3$ and $I_4$ which interact with each other (red lines) while each impurity has its own non-interacting bath consisting of two sites

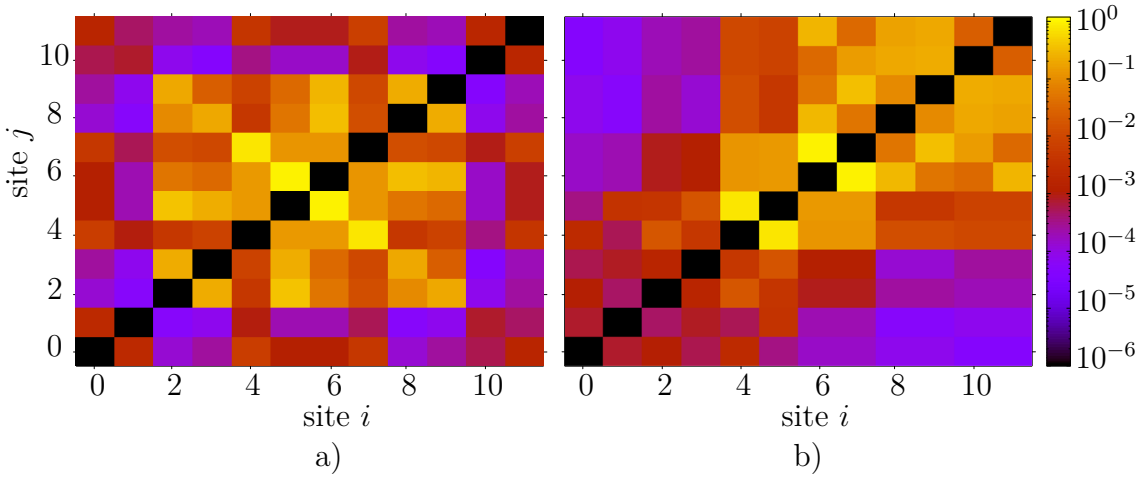


*Figure 3.5: Mutual information $I_{i,j}$ as defined in Eq. (3.3.1) for the system described in Fig. 3.4. a) Mutual information for the unordered system according to panel a) of Fig. 3.4. The highest entanglement is clearly present between the impurity sites and between the bath sites of the degenerate impurities. b) Mutual information after the reordering as described in panel b) of Fig. 3.4. The stronger entangled sites are laying closer together which is reflected in $I_{i,j}$ being more diagonal. The stronger entangled degenerate sites are now located on the upper right part of the system. This is also advantageous since the possible maximal bond dimension there is much smaller than in the middle of the system. The systems parameters are described as in Fig. 3.4.*

$B_{i,n}$ which only couple via simple single particle hopping to their impurity (black lines). The impurities 2 and 3 and their bath sites are degenerate. Since we assume that the interaction between the impurity sites generate much more entanglement, we placed them close to each other and tried to keep the distance between impurity sites and bath sites to a minimum. In panel b) the system after reordering is displayed. While the impurity sites are still located in the middle of the system, they are reshuffled as well as the bath sites. In the reordered system the degenerate sites are located next to each other on the right hand site of the system. They are strongly entangled with each other which can be seen clearly in Fig. 3.5 where we show the mutual information before a) and after b) the reordering. The reordering clearly locates the stronger entangled sites near each other as indicated by the more diagonal form of $I_{i,j}$ in figure b). The cost function value was decreased by the reordering from originally $\chi = 79.5$ to $\chi_{ordered} = 44.3$ indicating a moderate improvement. Another reordering of the already reordered system only yields swapping between one ore two of the degenerate sites with nearly constant cost function values. This clearly shows that we obtained the optimal ordering or at least an ordering which is very close to it.

It is not always as obvious as in this case how to order the sites optimally or what kind of order is good starting guess. System size, other physical parameters or other models can alter the structure significantly. In Fig. 3.6 a) we show our standard ordering for the real three band material $Sr_2VO_4$ with two-site dynamical cluster approximation in real space.

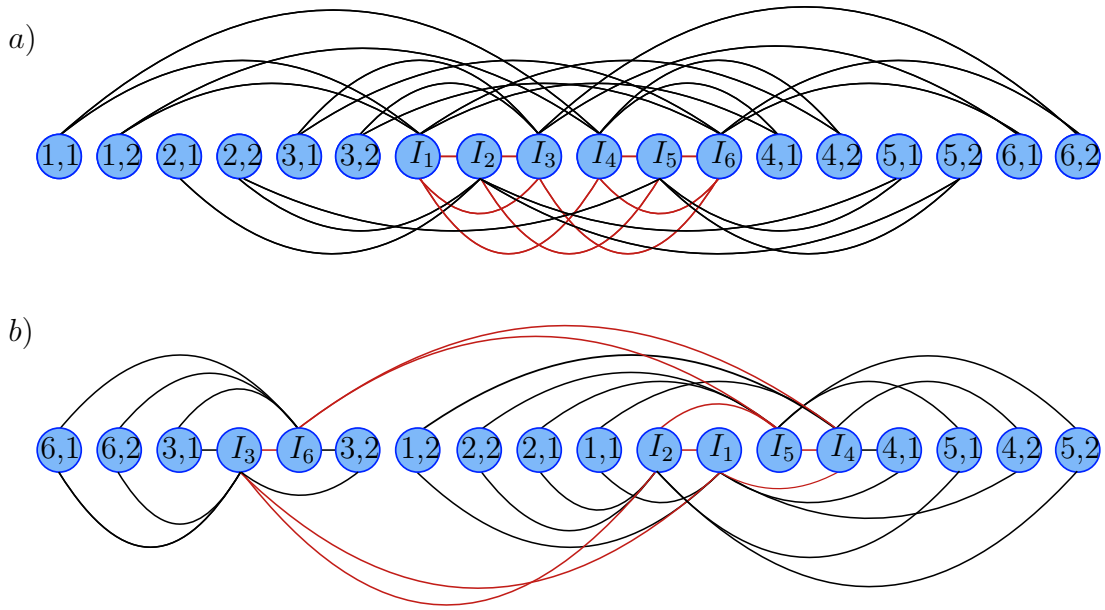


*Figure 3.6: a) The two-site dynamical cluster approximation* $Sr_2VO_4$ *model ordering in our dynamical mean-field theory calculations. We typically place the impurities in the middle of the system and the bath sites symmetrically around it so the distance to the impurity sites is not too large. The model consists of three bands, with band* 2 *and* 3 *being degenerate. Because of the two-site dynamical cluster approximation each band is described by two impurity sites (*$I_1$ *and* $I_4$ *for band* 1*,* $I_2$ *and* $I_5$ *for band* 2*, and* $I_3$ *and* $I_6$ *for band* 3*) each having a bath. The bath sites only have an on-site energy and couple via single-particle hopping with two impurities belonging to the same band. The impurities themselves couple with each other in a more complicated way explained in section 7. Between the impurities belonging to the same band exist single-particle hopping. b) New ordering of the same system obtained with the Fiedler vector. Our initial ordering was not a good choice since we observe significant changes. While the impurity sites describing the degenerate bands are still located next to each other, the third band was separated and placed on the left edge of the system. As for the Hubbard model, the bath sites are located around the impurity sites. But It seems that the entanglement generated by the dynamical cluster approximation is stronger than the entanglement generated by the model specific interactions. In the new ordering the Hubbard-Kanamori interaction is long-ranged while interaction induced by the dynamical cluster approximation is short-ranged. The data was obtained with an interaction strength* $U = 6$*,* $J = 0.7$*, chemical potential* $\mu = 1.3$ *and a bond dimension for the ground state search* $m = 2000$*.*

In this case we have six impurities, where $I_1$, $I_2$ and $I_3$ as well as $I_4$, $I_5$ and $I_6$ interact with each other via a complex interaction Hamiltonian. Because of the dynamical cluster approximation there is also single particle hopping between the impurity sites $I_1$ and $I_4$, $I_2$ and $I_5$, and $I_3$ and $I_6$, which describe different momentum patches on the bands 1, 2 and 3 respectively. The second and third band are degenerate. As with the Hubbard model we place the impurity sites in the middle of the system and the bath sites symmetrically around them. This time in the reordered system Fig. 3.6 b) the impurity sites

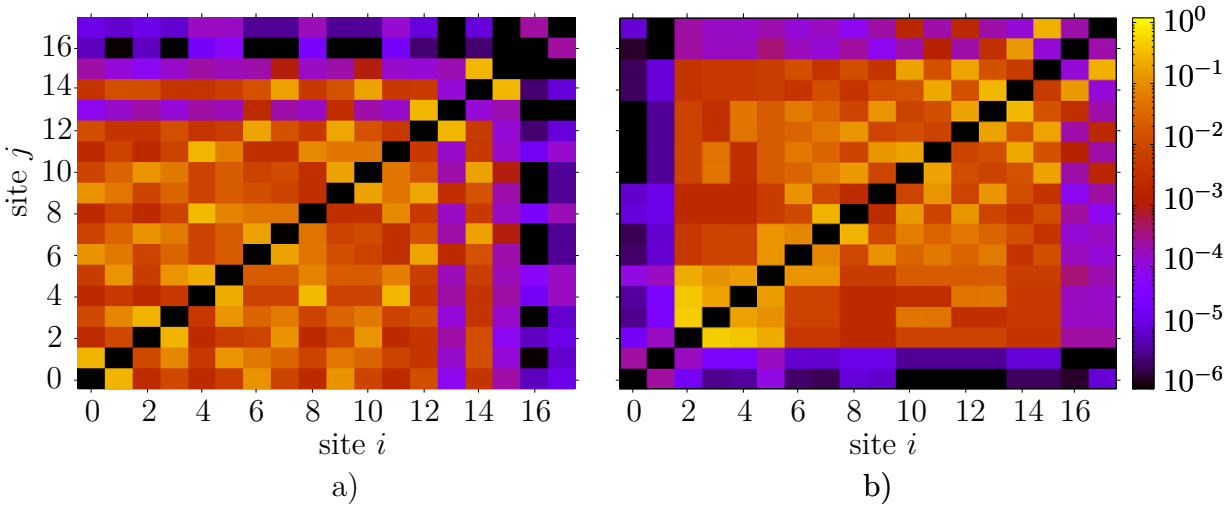


*Figure 3.7: Mutual information $I_{i,j}$ as defined in Eq.* (3.3.1) *for the system described in Fig. 3.6. a) Mutual information for the unordered system according to panel a) of Fig. 3.6. There exist very strong entanglement between some bath sites of the same bath which are located next to each other (e.g. site* 14 *and* 15*) as well as very long-ranged entanglement (e.g. between site 0 and 9). In general the system seems to be very entangled over a wide range of sites. b) Mutual information after the reordering as described in panel b) of Fig. 3.6. The stronger entangled sites are laying closer together which is reflected in $I_{i,j}$ being more diagonal. While the impurity sites describing the degenerate bands are mostly entangled with themselves, the impurities of band* 1 *are strongly entangled with their bath as well. This shows that even for one system there can be different entanglement structures present and that an investigation of this structure can possible yield interesting insights of the physics taken place. The systems parameters are described as in Fig. 3.6.*

are split up. The impurity sites describing the degenerate bands are kept together while the first band and the associated bath sites are located on the left edge of the system. It seems that at least for the chosen physical parameters, the entanglement generated by the dynamical cluster approximation is much bigger than the entanglement created by the normal interaction between band 3 (impurity sites 5 and 6) and band 1 or 2 (impurity sites 1, 2 and 3, 4).
In general, Fig. 3.7 shows significantly more entanglement than was present in the Hubbard model. This is also reflected by the cost function value of $\chi = 202.7$ before and $\chi_{ordered} = 121.0$ after the reordering. Even after the reordering localises the entanglement clearly, it is obvious that this system still exhibits long-range entanglement and will need a much higher bond dimension for the MPS describing the ground state. The one-dimensional structure is clearly not the optimal choice to minimise the distance between all strongly entangled sites.

## 3.4 Other Network Topologies

Instead of changing the order of the sites of our MPS to minimise the overall entanglement Eq. (3.3.3), it is also possible to change the topology of our MPS network. A very typical example are multi-band DMFT problems or a multi-site dynamical cluster approximation of a single-band problem. In all these cases we have several impurity sites which interact with each other in a complex way. This does not have to generate strong entanglement between the impurity sites, but is often a good guess for strong correlations. Thus, it is preferable to locate the impurity sites very close to each other. Since each of the impurity sites has its own bath, this will necessarily generate artificial long range interactions if we choose an one-dimensional chain as MPS topology. On the one hand, this increases the bond dimension of the Hamiltonian, which by itself leads to longer computation times. On the other hand, this ordering increases the chance of having long range entanglement. It is therefore definitely worth avoiding these structures.

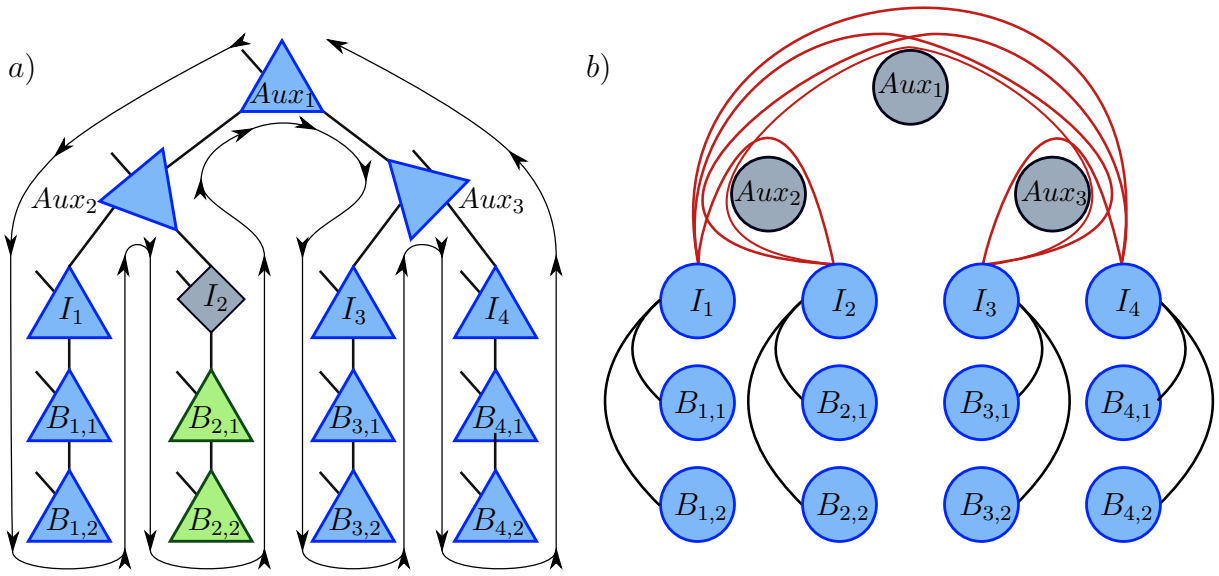


*Figure 3.8: a) Graphical representation of a BTT for the same system as in Fig. 3.4, namely the four-site dynamical cluster approximation Hubbard model. We depicted the tensor structure here, i.e. each black line connecting two tensors is representing a contraction while open lines indicating the local index connecting with the local basis. Each impurity couples only to its own bath and to the other impurities. In this structure the bath sites are directly located next to their impurities which avoids the main bulk of artificial long-range interactions. Instead of directly connecting the impurity sites, we introduce four-dimensional auxiliary tensors connecting always two of them. This reduces the amount of entanglement information carried through the impurity and thus increasing their bond dimensions. b) In this figure we depicted the interactions occurring in the model. The impurity interactions (red lines) are drawn around the auxiliary sites to indicate the way the information about them has to be carried through the system with a series of SVDs. The interactions between the impurity sites and the bath sites are very local.*

Instead of using an one-dimensional chain as our system topology, together with C.Hubig we developed the idea to use binary tree tensors (BBT) depicted in Fig. 3.8. In this sense, we introduce four-dimensional auxiliary tensors (grey sites in the figure) each connecting two impurity tensors. If there are more than two impurities, the auxiliary tensors are connected by another auxiliary tensor and so on. This reduces the distance between strongly interacting sites, e.g. the impurity sites with their bath sites and the impurity sites with themselves. For a large number of impurity sites it also avoids the entanglement information between two impurities being transported through impurities located in between. Instead the information about the entanglement of two impurities is only transported through auxiliary tensors. The drawback is that the auxiliary sites are four-dimensional tensors which have much worse scaling properties than the three-dimensional ones of normal MPS.
However, DMRG and time evolution methods are all easily generalised to BTTs. In Fig. 3.8 a) we also display a typical sweep through a BTT which produces, as is the case of standard MPS on an one-dimensional chain, a unique left or right canonical state. This structure looks advantageous compared to a normal one-dimensional MPS chain. Especially if we compare which sites are interacting with each other (Fig. 3.8 b) and Fig. 3.4), the BTT structure seems to be more local. Unfortunately, entanglement is not only generated by direct interactions between sites. As can be seen in the data of the mutual information, the bath sites of different impurities are also entangled with each other. Especially the degenerate sites are good examples for this. BTTs can increase the distance of these entangled bath sites compared to reordered MPS systems, which makes them unfavourable for small systems. Since the average distance between two sites in an one-dimensional chain increases much faster than in our BTT structure, we expect better performance of BTTs for large systems. This was confirmed with our first test calculations where we observed that BTTs perform better than MPS only for systems which are sufficiently large enough, i.e. at least four impurity sites and each impurity site coupled to at least six bath sites. Unfortunately, we do not deal with such big systems in our DMFT calculations.
A more common approach used in quantum chemistry [21,44,90,97] and since 2017 also in the many-body community [40] are so-called tree tensor networks (TTN) or fork tensor-product states. The fork tensor-product states introduced by Bauernfeind et al. are comparable to our BTTs without the auxiliary tensors. Therefore, the impurity sites itself are represented by four-dimensional tensors. As we already discussed, this leads to tensors with very high bond dimensions, limiting the usage of these structures. The model discussed by Bauernfeind et al. [40] was a very simple, completely degenerate three-band model. To our knowledge any step towards more realistic models was accompanied with an unfeasible increase of bond dimensions and computation times.
The TTN are more general since they allow the dimension of tensors to vary from site to site depending on the entanglement structure of the system. Instead of fixing the topology based on intuition and on possible interactions as done with our BTTs and the fork tensor-product stated of Bauernfeind et al., for TTN the mutual information of a system

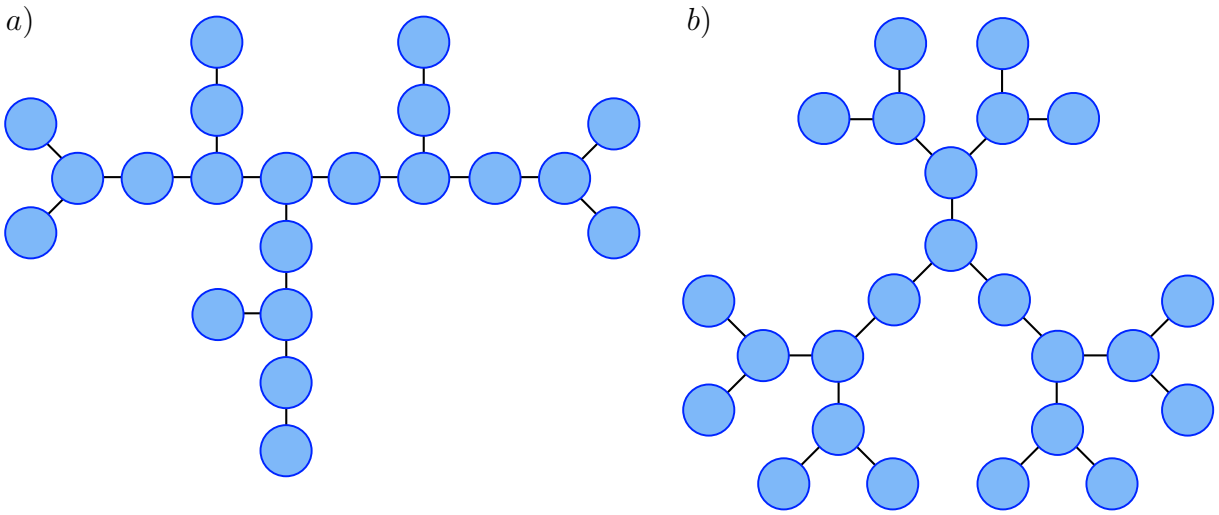


*Figure 3.9: a) An example of an approximated minimum spanning tree (MST). Each dot represents a site described by a tensor connected via the black lines to different number of other tensors. For the sake of clarity we resigned from drawing the lines for the physical indices. The maximum dimension of the tensors is therefore four. The structure is given completely by the entanglement structure of a foregoing calculations or by the existing interactions of the model. b) An example of a minimum entangled tree (MET). Again, we neglected the lines for the physical indices which have to be added to each site. The shape of the tree for a given maximal dimension (in this case 4) is given by the minimisation of the number of renormalised states needed for an exact solution. After the shape of the tree is determined, the sites of the lattice have to be mapped to it via an optimisation of the overall mutual information, e.g. a genetic algorithm.*

is calculated and used to build up a general network system. In general, one can distinguish minimum-spanning trees (MST) and minimum-entangled trees (MET)[44]. The MST (Fig. 3.9a) ) are obtained by taking the entanglement spectrum and ordering the sites according to the strongest entanglement interactions. The dimension of the tensors can vary depending on the number of strongly entangled sites. E.g. if a site is strongly entangled with three other sites, it will be connected directly to all three of them, forming a node. A site only strongly entangled with a single other site will only be connected to that site, forming the end of a branch. Thus, an MST is an irregular formed network with probably the lowest bond dimension needed to obtain a good ground state. This does not necessarily mean that this structure is the optimal topology for DMRG and time evolution methods. Convergence and sweep times can be slower because the irregular structure can lead to very slow information transport through the system or a lot of unnecessary optimisations are performed if a branch is already converged but must be transferred. A different approach is to optimise the convergence properties by defining the tree such that the number of renormalised states required to achieve an exact calculation is minimised. After obtaining such a so-called MET (Fig. 3.9b) ), a genetic algorithm[98] is used to place the system sites optimally in this tree. Nakatani et al.[44] showed that MST con-

verge slower but produce better energies as METs which confirms our argumentations. Using entanglement information to reorder not only the order of the tensor sites but the network topology itself seems to be a promising ansatz to improve computations even further. The entanglement is not only determined by the present interactions between sites but also by their filling, by the physical parameters of the system and by the state we are calculating. Thus, it is recommended to use generic algorithms to determine the optimal topology for each ground state search and each time evolution performed in the context of DMFT. For further improvements we definitely recommend to consider MST and MET as an alternative route to normal one-dimensional MPS or BTTs.

# Chapter 4

# Time Evolution Methods

Dynamical quantities are typically the most interesting properties of real materials and theoretical models. The computation of these quantities, such as dynamical structure factors, correlations functions, decay times, thermalisation properties and other dynamical quantities requires to develop suitable methods for time-evolving an MPS.
In principle, two approaches can be distinguished for tensor networks. The first class consists of methods that compute a time dependent state $|\psi(t)\rangle$ or an operator $\hat{O}(t)$ explicitly as a time dependent tensor network. The Taylor expansion of the evolution operator, the time evolution with block decimation (TEBD)[45,68,99] and the time-dependent variational principle (TDVP)[46,100] are methods that are based on this idea. These approaches create explicit time-evolved states $|\psi(t)\rangle$ at discrete times with time step $\delta t$ that can be further manipulated and used to compute observables at the corresponding times $t$. Typically for this kind of methods, the computation of each time step is quite costly, which renders the choice of very small time steps $\delta t$ impractical. Therefore, the resulting data sets for time-dependent observables tend to be sparsely discretised. These methods can further be distinguished into two sub categories. Some methods like TEBD or Padé expansions[101] construct a suitable approximation of the exact time evolution operator $U(t)$ and then apply this operator consecutively on the MPS. Other methods project the Hamiltonian first into a suitable subspace and then evolve the projected MPS in this subspace exactly with the projected Hamiltonian. This ansatz was first proposed by Feiguin et al.[102] and was reworked seven years later by Haegeman to TDVP. While the first category of approaches offers more freedom in the sense of allowing to choose suitable approximations to the current physical system and is, in general, easier to implement since it only requires to construct the operator $\hat{U}(t)$, the second category has the advantage that important properties like the norm and energy conservation are guaranteed by construction.
The fundamental idea of the second class of approaches for time-evolving an MPS is to construct a suitable subspace of the whole Hilbert space with a very small dimension in which time-dependent observables can be computed numerically exactly. Methods based on this ansatz allow to compute observables at arbitrary times $t$ without computing the actual states explicitly, which is much cheaper, in general, than computing explicit states. Furthermore, the arbitrarily dense structure of the data points for the time-dependent ob-

servables is very useful for the high-frequency regime of frequency-dependent observables obtained with subsequent Fourier transforms, which can be limited by the discretisation of the data otherwise. The best-known scheme using this idea is the Chebyshev method [103,104].
Finally, we want to mention the Krylov subspace method [105,106], which combines advantages of both classes. A subspace is created that allows to evaluate observables at arbitrary time points but the subspace is also used to compute an explicit state $|\psi(t)\rangle$ represented as an MPS. This allows to combine the advantages of both methods at moderate numeral costs.
The aim of this chapter is not to give an overview over all possible time evolution methods but rather to present the three most important ones in the context of DMRG as an impurity solver of dynamical mean-field theory. In this regard, we will start this chapter with an introduction to TEBD that will be short since we cannot use it due to long-range interactions being present in our models. Although it can be extended from systems with next-nearest neighbour interaction to problems with arbitrary interaction types [80], it is questionable if the method after this adaptation is still competetive with other methods when applied to larger systems. The focus of this this chapter will be more on the Krylov subspace method, its MPS based implementation and several improvements we developed during this thesis to increase its performance significantly. However, even with these improvements the Krylov method is still not competitive with the time-dependent variational principle in most cases. Consequently, TDVP will be the method of choice in all our calculations. It will also be the last method we present in this chapter.
In the end we will discuss possible ways of computing the long-time behaviour with cheaper methods than Krylov, TDVP and TEBD. The best-known method is linear prediction [107]. These ideas are crucial to reduce numerical artefacts in Green's functions, self-energies and other physical quantities without increasing the numerical effort dramatically.

## 4.1 Time Evolution with Block Decimation

In 2004 Guifre Vidal et al. [45] developed the algorithm "time-evolution with block decimation" (TEBD) directly within the MPS formalism. Similar ideas have been pursued starting from the traditional DMRG formulation, which resulted in a fast success of TEBD also for the environment-system formulation of DMRG [68,99]. Numerous methods widely known under the terms "Trotter decompositions", "tDMRG, ""tMPS" and "TEBD" as well as methods that do not use any of these labels explicitly are all referring to the same fundamental concept when applied to MPSes or the traditional DMRG and are used in a completely confusing manner [43,101,106,108].
All these methods follow the same idea. First, they approximate the time evolution operator $\hat{U}(\delta t)$ via a Trotter-Suzuki decomposition of $\hat{H}$ into parts $\hat{H}_1, \hat{H}_2, \ldots$ that consists

of mutually commuting small operators

$$\hat{H}_i = \sum_{k=1}^{N_i} \hat{h}_{i,k}. \tag{4.1.1}$$

The fundamental idea now is that while the time evolution operator $\hat{U}(\delta t) = \exp(-i\hat{H}\delta t)$ is difficult or impossible to compute, the exponential $\exp(-i\hat{H}_i t)$ can be computed exactly if $\hat{H}_i$ only acts non-trivially on a small part of the system. The only conditions are that the terms $\hat{h}_{i,k}$ can be diagonalised efficiently and that all terms commute $[\hat{h}_{i,k}, \hat{h}_{i,l}] = 0 \; \forall i, k, l$. For the sake of clarity, for the remaining part of the explanation we will consider an explicit example for $\hat{H}$, i.e. the Heisenberg spin chain with nearest-neighbour interactions

$$\hat{H} = \sum_{i=1}^{L} \hat{s}_i \hat{s}_{i+1}. \tag{4.1.2}$$

To follow the idea of TEBD we have to split $\hat{H}$ into parts that only contain mutually commuting operators that act non-trivial on a small part of the system. In this example it is advantageous to collect $\hat{s}_i \hat{s}_{i+1}$ for all even $i$ into $\hat{H}_1$ and all terms with odd $i$ into $\hat{H}_2$. Since calculating $\exp(-i\hat{s}_i\hat{s}_{i+1}\delta t)$ only requires the exponentiation of a $(2S+1)^2 \times (2S+1)^2$ matrix, with $S$ being the length of the local spin, each term of $\exp(-i\hat{H}_A\delta t)$ and $\exp(-i\hat{H}_B\delta t)$ can be computed individually. E.g., for $S = \frac{1}{2}$ the fundamental step is to diagonalise and hence exponentiate a $4 \times 4$ matrix, which can be done exactly and efficiently.
Then, with the first order Baker-Campbell-Hausdorff formula we can write the time evolution operator as

$$e^{-i\hat{H}\delta t} = e^{-i(\hat{H}_1+\hat{H}_2)\delta t} = e^{-i\hat{H}_1\delta t} e^{-i\hat{H}_2\delta t} e^{-i[\hat{H}_1,\hat{H}_2]\delta t^2}. \tag{4.1.3}$$

If the decomposition into $\hat{H}_1$ and $\hat{H}_2$ is fixed, we can write the first order TEBD time evolution as

$$\hat{U}^{TEBD1}(\delta t) = e^{-i\hat{H}_1\delta t} e^{-i\hat{H}_2\delta t} + \mathcal{O}(\delta t^2), \tag{4.1.4}$$

and clearly see that we have a second-order error in $t$ as long as we exponentiate $\hat{H}_1$ and $\hat{H}_2$ exactly. In this case, the approach generates a unitary approximation of $\hat{U}(\delta t)$ and hence preserves the norm of the time evolved state.
The second order symmetrised Trotter-Suzuki decomposition allows us to write

$$\hat{U}^{TEBD2}(\delta) = e^{-i\hat{H}_1\frac{\delta t}{2}} e^{-i\hat{H}_2\frac{\delta t}{2}} e^{-i\hat{H}_2\frac{\delta t}{2}} e^{-i\hat{H}_1\frac{\delta t}{2}} + \mathcal{O}(\delta t^3) \tag{4.1.5}$$

$$= e^{-i\hat{H}_1\frac{\delta t}{2}} e^{-i\hat{H}_2\delta t} e^{-i\hat{H}_1\frac{\delta t}{2}} + \mathcal{O}(\delta t^3), \tag{4.1.6}$$

with a third-order error in $t$. The generalisation of the first- and second-order TEBD algorithm to more complex Hamiltonians with possibly more than two summands $\hat{H}_i$ is straightforward. In the first step, the decomposition of $\hat{H}$ has to be determined. Afterwards, for first-order TEBD all $\hat{H}_i$ are exponentiated sequentially. For second-order

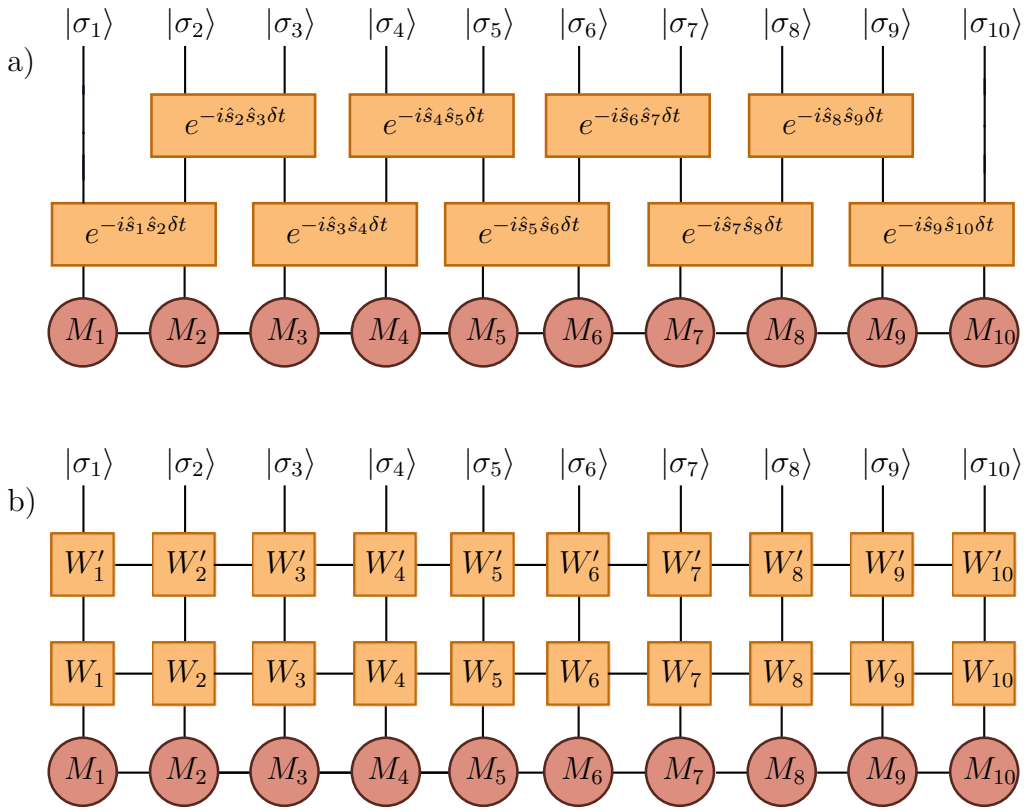


*Figure 4.1: a) Graphical representation of the application of the two parts of the Hamiltonian $\hat{H}_1$ and $\hat{H}_2$ in a single TEBD step. All terms of $H_1$ can be applied at the same time as well as all terms of $H_2$. Since the terms $\hat{s}_i\hat{s}_{i+1}$ are small, they can be exponentiated without any problems. b) As during the construction of an MPS the operators acting on several sites can be expressed in terms of single site operators after applying SVDs, thus conserving the structure of an MPS. After the contraction of the MPOs and the MPSes and a possible truncation, the next TEBD step can be performed immediately with the same operators.*

TEBD all terms $\hat{H}_i$ have to be exponentiated with half the time step applied sequentially to $|\psi\rangle$ and then the process is repeated in reverse order as indicated in Eq. (4.1.5). A graphical representation of a single TEBD step for our example of the Heisenberg spin chain is depicted in Fig. 4.1.
Time evolution with TEBD is extremely fast and well-behaved. The two only sources of errors are the Trotter error from the decomposition and the truncation error during the evolution. Both can be tuned to be arbitrarily small with additional numerical effort. The main drawback of this method is the analytical effort to separate the Hamiltonian $\hat{H}$ into mutually commuting parts and the need of nearest-neighbour interactions. Especially for complicated Hamiltonians with a lot of interactions between different sites of the system, it can be impossible or very hard to find commuting parts that are sufficiently large so that only a limited number of Hamiltonians $H_i$ has to be considered. In case of Hamiltonians with long-range interactions, the corresponding sites can be moved adjacent to each

other, previous to each time step, with the help of so called swap gates [40]. However, this is not only cumbersome to implement, but also increases the numerical effort.

## 4.2 Krylov Approximation

The key idea of the Krylov subspace method is to evade costly matrix-matrix operations, which become easily infeasible in the MPS setting. This can be done by not applying $exp(-i\hat{H}\delta t)$ to $|\psi\rangle$ directly, but rather constructing a suitable low-dimensional subspace and projecting the operator application into this subspace. In this subspace one can approximate the operator by a simpler effective matrix and can set up a minimisation problem to search for the tensor that minimises the distance to the actual solution of the problem, i.e. the time evolved state. This is more effective than solving the original problem because the Krylov method can construct this subspace by a series of cheaper matrix-vector and vector-vector operations that successively construct an orthonormal basis. The method presented here is basically a variation of the Lanczos algorithm and a well-known approach in the numerical linear algebra community [47].
We start with defining the set of vectors

$$\mathcal{K}_m(\hat{H}, |\psi\rangle) := \text{span}\{\hat{H}^k|\psi\rangle | 0 \leq k \leq m\}, \tag{4.2.1}$$

which form a span of the Krylov subspace based on the initial vector $|\psi\rangle$ and several multiplications of the matrix $\hat{H}$. We construct the orthonormal basis $\{|\phi_k\rangle\}_{0\leq k\leq m}$ of $\mathcal{K}_m(\hat{H}, |\psi\rangle)$ and at the same time a matrix $\hat{T}$ that is the projection of $\hat{H}$ in that subspace iteratively as follows:

- We first set the initial vector as first basis vector $|\phi_0\rangle = |\psi\rangle$ under the assumption that $|\psi\rangle$ is normalised.
- Any other basis vector $|\phi_{k+1}\rangle$ for $0 \leq k \leq m-1$ can be constructed from $\{|\phi_0\rangle, \ldots, |\phi_k\rangle\}$ by
  - computing $|v_k\rangle = \hat{H}|\phi_k\rangle$,
  - computing $T_{k,k} = \langle v_k|\phi_k\rangle$
  - orthogonalising the new vector with respect to all previous basis vectors $|w_k\rangle = |v_k\rangle - \sum_{j=1}^{k}\langle v_k|\phi_j\rangle|\phi_j\rangle$,
  - normalising the new basis vector $|\phi_{k+1}\rangle = \frac{|w_k\rangle}{||w_k\rangle||}$.
  - computing $T_{k,k+1} = T_{k+1,k} = \langle\psi_{k+1}|\hat{H}|\phi_k\rangle$

If the matrix $\hat{H}$ is hermitian, the procedure simplifies, since $|v_k\rangle$ only has a non-zero overlap with the two previous basis states $|\phi_{k-1}\rangle$ and $|\phi_k\rangle$.
After we build up the subspace, we can apply the Krylov method to the time evolution

by searching for the vector $|u\rangle$ of the Krylov subspace that minimises the distance to the exact time evolved state $\hat{U}(\delta t)|\psi\rangle$

$$\hat{U}(\delta t)|\psi(t)\rangle \approx \underset{|u\rangle\in\mathcal{K}(\hat{H},|\psi(t)\rangle)}{\arg\min} |||u\rangle - \hat{U}(\delta t)|\psi(t)\rangle||^2 =: |\psi'(t+\delta t)\rangle. \tag{4.2.2}$$

Since $\hat{U}$ is linear, the solution of equation Eq. (4.2.2) is given by

$$|\psi'(t+\delta)\rangle = \hat{P}^\dagger \hat{U}(\delta)\hat{P}|\psi(t)\rangle, \tag{4.2.3}$$

with $\hat{P} := \sum_{j=0}^{m-1} |\phi_j\rangle\langle\phi_j|$ being the projector on the Krylov subspace $\mathcal{K}_m(\hat{H}, |\psi(t)\rangle)$. We now want to expand the time evolution operator in the previous equation

$$\begin{aligned}|\psi'(t+\delta t)\rangle &= \sum_{j=0}^{m-1} |\phi_j\rangle\langle\phi_j| \sum_{n=0}^{\infty} \frac{(-i\delta t)^n}{n!}\hat{H}^n|\phi_0\rangle \\ &= \sum_{j=0}^{m-1}\sum_{n=0}^{m-1} \frac{(-i\delta t)^n}{n!}|\phi_j\rangle\langle\phi_j|\hat{H}^n|\phi_0\rangle + \mathcal{O}\left(\frac{\delta t^m}{m!}\right).\end{aligned} \tag{4.2.4}$$

Here we used the fact that the first basis vector $|\phi_0\rangle$ of the Krylov subspace is equal to $|\psi\rangle$ and that for sufficiently large $m$ we can neglect the higher order terms of the exponential. If the size of the Krylov subspace is chosen large enough, all vectors $\hat{H}^n|\phi_0\rangle \in \mathcal{K}_m(\hat{H}, |\psi\rangle)$ are located in the subspace. Thus, we can replace $\hat{H}$ with the effective matrix $(H_{\text{eff}})_{j,k} = \langle\phi_j|\hat{H}|\phi_k\rangle$ and reintroduce the exponential under the assumption that $m$ is sufficiently large

$$\begin{aligned}|\psi'(t+\delta t)\rangle &= \sum_{j=0}^{m-1}\sum_{n=0}^{m-1} \frac{(-i\delta t)^n}{n!}|\phi_j\rangle(H_{\text{eff}}^n)_{j,0} + \mathcal{O}\left(\frac{\delta t^m}{m!}\right) \\ &= \sum_{j=0}^{m-1} |\phi_j\rangle(e^{-iH_{\text{eff}}\delta t})_{j,0} + \mathcal{O}\left(\frac{\delta t^m}{m!}\right).\end{aligned} \tag{4.2.5}$$

$H_{\text{eff}}$ can be computed very efficiently during the construction of the Krylov subspace basis and its dimension is in general very small, i.e. in most cases significantly smaller than 12. This means the exponential can be computed fast through direct diagonalisation.
In the end, the time-evolved state is obtained by summing up the MPSes representing the Krylov vectors with the appropriate pre-factors given by $(e^{-iH_{\text{eff}}\delta t})_{j,0}$. Since the summation of MPSes increases the bond dimension significantly, the time evolved state $|\psi'(t+\delta t)\rangle$ will have a much higher bond dimension than $|\psi(t)\rangle$. To keep the bond dimension low for the next time step, a couple of SVDs are used to truncate $|\psi'(t+\delta t)\rangle$ while moving through the state from left to right and back. Afterwards, the next time step can be computed with the exact same approach.
Additionally, to the step size and truncation error in the Krylov method we also have to check convergence with respect to the Krylov space dimension. Since the subspace is build iteratively by adding newly calculated basis vectors, there is a good way of doing this.

Computing the effective matrix $H_{\text{eff}}$ and the coefficient vector $(e^{-iH_{\text{eff}}\delta t})_{j,0}$ is cheap and can be done easily in every iteration of the creation of the Krylov basis. If the changes of this vector are below a desired threshold, which should be of the order of the truncation threshold, the size of the Krylov subspace is sufficiently large.

### 4.2.1 Variational Orthogonalisation

Lanczos algorithms and thus also the Krylov method are suffering from orthogonality problems. The iterative construction of the Krylov basis is inherently unstable for finite precision arithmetics. This becomes even worse for MPS arithmetics where the constant addition and subtraction of states leads to an increased bond dimension. It is therefore crucial to truncate states to the desired precision to keep operations feasible. The truncation does not take the previously achieved orthogonality properties of the basis set into account and tends to destroy them even faster than typically for Lanczos methods. Simply constantly checking for orthogonality and if necessary reorthogonalising the basis set, will not only increase the numerical effort significantly but also introduce new truncation errors, which may often entail the same problem as before. This happens because every orthogonalisation consists of additions and subtractions, which will increase the bond dimension of the MPS significantly. In our experience the better approach is to use a variational procedure to construct the basis vector under the constraint that it is orthogonal to all previous MPSes. This can be done with a previously set bond dimension and thus truncation becomes unnecessary.
To explain how this works, we define a set of $M$ other MPSes $\{|o^A\rangle, |o^B\rangle, \ldots, |o^M\rangle\}$ against which we want to orthogonalise a given MPS $|\psi\rangle$ on a system of size $N$ to obtain a new state $|r\rangle$. The corresponding tensors describing the MPS are $\{\Psi_l\}_{l=1}^N$ for $|\psi\rangle$, $\{\{O_l^A\}_{l=1}^N, \ldots, \{O_l^M\}_{l=1}^N\}$ for the $M$ MPSes we want to orthogonalise against, and $\{R_l\}_{l=1}^N$ for our resulting state $|r\rangle$. The following procedure is done iteratively over all sites of the system. We therefore assume that each state is always in the mixed-canonical form with respect to site $l$. Our aim is to minimise the distance

$$|| \, |\psi\rangle - |r\rangle||, \tag{4.2.6}$$

under the constraint that the resulting state $|r\rangle$ is orthogonal to the other given MPSes $\langle r|o^{jJ}\rangle = 0 \quad \forall \; J \in [A, M]$. We can rewrite this problem by using Lagrange multipliers $\lambda^J$. Then, we have to minimise

$$\langle r|\psi\rangle + \langle r|r\rangle + \sum_{J=A}^{M} \lambda^J \langle r|o^J\rangle = 0, \tag{4.2.7}$$

with respect to $\langle r|$ and $\lambda^J$. We now want to focus on optimising a single tensor on site $l$ and differentiate with respect to the tensor $R_l^\dagger$ and $\lambda^J$ to obtain the equations

$$-\psi_E + R_l + \sum_{j=A}^{M} \lambda^J o_E^J = 0, \tag{4.2.8}$$

$$o_E^J \cdot R_l^\dagger = 0 \Leftrightarrow o_E^{J\dagger} \cdot R_l = 0 \quad \forall\ J \in [A, M]. \tag{4.2.9}$$

We define $\Psi_E$ and $o_E^J$ as the tensors obtained from taking the overlap between $|r\rangle$ and $|\psi\rangle$ and between $|r\rangle$ and $|o^J\rangle$ respectively and removing the tensor $R_l^\dagger$. Vectorising $R_l$ as $r$, $\psi_E$ as $\psi$ and collecting the vectorised tensors $o_E^J$ as columns in the matrix $o$ as well as the Lagrange multipliers in the vector $\lambda$, we can summarise the equations in two compact matrix equation

$$r = \psi - o\lambda, \tag{4.2.10}$$

$$0 = o^\dagger r. \tag{4.2.11}$$

Multiplying the first equation from the left with $o^\dagger$ allows us to insert the second equation into the first and solving for $\lambda$

$$\lambda = (o^\dagger o)^{-1} o^\dagger \psi. \tag{4.2.12}$$

$o^\dagger\psi$ denotes the vector of overlaps between the vectors we want to orthogonalise against $\langle o^J|$ and the input state $|\psi\rangle$, while $o^\dagger o$ is the matrix of overlaps between the states $|o^J\rangle$. Since we typically have a limited number of constraints, this matrix is in general relatively small and can be inverted exactly. Inserting Eq. (4.2.12) into Eq. (4.2.10) we obtain

$$r = \psi - o(o^\dagger o)^{-1} o^\dagger \psi, \tag{4.2.13}$$

which can be reshaped back into the optimised tensor $R_l$. As in DMRG we move to the next site with help of an SVD and repeat the procedure there, thus optimising the state $|r\rangle$ iteratively in the whole system. Since this is a variational approach, it is necessary to do several sweeps through the whole system to guarantee a converged and globally optimised result.
There are two issues with this approach that have to be treated carefully:

1. We optimise each tensor inside of the space spanned by a single tensor. Thus, we limit our bond dimension similarly to single site DMRG. This can result in a resulting state $|r\rangle$ that differs from the result obtained from the normal Gram-Schmidt procedure. However, in general these differences are so small that we can neglect them and even if not, we can adjust the method to optimise two neighbouring sites at the same time similarly to two-site DMRG allowing for an increase of the bond dimension. Since the SVD used to split the merged sites is truncating the MPS again after we orthogonalised the tensor, it is necessary to add a few additional sweeps after the two-site orthogonalisation where we use single-site orthogonalisation. The latter ensures that the orthogonalisation is exact since it does not require truncations.

2. The bond dimension at the boundaries of an MPS is typically very small and thus limits the variational space to e.g. only $d$ parameters. Orthogonalising an MPS against multiple other states $\{|o^A\rangle, |o^B\rangle, \ldots, |o^M\rangle\}$ in such a small optimisation space can be challenging or impossible. Our solution is to orthogonalise only against a small number of states in the beginning, if the norm of the resulting tensor $R_l$ does not become too small. While moving towards the centre of the MPS, the bond dimension and therefore the optimisation space become large enough that this criterium can be weakened or abandoned completely. In the following sweeps we give up this criterium completely to ensure that we obtain the solution of our optimisation.

### 4.2.2 Tensor-Optimised Implementation

There is a crucial difference between numerical linear algebra and tensor networks. For dense matrices the expectation value $aXb$, with $a$ and $b$ being vectors and $X$ being a matrix only can be computed by first applying $X$ to $a$ and then computing the overlap with $b$. For tensor networks there is a difference between calculating the expectation value $\langle a|\hat{X}|b\rangle$ represented by a tensor network directly or first evaluating $\hat{X}|b\rangle = |\tilde{b}\rangle$ and then computing $\langle a|\tilde{b}\rangle$. In principle, the same contractions are performed but in different orders. This makes a huge difference and in fact calculating the overlap is much cheaper than even the application $\hat{X}|b\rangle$. To illustrate this, we displayed the contraction order of both cases in Fig. 4.2. Keeping this in mind, it is efficient to reorder the Krylov algorithm such that we need one MPO-MPS application less to calculated the Krylov space. Since we build up around several thousand Krylov subspaces per DMFT iteration, this sums up to a reasonable improvement of the time evolution. The adapted Krylov method is used as follows:

- The initial vector is set as first basis vector $|\phi_0\rangle = |\psi\rangle$ under the assumption that $|\psi\rangle$ is normalised.
- The first matrix element $T_{0,0} = \langle\phi_0|\hat{H}|\phi_0\rangle$ is calculated.
- Any other basis vector $|\phi_{k+1}\rangle$ for $0 \leq k \leq m-1$ and the presentation of $\hat{H}$ in the Krylov space $\hat{T}$ is constructed from $\{|\phi_0\rangle, \ldots, |\phi_k\rangle\}$ by
  - computing $|v_k\rangle = \hat{H}|\phi_k\rangle$,
  - orthogonalising the new vector with respect to all previous basis vectors $|w_k\rangle = |v_k\rangle - \sum_{j=1}^{k}\langle v_k|\phi_j\rangle|\phi_j\rangle$,
  - normalising the new basis vector $|\phi_{k+1}\rangle = \frac{|w_k\rangle}{|||w_k\rangle||}$,
  - computing $T_{k+1,k} = T_{k,k+1} = \langle\phi_{k+1}|\hat{H}|\phi_k\rangle$,
  - and computing $T_{k+1,k+1} = \langle\phi_{k+1}|\hat{H}|\phi_{k+1}\rangle$.

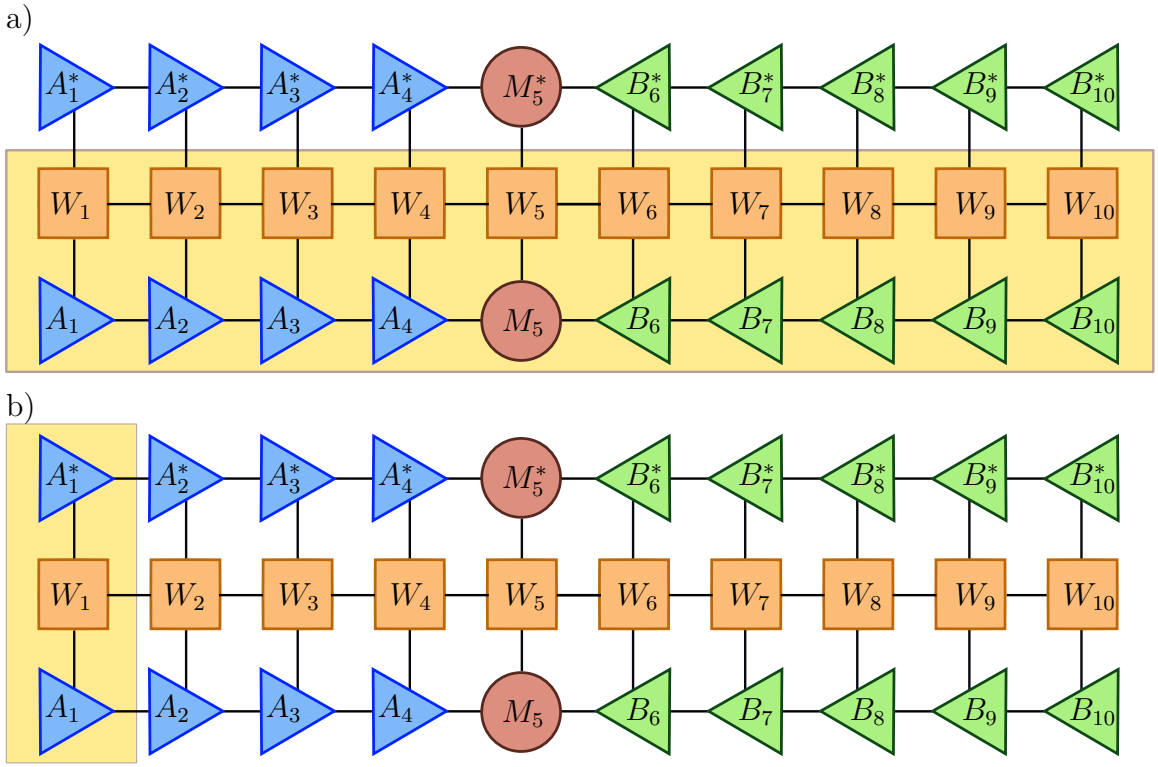


*Figure 4.2: Graphical representation of the expectation value $\langle\psi|\hat{H}|\psi\rangle$ written in MPS notation. a) The expectation value can be computed by first applying the Hamiltonian on the state $|\phi\rangle = \hat{H}|\psi\rangle$ and then determining the overlap $\langle\psi|\phi\rangle$. This means the tensors in the yellow block have to be contracted first and then with the A, M and B tensors on the top. b) The most efficient way of contracting the whole network would be to start with the left-most or right-most tensors (yellow block) and contracting them. The results is contracted with the tensors next to them up to the other end of the system.*

The application of an MPO to an MPS becomes significantly costly for large MPOs. Additionally, it is necessary to orthogonalise the resulting state against at least two other Krylov vectors. Therefore, another important tensor network related improvement is the application of an MPO to an MPS with a simultaneous orthogonalisation to a set of other vectors. This is done in the same manner as the orthogonalisation in section 4.2.1, except that the target environment tensor is not just the input MPS but the contraction of the input MPS $|\psi\rangle$, input MPO $\hat{H}$ and the MPS $|r\rangle$ that is to be optimised.
This reduces the increase of computation time for each additional Krylov vectors (in line with the exponential growth of the bond dimension during very operator application step) to a much slower rate. It is recommended to introduce a subspace expansion step similarly to the DMRG procedure in section 3.2, to capture the increase of the minimal necessary bond dimension rather than generating an MPS with a large bond dimension and then truncating it.

### 4.2.3 Reusing the Krylov-Subspace

If we have a set of Krylov vectors that proved sufficient to calculate $e^{i\hat{H}(t+\delta t)}$, that same Krylov subspace can also be sufficiently big to calculate $e^{i\hat{H}(t+2\delta t)}$ and potentially $e^{i\hat{H}(t+3\delta t)}$, $e^{i\hat{H}(t+4\delta t)}$ etc. Using the same Krylov subspace to calculate several time steps instead of computing a new Krylov subspace for each time step is desirable since it saves a lot of computational effort.
As described above, we need a certain number of Krylov vectors $m$ to represent the Hamiltonian $H_{\text{eff}}$ in the Krylov subspace precisely enough for a good description of the time evolved state $|\psi'(t+\delta t)\rangle$. From Eq. (4.2.5) it is obvious that this number $m$ depends on the time step size $\delta t$ since

$$\begin{aligned}|\psi'(t+\delta t)\rangle &= \sum_{j=0}^{m-1} |\phi_j\rangle (e^{-iH_{\text{eff,exact}}\delta t})_{j,0} + \mathcal{O}\left(\frac{\delta t^m}{m!}\right) \\ &= \sum_{j=0}^{m-1} |\phi_j\rangle (e^{-iH_{\text{eff}}\delta t} e^{-iH_{\text{errors}}\delta t})_{j,0} + \mathcal{O}\left(\frac{\delta t^m}{m!}\right). \end{aligned} \tag{4.2.14}$$

The bigger the time step, the bigger the errors introduced by $H_{\text{eff, exact}} = H_{\text{eff}} + H_{\text{errors}}$ in the exponential, since they get multiplied by $\delta t$. Additionally, the time step error $\mathcal{O}\left(\frac{\delta t^m}{m!}\right)$ itself is growing with larger time steps. Assume that the Krylov subspace used to determine the time evolved state $|\psi'(t+n\delta t)\rangle$ cannot be used to compute an additional time step $|\psi'(t+(n+1)\delta t)\rangle$, because the errors would be too large. Adding another Krylov vector $m \to m+1$ can lower the errors enough for determining additional time steps with the same Krylov basis. The advantage is that the numerical effort for computing another Krylov vector can in some cases be smaller than setting up a complete new Krylov basis. A. Swoboda in collaboration with us developed a heuristic estimator to decide whether building up a new Krylov basis or adding just a new Krylov vector to the already existing basis is better in terms of computation times. Apart from the actual computation cost for a single Krylov vector compared to a complete new Krylov basis, the heuristic also takes into account how many time steps can possibly be calculated with both ansatzes. The heuristic is based on observations on the last calculations of Krylov vectors and is not simple to tune due to the increasing cost to generate each Krylov vector. Without truncating the generated Krylov vectors, the bond dimension of each new vector will grow by a factor proportional to the MPO bond dimension. That means, even if generating a third basis vector was much cheaper than calculating a new set of Krylov vectors in the previous step, generating a new basis consisting of three vectors can be much cheaper than adding a fourth one in the next iteration. Where exactly the crossover of both approaches is located depends on the initial state, the system and the time step. Thus, the heuristic has to be constantly adapted during the calculation of the time evolutions.
The reuse of the Krylov subspace is obviously more effective for imaginary time than for real time evolutions. The former is basically a projection to the ground state for $\tau \to \infty$. For short times the time evolved state will change fast, because of the exponentially fast decaying high energy contributions of the Hamiltonian spectrum, while for longer times

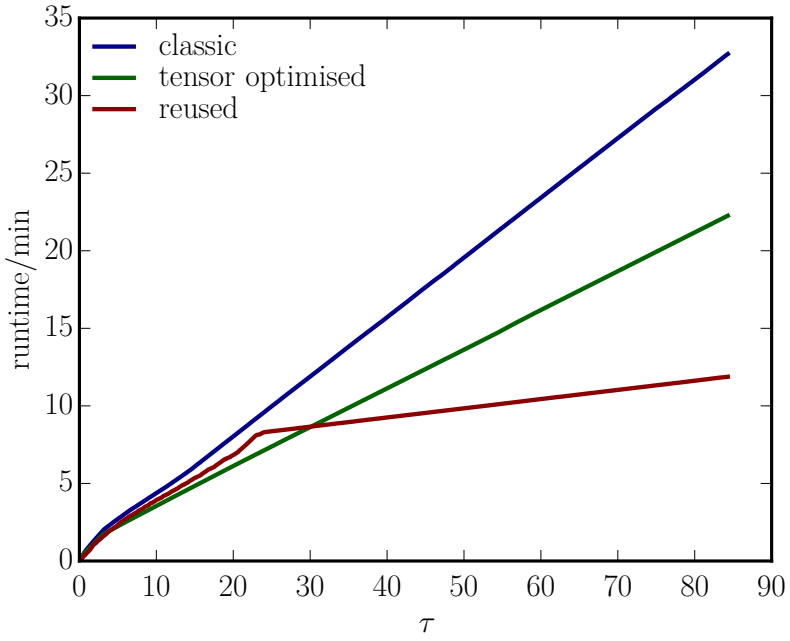


*Figure 4.3: Runtimes of Krylov time evolutions with different options for the two-site DCA model in momentum space with interaction strength $U = 7t$, nearest neighbour hopping $t = 1$, next-nearest neighbour hopping $t_p = -0.15t$ and five bath sites. The classic implementation of the Krylov method (blue line) is the slowest calculation. By adapting the method to be tensor optimised and orthogonalising the Krylov basis states variational (green line) the method can be improved significantly. Reusing the Krylov subspace based on our heuristic (red line) leads to the fastest calculation. Up to $\tau = 22$ the heuristic is not optimally tuned and leads to a bad performance. From there on the Krylov subspace can be used for the rest of the time evolution leading to a very fast computation.*

the time evolved state $|\psi(t)\rangle$ approaches the ground state exponentially slow. Since $|\psi(t)\rangle$ is changing slowly, the Krylov basis will also change only slowly over time. Especially at later times in the time evolution, this allows to reuse the Krylov subspace over long time periods, which generates a massive decrease of computation times.
In contrast, for real-time evolutions the heuristic has problems to predict the number of needed Krylov vectors for the next time step, since the oscillating behaviour of the evolution and finite-size effects are hard to predict without taking into account the complete previous time evolution.

### 4.2.4 Conclusion

With all improvements mentioned, time evolution with the Krylov method becomes relatively fast and well-controlled. Furthermore, the Krylov method can be easily applied to all kind of Hamiltonians without any changes of the method and generalises very easily to other tensor network states such as binary tree tensors. The only parts needing adaptation for other network topologies are the calculation of expectation values as well as the operator application with simultaneous orthogonalisation against previous Krylov vectors.
In Fig. 4.3 the runtime changes of the different improvements can be seen for a simple imaginary-time evolution. In this case all improvements lead to a reduction of the runtime by a factor 3.5. Depending on the model and the form of the time evolution the runtime reduction can be even bigger.

## 4.3 Time-Dependent Variational Principle

We assume that the state $|\psi\rangle$ is in a mixed canonical representation with respect to site $l$. As a starting point we define the single-site tangent space $T_{|\psi\rangle}$ of a given MPS $|\psi\rangle$ as the space spanned by all variations of a single tensor of the MPS $|\psi\rangle$. In general, an MPS has more than one tensor and thus the space is spanned by all possible variations on all existing tensors in the MPS, but a variation is always only done on a single tensor while all others are kept constant.
If we consider a time evolution of the state $|\psi(t)\rangle$ with an infinitesimally small time step $\delta t$, the time evolved state $|\psi(t+\delta t)\rangle$ is an element of the tangent space. The key idea of the time-dependent variational principle (TDVP) is to approximate a time evolution with a finite time step by projecting the time evolution, represented by the time-dependent Schrödinger equation, into the tangent space and solving it there. This results in time evolution equations for each tensor of the MPS in the tangent space, which are solved subsequently. The approach was first proposed in the context of MPSes by Haegeman et al.[46].
We now want to derive the time-evolution equations for the tensors of the state $|\psi\rangle$. Therefore, we define the projector $\hat{P}_{T_{|\psi\rangle}}$ onto the tangent space as

$$\hat{P}_{T_{|\psi\rangle}} = \sum_{l=1}^{L} \hat{P}_{l-1}^{L,|\psi\rangle} \otimes \hat{\mathbb{1}}_l \otimes \hat{P}_{l+1}^{R,|\psi\rangle} - \sum_{l=1}^{L-1} \hat{P}_l^{L,|\psi\rangle} \otimes \hat{P}_{l+1}^{R,|\psi\rangle}, \tag{4.3.1}$$

with $\hat{P}_l^L$ projecting on the part of the state $|\psi\rangle$ from the left edge of the system up to site $l$. $\hat{P}_l^R$ projects on the part of the state $|\psi\rangle$ from the right edge of the system up to site $l$, respectively. If we write the state $|\psi\rangle$ in the mixed-canonical representation

$$\begin{aligned} |\psi\rangle &= A^{\sigma_1} \cdots A^{\sigma_{l-1}} M^{\sigma_l} B^{\sigma_{l+1}} \cdots B^{\sigma_L} |\sigma_1, \ldots, \sigma_L\rangle \\ &= \sum_{a_{l-1}, b_l} M^{\sigma_l}_{a_{l-1}, b_l} |a_{l-1}\rangle_A |\sigma_l\rangle |b_l\rangle_B, \end{aligned} \tag{4.3.2}$$

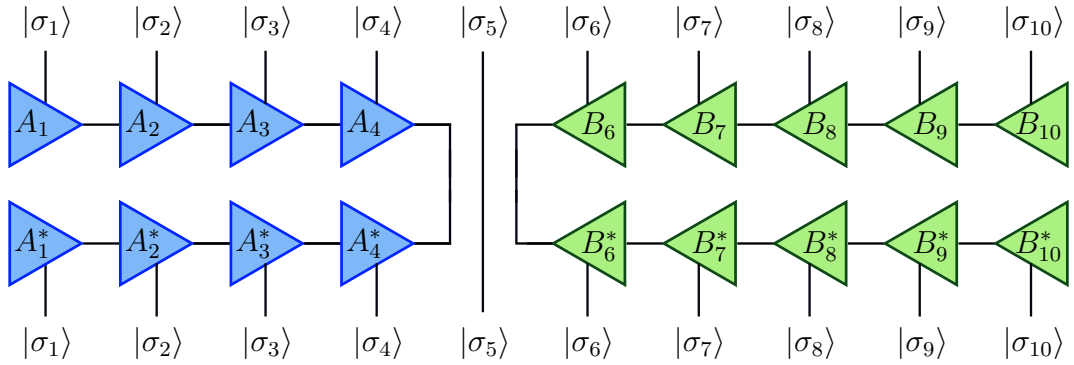


*Figure 4.4: Graphical representation of the projector $\hat{P}_4^L \otimes \hat{\mathbb{1}}_5 \otimes \hat{P}_6^R$, which is representative for the terms of the first sum in Eq. (4.3.5). The A and B tensors are the left- and right-normalised tensors of the state $|\psi\rangle$. The terms of the second sum are constructed in the same manner, by replacing the straight vertical line in the fifth bond by the corresponding A matrices.*

with $|a_{l-1}\rangle_A$ and $|b_l\rangle_B$ as defined in Eq. (2.1.17) and Eq. (2.1.17) respectively, the projectors take the following form

$$\hat{P}_l^L = \sum_{a_{l-1}} |a_{l-1}\rangle_A \langle a_{l-1}|_A, \tag{4.3.3}$$

$$\hat{P}_l^R = \sum_{b_l} |b_l\rangle_B \langle b_l|_B. \tag{4.3.4}$$

The first sum consists of terms that project all tensors to the left and right of site $l$ on the state $|\psi\rangle$ while the site $l$ stays unchanged, see Fig. 4.4 for a graphical representation. Thus, they filter for all states that have only changes on a single tensor. The second term removes all those states that are identical with the state $|\psi\rangle$ itself.
The key idea is now to insert the projector in the time dependent Schrödinger equation

$$\begin{aligned}\frac{\partial}{\partial t}|\psi\rangle &= -i\hat{P}_{T|\psi\rangle}\hat{H}|\psi\rangle \\ &= -i\sum_{l=1}^{L} \hat{P}_{l-1}^{L,|\psi\rangle} \otimes \hat{\mathbb{1}}_l \otimes \hat{P}_{l+1}^{R,|\psi\rangle}\hat{H}|\psi\rangle + i\sum_{l=1}^{L-1} \hat{P}_l^{L,|\psi\rangle} \otimes \hat{P}_{l+1}^{R,|\psi\rangle}\hat{H}|\psi\rangle.\end{aligned} \tag{4.3.5}$$

This equation is still not solvable, but we can approximate it by solving each term individually. By applying a symmetrised second error Suzuki-Trotter decomposition similarly to TEBD we separate the time evolution of $|\psi\rangle$ into individual and sequentially applicable time evolutions. If we define

$$\hat{h}_{1,l} = \hat{P}_{l-1}^L \otimes_l \hat{\mathbb{1}}_l \otimes \hat{P}_{l+1}^R \hat{H}, \tag{4.3.6}$$

$$\hat{h}_{2,l} = \hat{P}_l^L \otimes \hat{P}_{l+1}^R \hat{H}, \tag{4.3.7}$$

we can write the time evolution operator with the symmetrised second order Suzuki-Trotter decomposition as

$$\hat{U}(t+\delta t) = e^{-ih_{1,1}\frac{\delta t}{2}} e^{ih_{2,1}\frac{\delta t}{2}} e^{-ih_{1,2}\frac{\delta t}{2}} \dots e^{-ih_{1,2}\frac{\delta t}{2}} e^{-h_{2,1}\frac{\delta t}{2}} e^{-ih_{1,1}\frac{\delta t}{2}} + \mathcal{O}(\delta t^3). \tag{4.3.8}$$

This means we have to solve $L$ equations describing a forward time evolution of the form

$$\frac{\partial}{\partial t}|\psi\rangle = -i\hat{P}^L_{l-1} \otimes \hat{\mathbb{1}}_l \otimes \hat{P}^R_{l+1}\hat{H}|\psi\rangle, \tag{4.3.9}$$

and $L-1$ terms describing a backward time evolution written as

$$\frac{\partial}{\partial t}|\psi\rangle = +i\hat{P}^L_{l} \otimes \hat{P}^R_{l+1}\hat{H}|\psi\rangle. \tag{4.3.10}$$

We can obtain effective single-site equations by multiplying each individual equation of the form of Eq. (4.3.9) with $|\psi\rangle$ from the left but omitting the tensor on site $l$. Another set of equations can be obtained by multiplying each individual equation of the form of Eq. (4.3.10) from the left with the state $|\psi\rangle$ having an open bond between site $l-1$ and $l$. Thus, the equations can be written as

$$\frac{\partial}{\partial t}M_l = -i\hat{H}^{\text{eff}}_l M_l, \tag{4.3.11}$$

$$\frac{\partial}{\partial t}C_l = i\hat{\hat{H}}^{\text{eff}}_l C_l, \tag{4.3.12}$$

with $M_l$ being just the tensor of $|\psi\rangle$ on site $l$ while $C_l$ is the singular value matrix between site $l$ and $l+1$ obtained after bringing all tensors to the left of site $l+1$ into the left-canonical form and all tensors to the right of site $l$ into right canonical form with successively applied SVDs. We refer from defining the effective matrices $\hat{\hat{H}}^{\text{eff}}_l$ and $\hat{H}^{\text{eff}}_l$ of the two time evolution equations in form of equations, but rather give a graphical definition in Fig. 4.5 and Fig. 4.6. At this stage we just have to use one of the usual methods for exponentiating a matrix to solve all $2L-1$ equations successively and apply the resulting operators in the correct order to $|\psi\rangle$ according to Eq. (4.3.8).

TDVP is advantageous for multiple reasons: First, it is unitary, i.e. preserves both the norm and the energy of the time-evolved state by construction. Second, it exists in a single-site and two-site version with the single-site version scaling similar to the single-site DMRG. This is the case because TDVP in the limit of taking $t \to -i\infty$ represents a ground state search. In other words, TDVP and DMRG without subspace expansion just differ in the sense that in TDVP the local eigensolver is replaced by a local exponentiation. Third, it calculates the time-evolved state directly instead of building up a subspace, which potentially can involve heavy calculations including basis states with high bond dimensions. Finally, it requires only a single MPO representation of the Hamiltonian $\hat{H}$. We do not have to analytically separate the Hamiltonian as in TEBD.

One of the disadvantages of TDVP is that even if one time step with time $\delta t$ has an error of $\mathcal{O}(\delta t^3)$, we observe relatively large errors due to the projection in the tangent space itself if the Hamiltonian has long range interaction (i.e. not nearest-neighbour). This is not surprising since even for a Hamiltonian with nearest-neighbour interaction the single-site TDVP induces a projection error while two-site TDVP does not [46]. Therefore, it seems reasonable that a higher order TDVP like three-site or even more would be able

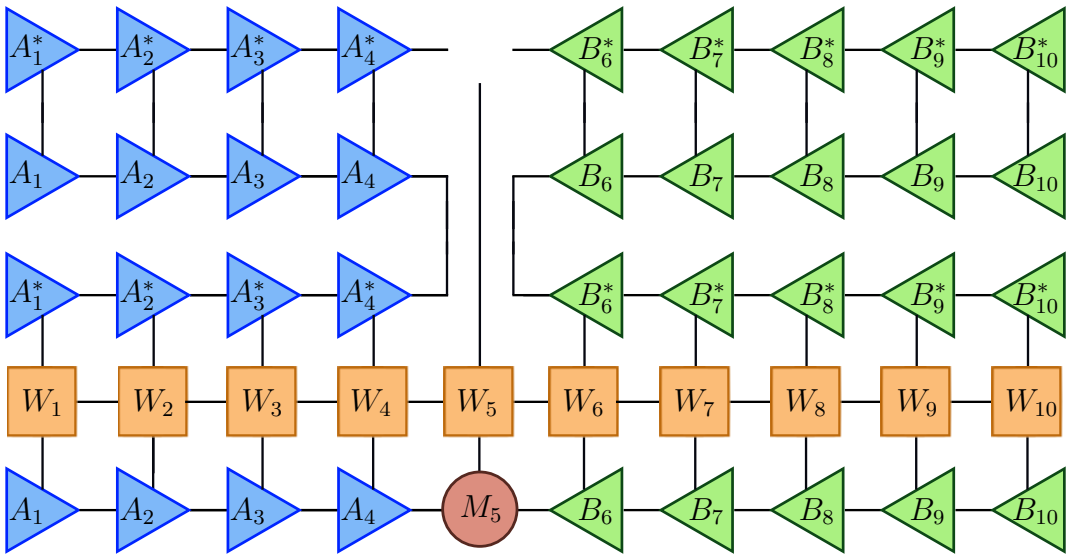


*Figure 4.5: Graphical representation of the right-hand side of the effective single-site time forward evolving Schrödinger equation Eq.* (4.3.11)*. The first row from the bottom is the original MPS in the mixed-canonical representation, the second row is the Hamiltonian, the third and fourth row is representing the the projector* $\hat{P}_4^L \otimes \hat{\mathbb{1}}_5 \otimes \hat{P}_6^R$ *and the last row is the state* $|\psi\rangle$ *with site* 5 *missing, which we multiplied from the left to the Schrödinger equation. Because of the orthogonalisation properties of the A and B matrices, the upper two rows simplify to unit matrices.*

to overcome this drawback at the cost of longer calculation times. Unfortunately, this error increases with smaller time steps indicating a competition between the time-step error and the truncation error.
After testing the presented time evolutions extensively, two-site, second-order TDVP is the method of choice for all our calculations if not stated otherwise.

## 4.4 Long Time Behaviour

For real-time as well as for imaginary-time evolutions we have to deal with the fact that we cannot evolve our states with these methods until infinity. In the context of DMFT we only consider physical quantities that approach zero for large, but not excessive times. However, to save a lot of computational effort and to guarantee that the computed quantities are evolved far enough for further computations, it is important to think about up to which times the states have to be time-evolved.
A reasonable approach for states being evolved long enough as well as for observables being simple enough is so-called linear prediction [107,109]. For cases where we cannot reach the regime that allows linear prediction to be applicable, we propose an ansatz that, at least for imaginary-time evolution, can allow us to shorten computation times. By projecting the low-energy states out of the state $|\psi\rangle$, which is to be time-evolved, we only

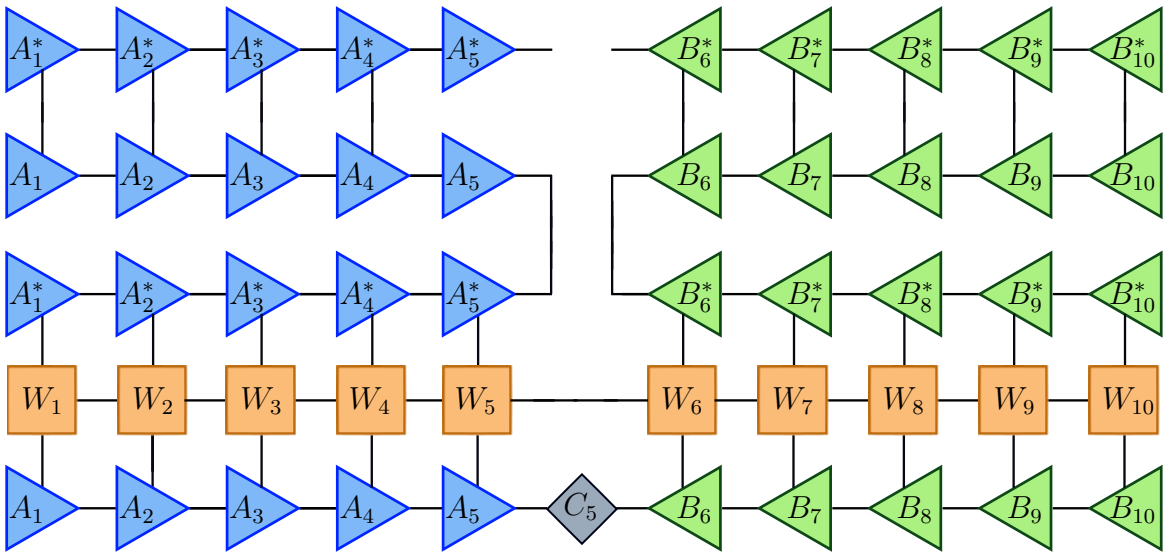


*Figure 4.6: Graphical representation of the right hand site of the effective centre matrix backward evolving Schrödinger equation Eq.* (4.3.12)*. The description of each row is explained in Fig. 4.5.*

have to evolve the relatively fast decaying high energy contribution. The drawback for this approach is that we have to perform more DMRG calculations to determine the low-energy spectrum.
In the following two subsections we will discuss the linear prediction as well as the projection ansatz.

### 4.4.1 Linear Prediction

We start with a series of complex data $x_0, x_1, \ldots, x_N$ obtained at equidistant time points $t_n = n\delta t$. For the times $t > t_N$ the data points $\tilde{x}_{N+1}, \tilde{x}_{N+2}, \ldots$ can be predicted with the ansatz

$$\tilde{x}_n = -\sum_{i=1}^{p} \alpha_i x_{n-i}. \tag{4.4.1}$$

The predicted values $\tilde{x}_n$ for $n > N$ are assumed to be linear combinations of the previous $p$ data points. The coefficients $\alpha_i$ are determined from the known data set by minimising the cost function

$$\chi = \sum_{n \in \mathcal{N}_{fit}} |\tilde{x}_n - x_n|^2 / w_n, \tag{4.4.2}$$

in the fit interval $\mathcal{N}_{fit} = \{n | t_n \in (t_N - t_{fit}, t_N]\}$. We have to choose $t_{fit}$, the starting point of the fit interval, in such a way that we avoid to include the short-time in the prediction of the long time behaviour and such that we include enough data points for the fit to a have good statistic and to use a large number $p$ of coefficients. Barthel et al. proposed

$t_{fit} = t_N/2$[107] and we stick to it. The weights $w_n$ are typically chosen to be one in our calculations. We can solve the minimisation problem by differentiation with respect to the coefficients $a_i$. After defining

$$R_{j,i} = \sum_{n \in \mathcal{N}_{fit}} x^*_{n-j} x_{n-i}/w_n, \tag{4.4.3}$$

$$r_j = \sum_{n \in \mathcal{N}_{fit}} x^*_{n-j} x_n/w_n, \tag{4.4.4}$$

we can rewrite the problem as a matrix equation

$$R\boldsymbol{a} = -\boldsymbol{r}. \tag{4.4.5}$$

For positive $w_n$ the matrix $R$ is positive-definite and the minimisation problem can readily be solved by $\boldsymbol{a} = -R^{-1}\boldsymbol{r}$. This ansatz generates exponentially decaying and increasing as well as oscillating data points. This can be seen when we introduce the vectors $\boldsymbol{x}_n := [x_{n-1}, \ldots, x_{n-p}]$ and write Eq. (4.4.1) as a matrix equation

$$\tilde{\boldsymbol{x}}_{n+1} = A \cdot \boldsymbol{x}_n, \tag{4.4.6}$$

with the matrix

$$A = \begin{bmatrix} -a_1 & -a_2 & -a_3 & \ldots & -a_p \\ 1 & 0 & 0 & \ldots & 0 \\ 0 & 1 & 0 & \ldots & 0 \\ \vdots & \ddots & \ddots & \ddots & \vdots \\ 0 & \ldots & 0 & 1 & 0 \end{bmatrix}. \tag{4.4.7}$$

We can clearly see that any predicted data point $x_{N+m}$ for $m > 0$ is obtained by applying powers of $A$ to the initial vector $\boldsymbol{x}_N$ and taking the first element of the resulting vector

$$\tilde{x}_{N+m} = [A^m \cdot \boldsymbol{x}_N]_1 = \sum_{i=1}^{p} c_i \alpha_i^m. \tag{4.4.8}$$

In the last step we performed a right eigenvector decomposition of $A$ with eigenvalues $\alpha_i$ and eigenvectors $\boldsymbol{v}_i$. The $c_i$ are obtained form the overlap of $\boldsymbol{x_N}$ and the eigenvectors of $A$.
Since each complex number can be written as an exponential, we define $\alpha_i = e^{ia-b}$, seeing that linear prediction uses a combination of $p$ exponentially decaying, exponentially growing and oscillating functions to predict the data points $x_{N+m}$ for $m > 0$. Physical insights dictate to exclude exponentially growing terms and impose that all $|\alpha_i| \leq 1$ since we predict the long-time behaviour of physical observables. Barthel et al. proposed to discard all numerically obtained coefficients with $\alpha_i > 1$ to enforce this physical property. These unphysical solutions can be obtained because of finite-size effects being present in the fitting data or because of a very bad fitting result. Since the error of linear prediction

is approximately a function of $p\delta t$, Barthel et al.[107] proposed to use $p = \frac{t_{fit}}{2\delta t}$ moments for the fitting procedure to achieve a good compromise between having a large number of exponentials to superpose , i.e. a large $p$, and having a good statistics for the fit of the coefficients $\alpha_i$, i.e. a small $p$.
In practice, we start with the fit interval $\mathcal{N}_{fit} = \{n|t_n \in (t_N - t_{fit}, t_N]\}$, the interval border $t_{fit} = t_N/2$ and $p = \frac{t_{fit}}{2\delta t}$ moments as discussed above and check the quality of the fit by computing the cost function value and by determining the proportion of discarded coefficients $c_i$, which we call discarded weight $d$. For imaginary time evolution there is, in general, no reason to change any of these choices. If, in the case of real-time evolution, we observe that the discarded weight is to big (i.e. $d > 0.1$), we assume that this is due to finite size effects. Therefore, we shift the interval by 40 data points to earlier times, determine a new value for $p$ and fit the data set anew. This is repeated until the discarded weight drops below the threshold of 0.1. In extensive tests this has been proven to yield the best result.
In both cases, real-time as well as imaginary-time evolution, the calculated Green's functions are expected to decay exponentially for large times, making linear prediction a well-suited method to predict the functions to large times in the context of DMFT.

### 4.4.2 Projection of Low Energy States

For imaginary time-evolution it is clear that the long time behaviour of observables like the Green's function $G(\tau)$ are determined by the low-energy part of the Hamiltonian spectrum. If $|\phi_n\rangle$ denotes the eigenbasis of the Hamiltonian $\hat{H}$ with eigenenergies $E_n$ in ascending order, we can write any state $|\psi\rangle$ as a superposition of eigenbasis vectors

$$|\psi\rangle = \sum_n c_n |\phi_n\rangle, \tag{4.4.9}$$

with complex coefficients $c_n = \langle\psi|\phi_n\rangle$. E.g. a typical observable that we have to calculate in the context of DMFT is the greater Green's function $G^>(\tau)$

$$\begin{aligned} G^>(\tau) = \langle\phi_0|c(0)c^\dagger(\tau)|\phi_0\rangle &= \langle\phi_0|c(0)e^{-\tau(\hat{H}-E_0)}c(0)|\phi_0\rangle \\ &= \sum_n |c_n|^2 e^{-\tau(E_n-E_0)}. \end{aligned} \tag{4.4.10}$$

Depending on the energy difference of the low lying states of the Hamiltonian spectrum, the state $c(\tau)|\phi_0\rangle := |\psi(\tau)\rangle$ has to be calculated to very high times $\tau$ to simply decay exponentially with only a couple of relevant terms. This is necessary for linear prediction to be successfully applicable. But if we know the $N_{low}$ lowest states of the Hamiltonian spectrum and their eigenenergies, we can separate the observable into a part that we can calculate exactly and another part that we have to treat with one of our time evolution

methods

$$G^{>}(\tau) = \langle\phi_0|c(0)c^{\dagger}(\tau)|\phi_0\rangle = \sum_{n=0}^{N_{low}} |c_n|^2 e^{-\tau(E_n-E_0)} + \sum_{n=N_{low}+1} |c_n|^2 e^{-\tau(E_n-E_0)}$$
$$= G^{>}_{low}(\tau) + G^{>}_{high}(\tau). \tag{4.4.11}$$

The slowly decaying part $G^{>}_{low}(\tau)$ is known exactly for arbitrary times while $G^{>}_{high}(\tau)$ decays much faster as long as we extracted enough low lying states. For the latter we can use linear prediction to extrapolate the observable to small values if we have time evolved the state long enough.
With DMRG, in principle, it is possible to compute the whole spectrum of the Hamiltonian iteratively. After we found the ground state $|\phi_0\rangle$ we start a new DMRG search with the condition that the new state must be orthogonal to the already found ground state $|\phi_0\rangle$. DMRG should calculate in this case the lowest lying excited eigenstate $|\phi_1\rangle$ of $\hat{H}$. In the next step we start DMRG with the condition that the new state should be orthogonal to $|\phi_0\rangle$ and $|\phi_1\rangle$. In practice, we are only interested in the low energy spectrum and practice showed that we only have to determine the $4-6$ lowest-lying eigenstates to see a significantly faster decay for observables like the greater or lesser Green's function.
There are several drawbacks with this approach:

- The low-lying eigenstates have to be determined iteratively one by one. There is no way of parallelising the computation. For relatively strong entangled systems performing six DMRG calculations one after the other with the sufficient precision can take some time and may take longer than the time saved during the time evolution.

- It is not known beforehand how many states actually have to be calculated. The number depends, on the one hand, on the eigenenergies. A significant energy jump from one state to the next is needed to see any difference in decaying times of the observables if those states are projected out of the excited state $|\psi(\tau)\rangle$. Especially for degenerate systems this can be hard to achieve, if, for example, the four low-lying eigenstates next to the ground state have the same energy.
  On the other hand, the calculated eigenstates $|\phi_n\rangle$ need to have a significant weight in $|\psi(\tau)\rangle$, i.e. $c_n = \langle\phi_n|\psi(\tau)\rangle$ should be large enough. If the weights are too small, the contribution of this state to the observable is negligible and we see no change in the decay times.

- In general, the high energy states of the spectrum are more entangled than the low energy ones. Using the same truncation threshold or the same truncated weight for the time evolution of $|\psi\rangle_{high}$ as for the full state $|\psi\rangle = |\psi\rangle_{low} + |\psi\rangle_{high}$ can lead to higher bond dimensions and thus slower computation. Therefore, it must be checked how much the precision for the time evolution of $|\psi\rangle_{high}$ can be tuned down. This can highly depend on the amount of states projected out of $|\psi\rangle$ and

their total weight as well as on the system and its entanglement properties itself. It is therefore difficult to find a general rule for this issue.

- If symmetries are used, the low energy spectrum has to be determined for each symmetry sector of the excited states separately. This increases the numerical effort significantly.

Summarising, this method is useful, if DMRG calculations of the low-lying eigenstates can be performed much faster than the time evolution and if the low-energy spectrum is not strongly degenerate. Furthermore, the observables that are to be computed have to decay very slowly for gaining a significant speed-up by projecting out the low-energy states. Finally, it must be clear how precise the DMRG calculations have to be performed to obtain sufficiently good enough results. These conditions are very hard to guarantee for widely changing Hamiltonians in DMFT calculations. Unfortunately, we did not find any situation to apply this approach in a general way in the DMFT context.

# Chapter 5

# Dynamical Mean-Field Theory

One of the fundamental aims of solid state physics is the description of real materials. Unfortunately, the quantum lattice models for these real three-dimensional materials become so complicated and strongly entangled that these interesting compounds cannot be solved efficiently. In fact, there exist several methods, so-called mean-field techniques, that can solve such kind of problems with increasing accuracy in higher dimensions (e.g. more than three). Furthermore, multiple methods are known that solve one-dimensional problems very efficiently such as DMRG or exact diagonalisation (ED) [14,110,111]. A reasonable ansatz is to use these methods that perform great in one dimension and apply them to two-dimensional finite problems. Even if large two-dimensional systems are not treatable, by solving small systems and increasing the system size in an appropriate manner, results can be extrapolated to the thermodynamic limit while getting rid of finite-size effects. However, these ansatzes are still work in progress and suffer under severe limitations with respect to entanglement properties, sign problems and more.
Another approach is to use so-called *quantum embedding* techniques like density functional theory (DFT) [33,112,113,114], dynamical mean-field theory (DMFT) [29,31,32,33] or density matrix embedding theory (DMET) [6,16,115]. The core idea is to treat only a part of the infinitely large lattice exactly, which is called the impurity cluster, and summarise the rest of the lattice in a mean-field environment that is acting on the impurity cluster itself. The "artificial" interaction between cluster and environment has to be approximated consistently during the calculations. Essentially, these methods consist of mapping a complex lattice problem to an auxiliary impurity problem, solving it with an appropriate method and using the result to update the interaction between environment and cluster. As in other mean-field theories, these steps are repeated iteratively until convergence of physical quantities is observed. The approach considers all local interactions completely and even allows for time-dependent fluctuations while approximating the environment as non-interacting (see Fig. 5.1). This reduces the complexity significantly and at the same time results in very good descriptions of real materials. Therefore, even if the full lattice problem cannot be solved, this approach allows to compute interesting and important physical quantities to a very high quality.
A great deal of these methods like DFT, DMFT or spectral density functional theory

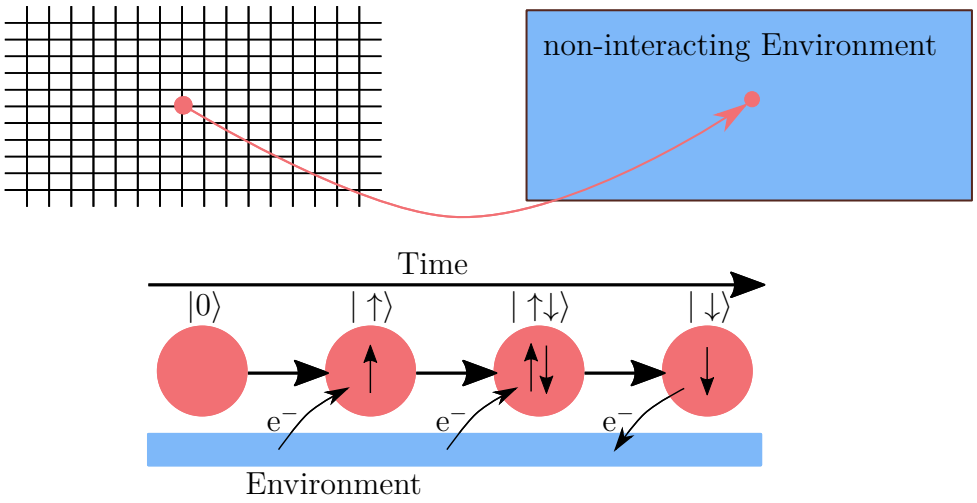


*Figure 5.1: Conceptional idea of DMFT. A single site of the infinitely large lattice is taken out of the system and placed in a non-interacting environment. On this site, called impurity, the electrons interact normally. We consider systems where the local state space consists of no electrons, a single electron or two electrons. Over time, the electrons can jump from the environment on the impurity site and back into the environment. This interaction is described by the hybridisation, which has to be determined self-consistently during DMFT.*

(SDFT) originate from the Baym-Kadanoff equations[33,116]. They differ mainly in the physical quantity they aim to calculate and the physics they consider to do so. In this thesis, we work with DMFT to determine the local interacting single-particle Green's function of the Hubbard model and real materials. This quantity already contains a lot of interesting information that allow for instance to compute local observables or the spectral function of the interacting model, which allows to determine whether the system is an insulator, a conductor or a superconductor.
In the following sections we will first discuss the theoretical background of DMFT based on the Baym-Kadanoff equations following Kotliar et al.[33]. Afterwards, we will present different impurity solvers, which can be used to solve the auxiliary impurity problem generated by DMFT and argue why we use DMRG. The specific details of a DMFT iteration in terms of formulas, assumptions, conditions and chosen numerical parameters is discussed in great detail afterwards. This allows other researchers to build there own working DMFT+DMRG code and reproduce our data. Model specific details of the implementation and deviations from the standard approach are discussed in chapter 6 for the case of the Hubbard model and in the chapters 7 and 8 for real material studies of $Sr_2VO_4$ and $Sr_2RuO_4$, respectively. We close the discussion about dynamical mean-field theory by introducing cluster extensions to DMFT, specifically the dynamical cluster approximation (DCA). Since DMRG approximates the complex interactions taking place in two-dimensional lattice models by only taking into account local interactions, all computed quantities, such as self-energies, Green's functions, and hybridisations, are momentum independent. DCA in its different forms restores some of the momentum de-

pendence by reintroducing non-local interactions. This allows to deal with full models on a more realistic level, but it also restores some of the complexity of the original problem.

## 5.1 Baym-Kadanoff Equations

The aim of this section is to give an idea of how to derive the relationship between the infinitely large lattice problem and the auxiliary cluster plus environment system. We will follow Kotliar et al.[33] in the next sections to derive the so-called Baym-Kadanoff equations, which allow to determine physical quantities such that they satisfy macroscopic conservation laws[117]. The first step is to choose the quantity that is to be computed. In the case of DMFT this is the local electron Green's function

$$G_{\sigma',\sigma}(x',x) = -\langle T_\tau \hat{\psi}_{\sigma'}(x')\hat{\psi}^\dagger_\sigma(x)\rangle. \tag{5.1.1}$$

$\hat{\psi}^\dagger_\sigma$ and $\hat{\psi}_\sigma$ are the creation and annihilation operators of an electron with spin $\sigma$ at position $\vec{r}$ and time $\tau$, which are summarised in the variable $x = (\vec{r}, \tau)$. $T_\tau$ denotes the time ordering operator with respect to the time $\tau$. To keep the notation clean, we will omit the spin indices. We now want to determine a set of equations that allow to determine $G$. Therefore, we define the action

$$S = \int \mathrm{d}x \hat{\psi}^\dagger(x)\partial_\tau \hat{\psi}(x) + \int \mathrm{d}\tau \hat{H}(\tau), \tag{5.1.2}$$

with $\hat{H}(\tau)$ being the Hamiltonian of the lattice system. By adding a source term $J(x,x')$ to $S$ and writing the partition sum in the following way

$$Z[J] = \exp(-F[J]) = \int \mathcal{D}[\psi^\dagger\psi] e^{-S-\int \mathrm{d}x\mathrm{d}x' J(x,x')\psi^\dagger(x)\psi(x')}, \tag{5.1.3}$$

we can find an expression for the Green's function via a variation of the free energy with respect to the source term. This will yield the expectation value of $\psi^\dagger(x)\psi(x')$, which results in the relationship

$$G(x,x') = -\langle T_\tau \hat{\psi}_{\sigma'}(x')\hat{\psi}^\dagger_\sigma(x)\rangle = \left.\frac{\delta F}{\delta J(x,x')}\right|_{J=0}. \tag{5.1.4}$$

The equation determines the Green's function dependent on the source term and vice versa. At this point, we will split up the action $S = S_0 + \lambda S_1$ into a non-interacting part $S_0$, which can be solved easily, and an interacting part $S_1$, which contains the complicated physics. With the parameter $\lambda$ the interacting part can be turned on and off. In the non-interacting case $\lambda = 0$, the following expression for the free energy can be obtained

$$\begin{aligned} e^{-F_0[J_0]} &= \int \mathcal{D}[\psi^\dagger\psi] \exp\left[-\int \mathrm{d}x\mathrm{d}x' \psi^\dagger(x)\left(\frac{\partial}{\partial\tau} - \mu + \hat{H}_0 + J_0\right)\psi(x')\right] \\ &= \mathrm{Det}\left(\frac{\partial}{\partial\tau} - \mu + \hat{H}_0 + J_0\right). \end{aligned} \tag{5.1.5}$$

By taking the logarithm, we obtain

$$F_0[J_0] = -\mathrm{Tr}\ln(G_0^{-1} - J_0). \tag{5.1.6}$$

$G_0 = (\partial\tau - \mu + \hat{H}_0)^{-1}$ is the usual non-interacting Green's function since $\hat{H}_0$ is the non-interacting Hamiltonian. By performing a variation of the free energy with respect to $J_0$ as derived in Eq. (5.1.4), we can write down the interacting Green's function

$$G = \frac{\delta F_0[J_0]}{\delta J_0} = (G_0^{-1} - J_0)^{-1}. \tag{5.1.7}$$

It follows that the source field $J_0$ is the interacting self-energy $J_0 = \Sigma$, which describes all the interactions of the system. Thus, we recovered the usual Dyson equation, which allows to compute the Green's function when knowing the self-energy. To determine an equation for $\Sigma$, we perform a Legendre transformation on the free energy $F[J]$ and obtain the functional

$$\Gamma[G] = F[J[G]] - \mathrm{Tr}(J[G]G), \tag{5.1.8}$$

dependent only on the Green's function $G$ with the trace defined as

$$\mathrm{Tr}(JG) = \int \mathrm{d}x\mathrm{d}x' J(x,x')G(x',x). \tag{5.1.9}$$

For $\lambda = 0$, we replace $J$ with the self-energy and obtain

$$\Gamma_0[G] = -\mathrm{Tr}\ln[G_0^{-1} - \Sigma[G]] - \mathrm{Tr}[\Sigma[G]G]. \tag{5.1.10}$$

Now, in the interacting case $\lambda = 1$ the functional is changed slightly to

$$\Gamma_{\mathrm{BK}}[G] = -\mathrm{Tr}\ln[G_0^{-1} - \Sigma[G]] - \mathrm{Tr}[\Sigma[G]G] + \Phi_{\mathrm{BK}}[G], \tag{5.1.11}$$

where all the complicated interaction physics is put into the non-trivial functional $\Phi_{\mathrm{BK}}[G]$. We will refer to $\Gamma_{\mathrm{BK}}[G]$ as the Baym-Kadanoff functional. From the derivation of Eq. (5.1.7) it is clear that in the interacting case $J$ vanishes. This must be the case since for $\lambda = 1$ the non-interacting Hamiltonian $\hat{H}_0$ becomes the interacting Hamiltonian $\hat{H}$, which by definition already includes all the interaction physics. Thus, Eq. (5.1.7) becomes

$$G = (G^{-1} - J)^{-1}, \tag{5.1.12}$$

leading to $J = 0$. Therefore, the differential of the Baym-Kadanoff functional

$$\delta\Gamma_{\mathrm{BK}} = -\mathrm{Tr}[\mathrm{J}\delta\mathrm{G}], \tag{5.1.13}$$

shows that in the interacting case $\Gamma[G]$ is stationary and equal to the free energy of the system. With the property of stationary we can use the saddle-point equation with Eq. (5.1.11) and obtain

$$\frac{\delta\Gamma_{\mathrm{BK}}[G]}{\delta G} = \mathrm{Tr}\left[\frac{\delta\Sigma}{\delta G}[(G_0^{-1} - \Sigma)^{-1} - G]\right] - \Sigma + \frac{\delta\Phi_{\mathrm{BK}}[G]}{\delta G} = 0. \tag{5.1.14}$$

The first term in parentheses vanishes because of the Dyson equation. This leaves us with

$$\Sigma[G] = \frac{\delta \Phi_{\mathrm{BK}}[G]}{\delta G}, \tag{5.1.15}$$

with the exact form of $\Phi_{\mathrm{BK}}$ unknown. In principle, the Green's function $G$ and self-energy $\Sigma$ can be determined self-consistently with the two equations Eq. (5.1.7) and Eq. (5.1.15). Solving the exact functional in Eq. (5.1.15) results in the so-called spectral density functional theory. Unfortunately, summing up the diagrams describing $\Phi_{\mathrm{BK}}$ is nearly impossible. However, DMFT approximates this functional by a sum of all two-particle irreducible skeleton graphs[33]. This approximation becomes exact in the limit of an infinite lattice coordination number[29] and corresponds to having a momentum-independent self-energy. The sum can be performed exactly by introducing an auxiliary quantum impurity model with a self-consistency condition[30,31] and solving it with an impurity solver.

## 5.2 Impurity Solvers

Since DMFT reduces the complex two-dimensional lattice problem to an impurity problem coupled to a non-interacting bath, which must be solved self-consistently, the fundamental question of DMFT is which kind of impurity solver is to be used. There exists a wide variety of solvers each with their unique approaches and, therefore, with their own strengths and weaknesses. In the following, we will focus on some of the more known solvers to provide a context to understand why we have chosen to work with DMRG on the three problems presented in the chapters 6, 7 and 8.

- We will start with the widely known continuous-time quantum Monte Carlo[15,34,118] (CTQMC) approach, which is the method of choice for a wide variety of quantum impurity models. For a very detailed description of the development, concepts, implementation details and examples of CTQMC we refer to Gull et al.[34]. The basic idea is very simple and begins with a Hamiltonian split into two parts $\hat{H} = \hat{H}_1 + \hat{H}_2$. Then, the partition sum can be written by expanding it in powers of $\hat{H}_2$

$$\begin{aligned} Z &= \mathrm{Tr}\; T_\tau e^{-\beta \hat{H}_1} \exp\left( - \int_0^\beta \mathrm{d}\tau \hat{H}_2(\tau) \right) \\ &= \sum_k (-1)^k \int_o^\beta \mathrm{d}\tau_1 \ldots \int_{\tau_{k-1}}^\beta \mathrm{d}\tau_k \; \mathrm{Tr}\left( e^{-\beta \hat{H}_1} \hat{H}_2(\tau_k) \hat{H}_2(\tau_{k-1}) \ldots \hat{H}_2(\tau_1) \right). \end{aligned} \tag{5.2.1}$$

  It is necessary that the spectrum of the perturbation term $\hat{H}_2$ is bounded from above such that the terms are exponentially suppressed by the factor $k!$ of the exponential. The decomposition can be chosen quite freely with the only requirement being that the time evolution with respect to $\hat{H}_1$ and the contractions of fermion operators $\hat{H}_2$ can be performed easily. However, in the context of impurity models a couple of

typical decompositions known as hybridisation or interaction expansions exist, the latter sometimes also called weak coupling expansions. They are based on different ways of splitting up the Hamiltonian and are suited to different extents for certain classes of problems.
Anyways, Monte Carlo methods are statistical methods and a physical quantity $A$, as for example a Green's function, is calculated via an expectation value over the configuration space $\mathcal{C}$ with weight $p$ of the quantity $\mathcal{A}(x)$

$$\langle A \rangle_p = \frac{1}{Z} \int_{\mathcal{C}} \mathrm{d}x \mathcal{A}(x) p(x). \tag{5.2.2}$$

This approach becomes problematic if the weights $p(x)$ become negative due to, for example, the anti-commutation relations of fermionic operators. The weights can no longer be regarded as probabilities and are replaced by the absolute value of the weight $\rho(x) = |p(x)|$. Therefore, the expectation value has to be written as

$$\langle A \rangle = \frac{\langle A \cdot \mathrm{sign} \rangle_{|p|}}{\langle \mathrm{sign} \rangle_{|p|}}, \tag{5.2.3}$$

which suffers under exponentially growing errors with decreasing temperature. The so-called sign-problem is the accurate measurement of the near-zero sign from individual measurements that have either $+1$ or $-1$ as a pre-factor. This problem has been proven to be nondeterministic polynomial (NP) hard [119]. The severity of the sign problem depends significantly on the model and the chosen representation, i.e. basis choices etc. In general, impurity models have a much less severe sign problem than full lattice problems. However, if the sign problem is present, because the temperature is too low, the problem is not symmetric enough or an interaction is too strong, it prevents CTQMC from obtaining trustworthy results. Because of its formulation, CTQMC computes the Green's functions and self-energies on the imaginary-frequency axis. Unfortunately, interesting physical quantities such as spectral densities $A(\omega)$ or response functions are defined on the real-frequency axis. The standard approach is to use analytical continuations like max-Ent or Padé to extrapolate the physical quantities to the real-frequency axis. This has to be done very carefully since analytic continuations are in general numerically ill-defined.

- The numerical renormalisation group (NRG) developed in 1975 by K.G. Wilson [35] allows to calculate physical quantities directly on the real-frequency axis at zero temperature. The key idea is to course grain the hybridisation $\Lambda$, which describes the interaction of the impurity with the environment, via a logarithmic discretisation. This generates a so-called semi-infinite Wilson chain, which is cut after some number of sites to allow numerical calculations. This Wilson chain consists of sites with on-site energies and nearest neighbour hopping terms whose amplitudes decrease exponentially fast along the chain. NRG starts with diagonalising the combined

system of the impurity site and the first site of the Wilson chain. Due to the very specific setup, the Wilson chain guarantees so-called energy-scale separation. This allows NRG to discard the high energy spectrum of the combined sites and merge the remaining energy levels into an effective site while still having a very good description of the low-energy spectrum of the system. This effective site is then combined with the next site of the Wilson chain and the procedure is repeated until the last site of the system is reached. In the end, NRG produces a very precise low-energy spectrum of the lattice model and thus also a very good description of the ground state and the interacting zero-temperature Green's function.
NRG generates physical quantities with a very high resolution at low frequencies. However, it can be problematic and numerically unfeasible if the spectral function has a rich structure at high frequencies since NRG with its logarithmic discretisation is focused on the low-energy behaviour.
Anyways, only recently it was shown that NRG is able to successfully calculate the Green's function of a multi-band problem with more than two bands[18]. Since each band has its own exponentially decaying Wilson chain, it is challenging how to adapt NRG to ensure energy scale separation and efficiency at the same time. It is therefore questionable if NRG will be able to deal with dynamical cluster approximations or multi-band systems where multiple impurities with their own baths are present. For further details on NRG and its applications we refer the interested reader to the vast amount of literature[120,121,122,123].

- Exact diagonalisation (ED) as an impurity solver for DMFT was first presented by Caffarel and Krauth in 1995[14]. ED diagonalises either the whole Hamiltonian or at least the symmetry sectors in which the global ground state and the interacting Green's functions are located. This part is very time consuming and is severely limited by the size of complete system because the relevant Hilbert space grows exponentially with system size.
  While with CTQMC the infinitely large environment is typically integrated out and therefore treated exactly, with ED a finite and discrete approximation of the environment has to be found. We will refer to this approximation as the bath. Given a hybridisation $\Delta(z)$, which describes the interaction between impurity sites and the continuous environment, a finite discretised version of the bath can be constructed either on the real-frequency or on the imaginary axis. How this can be done is described in detail in section 5.3.1. The energies of the environment are represented by poles in the hybridisation and are located close to the real-frequency axis. Therefore, it is clear that we can find a very good description of the hybridisation on the imaginary-frequency axis with only a few effective discrete energies since the detailed structure of the distribution and strength of the poles is smeared out far away of the real-frequency axis. Typically, we need two to ten sites to have a reasonable description of $\Delta(i\omega_n)$ on the imaginary axis. In contrast, on the real axis typical bath sizes for a good description of the hybridisation $\Delta(\omega)$ are 80 to 120 sites.

For systems with up to six sites, ED can, in general, calculate the whole spectrum of the Hamiltonian and therefore also the Green's function pretty easily. For larger systems this is not possible anymore, but for up to 16 sites the zero-temperature Green's function can still be determined with the Lanczos algorithm [110,124] efficiently. This obviously limits ED in the context to DMFT on the imaginary axis. Furthermore, it limits ED to DMFT problems with only a couple of conducting bands or with a low-order dynamical cluster approximation. We want to end the paragraph about ED with presenting the two step procedure that is the heart of ED. First, the ground state $|E_0\rangle$ of the system has to be determined with the usual Lanczos procedure. Second, the Green's function is split into the lesser and greater Green's function

$$G(i\omega_n) = G^{>}(i\omega_n) + G^{<}(i\omega_n), \tag{5.2.4}$$

which correspond to particle and hole excitations, respectively. Then, the Green's functions are written down as continued-fraction expansions

$$G^{>}(i\omega_n) = \cfrac{\langle E_0|dd^\dagger|E_0\rangle}{i\omega_n - a_0^{>} - \cfrac{(b_1^{>})^2}{i\omega_n - a_1^{>} - \cfrac{(b_2^{>})^2}{i\omega_n - a_2^{>} - \dots}}}, \tag{5.2.5}$$

$$G^{<}(i\omega_n) = \cfrac{\langle E_0|d^\dagger d|E_0\rangle}{i\omega_n - a_0^{<} - \cfrac{(b_1^{<})^2}{i\omega_n - a_1^{<} - \cfrac{(b_2^{<})^2}{i\omega_n - a_2^{<} - \dots}}}. \tag{5.2.6}$$

For simplicity we will skip the superscripts $>$ and $<$ for the following definitions. The coefficients $a_i$ and $b_i$ can be determined during the Lanczos algorithm and are just expectation values of the Hamiltonian

$$a_i = \langle p_i|\hat{H}|p_i\rangle, \tag{5.2.7}$$

or overlaps of Lanczos vectors

$$b_i^2 = \frac{\langle p_i|p_i\rangle}{\langle p_{i-1}|p_{i-1}\rangle}, \tag{5.2.8}$$

with $|p_{i+1}\rangle = \hat{H}|p_i\rangle - a_i|p_i\rangle - b_i^2|p_{i-1}\rangle$. The greater and lesser Green's function only differ in their starting state $|p_0^{>}\rangle = d^\dagger|E_0\rangle$ and $|p_0^{<}\rangle = d|E_0\rangle$, respectively. As for CTQMC calculations, ED produces physical quantities on the imaginary-frequency axis and have to be extended to the real-frequency axis with analytic continuations to obtain most of the physically interesting quantities.
Typical problems for ED that require fine tuning for most models, are degeneracies of ground states and numerical instabilities of the Lanczos method. However, ED has proven to be a reliable and high quality impurity solver for small systems and is still widely used [37,125,126].

- An alternative to ED is the density matrix renormalisation group (DMRG), which we described in the previous chapters in great detail. DMRG computes the ground state of the lattice directly with a variational approach. This is much cheaper than computing the whole spectrum, especially for large systems. The drawback compared to ED is that determining the Green's functions and self-energies after the ground state search requires more numerical effort. Nevertheless, this approach allows to solve much bigger systems than with ED while preserving a reasonable resolution for physical quantities.
  DMRG can be used to compute Green's function on the real-frequency axis [36,39,127,128] as well as on the imaginary axis [40,129] and produces in both cases very good results that are in agreement with other methods like CTQMC [103,129]. ED and DMRG are both methods working at temperature $T = 0$, but can, in principle, be extended to finite but low temperatures as long as the low-energy spectrum can be computed. With ED this can be done quite easily for small systems while for DMRG this requires performing additional ground state searches in the subspace of the Hilbert space orthogonal to all already found eigenstates. These calculations are in general more time consuming due to bad entanglement properties since area laws do not apply.
  Because interesting physical quantities like the spectral density $A(\omega)$ or response functions in general are defined on the real-frequency axis, there is a strong tendency to work directly with real frequencies. However, DMRG reaches its limits with most multi-band band models or dynamical cluster approximations. In those systems in general three or more impurity sites have to be considered, each with its own bath. The total system size can easily exceed 300 sites with potentially artificial long-range interactions. This increases entanglement in those systems dramatically and leads to unbearable computation times. Therefore, a reasonable approach for multi-band and dynamical cluster approximation problems is to perform DMFT+DMRG on the imaginary axis since the smaller systems can be considered to have less numerical complexity. Then, analytical continuations or other approaches can be used to obtain physically more interesting real-frequency Green's function $G(\omega)$. This is the approach we will follow in the remaining part of the thesis.

After we presented a small excerpt of the wide variety of impurity solvers, it is obvious that all methods have certain strengths and weaknesses. It is not always clear whether a specific model can be solved with a certain impurity solver, especially in the case of CTQMC with its sign problem or in the case of DMRG where entanglement properties of a system are not predictable. Since the more interesting physical systems tend to have multiple bands, momentum-dependent properties or both, an impurity solver that can deal with big systems, multiple impurities and is able to produce reliable results at sufficiently low enough temperatures is definitely needed in the solid state community.
Using DMRG as an imaginary-time impurity solver for DMFT proposed by Wolf et al. in 2015 [129] was motivated by exactly this reasoning. In the following sections we will present the ideas and underlying derivations of this method following Wolf et al. We will

do this in great detail and will also comment on implementation issues and parameter choices to allow other researchers to reproduce our results.

## 5.3 Step By Step: A Full DMFT Iteration

In the following sections we want to give a detailed overview of the different steps of a full DMFT iteration with DMRG used as impurity solver. This will not only include analytical expressions, but also typical choices of numerical parameters, thresholds and implementation details. We will also discuss why we choose certain approaches over others and which parts of the method can be improved in the future and in which way.
This section is the basis of the following chapters where we will discuss different models and the results obtained with DMFT+DMRG.

### 5.3.1 Hybridisation

Each DMFT iteration starts with a hybridisation $\mathbf{\Delta}(z)$ describing the coupling between the impurity sites and the environment with $z$ being a complex or real frequency. The hybridisation has to be determined with the help of the self-consistency equations of DMFT in such a way that the impurity problem gives rise to the same Green's function and self-energy as the original two-dimensional lattice model. This means $\mathbf{\Delta}(z)$ obtained in iteration $n$ is used as the starting ground for iteration $n+1$ until the hybridisation of consecutive iterations does not change anymore. At the very start of the DMFT calculation any kind of hybridisation can be used. However, the choice determines how many iterations are needed to converge to the self-consistent DMFT solution and how complicated the calculations will be numerically because of entanglement properties of the constructed impurity problems. In section 5.3.4 we will discuss the self-consistency equation of DMFT and also comment on how to determine a start hybridisation for the first iteration.
Given a hybridisation function $\mathbf{\Delta}(z)$, there are two ways to set up an impurity problem: On the real-frequency axis one can use typical schemes described by Bulla et al.[130], Žitko[131] and others[35,132] to find a discretisation of the continuous bath. Typically in this schemes, the hybridisation is separated into intervals and the average and mean values in these intervals are used as bath energies and hopping elements.
On the imaginary axis, also called Matsubara axis, the hybridisation is fitted with an analytic expression. For impurity problems this expression can be obtained from the definition of the non-interacting single-particle impurity Green's function $\mathcal{G}_0(z)$ as an inverse operator of the Hamiltonian

$$(z - \hat{H})\mathcal{G}_0(z) = 1. \tag{5.3.1}$$

We consider a general impurity Hamiltonian $\hat{H}$, which consist of a local model-dependent interaction Hamiltonian $\hat{H}_{\text{int}}$, a single-particle Hamiltonian $\hat{H}_{\text{single}}$ describing on-site energies of the impurity sites and single-particle hopping between them, the coupling between

impurity and bath sites $\hat{H}_{\text{hyb}}$ and the non-interacting bath itself $\hat{H}_{\text{bath}}$

$$\hat{H} = \hat{H}_{\text{int}} + \hat{H}_{\text{single}} + \hat{H}_{\text{hyb}} + \hat{H}_{\text{bath}}, \tag{5.3.2}$$

$$\hat{H}_{\text{single}} = \sum_{\alpha\beta} \mu_{\alpha\beta} d^{\dagger}_{\alpha} d_{\beta} \tag{5.3.3}$$

$$\hat{H}_{\text{hyb}} = \sum_{l,\alpha,\sigma} V_{l,\alpha,\sigma} d^{\dagger}_{\alpha,\sigma} c_{l,\alpha,\sigma} + \text{h.c.}, \tag{5.3.4}$$

$$\hat{H}_{\text{bath}} = \sum_{l,\alpha,\sigma} \epsilon_{l,\alpha,\sigma} c^{\dagger}_{l,\alpha,\sigma} c_{l,\alpha,\sigma}. \tag{5.3.5}$$

$d^{\dagger}_{\alpha}$ and $d_{\beta}$ are creation and annihilation operators on the impurity sites denoted with $\alpha$ and $\beta$, while $c^{\dagger}_{k}$ and $c$ act on the bath site $k$, which is describing an environment mode. Each bath site has an on-site energy $\epsilon_k$ and couples to the impurity sites via the hopping elements $V_{\alpha,k}$. The on-site energies and the single-particle hoppings between the impurity sites are described by $\mu_{\alpha\beta}$. In the following, we will consider only the single-particle Hamiltonian that is given by Eq. (5.3.2) without $\hat{H}_{\text{int}}$. We evaluate Eq. (5.3.1) by taking expectation values with respect to the complete basis set of bath states $|k\rangle$ and impurity states $|\alpha\rangle$ and inserting $\mathbb{1} = \sum_k |k\rangle\langle k| + \sum_\alpha |\alpha\rangle\langle\alpha|$ between the Hamiltonian and the Green's function. Then, we obtain

$$\begin{aligned} 1 &= \langle\alpha|(z - \hat{H})\mathcal{G}_0(z)|\alpha\rangle \\ &= (z - \hat{H}_{\alpha\beta})\mathcal{G}_{0,\beta\alpha}(z) - \hat{H}_{\alpha k}\mathcal{G}_{0,k\alpha}(z) \\ &= (z - \mu_{\alpha\beta})\mathcal{G}_{0,\beta\alpha}(z) - V^{*}_{\alpha k}\mathcal{G}_{0,k\alpha}(z), \end{aligned} \tag{5.3.6}$$

and

$$\begin{aligned} 0 &= \langle k|(z - \hat{H})\mathcal{G}_0(z)|\alpha\rangle \\ &= -\hat{H}_{k\beta}\mathcal{G}_{0,\beta\alpha}(z) + (z - \hat{H}_{kk})\mathcal{G}_{0,k\alpha}(z) \\ &= -V_{k\beta}\mathcal{G}_{0,\beta\alpha}(z) + (z - \epsilon_k)\mathcal{G}_{0,k\alpha}(z). \end{aligned} \tag{5.3.7}$$

Solving the last equation for $\mathcal{G}_{0,k\alpha}(z)$ and inserting it into Eq. (5.3.6) results in the non-interacting impurity Green's function

$$\mathcal{G}_{0,\beta\alpha}(z)^{-1} = z - \mu_{\alpha\beta} - V^{*}_{\alpha k}(z - \epsilon_k)^{-1} V_{k\beta}, \tag{5.3.8}$$

which can be written as

$$\boldsymbol{G}_0(z) = (z - \boldsymbol{\mu} - \boldsymbol{\Delta}(z))^{-1}, \tag{5.3.9}$$

which defines the hybridisation

$$\boldsymbol{\Delta}(z) = \sum_k \frac{\vec{V}^{\dagger}_k \vec{V}_k}{(z - \epsilon_k)}. \tag{5.3.10}$$

$\vec{V}_k = (V_{1k}\ V_{2k}\ \ldots\ V_{N_{imp}k})$ constitutes of hopping elements from bath site $k$ to each of the $N_{imp}$ impurity sites while $\vec{V}_k^\dagger$ is the transposed and complex conjugated vector. Thus, for an impurity model the hybridisation describes the single-particle hopping between bath and impurity sites as well as the on-site energies of the bath modes.
Now, on the imaginary-frequency axis we can define a cost function

$$\chi = \sum_n \omega_n^{-\alpha} ||\mathbf{\Delta}(i\omega_n) - \mathbf{\Delta}_{discr}(i\omega_n)||^2. \tag{5.3.11}$$

to determine the on-site energies and hopping elements of the bath sites. Numerically, this is not feasible for real frequencies. The poles, i.e. the on-site energies, are located on the real-frequency axis and for analytical reasons are typically slightly shifted to negative or positive imaginary values by introducing $z \to \omega \pm i\eta$ with an infinitesimal $\eta \in \mathbb{R}$. However, when performing integrations or summations on the real-frequency axis, $\mathbf{\Delta}(\omega)$ varies from very big values near to the poles to smaller ones far away from them. This will introduce numerical errors large enough to prevent qualitatively good solutions. On the imaginary axis $z \to i\omega$, the poles are located so far away that the hybridisation is sufficiently smooth to perform numerical operations precisely enough.
By using Eq. (5.3.10) to have an expression for $\mathbf{\Delta}_{discr}(i\omega_n)$ and fixing the number of bath sites $L_b$, the optimal bath parameters of the impurity problem can be found using a gradient search algorithm. In the cost function $\alpha$ is used to weight the fit more to small or high frequencies. Since we want to focus on the low-energy spectrum, typically we choose $\alpha = 1$ to enforce very good fits in the low-frequency regime even if there are not enough parameters to obtain a good fit over the whole frequency spectrum. Fig. 5.2 shows the obtained, optimal, discretised hybridisations for different bath sizes. For this model and parameter choice a bath with $L_b = 8$ sites gives perfect agreement while $L_b = 4$ sites are definitely not enough to even capture the qualitative behaviour of the hybridisation.
Since DMRG is working at temperature $T = 0$, the Matsubara frequencies $\omega_n = (2\pi n + 1)/\beta$ with $\beta = 1/T$ form a continuous set. Due to numerical limitations on a computer, continuous functions are saved only on so-called grid points. In our calculations we choose Matsubara frequencies at a fictitious temperature $\beta_{\text{eff}}$ as grid points. This has no effect on any physics taking place in the model as long as all steps in the DMFT calculation are performed precise enough. Of course, $\beta_{\text{eff}}$ sets a lower bound for the Matsubara frequencies $\omega_0 = 1/\beta_{\text{eff}}$ and has to be chosen large enough so that no relevant part of the hybridisation, self-energy or Green's function are cut away. Typically, we choose $\beta_{\text{eff}} = 100$ in our calculations. We also choose an upper limit $\omega_{\max} = 6$ for the Matsubara frequencies to improve the calculation speed for the fitting procedure and other computations during the DMFT loops. Similar to the lower bound, this can be done if the functions for arguments above $\omega_{\max}$ do not incorporate additional information.
In general, the hybridisation is a matrix-valued function and the Frobenius norm has to be used to determine the distance between the fit and the continuous hybridisation in the cost function $\chi$. However, in the majority of problems treated by DMFT the impurity sites decouple and it exists no single-particle hopping between them. Then, the hybridisation is reduced to a diagonal matrix, which allows to fit each diagonal component independently.

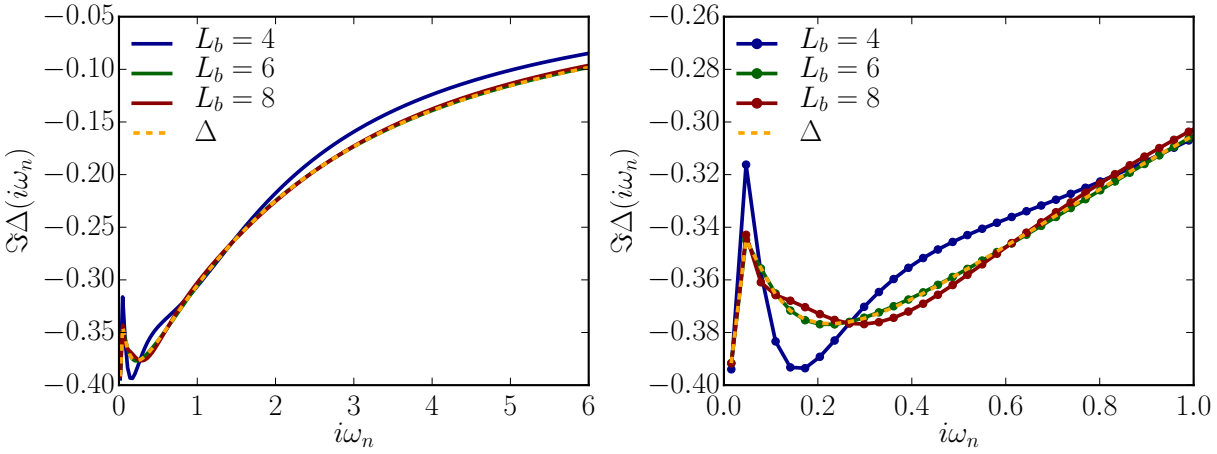


*Figure 5.2: Left panel: Different fits of a hybridisation function $\mathbf{\Delta}(i\omega_n)$ (blue dashed line) on the imaginary axis with $L_b = 4, 6, 8$ bath sites for the* xy*-band of the three-band model $Sr_2RuO_4$. Only the imaginary part is displayed. Clearly a fit with $L_b = 4$ bath is not good enough, while $L_b = 6$ sites only show small deviations for large frequencies. Right panel: The same functions as in the left figure but zoomed in for small small frequencies. Is is much better to see that only the fit with $L_b = 8$ bath sites gives very good agreement.*

i.e. each bath site couples only to a single impurity site independently on the rest of the lattice. That reduces the numerical effort for fitting $\mathbf{\Delta}$ dramatically since significantly less parameters have to be considered for the gradient search algorithm. In this case the norm in Eq. (5.3.11) reduces to a simple scalar norm.
Our standard approach to find the optimal fit $\mathbf{\Delta}_{discr}(i\omega_n)$ is to use a global gradient search algorithm implemented in PYTHON named *basinhopping*[133]. It consists of the following steps

- It generates random real values as hopping elements and on-site energies in the interval $[-1, 1]$. Those values are the starting point $x_0$ for the optimisation.
- Beginning from $x_0$ a gradient search algorithm calculates the gradient at the current position, uses this information to guess in which direction the next minimum is located and changes the parameter set to $x_{new}$ by moving in the direction of the guessed minimum. The program spends most of the time evaluating the cost function to determine the actual value of $\chi$ and calculate the gradient numerically. Implementing an analytic expression of the gradient reduces the amount of function calls dramatically and reduces the computations time (see Fig. 5.3b) ). To improve the performance further, the cost function and the gradient are compiled in c-code, which gives another huge speed-up.
- To avoid being stuck in local minima, after each local minimisation a test is performed to accept or reject the new parameters based on the cost function value. If

the cost function value is smaller after the optimisation, the new parameter set is accepted always. If not, the new parameter set is accepted with the probability

$$\exp\{-(\chi(x_{new}) - \chi(x_{old}))/T\}. \tag{5.3.12}$$

This probability is strongly dependent on the choice of the temperature $T$, which should roughly be comparable with the cost function values at the occurring minima to be efficient. Unfortunately, since we deal with different kind of models, hybridisations and numbers of bath sites $L_b$, the cost function values at the minima vary from $10^{-2}$ to $10^{-9}$. Experience shows that we can reliably determine the global minimum with $T = 1$. This means that nearly each step of the optimisation scheme is accepted.

- Since the optimisation routine cannot identify whether a minimum is local or global and the gradient search can move out of a found minimum at any time due to the choice $T = 1$, there is no clear criterium whether the algorithm was successful and can be stopped. Thus, we let the optimisation procedure perform 100 optimisation iterations and take the parameter set with the smallest cost function value as result. To avoid a dependence on the starting parameters and ensure that the global and a local minimum is found, we perform 20 independent optimisations from different starting sets $x_0$. In our experience several up to all of the independent calculations find the same optimal parameter set, which supports the claim that it is really the global minimum.

- The runtime is very dependent on the problem we have to deal with and in general relatively large for bigger systems. Experience shows that in later DMFT iterations the hybridisations only differs slightly from iteration to iteration. Therefore, in those cases it is advantageous to use the parameter set of the last iteration as a starting point for the fitting procedure and only perform a local search. To be reasonable sure that the global minimum is found, we perform five independent optimisations and take the best result. This reduces the numerical effort while allowing to find the ground state reliably. We do this from the fifth DMFT iteration on, where changes of the hybridisation from one iteration to the other are typically of the order $10^{-2}$.

Before we go over to the ground state search, we want to shortly comment on some parameter and PYTHON oriented choices regarding the optimisation scheme. PYTHON offers a wide variety of different minimisation functions[134] that are based on gradient algorithms (Powell[135], CG[136]), quasi Newton methods, which are working only with first derivatives (BFGS[136]) or methods, which are even using the Hessian (dogleg[136]). All these methods have their strength and weaknesses for different problems, but all give the same results in the test case of a Single-Impurity-Anderson-model. This is a very good sign for the reliability of our results.
Furthermore, all methods show an overfitting problem at the same number of parameters. This manifests itself in a lower bound of the cost function value (around $10^{-6}$ down to

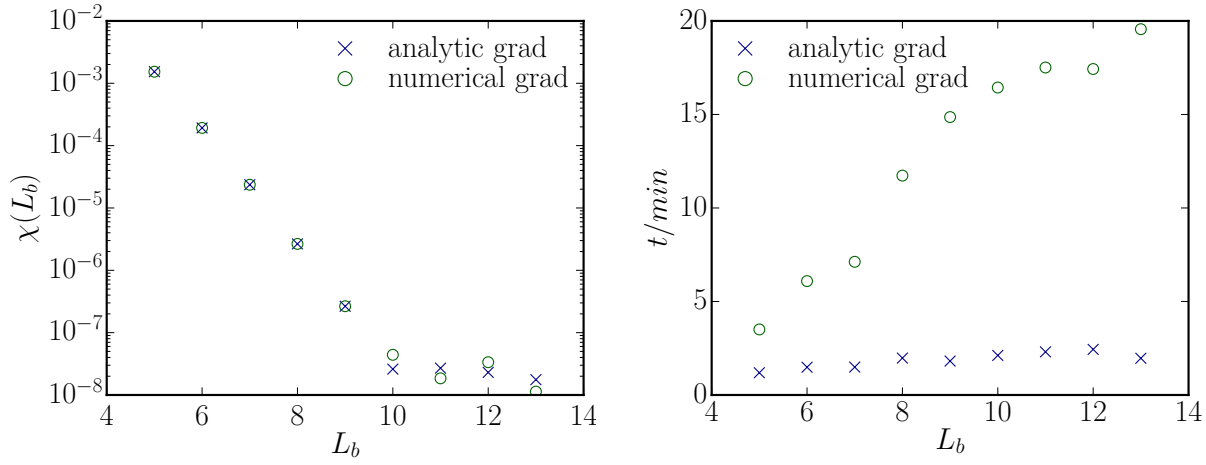


*Figure 5.3: Left panel: Best cost function value for fits of the hybridisation with different bath sizes $L_b$. The data was obtained from single site DMFT calculations of the Hubbard model with interaction strength $U = 5t$, next nearest neighbour hopping $t_p = -0.15t$ and at half filling in the first iteration. The hybridisation to fit is obtained from the non-interacting model. How to do this is explained in the end of section 5.3.4. Up to ten bath sites, each bath site more improves the fit quality. From there on we see overfitting, i.e. an increase of parameters do not improve the fit quality. There is no difference in the behaviour between using an analytic gradient and evaluating the gradient numerically. Right panel: Runtimes for the calculations in the left figure. Evaluating the gradient numerically takes more and more time the more bath sites and parameters we consider. Using the analytic gradient keeps the runtime approximately constant in this rather simple case. For other models there is also a significant increase of the computation time dependent on the number of parameters when using the analytic gradient.*

$10^{-9}$), which cannot be exceeded with any increase of the number of parameters as can be seen in Fig. 5.3. Each fitting procedure results in significantly different parameter sets while obtaining very similar cost function values. This means that two optimisations, described as above, will give two qualitatively different results for the global minimum. This not only leads to convergence problems in DMFT but also to solutions that have to be considered as unphysical. For instance, in the Hubbard-model without next-nearest neighbour hopping we expect at half-filling a completely antisymmetric set of bath parameters. This leads to the real part of the Green's function $G(i\omega)$ being zero and the imaginary part of $G(\omega)$ being symmetric with respect to $\omega = 0$. In other words the system is particle-hole symmetric. In the case of overfitting, in general, we do not obtain an antisymmetric parameter set, which leads to an asymmetric spectrum of the Hamiltonian and to no particle-hole symmetry.
Since the choice of the actual optimisation method seems to be without much influence, we choose the method of Broyden, Fletcher, Goldfarb, and Shanno (BFGS), which has proven to have good performance even for non-smooth optimisations[137].

The hybridisation fit can be further improved by adjusting the temperature $T$ of the acceptance probability to values close to typical results of $\chi$ at local minima or by a more evolved global optimisation scheme like simulated annealing[138] or particle swarm optimisation[139]. If runtimes of the fitting procedures exceed a tolerable limit, an implementation of the analytic expression of the Hessian and applying a method that is using the second order derivatives can improve the runtimes significantly.

### 5.3.2 Ground State Calculation

After a discrete description of the bath is found via the fitting procedure, the parts of the Hamiltonian Eq. (5.3.4) and Eq. (5.3.5) are completely defined. The remaining parts of the Hamiltonian $\hat{H}$, namely $\hat{H}_{\text{single}}$ in Eq. (5.3.3) and $\hat{H}_{\text{int}}$, are defined by the chosen model and will be discussed in more detail in the model-specific sections. We consider them as given here.
Thus, the Hamiltonian is completely defined and the ground state search with DMRG can be started. Depending on the form of $\hat{H}_{\text{int}}$ and $\hat{H}_{\text{single}}$, we can implement different symmetry quantum numbers in the MPS related methods. The conserved total particle number $N$ described by an $U(1)$-symmetry or the conserved $z$-component of the total spin of the system $\vec{S}_z$, also described by an $U(1)$-symmetry, are typical examples. In general, any number of symmetries of any symmetry group can be implemented as long as it can clearly be defined how a creation or annihilation operator changes the quantum numbers locally and independently of the state of the rest of the system.
In tabular 5.1 we listed the symmetries that are present in the models we work with. It is important to know at this level that DMRG can have problems with finding the

| Hubbard model | Hubbard-Kanamori | Spin-Orbit-coupling |
|---|---|---|
| U(1): N | U(1): N | U(1): N |
| SU(2): $\|\|\vec{S}\|\|$ | SU(2): $\|\|\vec{S}\|\|$ | U(1): $\vec{J}_z$ |
| $Z_4 \times Z_4$: $(k_x, k_y)$ | $Z_4 \times Z_4$: $(k_x, k_y)$ | |
| | $Z_2$: band parity | |

*Table 5.1: Present symmetries in the models we are dealing with in this thesis. A more detailed discussion about the symmetries and their origin is discussed in the model specific chapters. The total number of particles $N$ is conserved in each model. If there is a conserved total spin $||\vec{S}||$, we can choose between conserving the $SU(2)$ symmetry explicitly or just the z-component of the total spin $\vec{S}_z$, which is described by a $U(1)$ symmetry. The $Z_4 \times Z_4$ quantum number describing the conserved momentum vector, is only present if we work with the dynamical cluster approximation in momentum-space. For high patch numbers this symmetry can change to a different symmetry-class. Each band present in the Hubbard-Kanamori model has a conserved band parity. That symmetry as well as the conservation of the spin is vanishing if we add spin-orbit-coupling. However, in the correct basis we can use the conservation of the z-component of the total angular momentum $\vec{J}_z$.*

ground state reliably if not all symmetries are implemented. To ensure convergence to the global ground state, DMRG starts its optimisation with a randomly generated state. If a symmetry is not implemented, it can happen very easily that the starting state is located in a different symmetry sector than the global ground state or that during the early optimisations steps the part of the starting state in the correct symmetry sector is discarded. In those cases it is impossible for DMRG to converge to the global ground state and it simply computes the ground state of the accessible Hilbert space. Thus, repeated calculations with different random starting states can result in different results with significant energy differences. For DMFT, this can lead to severe convergence problems and unphysical results for the hybridisation or Green's function.
However, one can of course always insert artificial terms $\hat{H}_{\text{tunnel}}$ in the Hamiltonian to break the symmetries that are not implemented and allow DMRG to have access to all symmetry sectors, i.e. the whole Hilbert space. We will refer to those terms as the "tunnelling Hamiltonian". This approach has its disadvantages. To obtain the real ground state of the Hamiltonian $\hat{H}$, the artificial terms have to be removed at some point of the calculation. This has to be done over several sweeps with a slowly decreasing amplitude of $\hat{H}_{\text{tunnel}}$ to allow DMRG to have enough overlap with the global ground state when the artificial terms are removed completely and the symmetries are present again. If this is not the case, again DMRG will not be able to converge to the global ground state. Unfortunately, this ansatz slows down the DMRG ground state search significantly.
Usually, in DMRG calculations it is recommended to start with a very small bond dimension and increase it during the calculation to the desired value. In general, the starting state differs very strongly from the global ground state and thus even an imprecise optimisation step will change the state into the direction of the global ground state. By keeping bond dimensions low in those first steps improves the performance noteworthy. In contrast, in later iterations it is necessary to have a precise optimisation and thus a high bond dimension to allow for correct optimisations. Summarising, starting with a low bond dimension and increasing it during the DMRG calculation will generate a nice speed-up and not influence convergence negatively.
However, this approach is not compatible with the tunnelling Hamiltonian ansatz. To be sure that DMRG has enough overlap with the global ground state when $\hat{H}_{\text{tunnel}}$ is removed, the bond dimension must be high enough such that DMRG can take into account all relevant correlations and interactions. This means we have to determine the ground state of the original Hamiltonian $\hat{H}$ plus the tunnelling Hamiltonian and then slowly remove $\hat{H}_{\text{tunnel}}$ while staying close to the global ground state. This requires a high bond dimension before turning down the amplitude of $\hat{H}_{\text{tunnel}}$. Additionally, the artificial terms induce extra entanglement, which results, in general, in a higher bond dimension needed for the DMRG calculations. To avoid convergence issues, we rather implement all present symmetries of the Hamiltonian than to deal with the fine tuning of bond dimensions, number of sweeps and the amplitude of the tunnelling Hamiltonian. Especially, because the latter can be very parameter and model specific.
The other advantage and typically the main reason to implement symmetries is that the

dense tensors of the MPSes and MPOs decompose into separate blocks each describing a certain symmetry sector. These symmetry blocks can be treated independently of each other in most of the MPS operations, which allows to parallelise computations effectively. Additionally, each of those blocks has a smaller bond dimension $m$ than the original dense tensor. Since the computational cost of most MPS operations scales with $\mathcal{O}(m^3)$, this results into another speed-up.
The drawback of implementing symmetries in the context of DMFT is that we do not know in which symmetry sector the global ground state is located beforehand. Since the symmetry sectors are all orthogonal to each other, DMRG calculations have to be started in each sector separately, and the results have to be compared to determine the global ground state. This can be very time consuming if a lot of symmetries are implemented. Therefore, we developed the following scheme to reduce the amount of symmetry sectors in which we have to perform DMRG calculations. Note, that Fig. 5.4 shows a typical example for the ground states energies in different symmetry sectors and can help to understand the assumptions described in our approach.

- Before starting with the ground state search, we typically limit the range of certain quantum numbers if we have a strong indication that this can be done.
  E.g. in systems where the $SU(2)$-symmetry of the conserved total spin is present but only the $U(1)$-symmetry of the $z$-component is used, we can in general restrict ourself to positive or negative values of the quantum number related to $\vec{S}_z$. A high quantum number associated with $||\vec{S}||$ or $\vec{S}_z$ restricts the free movement of particles in the system. In general, this increases the energy of the ground states. Thus, we assume that the global ground state is located in symmetry sectors with smaller quantum numbers. In the case of the Hubbard-model with dynamical cluster approximation in momentum-space the vector of the total momentum is conserved. In general, we assume that the global ground state is located in the $(k_x, k_y) = (0, 0)$ symmetry sector.
  All these assumptions are based on experience and have to be checked regularly for new systems and parameter choices.

- Now we focus on the ground state search. Consider a system with a conserved total number of particles described by the quantum number on $N$ and a second quantum number $A$. We fix $A = A_{\text{fix}}$ and search for the ground state with respect to different quantum numbers $N$

  $$\min_N E(N, A_{\text{fix}}). \tag{5.3.13}$$

  Experience shows that $E(N, A_{\text{fix}})$ is a convex function of $N$ in all our models and thus has a unique minimum with respect to $N$. Instead of computing the ground state for each possible particle number, we use a bifurcation procedure to determine symmetry sector $N_{\text{min}}$ with tho smallest energy. Additionally, we can guess $N_{\text{min}}$ based on three computed ground states energies and a parabola fit to focus the

bifurcation procedure on the region that contains the minimum most probably (see Fig. 5.4).

- To find the global ground state with respect to all values of all quantum numbers, we chose the smallest value for the second quantum number $A_{\text{fix}} = A_{\text{min}}$ and determine the ground state with respect to $N$. Then, we increase the value of $A$ and again search for the ground state with respect to $N$. After this is done for all possible values of $A$, a comparison of the energies gives us the global ground state.
  In our experience, the minima of the ground state energy with respect to $N$ typically are located in symmetry sectors that are located very close to each other, in terms of the particle number $N$, when changing the second quantum number $A$. The sectors of the minimal ground state energy for different values of $A$ differ in most cases only by one particle more or less or have even the same particle number. In a typical example displayed in the right plot of Fig. 5.4, the ground state energies are found in the symmetry sectors with $N = 14$ or $N = 15$ particles.
  This property can be used to improve the ground state search performance further. After the ground state for a fixed second quantum number $A_{\text{fix}}$ is found at $N_{min}$, for a higher value of $A$ the first ground state searches are performed in the allowed sectors close to $N_{\text{min}}$. In most cases this will yield the global ground state immediately. Nevertheless, it has to be checked that the found minimum is indeed the global one with respect to $N$ by proofing that the neighbouring symmetry sectors have a higher ground state energy. However, this approach can reduce the necessary number of ground state searches from ten to three, which is a significant reduction of computation time in some models.

- If we have additional quantum numbers like the band parity in the Hubbard-Kanamori Hamiltonian or the momentum vectors in the DCA Hubbard model, we still follow the previously described approach. For each choice of $A$ and $N$, we search through all allowed choices of the additional quantum numbers and only save the one with lowest energy as $E(N, A)$. Then, all previous schemes can still be used.

As seen in Fig. 5.4, guessing were the minimum can be found based on a parabola fit is a good first try but far from being efficient. We recommend to improve this scheme after investigating how to describe $E(N, A_{\text{fix}})$ analytical or after making a more extensive numerical analysis of the ground state energy behaviour.
Another important observation is that ground state energies of different sectors are typically very close to each other. In terms of the smallest hopping element $V_{min}$ of the Hamiltonian the energy differences are $\delta E \approx 0.05 V_{min}$ and for models with more complicated interactions even smaller, e.g. around $\delta E \approx 10^{-4} V_{min}$. Therefore, it is highly recommended to perform the DMRG calculations with precisions being high enough and with enough sweeps to really obtain the correct ground state energies and be able to find the global ground state.
In general, we do not truncate the MPSes during the DMRG ground state search according to any truncation threshold or truncated weight since this can arise in bad convergence

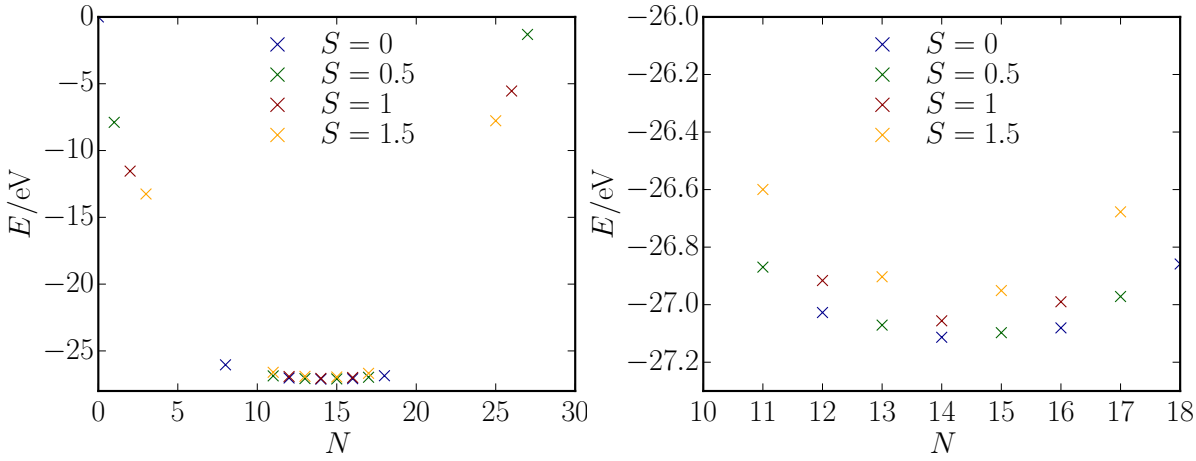


*Figure 5.4: Left panel: Ground state energies $E$ for different symmetry quantum numbers. $N$ describes the total number of particles and $S$ the total spin length according to $||\vec{S}||^2 = S(S+1)$. The system consist of 14 sites and can only contain 28 particles at most. The data was obtained from single site DMFT calculations of the Hubbard model with interaction strength $U = 5t$, next nearest neighbour hopping $t_p = -0.15t$ and at half filling in the first iteration. Thus, we expect to find the global ground state around $N = 14$ particles. We see clearly that the energy $E(N)$ is convex but that a parabola fit is definitely not sufficient to describe the functional form correctly. Right panel: Zoom in of the interesting area around $N = 14$. We see a nice parabola-like behaviour for each spin quantum number $S$ and that the lowest energies for each value of $S$ are lying close to each other in terms of the quantum number $N$ ($S = 0$ and $S = 1$: $N_{min} = 14$ while for $S = 0.5$ and $S = 1.5$: $N = 13$).*

properties. Instead, we stop our DMRG calculations after the ground state energy change from two consecutive sweeps drops below $10^{-7}$. After we determined the global ground state, we perform additional DMRG sweeps on it until the energy change is smaller than $10^{-11}$. The maximal bond dimension we choose for the ground state calculations depends on the actual model we investigate in. A typically choice for us is $m = 2000$ while using the $SU(2)$-symmetry of the conserved length of the total spin.
Another important aspect when using symmetries is how to deal with degenerate symmetry sectors. We encounter this problem mainly in the context of the $Sr_2VO_4$, which is a three band model with the first two bands being degenerate. The band parity quantum numbers fix an odd or even number of particles in the bands. It can happen that the system has degenerate global ground states $|\phi_1\rangle$ and $|\phi_2\rangle$ with the same energy but different particle distributions in the bands. E.g. the state $|\phi_1\rangle$ can have a particle distribution on the three bands $(N_1, N_2, N_3) = (6, 7, 6)$ while state $|\phi_2\rangle$ has $(N_1, N_2, N_3) = (7, 6, 6)$. In principle any combination of this eigenstates can be the ground state realised by the physical system and each choice give rise to different Green's functions. In a first approach,

we choose a symmetric combination as global ground state

$$|E_0\rangle = \frac{1}{\sqrt{2}}(|\phi_1\rangle + |\phi_2\rangle), \tag{5.3.14}$$

to have the degeneracy of the bands being reflected in observables like the occupation number of the bands. Then, all following steps of the DMFT iteration are performed on these two ground states separately and the physical results are combined accordingly. This is of course completely arbitrary and we could also have taken the combination

$$|E_0\rangle = \frac{1}{\sqrt{2}}(|\phi_1\rangle - |\phi_2\rangle), \tag{5.3.15}$$

which also gives rise to observables displaying the symmetry of the two degenerate bands. Or we could have taken any other combination, allowing spontaneous symmetry breaking. Unfortunately, only by using these superpositions we were able to reach convergence in some models for certain parameter regimes. But we also observed that DMFT was oscillating between two solutions back and forth while using this approach. However, it must definitely be investigated more rigorously how to deal with these situations.
Additionally, we want to remind the reader of section 2 where we discussed the geometry and reordering of an MPS. The optimal topology and ordering of the impurity model must be fixed during the ground state search and, in general, differs for the ground states of different symmetry sectors. Typically, we only reorder the global ground state. However, it can be advantageous to reorder the states during each DMRG calculation in each symmetry sector if the systems exhibits a lot of entanglement. Thus, reordering the MPSes reduces bond dimensions drastically and helps to find the global ground state with a high precision and small numerical effort.
In this section, we discussed in detail symmetry quantum numbers, the reasons why in general all of the symmetries of a Hamiltonian should be considered and implemented and how to obtain the ground state efficiently. After settling all these issues for a given model and finding the global ground state, we can proceed with computing the Green's function and self-energy of the system.

### 5.3.3 Matsubara Green's Functions

In the next step of the DMFT iteration, the interacting, single-particle, impurity Matsubara Green's function $\boldsymbol{G}(\tau)$ has to be computed

$$\begin{aligned} G_{i,j}(\tau) &= -\langle E_0|\mathcal{T}_\tau c_i(\tau'=0)c_j(\tau)^\dagger|E_0\rangle \\ &= -\theta(\tau)\langle E_0|c_i e^{-(\hat{H}-E_0)\tau}c_j^\dagger|E_0\rangle + \theta(-\tau)\langle E_0|c_i^\dagger e^{(\hat{H}-E_0)\tau}c_j|E_0\rangle \\ &= -\theta(\tau)G_{i,j}^{>}(\tau) + \theta(-\tau)G_{i,j}^{<}(\tau). \end{aligned} \tag{5.3.16}$$

$|E_0\rangle$ denotes the global ground state with ground state energy $E_0$, $c_i^\dagger$ and $c_j$ are creation and annihilation operators acting on the impurity sites $i$ and $j$, $\mathcal{T}_\tau$ is the time-ordering

operator with respect to the time $\tau$ and $\theta$ is the Heaviside step function. By measuring the decay over time of particle and hole excitations, the Green's function incorporates information over the single-particle spectrum.
To make discussion in this chapter easier, we define the greater $\boldsymbol{G}^{>}(\tau)$ and lesser Green's functions $\boldsymbol{G}^{<}(-\tau)$ in Eq. (5.3.16). The computation of $\boldsymbol{G}(\tau)$ can be shortened by determining the greater and lesser Green's function separately and in parallel. Afterwards, the can be combined combine to the Matsubara Green's function. In practice, we will first calculate the excited states

$$|\psi_j^{>}\rangle = c_j^{\dagger}|E_0\rangle, \tag{5.3.17}$$
$$|\psi_j^{<}\rangle = c_j|E_0\rangle, \tag{5.3.18}$$

and evolve them in time with TDVP or another method to

$$|\psi_j^{>}(\tau)\rangle = e^{-(\hat{H}-E_0)\tau}|\psi_j^{<}\rangle, \tag{5.3.19}$$
$$|\psi_j^{<}(\tau)\rangle = e^{-(\hat{H}-E_0)\tau}|\psi_j^{>}\rangle, \tag{5.3.20}$$

respectively. By computing the overlaps of $|\psi_j^{>}(\tau)\rangle$ and $|\psi_i^{<}(\tau)\rangle$ with the excited states at $\tau = 0$, $G_{i,j}^{>}(\tau)$ and $G_{i,j}^{<}(\tau)$ can be determined for each time $\tau$. In total, to determine an $n \times n$ Greens function at most $2n$ time evolutions have to be performed, i.e. the time evolutions for particle and hole excitations of each impurity. With those, all components of the impurity Green's function can be determined with appropriate overlaps. The number of time evolutions can be further reduced by exploiting degeneracies of bands and DCA patches or by using existing symmetries, e.g. a particle-hole symmetry.
Calculating the time evolution is in general the most time-consuming step of the whole DMFT iteration. The necessary time can be massively reduced by performing these calculations in parallel on multiple cores. The different time evolutions for holes and particles as well as for different bands differ significantly in their runtime. Thus, an intelligent core handling results in further improvements.
Since we do imaginary-time evolutions, $\boldsymbol{G}^{>}(\tau)$ and $\boldsymbol{G}^{<}(-\tau)$ decay exponentially fast to zero as can be seen in the left panel of Fig. 5.5. The short-time behaviour incorporates the high energy information of the Hamiltonian spectrum while the long-time behaviour is governed by the lowest lying eigenstates of the spectrum. This can also be seen very clearly if we expand the excited state $|\psi_j^{>}(\tau)\rangle$ in the eigenstates of the Hamiltonian $|\phi_n\rangle$

$$G_{i,j}^{>}(\tau) = \langle\psi_i^{>}(0)|\psi_j^{>}(\tau)\rangle = \sum_n e^{-(E_n-E_0)\tau}. \tag{5.3.21}$$

The high energy contributions will decay much faster because $E_n - E_0$ in the exponential is much smaller. For later times, the greater and lesser Green's functions will only constitute of a couple of slowly decaying exponential functions with a decay time determined completely by the low-energy spectrum of $\hat{H}$. In the next step, we want to Fourier transform $\boldsymbol{G}^{>}(\tau)$ and $\boldsymbol{G}^{<}(\tau)$ to obtain the Green's function $\boldsymbol{G}(i\omega_n)$. To avoid numerical oscillations in $\boldsymbol{G}(i\omega_n)$, the time-dependent Green's functions have to be computed up to times where

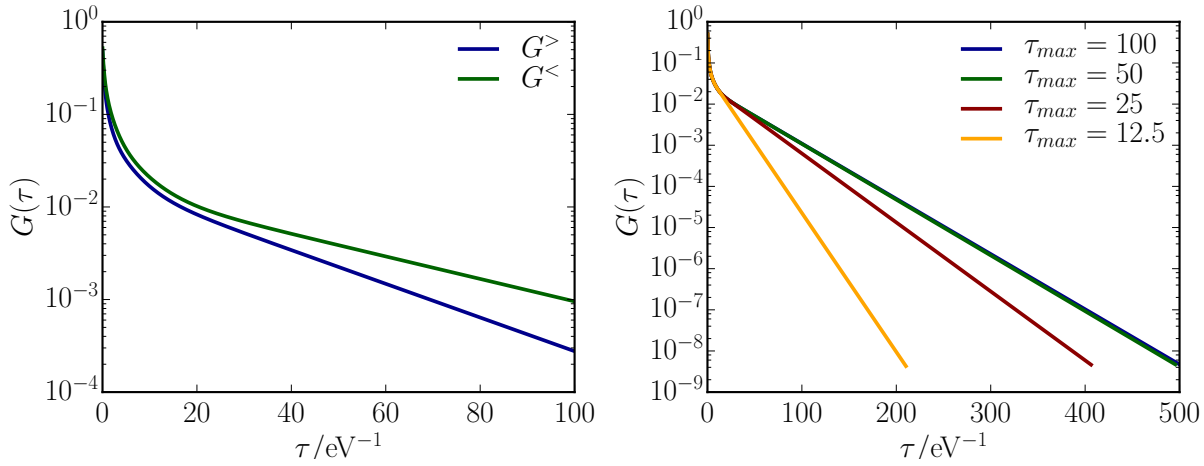


*Figure 5.5: Left panel: Greater and lesser Green's function. The data is obtained from single site DMFT calculation of the Hubbard model with interaction strength $U = 5t$, next nearest neighbour hopping $t_p = -0.15t$, nearest neighbour hopping $t = 1$ and at half filling in the first iteration. It is clear that the Green's functions decay exponentially fast but are not close to zero at $\tau = 100$. Right panel: The typical ansatz to extrapolate the Green's function to small values so numerical problems during the Fourier transform occur, is linear prediction. The plot shows the extrapolated Green's functions based on the same data set but cut off at different maximal times. It is obvious that $G(\tau)$ has to computed for large enough times such that the short-time behaviour is already decayed sufficiently. If the calculation is stopped too early, linear prediction will generate wrong Green's functions.*

$\boldsymbol{G}^>(\tau)$ and $\boldsymbol{G}^<(\tau)$ are close to zero. We clearly want to avoid to use any expensive MPS methods to do these calculations up to such long times because the long-time behaviour typically does not include any new information. At this stage, the time evolution can be stopped and linear prediction can be used to extrapolate $G^>_{i,j}(\tau)$ and $G^<_{i,j}(-\tau)$ to times where they decay below a threshold, e.g. $5 \cdot 10^{-8}$.
The right panel of Fig. 5.5 shows extrapolated Green's functions obtained with linear prediction from the same data set cut at different maximal times $\tau_{\max}$. If the maximal time is chosen too small, typically, the linear prediction will not capture the low energy physics correctly and the extrapolation will decay too fast. In our experience it is always a secure and good choice to time-evolve the states until $\tau_{\max} = 100$ but the choice depends highly on the low-energy spectrum of the Hamiltonian and more precisely on the energy differences between the low-energy states. The difference is bounded from below by the smallest energy scale in the impurity Hamiltonian, which is, in general, an on-site energy $\epsilon_k$ of a bath site.
The Hamiltonian parameters are obtained with the fit of the hybridisation $\boldsymbol{\Delta}(i\omega_n)$. In general, we observe that the fitting procedure tends to locate several of the on-site energies at values that are smaller than $\omega_0$, i.e. the lower end of the fitting interval, which is

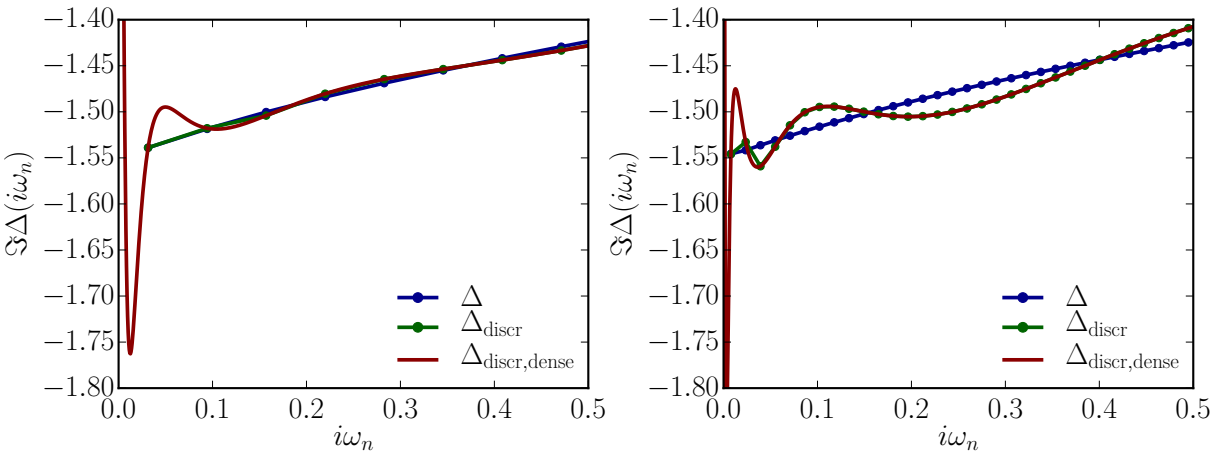


*Figure 5.6: Left panel: Imaginary part of the hybridisation (blue line) of the first iteration of a single-site DMFT calculation of the Hubbard model with nearest neighbour hopping $t = 1$ and next-nearest neighbour hopping $t_p - 0.15t$, interaction strength $U = 7t$, chemical potential $\mu = -2t$ and $L_b = 7$ bath sites. The effective temperature is $\beta = 100$. The optimal fit (green line) obtained in the fitting interval $[\omega_0, 6]$ seems to have a very good agreement with the hybridisation. If we plot the same function on more densely spaced grid points starting from $\omega_n = 0$ (red line), we see significant differences between the two functions. A very strong oscillation is located outside of the fitting interval, which clearly indicates that we need more bath sites to describe the hybridisation correctly. Right panel: The same model with the same functions but with a different effective temperature $\beta = 400$. It is now more obvious that the amount of bath sites is not sufficient for a good fit. Additionally, since the fitting interval was moved to smaller values the extremum of the fit is also pushed to smaller frequencies such that it is still located outside of the fitting interval.*

set by $\beta_{\text{eff}}$. We believe that is the case because the hybridisation is a sum of functions of the form

$$\mathbf{\Delta}_{\text{discr},k}(i\omega_n) = \frac{\vec{V}_k^\dagger \vec{V}_k}{i\omega_n - \epsilon_k}. \tag{5.3.22}$$

These functions have a pole at $i\omega_n = \epsilon_k$ and therefore the imaginary part has a minimum at $i\omega_n = \epsilon_k$ and the real part at $i\omega_n = 0$. The strongest change of these functions with respect to $i\omega_n$ is always near the extrema. Summing up the terms $\mathbf{\Delta}_{\text{discr},k}$ and obtaining a function similar to the form of $\mathbf{\Delta}$ without oscillations is, in general, very hard to achieve with a limited number of terms, especially near the extrema. Since we typically use only a small number of bath sites, it is reasonable for the fitting procedure to locate some of the poles at frequencies below the fitting interval. By doing this, the oscillations of the fit are not so strong inside the fitting interval, which leads to better cost function values. This can be seen clearly in the left panel of Fig. 5.6. The extremum is located outside of the fitting interval and the remaining oscillations are intersecting the hybridisation

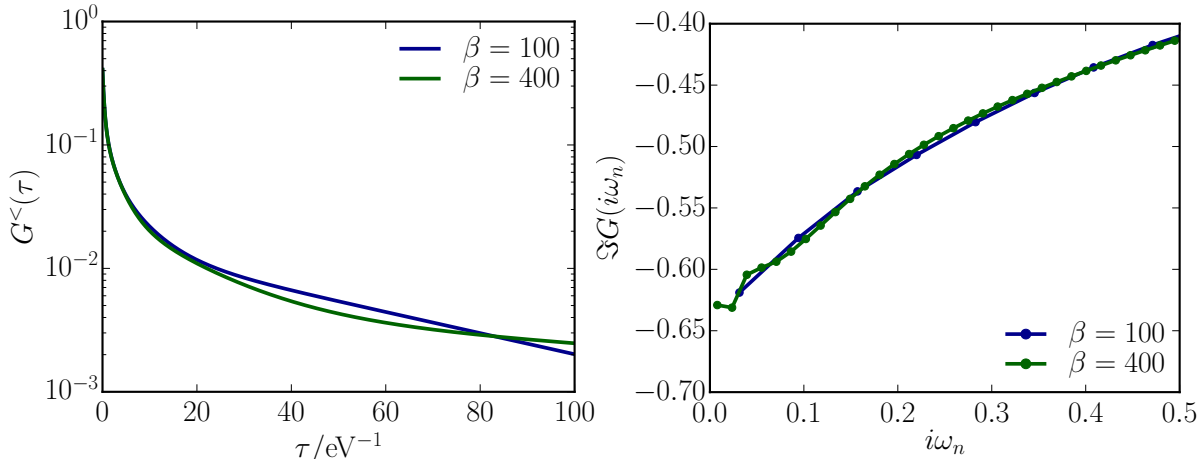


*Figure 5.7: Left panel: The lesser Green's function obtained for different effective temperatures $\beta$ for the same model as in Fig. 5.6. For $\beta = 100$ (blue line) the Green's function decays with a constant rate towards zero from $\tau \approx 20$ on. For $\beta = 400$ the constant decay starts at $\tau = \approx 100$ or even later. For linear prediction to be reliably applicable, the Green's functions have to decay linearly for a sufficiently large period. Right panel: Corresponding Matsubara Green's functions. The differences between the two cases are very small and most notably at small frequencies.*

directly at the grid points. Thus, a very good value for $\chi$ can be obtained. By increasing $\beta_{\text{eff}}$ and thus lowering the lower bound of the fitting interval, the strongest oscillations are pushed to smaller frequencies. This is shown by the right plot of Fig. 5.6 where the effective temperature is changed from $\beta = 100$ to $\beta = 400$. The extremum is now located nearer to the fitting interval, which leads to stronger oscillations and less good agreement inside the fitting interval. Most importantly, this also lowers some of the on-site energies of the bath sites.

For the shown examples, the smallest on-site energy is $\epsilon_{\text{low}} \approx 1.0 \cdot 10^{-2}$ for $\beta = 100$ and $\epsilon_{\text{low}} \approx 2.6 \cdot 10^{-3}$ for $\beta = 400$. In the latter case, this obviously leads to smaller energy differences between the low-energy eigenstates and therefore to a slower decay of the Green's functions, which can be seen in the left plot of Fig. 5.7 for the lesser Green's function. Evolving the Green's function up to $\tau_{\text{max}} = 100$ for $\beta = 100$ is sufficient to see the linear decay clearly, but for $\beta = 400$ this is not a good choice since the decay rate of $\boldsymbol{G}^<(\tau)$ is still changing. Therefore, linear prediction cannot extrapolate the Green's function reliably, which can result in a wrong long-time behaviour that depends strongly on the current iteration and thus can hinder convergence. The right plot of Fig. 5.7 shows the corresponding Matsubara Green's functions, which differ mainly in the low-frequency regime related strongly to the long-time behaviour. Even small changes in this regime can be problematic for the convergence of DMFT since the fit of the hybridisation has a strong weight for small frequencies.

Concluding, the choice of the maximal time $\tau_{\text{max}}$ up to which the state $|\psi\rangle(\tau)$ has to

be evolved in a way that linear prediction is applicable is influenced by the Hamiltonian parameters. Since they are obtained with a fit of the hybridisation, they depend on the used frequency grid and thus on the choice of $\beta_{\text{eff}}$.
Additionally, there are a couple of things that have to be taken care of:

- For each calculation it has to be checked whether the time evolution is computed with a precision that is high enough. If not, the Green's function typically decays too fast and has a wrong long-time behaviour. This leads to a wrong small frequency behaviour of the Green's function, self-energy and hybridisation. If this error is severe, the imaginary part of the hybridisation will be positive for small Matsubara frequencies, which clearly indicates unphysical behaviour.

- If a Green's function starts growing for long times, this is a clear indication that the ground state found is not the global one.

- If the norm of the time-evolved state decays faster to zero than the Greens function itself, this can lead to numerical instabilities and wrong results. Therefore, we stop calculations if

  $$|||\psi(\tau)\rangle||^2 < 10^{-6} \tag{5.3.23}$$

  Typically, in these cases the Green's function has already decayed so much in a linear fashion that linear prediction can be applied safely.

After computing the time evolutions correctly and combining the results according to Eq. (5.3.16) to $G_{i,j}(\tau)$, each component of the Green's function can be Fourier transformed separately. Since DMRG works at temperature $T = 0$, the integral in the Fourier transform has to be computed over the whole $\tau$-axis

$$G_{i,j}(i\omega_n) = \int_{-\infty}^{\infty} \mathrm{d}\tau G_{i,j}(\tau) e^{-i\omega_n \tau}. \tag{5.3.24}$$

Practically, $G_{i,j}(\tau)$ decays to zero at finite times and only has to be integrated on its finite support. The Green's function is known only at certain supporting points $(\tau_m, G_{i,j}(\tau_m))$ given by the time step $\delta\tau$. If the grid points are located close enough together, the Green's function can be assumed to be linear in between. This allows the Fourier transform integral to be computed analytically

$$\begin{aligned} G_{i,j}(i\omega_n) &= \int_{-\infty}^{\infty} \mathrm{d}\tau G_{i,j}(\tau) e^{-i\omega_n \tau} = \sum_{m=0}^{N} \int_{\tau_m}^{\tau_{m+1}} \mathrm{d}\tau (a_m \tau + b_m) e^{-i\omega_n \tau} \\ &= \sum_{m=0}^{N} \frac{a_m}{\omega_n} \left( \left( \frac{1}{\omega_n} - i\tau_{m+1} \right) e^{i\omega_n \tau_{m+1}} - \left( \frac{1}{\omega_n} - i\tau_m \right) e^{i\omega_n \tau_m} \right) \\ &\quad - \frac{i b_m}{\omega_n} \left( e^{i\omega_n \tau_{m+1}} - e^{i\omega_n \tau_m} \right), \end{aligned} \tag{5.3.25}$$

where we defined

$$a_m = \frac{G_{i,j}(\tau_{m+1}) - G_{i,j}(\tau_m)}{\tau_{m+1} - \tau_m}, \tag{5.3.26}$$

$$b_m = G_{i,j}(\tau_m) - a_m \tau_m. \tag{5.3.27}$$

The difference between the numerical approach and the analytical solution is that the latter treats the exponential in the integral exactly. This is important since numerical methods for calculating integrals, like the Trapez rule or the Simpsons rule, assume that the whole integrand is linear between the supporting points or can be approximated by polynomials up to a certain order. For the integrand in Eq. (5.3.24) this is definitely not true for high frequencies since the exponential starts oscillating strongly on a period smaller than the time step $\delta\tau$. This reflects itself in $G_{i,j}(i\omega_n)$ being periodic with a period $2\pi/\delta\tau$ (see the left panel of Fig. 5.8). Solving the integral analytical will avoid this artificial behaviour and additionally results in a computational speed-up.
The time step $\delta\tau$ determines the resolution of the time-dependent Green's function, which has a direct influence on the quality of $\boldsymbol{G}(i\omega)$. The right plot of Fig. 5.8 shows the high-frequency behaviour of the Matsubara Green's function, which clearly depends on $\delta\tau$. The diagonal elements of $\boldsymbol{G}(i\omega)$ for high frequencies have to decay with $\Im G_{j,j}(i\omega_n) \to -1/\omega_n$ as $\omega_n \to \infty$, which is clearly not the case for the TDVP calculation with $\delta\tau = 0.1$ (blue line) in Fig. 5.8. Since the high frequency behaviour incorporates information mainly about the small-scale structure of $G_{i,j}(\tau)$, the time step $\delta\tau = 0.1$ is too large and cannot resolve the correct fine structure of the time-dependent Green's function. This also prevents to resolve the derivatives of $G_{i,j}(\tau)$ correctly, which are zero for too-large time steps. Since $G_{i,j}(\tau)$ changes the fastest for small times, smaller time steps are especially needed for small times.
It is not recommended to just decrease the time step in TDVP calculations since the projection error of TDVP becomes significantly large for small time steps, as discussed in section 4.3. Additionally, the computation time would increase dramatically if the time step is decreased by a factor ten or 100. Therefore, we propose to use the Krylov method to determine $|\psi(\tau)\rangle$ up to a time $\tau_c$ where the time evolution is proceeded with TDVP. The advantage of Krylov is that the original, relatively large time step $\delta\tau = 0.1$ can still be used since any state $|\psi(\tau')\rangle$ at times $\tau < \tau' < \tau + \delta\tau$ can algebraically be calculated without much additional effort. To see this we start from Eq. (4.2.5) where the evolved state $|\psi'(t + \delta\tau)\rangle$ is computed by the application of the exponential of the effective Hamiltonian $H_{\text{eff}}$ in the Krylov subspace. In a next step we have to diagonalise

the effective Hamiltonian $H_{\text{eff}} = V^{-1}DV$ and sum up Krylov vectors

$$\begin{aligned}
|\psi'(t+\delta\tau)\rangle &= \sum_{j=0}^{m-1} |\phi_j\rangle (e^{-iH_{\text{eff}}\delta\tau})_{j,0} + \mathcal{O}\left(\frac{\delta\tau^m}{m!}\right) \\
&= \sum_{j=0}^{m-1} |\phi_j\rangle \left[ V^{-1} \begin{pmatrix} e^{-id_1\delta\tau} & 0 & 0 & \dots \\ 0 & e^{-id_2\delta\tau} & 0 & \dots \\ \vdots & \vdots & \vdots & \ddots \end{pmatrix} V \right]_{j,0} + \mathcal{O}\left(\frac{\delta\tau^m}{m!}\right) \\
&= \sum_{j=0}^{m-1} |\phi_j\rangle \sum_n \overline{V}_{j,n} V_{0,n} e^{-id_n\delta\tau} + \mathcal{O}\left(\frac{\delta\tau^m}{m!}\right), \qquad (5.3.28)
\end{aligned}$$

with $d_n$ denoting the eigenvalues of $H_{\text{eff}}$ and $\overline{V}$ being the complex conjugate vector of $V$. To compute the time evolved state $|\psi(\tau+n\delta\tau')\rangle$ at intermediate time points with step size $\delta\tau' \ll \delta\tau$ and $n \in [1, 2, \dots, \delta\tau/\delta\tau']$, the $\delta\tau$ in Eq. (5.3.28) has to be replaced by $n\delta\tau'$. This obviously only changes the coefficients for the summation of the Krylov vectors. These algebraic calculations are comparatively cheap. Thus, we can easily determine $G_{i,j}(\tau)$ on a very fine time grid without much additional effort. Furthermore, the errors of the Krylov time evolution, namely time step error as well as the error of an insufficiently large Krylov subspace, are even smaller because $\delta\tau' \ll \delta\tau$. This means the function values $G_{i,j}(\tau)$ at the intermediate time points are computed with a very good accuracy.

In our experience one can obtain very good results for the Fourier transformed Green's function $\boldsymbol{G}(i\omega)$ with a time step $\delta\tau = 0.1$ for both the Krylov and the TDVP time evolution and a step size $\delta\tau' = 5 \cdot 10^{-4}$ between the intermediate time points obtained during the Krylov calculation. Typically, at $\tau_c \in [2, 4]$ the Krylov method is stopped and replaced by a TDVP calculation. In the right plot of Fig. 5.8 (green line) it can be seen that the correct high-frequency behaviour is restored by this ansatz. The higher resolution for small times is not only crucial for the correct high-frequency behaviour of the Green's function but also has an immediate effect on the high-frequency behaviour of the self-energy $\boldsymbol{\Sigma}(i\omega_n)$ and the hybridisations via the Dyson equation and the self-consistency equations of DMFT.

We want to end this section with a short remark about calculations involving $SU(2)$-symmetric operators. If the ground state $|E_0\rangle$ itself has a non-zero $SU(2)$ quantum number, an excitation will lower and rise the quantum number at the same time creating a superposition of states from different symmetry sectors. In general, this will lead to higher bond dimensions and slower calculations. Instead of time evolving this superposition, it is more efficient to project the state in the different symmetry sectors, evolve each state separately and combine the Green's functions in the end

$$\begin{aligned}
G_{i,j}(\tau) &= -\theta(\tau)\langle E_0|c_i e^{-(\hat{H}-E_0)\tau} c_j^\dagger |E_0\rangle + \theta(-\tau)\langle E_0|c_i^\dagger e^{(\hat{H}-E_0)\tau} c_j |E_0\rangle \\
&= -\theta(\tau)\langle E_0|c_i(\mathbb{P}_\uparrow + \mathbb{P}_\downarrow) e^{-(\hat{H}-E_0)\tau} (\mathbb{P}_\uparrow + \mathbb{P}_\downarrow) c_j^\dagger |E_0\rangle \\
&\quad + \theta(-\tau)\langle E_0|c_i^\dagger(\mathbb{P}_\uparrow + \mathbb{P}_\downarrow) e^{(\hat{H}-E_0)\tau} (\mathbb{P}_\uparrow + \mathbb{P}_\downarrow) c_j |E_0\rangle \\
&= -\theta(\tau)(G_{i,j}^{>,\uparrow}(\tau) + G_{i,j}^{>,\downarrow}(\tau)) + \theta(-\tau)(G_{i,j}^{<,\uparrow}(\tau) + G_{i,j}^{<,\downarrow}(\tau)). \qquad (5.3.29)
\end{aligned}$$

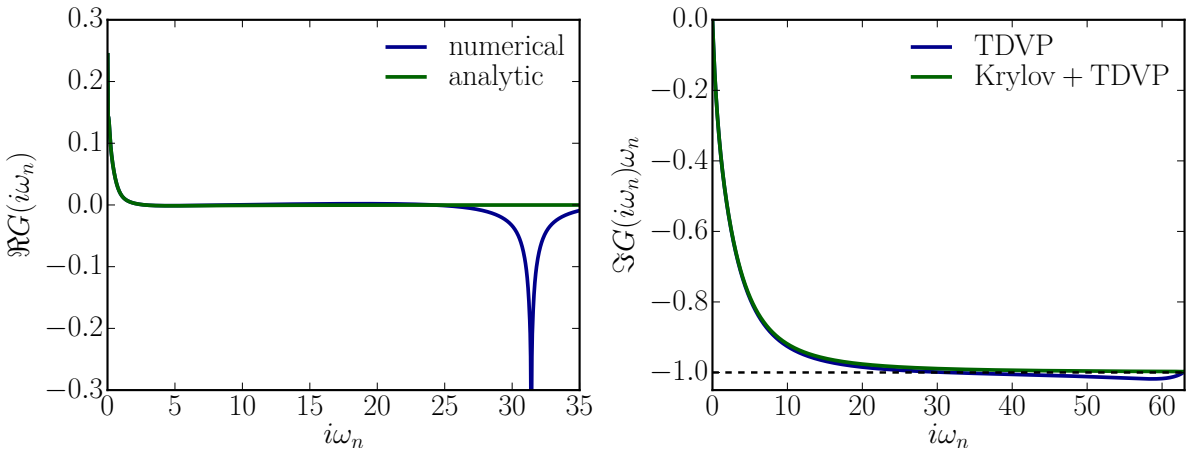


*Figure 5.8: Left panel: Real part of the Matsubara Green's function $G(i\omega_n)$. Using a standard numerical integration method to solve the Fourier integral, e.g. the Numpy trapez function or the Scipy Simpson rule, a periodic signal with period $T = 2\pi/\delta t \approx 62$ is obtained (blue line). We only display half of the period because the deviation from the result where the integral was solved analytically (green line) is obvious. The differences originate solely from whether the exponential in the integrand is treated exactly or approximately. Right panel: Imaginary part of the Green's function multiplied by $\omega_n$. The TDVP calculation with $\delta t = 0.1$ is not showing the correct high-frequency behaviour (blue line). Since the high frequencies mainly give information about the small scale behaviour of $G(\tau)$, smaller time steps allow to obtain the correct Green's function. Since $G(\tau)$ is changing the fastest for small times, it is sufficient to use a higher resolution only for the first time steps. The Krylov+TDVP approach with the changing time $t_c = 4$ serves exactly this purpose and shows the correct behaviour (green line).*

The projectors $\mathbb{P}_\uparrow$ and $\mathbb{P}_\downarrow$ project into the $SU(2)$ symmetry sectors with the lower and higher quantum number, respectively. We also define the greater Green's functions in the upper and lower sector

$$G_{i,j}^{>,\uparrow}(\tau) = \langle E_0 | c_i^\dagger \mathbb{P}_\uparrow e^{(\hat{H}-E_0)\tau} \mathbb{P}_\uparrow c_j | E_0 \rangle \tag{5.3.30}$$

$$G_{i,j}^{>,\downarrow}(\tau) = \langle E_0 | c_i^\dagger \mathbb{P}_\downarrow e^{(\hat{H}-E_0)\tau} \mathbb{P}_\downarrow c_j | E_0 \rangle \tag{5.3.31}$$

and respectively the lesser Green's function. After computing the greater and lesser Green's functions in the different symmetry sectors, they have to be combined to the full Green's functions $G_{i,j}^{>}(\tau)$ and $G_{i,j}^{<}(\tau)$ according to Eq. (5.3.29). In general, the Green's functions $G_{i,j}^{>,\uparrow}(\tau)$ and $G_{i,j}^{>,\downarrow}(\tau)$ are calculated up to different times due to the different energy spectra in the different symmetry sectors. A simple addition of these two functions leads to a small but significant jump in the resulting data set, which results in oscillations in the Fourier transformed Green's function $G_{i,j}(i\omega)$. To avoid those numerical artefacts, both functions $G_{i,j}^{>,\uparrow}(\tau)$ and $G_{i,j}^{>,\downarrow}(\tau)$, must be extrapolated with linear prediction to the same time $\tau$. This has to be done similarly for the corresponding terms of the lesser

Green's function.

### 5.3.4 Self-Consistency Equation

After the non-interacting impurity Green's function $\boldsymbol{G}(z)$ is computed, a new hybridisation can be computed and used as to start the next DMFT iteration. This is done by using the self-consistency equation of DMFT. Since all derivations in this section are valid on the imaginary as well as on the real-frequency axis, we will denote all functions as depending on the variable $z$, which can either be the Matsubara frequency $i\omega_n$ or the real-frequency $\omega$.
The self-consistency equation of DMFT is given by

$$\boldsymbol{G}(z) = \boldsymbol{G}_{\text{latt}}(z), \tag{5.3.32}$$

with $\boldsymbol{G}_{\text{latt}}$ being the local interacting lattice Green's function

$$\boldsymbol{G}_{\text{latt}}(z) = \int_{1.BZ} \mathrm{d}\vec{k} \frac{1}{z\mathbb{1} - \boldsymbol{\epsilon}(\vec{k}) - \boldsymbol{\Sigma}_{\text{latt}}(z)}. \tag{5.3.33}$$

Thus, $\boldsymbol{G}_{\text{latt}}$ can be calculated by integrating the lattice self-energy $\boldsymbol{\Sigma}(z)_{\text{latt}}$ and lattice dispersion relation $\boldsymbol{\epsilon}(\vec{k})$ over the 1st Brillouin zone (BZ) in momentum-space. For simplicity, we well omit the unit matrix $\mathbb{1}$ next to the variable $z$ for the rest of the section.
To determine the new hybridisation $\boldsymbol{\Delta}(z)$ for the next DMFT iteration $n+1$, the self-energy $\boldsymbol{\Sigma}(z)$ of the impurity problem in the actual DMFT loop $n$ has to be computed. Since the hybridisation of iteration $n$ is known, the non-interacting Green's function $\boldsymbol{G}_0^{-1}(z)$ can always be computed with Eq. (5.3.9). For this computation, the discretised version $\boldsymbol{\Delta}_{\text{discr}}$ of the hybridisation has to be used always. Then, the impurity self-energy can be obtained with the help of the Dyson equation

$$\boldsymbol{\Sigma}(z) = \boldsymbol{G}_0^{-1}(z) - \boldsymbol{G}^{-1}(z). \tag{5.3.34}$$

From the Dyson equation it is also possible to derive the analytic form of the interacting impurity Green's function

$$\boldsymbol{G}(z) = \frac{1}{z - \boldsymbol{\mu} - \boldsymbol{\Delta}(z) - \boldsymbol{\Sigma}(z)}. \tag{5.3.35}$$

This form can be inserted in the consistency equation Eq. (5.3.32), which leads to the new hybridisation

$$\begin{aligned} & \boldsymbol{G}(z) = \boldsymbol{G}_{\text{latt}}(z) \\ \Leftrightarrow \; & \frac{1}{z - \boldsymbol{\mu} - \boldsymbol{\Delta}(z) - \boldsymbol{\Sigma}(z)} = \boldsymbol{G}_{\text{latt}}(z) \\ & \Leftrightarrow \boldsymbol{\Delta}(z) = z - \boldsymbol{\mu} - \boldsymbol{\Sigma}(z) - \boldsymbol{G}_{\text{latt}}^{-1}(z). \end{aligned} \tag{5.3.36}$$

To determine the new hybridisation $\boldsymbol{\Delta}(z)$ for the next DMFT iteration $n+1$, the self-energy $\boldsymbol{\Sigma}(z)$ of the impurity problem has to be inserted in Eq. (5.3.36) directly as well as in the lattice Green's function $G_{\text{latt}}(z)$ under the assumption

$$\boldsymbol{\Sigma}(z) = \boldsymbol{\Sigma}_{\text{latt}}(z). \tag{5.3.37}$$

The hybridisation obtained with the self-consistency equation is used to built up the impurity Hamiltonian for the next DMFT iteration. Only if the obtained impurity self-energy gives rise to the same Green's function in the impurity problem and the lattice problem, the hybridisation will not change anymore from one DMFT iteration to the next. The straightforward ansatz to determine $\boldsymbol{\Sigma}(z)$ via the Dyson equation and inserting it into Eq. (5.3.36) is numerically not optimal. Small numerical errors in calculated quantities, like the interacting impurity Green's function, can be blown up by the multiple inversions. A much better way of calculating the hybridisation was proposed by Aoki et al.[140] in the context of non-equilibrium DMFT but is also applicable in the equilibrium case. The fundamental idea is to rearrange all necessary formulas such that all inversion are performed on functions of the form $1 + f(z)$.
We start with the interacting impurity Green's function and reformulate it in an integral form

$$\begin{aligned} \boldsymbol{G} &= \boldsymbol{g} + \boldsymbol{g}\boldsymbol{\Delta}\boldsymbol{G} && (5.3.38)\\ &= \boldsymbol{g} + \boldsymbol{G}\boldsymbol{\Delta}\boldsymbol{g}, && (5.3.39) \end{aligned}$$

where we defined the isolated impurity Green's function

$$\boldsymbol{g}(z) = \frac{1}{z - \boldsymbol{\mu} - \boldsymbol{\Sigma}(z)}. \tag{5.3.40}$$

This means $\boldsymbol{g}$ can be calculated from $\boldsymbol{G}$ via

$$\boldsymbol{g} = (1 + \boldsymbol{G}\boldsymbol{\Delta})^{-1}\boldsymbol{G}. \tag{5.3.41}$$

Next, the momentum-resolved Green's functions $\boldsymbol{G}_k$ is computed

$$\boldsymbol{G}_k = \frac{1}{\boldsymbol{g}^{-1} - \boldsymbol{\epsilon}_k}, \tag{5.3.42}$$

which, too, can be written in an integral form

$$\begin{aligned} \boldsymbol{G}_k &= \boldsymbol{g} + \boldsymbol{g}\boldsymbol{\epsilon}_k\boldsymbol{G}_k \\ \boldsymbol{G}_k &= \boldsymbol{g} + \boldsymbol{G}_{\boldsymbol{k}}\boldsymbol{\epsilon}_k\boldsymbol{g}. && (5.3.43) \end{aligned}$$

As before, we can reformulate the last equation to obtain

$$\boldsymbol{G}_k = (1 - \boldsymbol{g}\boldsymbol{\epsilon}_k)^{-1}\boldsymbol{g}. \tag{5.3.44}$$

In the next step, we sum Eq. (5.3.43) over $\vec{k}$ and use $\boldsymbol{G} = \sum_{\vec{k}} \boldsymbol{G}_k$ as well as $\sum_{\vec{k}} \boldsymbol{\epsilon}_k = 1$ to obtain

$$\boldsymbol{G} = \boldsymbol{g} + \boldsymbol{g} \sum_{\vec{k}} \boldsymbol{\epsilon}_k \boldsymbol{G}_k. \tag{5.3.45}$$

Comparing this equation with Eq. (5.3.38) we realise that

$$\boldsymbol{\Delta G} = \sum_{\vec{k}} \boldsymbol{\epsilon}_k \boldsymbol{G}_{\boldsymbol{k}} = \boldsymbol{G}_1. \tag{5.3.46}$$

Before we can solve for $\boldsymbol{\Delta}$, we insert Eq. (5.3.39) and Eq. (5.3.43) on the left and right hand side of the last equation, respectively, and obtain

$$\boldsymbol{\Delta} + \boldsymbol{\Delta G \Delta} = \sum_{\vec{k}} \boldsymbol{\epsilon}_k + \boldsymbol{\epsilon}_k \boldsymbol{G}_k \boldsymbol{\epsilon}_{\boldsymbol{k}} = \boldsymbol{G}_2. \tag{5.3.47}$$

Now, we can determine the hybridisation via a stable inversion

$$\boldsymbol{\Delta} = (1 + \boldsymbol{G}_1)^{-1} \boldsymbol{G}_2. \tag{5.3.48}$$

Summarising, starting with the interacting impurity Green's function $\boldsymbol{G}$ we can calculate

1. the isolated impurity Green's function $\boldsymbol{g}$ via Eq. (5.3.41)
2. the momentum-resolved Green's function $\boldsymbol{G}_k$ with Eq. (5.3.44)
3. the auxiliary Green's functions $\boldsymbol{G}_1$ and $\boldsymbol{G}_2$ with Eq. (5.3.46) and Eq. (5.3.47)
4. and finally the hybridisation $\boldsymbol{\Delta}$ via Eq. (5.3.48)

By avoiding to invert the functions itself and inverting only quantities of the structure $1 + f(z)$, in some calculations we were able to reduce the precision of the time evolutions needed for convergence of DMFT by one order of magnitude. With the obtained hybridisation $\boldsymbol{\Delta}(z)$ the next DMFT iteration can be started with the same steps as described in the previous sections.
At this point, we want to answer the question how to start the first DMFT iteration. An obvious choice for the initial hybridisation is to use a converged result of a DMFT calculation based on a model that does not differ strongly from the actual problem. That can be the same model with a slightly different chemical potential or interaction strength or a single-site DMFT solution as the starting point for a two-site DCA calculation. Sometimes none of these hybridisations are obtainable, the DMFT calculation is not supposed to be biased by the available hybridisations or another result is to be confirmed by using a different initial $\boldsymbol{\Delta}(z)$,. In those cases the hybridisation of the non-interacting model can always be determined with the consistency equation of DMFT and used as the starting point of the first DMFT loop. Since the chemical potential and the dispersion relation are known, by simply setting the self-energies $\boldsymbol{\Sigma} = \boldsymbol{\Sigma}_{\text{latt}} = 0$ the non-interacting hybridisation

can obtained from Eq. (5.3.36).
Different starting hybridisations can influence the convergence properties of DMFT drastically. Not only the number of iterations until convergence can change but also the entanglement properties of the created impurity problems. Therefore, it is strongly recommended to start DMFT calculations with hybridisations that are as close as possible to the suspected converged result. With the ongoing development of neural networks, it could be worth trying to design an artificial intelligence that is able to guess starting hybridisation based on already converged results.

### 5.3.5 Mixing Iteration Results

DMFT can be understood as a map $\Gamma$ from one hybridisation $\mathbf{\Delta}_i$ to a new one $\mathbf{\Delta}_{i+1}$

$$\Gamma\{\mathbf{\Delta}_i\} = \mathbf{\Delta}_{i+1}. \tag{5.3.49}$$

Convergence can only be obtained if this map is a contraction close to the solution of the self-consistency equation $\Gamma\{\mathbf{\Delta}^*\} = \mathbf{\Delta}^*$. The properties of the map, namely how many fix-points exist and how strong the contraction towards a stable fix-point is, are determined by the model and the chosen physical parameters. During the DMFT calculation, information about the map $\Gamma$ can be obtained from the series of computed hybridisations and also from their changes, e.g. how they change and how strong based on the input of $\Gamma$. This information can be used to improve convergence by increasing or decreasing modifications on the hybridisations. This can be especially useful in cases of a critical slowing down of the convergence near physically interesting points or for models near a phase transitions where DMFT tends to jump back and forth between two alternating solutions. These methods are known as mixing schemes and a lot of effort has been devoted to developing very efficient schemes to accelerate convergence[141,142].
The standard ansatz we described in the previous section, i.e taking the determined hybridisation from the DMFT consistency equation as the input for the next iteration, is not using any information obtainable from the $\mathbf{\Delta}_i$ form different iterations $i$. A slightly improved ansatz is so-called linear mixing where the last two hybridisations are combined to get a new hybridisation for the next iteration

$$\mathbf{\Delta}_{i,\mathrm{lin}}(z) = \alpha\mathbf{\Delta}_i(z) + (1-\alpha)\mathbf{\Delta}_{i-1}(z). \tag{5.3.50}$$

The mixing factor $\alpha \in (0, 1]$ determines how strong the hybridisations of the two consecutive iterations are mixed. It has been shown for a small enough $\alpha$ that DMFT is guaranteed to converge for most systems[143] with the drawback of a very slow convergence rate. This is similar to a gradient search algorithm where it can be beneficial to reduce the step size to reach the minimum one is seeking. Since each iteration of the DMFT calculation is, in general, very expensive, it is not practical to choose $\alpha$ too small. Of course, an adaptive choice of $\alpha$, which lead to smaller values during the calculation if needed, seems to be a reasonable approach if convergence problems are encountered.

However, up to now we have not found an efficient and automatic way to determine convergence problems and adjusting $\alpha$ accordingly.
A more sophisticated approach was developed by Broyden in 1965[144]. The underlying idea is to take into account the information gathered during the exploration of the optimisation space by DMFT. In the following paragraph, we will present Broyden's mixing scheme based on Rok Žitko[145] who showed that Broyden's method, up to that point widely used only in the DFT community, can be successfully applied to DMFT problems. Let $V$ be an $N$-dimensional vector and $F$ a mapping. In the DMFT context $V^{(i)}$ is the discretised hybridisation of iteration $i$ with $N$ data points and $F$ is the vectorised difference between the input hybridisation and output hybridisation of one DMFT loop

$$F(\Delta_{\text{input}}) = \Delta_{\text{output}}\{\Delta_{\text{input}}\} - \Delta_{\text{input}}. \tag{5.3.51}$$

Convergence of the DMFT calculation corresponds to solving $F(V) = 0$. An iterative approach for solving this problem is to use quasi-Newton-Raphson methods in which a new approximation for the hybridisation is given by

$$V^{(i+1)} = V^{(i)} - [J^{(i)}]^{-1} F^{(i)}, \tag{5.3.52}$$

with $J^{(i)}$ being the Jacobian of the DMFT convergence problem in iteration $i$ and $F^{(i)} = F(V^{(i)})$. Since the Jacobian is unknown, typically one starts with an initial and simple approximation

$$J^{(i)} = -\frac{1}{\alpha}\mathbb{1}, \tag{5.3.53}$$

which corresponds to a simple linear mixing in the first iteration with mixing parameter $\alpha$. The more DMFT iterations are performed, the more information about the mapping is known. This can be used to update the Jacobian or better its inverse $B^{(i)} = -[J^{(i)}]^{-1}$ iteratively

$$B^{(i+1)} = B^{(i)} + (\delta V^{(i)} - B^{(i)}\delta F^{(i)}) \otimes \delta F^{(i)}, \tag{5.3.54}$$

with

$$\delta V^{(i)} = \frac{V^{(i+1)} - V^{(i)}}{|F^{(i+1)} - F^{(i)}|}, \tag{5.3.55}$$

$$\delta F^{(i)} = \frac{F^{(i+1)} - F^{(i)}}{|F^{(i+1)} - F^{(i)}|}. \tag{5.3.56}$$

This scheme can be improved in such a way that it uses the information of all previous iterations to update the Jacobian[146]. Additionally, it can be optimised such that only the input $V^{(i)}$ and output hybridisations $F^{(i)}$ have to be saved instead of the whole Jacobian[147]. Combined together[148], Broyden's mixing can be written as

$$V^{(i+1)} = V^{(i)} + \alpha F^{(i)} - \sum_{j}^{i-1}\sum_{k}^{i-1} w_j w_k c_k^{(i)} \beta_{k,j}^{(i)} U^{(j)}, \tag{5.3.57}$$

with

$$c_k^{(i)} = (\delta F^{(k)})^\dagger F^{(i)}, \tag{5.3.58}$$
$$U^{(j)} = \alpha \delta F^{(j)} + \delta V^{(j)}, \tag{5.3.59}$$

and $(i-1) \times (i-1)$-dimensional matrices

$$\beta_{k,j}^{(i)} = [(w_0^2 \mathbb{1} + A^{(i)})^{-1}]_{k,j}, \tag{5.3.60}$$
$$A_{k,j}^{(i)} = w_k w_j (\delta F^{(j)})^\dagger \delta F^{(k)}. \tag{5.3.61}$$

If we use Broyden's mixing, we always use (5.3.57). The first two terms are describing simple linear-mixing while the last term are corrections originating from the previous iterations including the updates to the initial Jacobian. The weights $w_j$ can be chosen depending on the problem but are typically set to 1 [147,149]. The only exception is the first weight, which is chosen to be $w_0 = 0.01$, since in most cases the starting hybridisation is a bad choice and thus should be taken into account with less weight. By choosing the weights accordingly, one can reduce Broyden's mixing to Pulay mixing [150] or other mixing schemes like Anderson mixing [151].
In theory, the output hybridisation from one DMFT iteration ($F^{(i)}$) is at the same time the input hybridisation ($V^{(i+1)}$) of the next iteration. When mixing schemes are used, the hybridisations are altered of course, e.g. according to Eq. (5.3.57). But, with DMRG as an impurity solver the actual input hybridisation is always the discretised version $\mathbf{\Delta}_{\text{discr}}$ of the hybridisation after the fitting procedure. Especially if the number of used bath sites is too small to fit $\mathbf{\Delta}$ perfectly, there are significant differences between the obtained hybridisation from iteration $i$ and the used discretisation $\Delta_{discr}$ of iteration $i+1$. This can lead to wrong and overestimated corrections due to Broyden's mixing. Therefore, it is crucial to use the discretised hybridisations as $V^{(i)}$.
The mixing procedure can be refined by only taking into account a certain number rather than all recent iterations or by restarting the mixing scheme after a couple of DMFT loops. E.g. this can be helpful if the first steps of the DMFT calculations lead through a bad and untypical regime of hybridisations. In general, Broyden's mixing can overestimate corrections to $\mathbf{\Delta}$ easily, which can result in unphysical hybridisations, e.g. with a positive imaginary part for small frequencies. We recommend to supervise Broyden's mixing extensively and adjust the parameters to avoid unphysical results if they occur. Up to now, we only used the standard Broyden's mixing in situations where a convergence with the standard approach or simple linear mixing was not successful.

### 5.3.6 Convergence and Real Frequency Green's Function

All steps described in the previous sections combined form a single DMFT iteration, also called a single loop. At the end of each loop, the difference between the interacting impurity Green's functions $\boldsymbol{G}(i\omega_n)$ of the last two subsequent iterations is computed. We

define that DMFT has reached the self-consistent solution if the maximal difference over all frequencies is smaller than the chosen threshold $10^{-3}$

$$\forall_{i,j} \max_{\omega_n} \left( \boldsymbol{G}_{i,j}^{(m)}(i\omega_n) - \boldsymbol{G}_{i,j}^{(m-1)}(i\omega_n) \right) < 10^{-3}, \tag{5.3.62}$$

with $m$ indicating the current iteration. It can be useful in certain situations to check convergence with respect to the iteration $m-2$ if a small oscillating behaviour is observed and cannot be removed. The bound of $10^{-3}$ seems to be a very strong convergence criterium compared to other methods but is at the same time very reliable. Quite often, we observe that DMFT results change by less than $10^{-2}$ over several iterations but suddenly change in the order of $10^{-1}$. This indicates problems with the approached solution, which would not be be realised when taking $10^{-2}$ as a convergence criterium. However, we never observed this kind of behaviour when the maximal difference was dropping below $10^{-3}$.
Fig. 5.9 shows the rate of convergence over a couple of iterations in the case of a DMFT calculation with four-site dynamical cluster approximation. The rate of convergence and the actual changes can differ strongly between the different Green's function components. For example, the degenerate $(\pi, 0)$-patch Green's function needs three iterations longer to converge because the changes in the first iterations were much smaller compared to the other Green's function components.
After convergence is observed, the interacting impurity Green's function $\boldsymbol{G}(\omega)$ on the real-frequency axis has to be computed. There are a couple of ways to do this:

1. We can take the converged Hamiltonian and the corresponding ground state of the last iteration and perform a real-time evolution instead of an imaginary-time evolution

$$\begin{aligned} \boldsymbol{G}_{i,j}(t) &= -i\theta(t)(\langle E_0|c_i e^{-i(\hat{H}-E_0)t} c_j^\dagger |E_0\rangle + \langle E_0|c_i^\dagger e^{i(\hat{H}-E_0)t} c_j|E_0\rangle) \\ &= -i\theta(t)(G_{i,j}^{>}(it) + G_{i,j}^{<}(it)). \end{aligned} \tag{5.3.63}$$

   A Fourier transform of this function will result in the desired interacting impurity Green's function

$$\boldsymbol{G}_{i,j}(\omega) = \int_{-\infty}^{\infty} \mathrm{d}t \boldsymbol{G}_{i,j}(t) e^{-i\omega t}. \tag{5.3.64}$$

   This approach has several disadvantages. First, the Hamiltonian $\hat{H}$ is optimised and converged for calculations on the imaginary axis, i.e. for imaginary-time evolutions, the Matsubara Green's function and fits of the hybridisation on the imaginary-frequency axis. If, instead, real-time evolutions and real-frequency Green's functions are computed, the question arises whether the important physics on the real axis is even correctly described by the Hamiltonian. Typically, if DMFT is used for real-frequency calculations, the bath is discretised by approximately 100 sites to reflect the rich structure of the physical functions on the real-frequency axis. Thus, it is doubtful that the Hamiltonian of the converged DMFT calculation on

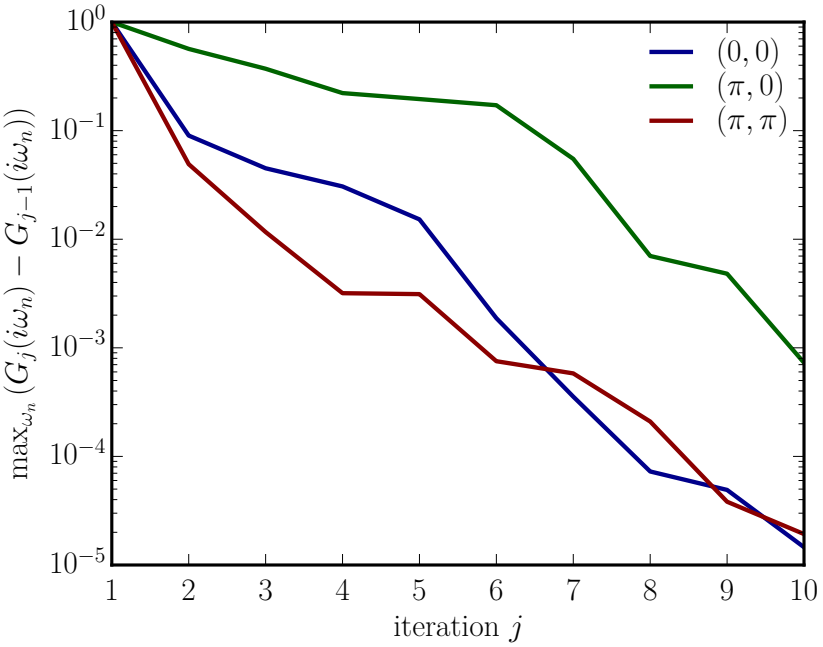


*Figure 5.9: Changes of the Green's functions in a four-site DCA calculation over all iterations until convergence. The data was obtained from a Hubbard model calculation with interaction strength $U = 7t$, next-nearest neighbour hopping $t_p = -0.15t$, nearest neighbour hopping $t = 1$ and $\mu = 1.3t$. Because of symmetry reasons, the Green's functions of the $(\pi, 0)$ and $(0, \pi)$ are degenerate. This seems to be the reason why the Green's functions of those patches takes longer to converge below the threshold of $10^{-3}$. However, the change of the Green's functions of the other patches decreases even further, which supports that we really found a fix point of the DMFT iteration.*

the imaginary axis with bath sizes of ten or even less sites is sufficient to obtain good real-frequency results.

Second, we have to account for finite size effects. Typically, for real-time evolution studies one considers DMRG systems with around 100 bath sites. This allows excitations to move around in the system and only be reflected at the end of the system at such long times that computed quantities already show pseudo convergence.This means that the long-time physics is already so dominant that extrapolation techniques like linear prediction can ignore the short-time physics and extrapolate the calculated quantities before finite size effects influence the signal.

With imaginary-time DMRG as an impurity solver for DMFT the bath sizes are typically smaller than 10. This means that finite size effects will be present before pseudo convergence sets in, which makes linear prediction untrustworthy. In a regime where it is not clear whether the short-time behaviour is still and finite size effects are already present, it is especially hard to determine a fitting interval for the

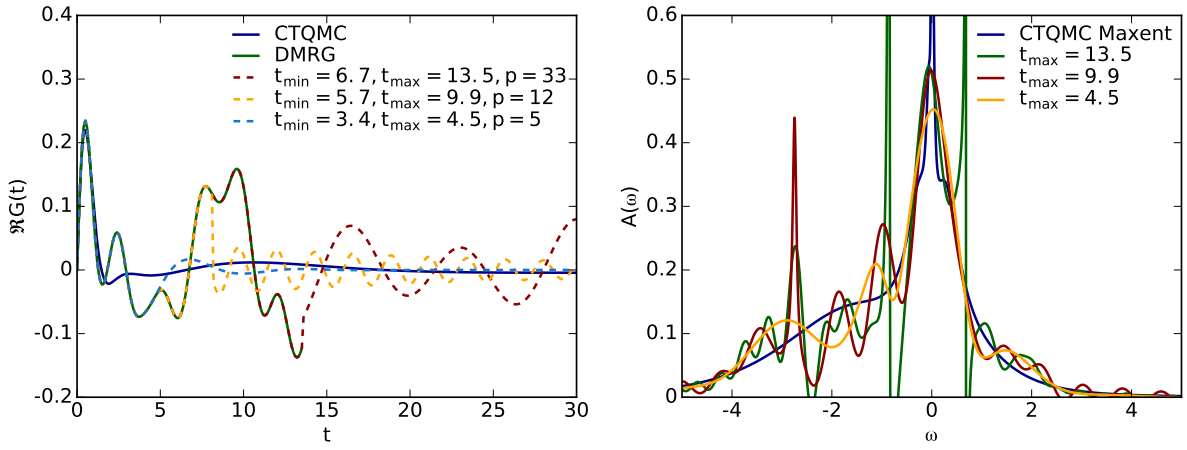


*Figure 5.10: Left panel: Comparison between the real part of the real-time Greens functions $\boldsymbol{G}_{11}(t)$ obtained with DMRG and with CTQMC. From $t \approx 2$ on the two curves start to differ qualitatively. The linear prediction preferred to fit the DMRG on the time interval $[3.4, 4.5]$ indicating that for later times there are already finite size effects present. Forcing the linear prediction to fit the DMRG data on different intervals and with different numbers of moments $p$, leads to strongly oscillating extrapolations. Right panel: Spectral functions $A(\omega)$ obtained via a Fourier transform of the Green's function of the left plot. The best agreement with CTQMC is obtained with the automatically determined fitting interval at small times. Other fitting intervals result in strong oscillations. However, we are not able to resolve the small peak at $\omega = 0$. The data was obtained from a real material study on $Sr_2RuO_4$ with a filling of four particles, $U = 2.3eV$, $J = 0.4eV$ and $L_b = 8$ bath sites. The CTQMC data was calculated at temperature $\beta = 200$.*

linear prediction. This can be seen in the left panel of Fig. 5.10 where we compared the extrapolated real-frequency Green's functions $\boldsymbol{G}(t)$ of DMRG with the Green's function obtained from CTQMC. The comparison has to be taken with care since the CTQMC data was computed with numerically ill-defined analytical continuation methods from $\boldsymbol{G}(\tau)$ and thus is very dependent on the used data. Therefore, we only expect to observe qualitative agreement. However, since CTQMC treats the infinitely large bath exactly and does not suffer under finite size effects, the dramatic differences from $\tau = 2$ on are a strong hint for finite size effects in the DMRG data.

This is confirmed by using linear prediction on the DMRG data. As described in section 4.4.1, linear prediction adjusts the fitting interval such that the discarded weight of the computed coefficients in the exponentials drops below 0.1. In this case, linear prediction prefers to fit $G(t)$ in the interval $[3.4, 4.5]$ with $p = 5$ moments, although $\boldsymbol{G}(t)$ was computed with MPS methods until $t_{\max} = 13.5$. This indicates that finite size effects influence $G(t)$ strongly from $t = 4.5$ on, at least. By enforcing

other fitting intervals and other amounts of moments $p$ for the linear prediction, we can increase agreement with the computed DMRG data for longer times, but at the cost of introducing slowly decaying oscillations in the extrapolation regime. This is another indication for the finite size effects present in the DMRG data.
The right plot Fig. 5.10 shows the corresponding spectral functions $A(\omega)$ to the Green's functions in the left panel. The best agreement with CTQMC is obtained with the automatically determined interval. But even then strong oscillations around the CTQMC results can be observed and the peak at $\omega = 0$ cannot be resolved. By shifting the fitting interval to later times, stronger oscillations, i.e. finite size effects, are created. When fitting the complete DMRG data until $t = 13.5$ the oscillations on the spectral function turn negative, which clearly indicates unphysical behaviour. Putting all these observations together, it is clear that the bath is too small to obtain qualitatively good real-time Green's function.
Another way of reducing finite size effects is to introduce a broadening term in the Fourier transform, which can for example be a Gaussian

$$\boldsymbol{G}_{i,j,\eta}(\omega) = \int_{-\infty}^{\infty} \mathrm{d}t \boldsymbol{G}_{i,j}(t) e^{-\frac{1}{2}\eta^2 t^2} e^{-i\omega t}, \tag{5.3.65}$$

or a Lorentzian broadening

$$\boldsymbol{G}_{i,j,\eta}(\omega) = \int_{-\infty}^{\infty} \mathrm{d}t \boldsymbol{G}_{i,j}(t) e^{-\eta t} e^{-i\omega t}. \tag{5.3.66}$$

The broadening term $\eta$ will suppress any long-time behaviour for times roughly larger than $t \approx 1/(2\eta)$. This ansatz is only useful if the finite size effects are not already present on very short time scales as in our example. Typically chosen values for the broadening term are in the range of $\eta \approx 10^3$ to $\eta \approx 10^{-1}$ and thus start to suppress $\boldsymbol{G}(t)$ significantly between $t \approx 500$ to $t \approx 5$. Since a product of two functions turns into a convolution after a Fourier transform, the real-frequency Green's function with the broadening function $f_\eta(t)$ will have the form

$$G_{i,j,\eta}(\omega) = \int_{-\infty}^{\infty} \mathrm{d}\nu G_{i,j}(\nu) \tilde{f}_\eta(\nu - \omega), \tag{5.3.67}$$

where $\tilde{f}_\eta(\omega)$ is the Fourier transform of $f_\eta(t)$. Thus, small features in the spectral function $\boldsymbol{G}(\omega)$, which can originate from physical processes, are smeared out and lost in $\boldsymbol{G}_\eta(\omega)$.
Another disadvantage of real-time evolutions is that these calculations are very expensive because entanglement grows exponentially during the time evolutions. Since the impurity systems in our models are, from the beginning on, very strongly entangled, this is especially inconvenient. One can limit the entanglement growth by splitting the time evolution in a way that the left and right state in the definition of the Green's function $\boldsymbol{G}(t)$ are evolved backwards and forwards in time, respectively,

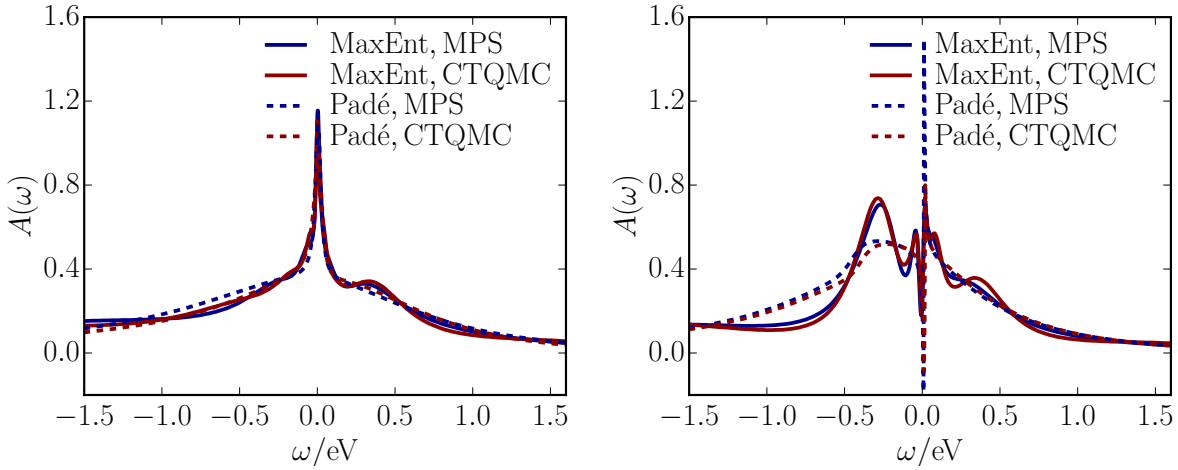


*Figure 5.11: Spectral functions $A(\omega)$ obtained via Maxent and Padé from CTQMC and DMRG data for the two relevant bands in the $Sr_2RuO_4$ model. The agreement between DMRG and CTQMC as well as the agreement between Maxent and Padé is very good. For the xz band, the Padé results seem to have a small issue at $\omega = 0$, where the spectral function is unphysical. The data was obtained from a real-material study on $Sr_2RuO_4$ with a filling of four particles, $U = 2.3eV$, $J = 0.4eV$ and $L_b = 8$ bath sites. The CTQMC data was calculated at temperature $\beta = 200$.*

with halved time steps

$$\begin{aligned} \boldsymbol{G}^{>}_{i,j}(t) &= \langle E_0 | c_i e^{-i(\hat{H}-E_0)t} c_j^\dagger | E_0 \rangle \\ &= (\langle E_0 | c_i e^{-i(\hat{H}-E_0)t/2})(e^{-i(\hat{H}-E_0)t/2} c_j^\dagger | E_0 \rangle) \\ &= \langle \psi_i^{>}(-t/2) | \psi_j^{>}(t/2) \rangle. \end{aligned} \tag{5.3.68}$$

This done by default in all our real-time calculations. However, for the example displayed in Fig. 5.10, computing a single time step at $t = 13.5$ we took two days, which is several times longer than the computation time of a complete DMFT loop on the imaginary axis. This shows that even if finite size effects set in at later times, it can be impossible to compute $\boldsymbol{G}(t)$ long enough due to the entanglement growth.

2. The real-frequency Green's function can also be obtained with the help of analytic continuations, like Maxent[152,153] or Padé[154,155], from the converged Matsubara Green's function $G(i\omega_n)$. Of course, these methods strongly depend on even small details of the provided data and thus are critical by itself. Additionally, to be able to apply analytic continuations on DMRG data, the data has to be combined with normal distributed noise. This will hide finite size effects, which become the stronger the less noise is used. However, Fig. 5.11 shows the comparison between the spectral functions $A(\omega)$ obtained with Maxent and Padé from CTQMC and DMRG data. We obtain qualitatively very good agreement. Additionally, the best

spectral function obtained from the real-time evolution is plotted to emphasise the differences between both approaches. It is obvious that the analytic continuation approach is much better suited to obtain good quality results on the real-frequency axis.
Since there is a lot of adjusting and guessing of parameters in the real-time evolution approach and because the analytic continuations are much faster and are giving better results, we prefer, if possible, to use analytic continuations methods to obtain the real-frequency Green's functions.

## 5.4 Dynamical Cluster Approximation

Dynamical mean-field theory focuses on a single site of an infinitely large lattice and treats this site and all local interactions exactly while the remaining sites are summarised as a mean-field acting on the single site. This approach is reasonable as long as non-local interactions are negligible. This locality means that the electron self-energy is momentum independent. In some models this is an insufficient ansatz and it is necessary to restore the $\vec{k}$-dependence to obtain reasonable results. A couple of methods exist for correlated electron systems that approximate non-local correlations to different degrees. The three most established methods are cellular DMFT, cluster perturbation theory and dynamical cluster approximation (DCA). We will focus in the following on DCA since it conserves the translational invariance of the lattice in contrast to cellular DMFT.
The fundamental idea of DCA is to partition the 1st Brillouin zone into $N_c$ patches in which the Green's function and self-energy are averaged over, respectively. In the limit $N_c \to \infty$ this approach is obtaining the exact result while $N_c = 1$ reproduces DMFT. This coarse graining can be written as

$$\mathbf{\Sigma}^{\mathrm{DCA}}(\vec{k}) \simeq \sum_{\vec{K}} \Phi_{\vec{K}}(\vec{k}) \mathbf{\Sigma}_c(\vec{K}), \tag{5.4.1}$$

with

$$\Phi_{\vec{K}}(\vec{k}) = \begin{cases} 1, & \text{if } k \text{ in patch } \vec{K}, \\ 0, & \text{otherwise}, \end{cases} \tag{5.4.2}$$

since we describe each patch by a representative cluster momentum $\vec{K}$, as can be seen in Fig. 5.12. We now proceed from the free energy, written down in Eq. (5.1.11), according to the work of Potthoff[156] and Okamato[157]. This time, we write the functional in terms of the self-energy $\mathbf{\Sigma}$ instead of the Green's function

$$\Omega[\mathbf{\Sigma}] = -\mathrm{Tr} \ln \left[ \boldsymbol{G}_0^{-1}[\mathbf{\Sigma}] - \mathbf{\Sigma} \right] - (\mathcal{L}\Phi)[\mathbf{\Sigma}]. \tag{5.4.3}$$

The last term is obtained from a Legendre transformation

$$(\mathcal{L}\Phi)[\mathbf{\Sigma}] = \Phi_{\mathrm{BK}}[\boldsymbol{G}[\mathbf{\Sigma}]] - \mathrm{Tr}[\mathbf{\Sigma}\boldsymbol{G}[\mathbf{\Sigma}]]. \tag{5.4.4}$$

At the stationary point $\delta\Omega[\boldsymbol{\Sigma}]/\delta\boldsymbol{\Sigma} = 0$ we obtain the Dyson equation $\boldsymbol{G} = \boldsymbol{G}_0^{-1} - \boldsymbol{\Sigma}$ with $\boldsymbol{G} = -\delta(\mathcal{L}\Phi)[\boldsymbol{\Sigma}]/\delta\boldsymbol{\Sigma}$, similar to the derivation of the self-consistency equation of DMFT. Since, in general, the Baym-Kadanoff functional $\Phi_{\mathrm{BK}}[\boldsymbol{G}]$ is unknown, the same is true for $(\mathcal{L}\Phi)[\boldsymbol{\Sigma}]$. While DMFT was approximating the Baym-Kadanoff functional, DCA keeps the exact functional but replaces the self-energy by the averaged version from Eq. (5.4.1). Thus, the complexity of the functional is reduced significantly, because the degrees of freedom are reduced to those of a finite-size cluster

$$(\mathcal{L}\Phi)[\boldsymbol{\Sigma}_c] = \Phi_{\mathrm{BK}}[\boldsymbol{G}_c] - \frac{N}{N_c}\sum_{\vec{K}} \mathrm{Tr}[\boldsymbol{\Sigma}_c(\vec{K})\boldsymbol{G}_c(\vec{K})], \tag{5.4.5}$$

with

$$\boldsymbol{G}_c(\vec{K}) = \frac{N_c}{N}\sum_{\vec{k}} \phi_{\vec{K}}(\vec{k})\boldsymbol{G}(\vec{k}) = \frac{N_c}{N}\sum_{\vec{k}} \phi_{\vec{K}}(\vec{k})\frac{1}{\boldsymbol{G}_0^{-1}(\vec{k}) - \boldsymbol{\Sigma}^{\mathrm{DCA}}(\vec{k})}. \tag{5.4.6}$$

The last equation shows that the cluster Green's function $\boldsymbol{G}_c$ is equal to the coarse-grained lattice Green's function on the right hand side. Similar to the derivation of the DMFT self-consistency equations, we can deduce from the stationary condition and the saddle-point equation

$$\Omega^{\mathrm{DCA}}[\boldsymbol{\Sigma}_c] = -\mathrm{Tr}\ln\left[-(\boldsymbol{G}_0^{-1} - \boldsymbol{\Sigma}^{\mathrm{DCA}})\right] + \Phi_{\mathrm{BK}}[\boldsymbol{G}_c[\boldsymbol{\Sigma}_c]] - \sum_{\vec{K}} \mathrm{Tr}[\boldsymbol{\Sigma}_c(\vec{K})\boldsymbol{G}_c(\vec{K})], \tag{5.4.7}$$

together with the help of Eq. (5.4.1), namely $\delta\boldsymbol{\Sigma}^{\mathrm{DCA}}(\vec{k})/\delta\boldsymbol{\Sigma}_c(\vec{K}) = \phi_{\vec{K}}(\vec{k})$, that

$$\frac{\delta\Omega^{\mathrm{DCA}}[\boldsymbol{\Sigma}_c]}{\delta\boldsymbol{\Sigma}_c} = -\mathrm{Tr}\left[\sum_{\vec{k}} \phi_{\vec{K}}(\vec{k})((\boldsymbol{G}_0^{-1} - \boldsymbol{\Sigma}^{\mathrm{DCA}})^{-1} - \boldsymbol{G}_c\right] + \frac{\delta\Phi_{\mathrm{BK}}[\boldsymbol{G}_c[\boldsymbol{\Sigma}_c]]}{\delta\boldsymbol{\Sigma}_c} - \boldsymbol{G}_c[\boldsymbol{\Sigma}_c] = 0. \tag{5.4.8}$$

The first term vanishes equivalently to the DMFT case because of the Dyson equation. Thus, we obtain

$$\frac{\delta\Phi_{\mathrm{BK}}[\boldsymbol{G}_c[\boldsymbol{\Sigma}_c]]}{\delta\boldsymbol{\Sigma}_c} = \boldsymbol{G}_c[\boldsymbol{\Sigma}_{\boldsymbol{c}}], \tag{5.4.9}$$

which allows us to solve the coarse-grained self-energy and the corse-grained Green's function with the help of Dyson equation and Eq. (5.4.9) self-consistently. After we showed analogously to the DMFT case in a rather theoretical derivation that the piecewise constant self-energies $\boldsymbol{\Sigma}^{\mathrm{DCA}}$ and Green's functions $\boldsymbol{G}^{\mathrm{DCA}}$ are indeed solutions to the Baym-Kadanoff functional, we now want to focus on what exactly will change in our presented DMFT scheme and how we will implement DCA in all its details.

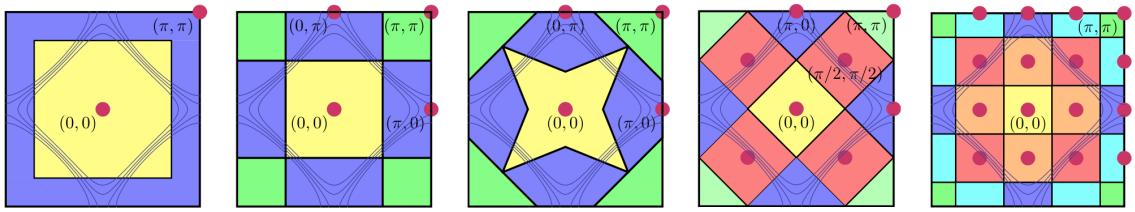


*Figure 5.12: Typical choices of the DCA patches in the 1st Brillouin zone for different number of patches. The red dots are the representative vectors $\vec{K}_k$ and the thin lines equipotential lines of the dispersion relation. Alternative choices of the patch form can be better suited to describe certain models. For four patches an alternative form is given in the picture. We will discuss the influences of different patch forms for the same number of patches in detail in chapter 6. The picture is taken from Gull et al.[53].*

- First, we introduce patches $P_{\vec{K}}$ in the 1st Brillouin zone and indicate them with a representative vector $\vec{K}$. Typically, we discretise the 1st Brillouin zone into $1000 \times 1000$ momentum vectors $(k_x, k_y)$. Of course, any other number of data points can be used as long as the resolution of the dispersion relation is good enough. As long as the volume of all patches is the same, the DCA functional expressed in real-space coordinates has only local interactions that are identical to the ones of the original DMFT problem. This means that no additional multi-particle interactions are introduced by DCA . The interaction Hamiltonian is just the same as for single-site DMFT applied to all DCA sites separately. The actual form of the patches is completely free. From a physical point of view it is recommended to choose patches such that they include regions with the same physical properties. In Fig. 5.12 typical momentum patches are shown as used by Gull et al.[53] or Ferrero et al.[50].

- Typically, we stay in the momentum-space representation of the DCA. In this case the self-energy, Green's function and hybridisation are all diagonal matrices and each diagonal element describes a single patch. Thus, they all get a label $\vec{K}$

$$G_{\vec{K}}(i\omega_n) = \frac{1}{i\omega_n - \mu - t_{\vec{K}} - \Sigma_{\vec{K}}(i\omega_n) - \Delta_{\vec{K}}(i\omega_n)}. \tag{5.4.10}$$

  To ensure that the impurity Green's functions $G_{\vec{K}}(i\omega_n)$ decay with $1/\omega_n^2$, a shift of the chemical potential $\bar{t}_{\vec{K}} = \sum_{\vec{k}\in P_{\vec{K}}} \varepsilon_{\vec{k}}$ has to be introduced. If the sum runs over the whole Brillouin zone, as in single-site DMFT, this shift becomes zero $\bar{t}_{\vec{K}} = \sum_{1stBZ} \varepsilon_{\vec{k}} = 0$ and the usual Green's function is obtained. Accordingly, the lattice Green's functions in DCA are also averaged over the patches and not the whole Brillouin zone anymore,

$$G^{\text{latt}}_{\vec{K}}(i\omega_n) = \sum_{\vec{k}\in P_{\vec{K}}} \frac{1}{i\omega_n - \varepsilon_{\vec{k}} - \Sigma_{\vec{K}}(i\omega_n)}. \tag{5.4.11}$$

| number of DCA sites | $\vec{R}_j$ | $\vec{K}_k$ |
|---|---|---|
| 2 | $\begin{pmatrix}0\\0\end{pmatrix}, \begin{pmatrix}\pi\\\pi\end{pmatrix}$ | $\begin{pmatrix}0\\0\end{pmatrix}, \begin{pmatrix}1\\0\end{pmatrix}$ |
| 4 | $\begin{pmatrix}0\\0\end{pmatrix}, \begin{pmatrix}0\\\pi\end{pmatrix}, \begin{pmatrix}\pi\\0\end{pmatrix}, \begin{pmatrix}\pi\\\pi\end{pmatrix}$ | $\begin{pmatrix}0\\0\end{pmatrix}, \begin{pmatrix}0\\1\end{pmatrix}, \begin{pmatrix}1\\0\end{pmatrix}, \begin{pmatrix}1\\1\end{pmatrix}$ |
| 8 | $\begin{pmatrix}0\\0\end{pmatrix}, \begin{pmatrix}\frac{\pi}{2}\\\frac{\pi}{2}\end{pmatrix}, \begin{pmatrix}\frac{\pi}{2}\\-\frac{\pi}{2}\end{pmatrix}, \begin{pmatrix}-\frac{\pi}{2}\\-\frac{\pi}{2}\end{pmatrix}, \begin{pmatrix}-\frac{\pi}{2}\\\frac{\pi}{2}\end{pmatrix}, \begin{pmatrix}0\\\pi\end{pmatrix}, \begin{pmatrix}\pi\\0\end{pmatrix}, \begin{pmatrix}\pi\\\pi\end{pmatrix}$ | $\begin{pmatrix}0\\0\end{pmatrix}, \begin{pmatrix}0\\1\end{pmatrix}, \begin{pmatrix}1\\0\end{pmatrix}, \begin{pmatrix}-1\\0\end{pmatrix}, \begin{pmatrix}0\\-1\end{pmatrix}, \begin{pmatrix}1\\1\end{pmatrix}, \begin{pmatrix}-1\\1\end{pmatrix}, \begin{pmatrix}0\\2\end{pmatrix}$ |
| 16 | $\begin{pmatrix}0\\0\end{pmatrix}, \begin{pmatrix}0\\\frac{\pi}{2}\end{pmatrix}, \begin{pmatrix}\frac{\pi}{2}\\0\end{pmatrix}, \begin{pmatrix}0\\-\frac{\pi}{2}\end{pmatrix}, \begin{pmatrix}-\frac{\pi}{2}\\0\end{pmatrix}, \begin{pmatrix}\frac{\pi}{2}\\\frac{\pi}{2}\end{pmatrix}, \begin{pmatrix}\frac{\pi}{2}\\-\frac{\pi}{2}\end{pmatrix}, \begin{pmatrix}-\frac{\pi}{2}\\-\frac{\pi}{2}\end{pmatrix}, \begin{pmatrix}-\frac{\pi}{2}\\\frac{\pi}{2}\end{pmatrix}, \begin{pmatrix}0\\\pi\end{pmatrix}, \begin{pmatrix}\pi\\0\end{pmatrix}, \begin{pmatrix}\frac{\pi}{2}\\\pi\end{pmatrix}, \begin{pmatrix}\pi\\\frac{\pi}{2}\end{pmatrix}, \begin{pmatrix}\pi\\-\frac{\pi}{2}\end{pmatrix}, \begin{pmatrix}-\frac{\pi}{2}\\\pi\end{pmatrix}, \begin{pmatrix}\pi\\\pi\end{pmatrix}$ | $\begin{pmatrix}-1\\2\end{pmatrix}, \begin{pmatrix}-1\\1\end{pmatrix}, \begin{pmatrix}-1\\0\end{pmatrix}, \begin{pmatrix}-1\\-1\end{pmatrix}, \begin{pmatrix}0\\2\end{pmatrix}, \begin{pmatrix}0\\1\end{pmatrix}, \begin{pmatrix}0\\0\end{pmatrix}, \begin{pmatrix}0\\-1\end{pmatrix}, \begin{pmatrix}1\\2\end{pmatrix}, \begin{pmatrix}1\\1\end{pmatrix}, \begin{pmatrix}1\\0\end{pmatrix}, \begin{pmatrix}1\\-1\end{pmatrix}, \begin{pmatrix}2\\2\end{pmatrix}, \begin{pmatrix}2\\1\end{pmatrix}, \begin{pmatrix}2\\0\end{pmatrix}, \begin{pmatrix}2\\-1\end{pmatrix}$ |

*Table 5.2: Representative vectors $\vec{K}_k$ for the patches in momentum-space and vectors $\vec{R}_j$ for the corresponding real-space sites for different numbers of patches in DCA. Together with Eq.* (5.4.12) *and Eq.* (5.4.13) *they form the proper Fourier transform between real- and momentum-space.*

- Each patch is represented by a single impurity and its corresponding self-energy and Green's function. Since we have several impurity sites, we can define a Fourier transformation and consider the model in momentum-space or in real-space by mapping the creation $c_j^\dagger$ and annihilation operators $c_j$ of site $j$ from real-space to their counterparts in momentum-space $\tilde{c}_k^\dagger$ and $\tilde{c}_k$ on site $k$

$$c_j = \sum_k e^{i\vec{R}_j\vec{K}_k}\tilde{c}_k, \tag{5.4.12}$$

$$c_j^\dagger = \sum_k e^{-i\vec{R}_j\vec{K}_k}\tilde{c}_k. \tag{5.4.13}$$

$\vec{R}_j$ and $\vec{K}_k$ and are the representative vectors of the sites in the real-space lattice and the patches in momentum-space. In Tab.5.2 the real- and momentum-space vectors for different numbers of patches are listed. In momentum-space the hybridisation is diagonal, i.e. each impurity couples only to its own bath. Therefore, the fitting

procedure can be performed for each component separately. Unfortunately, since the interaction term in real-space has the same structure as in DMFT on each impurity site, in momentum-space the interaction term is very complicated. In general, due to the Fourier transform it will generate interactions between all impurity sites. However, the structure of the Hamiltonian will reflect momentum conservation by construction. Therefore, between the impurity sites all interactions are allowed that conserve the total momentum of the system. This is guaranteed through the Fourier transform and the exponential pre-factors. Particles leaving the impurity sites correspond to a momentum transfer to the environment, which is conserved too. Thus, bath sites are only coupled to a single impurity site.
In contrast, the interaction Hamiltonian in real-space is quite simple, but due to the Fourier transform each bath site couples to all impurity sites. Additionally, the Fourier transform will introduce single-particle hopping between the impurities in real-space because of the different on-site energy shifts $t_{\vec{K}}$ of each impurity in momentum-space. These changes reflect the physical processes in a lattice since particles are allowed to jump between neighbouring sites back and forth and are also allowed to jump into the environment, move around there and come back to a different impurity site.
However, in each DMFT iteration it has to be decided if the Hamiltonian has to be represented in momentum-space with a complicated interaction term but a diagonal hybridisation or in real-space with a simple interaction Hamiltonian but impurity sites that couple to all bath sites of all impurities. In general, we cannot say that one of the two representations is better suited for DMFT calculations. While it seems that entanglement properties are, typically, better in real-space, in momentum-space additional quantum numbers are usable. Based on our experience, we suggest to implement the impurity Hamiltonian in momentum-space.

- After finding the ground state either in momentum- or real-space, the excited states for each impurity site and the time evolutions are computed. If the Hamiltonian was represented in real-space, the Green's functions are combined according to the Fourier transformation to obtain the imaginary-time Green's function in momentum-space. The determined Green's functions are Fourier transformed to the frequency domain and used to compute the new hybridisation for the next DMFT iteration with the help of the self-consistency equation and the adjusted Green's functions Eq. (5.4.10) and Eq. (5.4.11). Since the hybridisation is determined in momentums-space, it is diagonal and can be fitted according to the scheme described in the beginning of this chapter.

- If the dispersion relation $\varepsilon_{\vec{k}}$ has certain symmetries, it is advantageous to distribute the patches in the 1st Brillouin according to those symmetries. In that way, the corresponding impurity sites, Green's functions, self-energies and hybridisations are strongly degenerate. Thus, the computational effort of a DMFT loop can be reduced significantly by only computing some of the Green's function and using the

degeneracies to determine the remaining ones. For example, the dispersion relation

$$\varepsilon_{\vec{k}} = t\cos k_x + t\cos k_y + t'\cos k_x t\cos k_y \tag{5.4.14}$$

with any choice of $t$ and $t'$ is axially symmetric to the diagonal from $(-\pi, -\pi)$ to $(\pi, \pi)$. In other words $\varepsilon_{\vec{k}}$ is invariant under $k_x \leftrightarrow k_y$. All patches in Fig. 5.12 are distributed with the same symmetry. In the case of four-site DCA the $(\pi, 0)$- and $(0, \pi)$-patch are completely degenerate. Therefore, only one of these two Green's functions has to be determined as long as this symmetry is not spontaneously broken. The amount of degeneracies is even increasing for higher patch numbers, which reduce the numerical effort for higher DCA approximations significantly. To illustrate this, all degenerate patches in Fig. 5.12 are painted in the same colour.

The alternations and changes to our method when using DCA are small and simple. Significant changes for the calculations are the increased system size, compared to single-site DMFT, and the increased amount of interactions between the impurity sites. Unfortunately, this will also lead to a huge increase of the amount of entanglement in the systems, as we will discuss in the context of the Hubbard model. This is slightly countered by the fact that the necessary bath sizes for a reasonable fit of the hybridisation for each impurity site seem to decrease slightly with the number of patches. We assume this is due to the fact that smaller patches include less variation of the physics and therefore less bath sites are needed to describe the correct physical behaviour. This will be discussed in more detail in section 6 too.

# Chapter 6

# The Two-Dimensional Hubbard Model

The Hubbard model is considered to be the simplest model containing correlated electrons at arbitrary fillings. Moreover, it describes relatively well the physics of solid state lattices as well as numerous systems in quantum chemistry and material science. Especially the physics of correlation-driven Mott insulating states and their behaviour upon electron doping is a particularly interesting feature of the Hubbard model and is essential for a wide class of materials. A very important example are high-temperature copper-oxide superconductors, which are also known as cuprates[52]. A lot of these materials consist of weakly coupled two-dimensional layers of atoms organised in rectangular lattices. Very often, their properties can be described successfully by the two-dimensional Hubbard model.
Originally, the low-temperature physics of doped Mott insulators was described as being a Fermi liquid with a quasiparticle mass that diverges as the Mott insulating state is approached. This explanation by Brinkman and Rice[158] not only gave an intuitive picture of most data but also was supported by results of single-site DMFT calculations. However, since the fundamental assumption of DMFT is the locality of correlations, or in other words the momentum-independence of the electron self-energy, this approach is not well suited for materials such as the cuprates where electronic properties are essentially two-dimensional functions. Studies of cuprate materials show isotropic behaviour for quasiparticle lifetimes, velocity renormalisation for very high doping[159], strong momentum dependence for dopings that maximise the superconductivity transition temperature[7] and, close to the insulating phase, even pseudogap behaviour[8].
There also has been a lot of theoretical work like resonating valence bond theories[160,161], semianalytic ansatzes based on antiferromagnetic[162], or charge-density wave correlations[163], confirming the importance of momentum-dependent approaches beyond DMFT. But only the development of cluster dynamical mean-field methods, e.g. as DCA, allowed to tackle these kind of problems without using assumptions that bias certain solutions and causing debates on which correlations are physically more important to include. With

these cluster dynamical mean-field theories it had been shown that the two-dimensional Hubbard model can exhibit a pseudogap[164], Fermi arcs[9], and several other interesting features around the Fermi surface[9,165]. Furthermore, it had been shown that the insulating phase is separated from the region where the model is a weakly correlated metal by a sector-selective phase, which is characterised by some regions of the Brillouin zone exhibiting insulating and others metallic behaviour[48,165].
A drawback of cluster methods is that they approximate the complete model in an uncontrolled manner. Cluster sizes, cluster forms, and the number of clusters site can change physical quantities remarkably. Gull et al.[53] were the first to make an intensive study on which physical properties of the doping-driven Mott transition in the two-dimensional Hubbard model are robust features and which vary when certain features of cluster DMFT are changed. Furthermore, they were also the first to systematically investigate the differences between different cluster sizes and geometries.
These studies were performed with CTQMC and thus are only reliable for finite temperatures and weak interaction strengths. In fact, the interaction strength $U = 7t$, chosen by Gull et al., is slightly smaller than $U \approx 9t$ which is believed to be more relevant for systems that exhibit high-temperature superconductivity[10]. Another limitation of CTQMC, including the studies of Gull et al., is the sign-problem at low temperatures, which prevents to investigation of interesting questions like the exact nature of the low-temperature metallic state in the nodal region of the sector-selective phase, or the quantitative evolution of Fermi arcs with temperature and doping.
Therefore, in this chapter we want to show that DMRG+DMFT is not only able to reproduce the CTQMC data of Gull et al.[53] with $U = 7t$ reliably and comparably fast but is also able to produce results for intermediate interaction strengths at temperature $T = 0$. This regime can neither be reached by CTQMC with large clusters sizes at sufficiently low temperatures due to the sign problem nor by any other available method.
We start this chapter by presenting the Hubbard model, the occurring symmetries, and our implementation of the momentum quantum numbers, which plays a vital role for convergence properties in the case of four-site and eight-site DCA. Afterwards, we compare the results with Gull et al. to verify our method and investigate whether there exist qualitative differences between our DMRG results at $T = 0$ and the finite temperature computations of CTQMC. We will shortly discuss why eight-site DCA systems are currently not solvable with DMRG+DMFT and end the chapter by presenting our results for the intermediate interaction strengths $U = 9t$ and $U = 11t$ at temperature $T = 0$.

## 6.1 The Hubbard Hamiltonian

The starting point of each DMFT and DCA calculation is the definition of the model Hamiltonian $\hat{H}_{\text{latt}}$ for the underlying infinitely large two-dimensional lattice. In the case of the Hubbard model the system is described by

$$\begin{aligned}\hat{H}_{\text{latt}} &= \sum_{\vec{k},\sigma} \varepsilon_{\vec{k}} \tilde{d}^{\dagger}_{\vec{k},\sigma} \tilde{d}_{\vec{k},\sigma} + U \sum_i n_{i,\uparrow} n_{i,\downarrow} - \mu \sum_i (n_{i,\uparrow} + n_{i,\downarrow}) \\ &= \sum_{\vec{k}} \varepsilon_{\vec{k}} \tilde{N}_{\vec{k}} + \frac{U}{2} \sum_i N_i (N_i - 1) - \mu \sum_i N_i. \end{aligned} \tag{6.1.1}$$

with the typical Hubbard interaction on each site $i$ of the real-space lattice with strength $U$ and a chemical potential $\mu$ to control the filling of the lattice. The particle number operators are defined as

$$N_i = n_{i,\uparrow} + n_{i,\downarrow} = d^{\dagger}_{i,\uparrow} d_{i,\uparrow} + d^{\dagger}_{i,\downarrow} d_{i,\downarrow}, \tag{6.1.2}$$

$$\tilde{N}_{\vec{k}} = \tilde{d}^{\dagger}_{\vec{k},\uparrow} \tilde{d}_{\vec{k},\uparrow} + \tilde{d}^{\dagger}_{\vec{k},\downarrow} \tilde{d}_{\vec{k},\downarrow}. \tag{6.1.3}$$

The first term of $\hat{H}_{\text{latt}}$ represents the kinetic energy written in momentum space. To make the notation clearer, we denote all creation and annihilation operators acting in momentum space with a tilde. The kinetic energy of the single-particle states in momentum space is given by the dispersion relation

$$\varepsilon_{\vec{k}} = -2t(\cos k_x + \cos k_y) - 4t' \cos k_x \cos k_y, \tag{6.1.4}$$

with nearest neighbour hopping $t = 1$, next-nearest neighbour hopping $t' = -0.15t$, and two-dimensional momentum $\vec{k} = (k_x, k_y)$.
As described in the previous section, in the context of DMFT an auxiliary impurity problem is created by taking a single site out of the infinitely large lattice. On this site, called impurity, the same interaction as on each site of the lattice is present. Thus, we define the interaction Hamiltonian of our impurity model as

$$\hat{H}_{\text{int}} = \frac{U}{2} N(N-1), \tag{6.1.5}$$

and the single-particle on-site energy as

$$\hat{H}_{\text{sp}} = -\mu N, \tag{6.1.6}$$

both acting on the impurity site. The kinetic term vanishes since the dispersion relation averaged over the whole Brillouin zone is zero. Furthermore, the impurity is coupled via single-particle hopping to a non-interacting environment called bath. The coupling between impurity and environment is completely described by the hybridisation $\Delta(i\omega_n)$, which has to be determined self-consistently within DMRG. A discretisation of the bath

into a finite number of $L_b$ bath sites allows to write down the coupling and the bath Hamiltonian of the impurity problem as

$$\hat{H}_{\text{hyb}} = \sum_{l,\sigma} V_{l,\sigma} d_\sigma^\dagger c_{l,\sigma} + \text{h.c.}, \tag{6.1.7}$$

$$\hat{H}_{\text{bath}} = \sum_{l,\sigma} \epsilon_{l,\sigma} c_{l,\sigma}^\dagger c_{l,\sigma}, \tag{6.1.8}$$

where $c_{l,\sigma}^\dagger$ and $c_{l,\sigma}$ denote the creation and annihilation operators of an electron on bath site $l$. The on-site energies of the bath sites $\epsilon_{l,\sigma}$ and the single-particle hopping elements $V_{l,\sigma}$ are obtained by a fit of the hybridisation $\Delta(i\omega_n)$. Combining all terms, we obtain the complete Hamiltonian describing the impurity problem

$$\hat{H}_{\text{imp}} = \hat{H}_{\text{int}} + \hat{H}_{\text{sp}} + \hat{H}_{\text{hyb}} + \hat{H}_{\text{bath}}. \tag{6.1.9}$$

All DMFT results in this chapter are obtained with $\hat{H}_{\text{imp}}$.
When using multi-site DCA the resulting Hamiltonian is more complex. It is very important for entanglement properties and implementational details whether the impurity Hamiltonian is represented in real or momentum space. We will first show the momentum-space representation and afterwards transform the Hamiltonian to real space.
As discussed in the previous section, in the case of multi-site DCA each impurity site describes a single patch of the Brillouin zone. Thus, the number of patches is equivalent to the number of impurity sites $N_{\text{imp}}$. As for DMFT, in real-space the same interaction as in the original lattice model is present on each site

$$\hat{H}_{\text{int}}^{\text{real}} = \sum_{i=1}^{N_{\text{imp}}} \frac{U}{2} N_i (N_i - 1). \tag{6.1.10}$$

The interaction Hamiltonian $\hat{H}_{\text{int}}^{\text{real}}$ has to be Fourier transformed, as defined in Eq. (5.4.12), Eq. (5.4.13) and Tab. 5.2, to obtain the impurity Hamiltonian in momentum space

$$\hat{H}_{\text{int}}^{\text{mom}} = \frac{U}{2} \sum_{\sigma,\sigma'} \sum_{r,s,m,n=1}^{N_{\text{imp}}} \delta(\vec{K}_r - \vec{K}_s + \vec{K}_m - \vec{K}_n) \tilde{d}_{r,\sigma}^\dagger \tilde{d}_{s,\sigma} \tilde{d}_{m,\sigma'}^\dagger \tilde{d}_{n,\sigma'} - \frac{U}{2} \sum_i \tilde{N}_i. \tag{6.1.11}$$

The term $\delta(\vec{K}_r - \vec{K}_s + \vec{K}_m - \vec{K}_n)$ together with the representative momentum vectors $\vec{K}$ of the DCA patches assures that only two-particle interactions are allowed that conserve the total two-dimensional momentum. In general, those terms create a lot of entanglement between the impurity sites and between their corresponding bath sites, especially for higher DCA approximations.
The kinetic term in the momentum-space representation corresponds to an on-site energy and is obtained by averaging over the the dispersion relation inside of each patch $\tilde{t}_i = \sum_{\vec{k} \in P_{\vec{K}_i}} \varepsilon_{\vec{k}}$. As discussed in section 5.4, this guarantees the correct high frequency

behaviour of the Matsubara Green's function. Combining these terms with the on-site energy given by $\mu$, we obtain

$$\hat{H}_{\text{sp}}^{\text{mom}} = -\sum_{i=1}^{\tilde{N}_{\text{imp}}} (\mu - \tilde{t}_i)\tilde{N}_i. \tag{6.1.12}$$

Because each impurity site corresponds to an momentum $\vec{K}$ and because the model explicitly conserves the momentum between the patches, no single-particle hopping exists between the impurity sites in momentum space. This is reflected by the fact that the hybridisation, the self-energy, and the Green's function are all diagonal matrices. Therefore, each impurity site has an independent hybridisation, which can be fitted efficiently and in parallel with only a few parameters corresponding to a small number of bath sites $L_{b,i}$. This results in significant runtime improvements for large systems. In general, each bath can consist of a different number of bath sites, but in most cases they are all set to the same size $L_{b,i} = L_b$ for simplicity.
Since each impurity site can only couple to its own bath, we can label each bath site by an index $i$ for the impurity it belongs to and an index $l$ numbering the $L_b$ sites of this bath. Thus, we can write the bath and the coupling Hamiltonian in momentum space as

$$\hat{H}_{\text{hyb}}^{\text{mom}} = \sum_{l,i,\sigma} V_{l,i,\sigma} \tilde{d}_{i,\sigma}^{\dagger} c_{l,i,\sigma} + \text{h.c.}, \tag{6.1.13}$$

$$\hat{H}_{\text{bath}}^{\text{mom}} = \sum_{l,i,\sigma} \epsilon_{l,i,\sigma} c_{l,i,\sigma}^{\dagger} c_{l,i,\sigma}. \tag{6.1.14}$$

The bath sites are not denoted with a tilde because they are neither located in momentum nor in real space. The complete Hamiltonian is obtained by summing all terms

$$\hat{H}_{\text{imp}}^{\text{mom}} = \hat{H}_{\text{int}}^{\text{mom}} + \hat{H}_{\text{sp}}^{\text{mom}} + \hat{H}_{\text{hyb}}^{\text{mom}} + \hat{H}_{\text{bath}}^{\text{mom}}. \tag{6.1.15}$$

If we refer to momentum-space DCA, all results are obtained with $\hat{H}_{\text{imp}}^{\text{mom}}$.
Obviously, the whole Hamiltonian can also be represented in real space by applying the inverse Fourier transform on the impurity sites. The advantage of the real-space representation is that the interaction on the impurity sites is much simpler and completely local

$$\hat{H}_{\text{int}}^{\text{real}} = \sum_{i=1}^{N_{\text{imp}}} \frac{U}{2} N_i(N_i - 1), \tag{6.1.16}$$

because it only consists of the typical Hubbard interaction on each site. Since DCA restores some of the momentum dependence of the original lattice model, single-particle hopping between the impurity sites exists in real space

$$\hat{H}_{\text{sp}}^{\text{real}} = -\sum_{i=1}^{N_{\text{imp}}} \mu N_i + \sum_{\sigma} \sum_{\substack{i,j=1 \\ i \neq j}}^{N_{\text{imp}}} t_{i,j} c_{i,\sigma}^{\dagger} c_{j,\sigma}, \tag{6.1.17}$$

with hopping strength

$$t_{i,j} = \frac{1}{N_{\text{imp}}} \sum_{n=1}^{N_{\text{imp}}} \tilde{t}_n e^{-(\vec{R}_i - \vec{R}_j)\vec{K}_n}. \tag{6.1.18}$$

Mathematically, the finite hopping elements originate from the difference of the on-site energies of the impurities in momentum space. If all on-site energies were the same, $\tilde{t}_n = \tilde{t}$, Eq. (6.1.18) would result in a Kronecker delta and the single-particle hopping would vanish $t_{i,j} = \delta_{i,j} t$.
While the Hamiltonian of the non-interacting bath stays unchanged under the transformation of the impurity sites, the form of the coupling Hamiltonian changes significantly

$$\hat{H}^{\text{real}}_{\text{hyb}} = \sum_{l,i,j,\sigma} \tilde{V}_{l,i,j,\sigma} d^{\dagger}_{j,\sigma} c_{l,i,\sigma} + \text{h.c.}, \tag{6.1.19}$$

$$\hat{H}^{\text{real}}_{\text{bath}} = \sum_{l,i,\sigma} \epsilon_{l,i,\sigma} c^{\dagger}_{l,i,\sigma} c_{l,i,\sigma}. \tag{6.1.20}$$

Due to the Fourier transform, each bath site is now coupling with each impurity site with coupling strength

$$\tilde{V}_{l,i,j,\sigma} = \frac{1}{\sqrt{N_{\text{imp}}}} V_{l,i,\sigma} e^{-\vec{R}_j \vec{K}_i}. \tag{6.1.21}$$

This not only creates a complicated impurity system with a lot of single-particle hopping terms between many sites but also results in hybridisations, Green's functions, and self-energies having non-zero off-diagonal elements. Thus, fitting the hybridisation turns into a highly complicated and not well understood mathematical problem. Fortunately, it is always possible to fit the diagonal hybridisation in momentum space and transform the complete Hamiltonian into real space.
After we defined all necessary terms, the whole real-space Hamiltonian can be written as

$$\hat{H}^{\text{real}}_{\text{imp}} = \hat{H}^{\text{real}}_{\text{int}} + \hat{H}^{\text{real}}_{\text{sp}} + \hat{H}^{\text{real}}_{\text{hyb}} + \hat{H}^{\text{real}}_{\text{bath}}. \tag{6.1.22}$$

It is not known beforehand and has to be determined for each model heuristically whether the real-space or momentum-space representation of the DCA Hamiltonian is better suited for a specific problem in terms of entanglement and convergence properties.
However, we now focus on the symmetries present in the Hubbard model regardless of its representation. We want to emphasise that the DMFT Hamiltonian can be seen as a special case of $\hat{H}^{\text{real}}_{\text{imp}}$ with only one impurity $N_{\text{imp}} = 1$ and thus will not be mentioned specifically. Furthermore, the real-space and momentum-space representation of the Hubbard model are connected by a unitary Fourier transformation, which does not change the symmetry properties of the model. Therefore, for simplicity, we will only refer to $\hat{H}^{\text{mom}}_{\text{imp}}$ in the following discussion.

- The full Hamiltonian is clearly conserving the total particle number of the system, which is described by an $U(1)$-symmetry with quantum number $N$ since only pairs of creation and annihilation operators occur in $\hat{H}^{\text{mom}}_{\text{imp}}$.

- The length of the total spin $||\vec{S}||^2$ is also conserved because all pairs of annihilation and creation operators in the Hamiltonian act on electrons with the same spin. This corresponds to an $SU(2)$-symmetry with quantum number $S$ via $||\vec{S}||^2 = S(S+1/2)$.

- The Hubbard model also conserves the total momentum of the whole system. As described in section 5.4, each impurity site and also its corresponding bath sites in momentum-space belong to a patch in the first Brillouin zone. Each of those patches is associated with a representative momentum vector $\vec{K}_i$. Adding or removing a particle from an impurity site or a corresponding bath site will add or remove the associated momentum vector $\vec{K}_i$ from the total momentum of the system. The conservation of the total momentum in the interaction term $\hat{H}_{\text{int}}^{\text{mom}}$ is ensured by the Kronecker delta. Since each bath site only couples via single-particle hopping to a single impurity, it is clear that the whole Hamiltonian $\hat{H}_{\text{imp}}^{\text{mom}}$ conserves the total momentum.
  Due to the choice of the representative vectors in Tab. 5.2, we can describe the total momentum occurring in our multi-site DCA calculations by

$$\vec{K} = (k_x, k_y) = \left(\frac{\pi}{2}n, \frac{\pi}{2}m\right), \tag{6.1.23}$$

  with $n, m \in \mathbb{N}_0$ denoting the necessary two quantum numbers. Because the first Brillouin zone $\{(k_x, k_y)|k_x, k_y \in [-\pi, \pi]\}$ is $2\pi$-periodic, each momentum vector with quantum numbers $n > 3$ or $m > 3$ corresponds to a vector inside the Brillouin zone described by quantum numbers $n, m \in \{0, 1, 2, 3\}$. Thus, the momentum conservation is described by a $\mathbb{Z}_4 \times \mathbb{Z}_4$-symmetry group.
  As an example we will consider a two-site DCA system with $k$ particles on the impurity site and bath sites corresponding to the first patch and $l$ particles on the impurity site and bath sites belonging to the second patch. Then, the total momentum of the system is given by

$$\vec{K} = (k_x, k_y) = k \cdot (0,0) + l \cdot (\pi, \pi) = (l\pi, l\pi) = \begin{cases} (0,0) \text{ for } l \text{ even} \\ (\pi, \pi) \text{ for } l \text{ odd} \end{cases}, \tag{6.1.24}$$

  because of the translational properties of the Brillouin zone. The corresponding quantum numbers are

$$(n, m) = k \cdot (0,0) + l \cdot (2,2) = (2l, 2l) = \begin{cases} (0,0) \text{ for } l \text{ even} \\ (2,2) \text{ for } l \text{ odd} \end{cases}, \tag{6.1.25}$$

  due to the group properties of $\mathbb{Z}_4 \times \mathbb{Z}_4$. Thus, the total momentum of the system can be determined by the quantum numbers. The same is valid, even if more complicated, for four-site and eight-site DCA.
  The number and the choice of the patches, or more specific the choice of the representative vectors, determines which symmetry group can be used to describe the

momentum quantum numbers. In the case of two-site DCA and four-site DCA, all momentum vectors can also be described by $\vec{K} = (k_x, k_y) = (n\pi, m\pi)$ with $n, m \in \mathbb{N}_0$. Then, by the same argumentation as above, the quantum numbers belong to the symmetry group $\mathbb{Z}_2 \times \mathbb{Z}_2$. That both symmetry groups can be used in those cases is not surprising because $\mathbb{Z}_2$ is a subgroup of $\mathbb{Z}_4$. For two-site and four-site DCA not all allowed values for $n$ and $m$ are used when using the $\mathbb{Z}_4 \times \mathbb{Z}_4$ symmetry group, but only the even values, which directly correspond to the subgroup $\mathbb{Z}_2 \times \mathbb{Z}_2$. Similarly, the quantum numbers for eight-site and 16-site DCA with the representative vectors chosen in Tab. 5.2 can only be described by the $\mathbb{Z}_4 \times \mathbb{Z}_4$ symmetry group or by groups that include this symmetry.
In our calculations we limit the ground state search to symmetry sectors with total momentum $\vec{K} = (0, 0)$ since up to now, global ground states were always located in this sector for all parameters choices. This is reasonable since states with a higher total momentum have higher kinetic energies and are, in general, not the ground states of impurity systems.

Our experience with the Hubbard model implies that, in general, the real-space representation of the model generates less entanglement than the momentum-space representation. This results in significantly different runtimes and convergence properties in favour of a real-space description. This difference is even increasing for DCA approximations with a higher number of impurity sites.
Unfortunately, the momentum quantum numbers can not be implemented in real space. A necessary condition for implementing a quantum number is that the change of all quantum numbers of the system has to be well-defined for any application of creation or annihilation operators. This must be clear independently of the state of the rest of the system. In momentum space, adding a particle to an impurity site will increase the total momentum by the associated momentum vector regardless of the rest of the system. A creation operator $d_j^\dagger$ in real space corresponds, via the Fourier transform, to a sum of creation operators acting on all impurity sites in momentum space $\tilde{d}_k^\dagger$. Without having information about the occupation of all other impurity sites in real space, and thus about the occupation in momentum space, it is not clear how the creation operator $d_j^\dagger$ is changing the quantum numbers of the total momentum.
This is problematic because we observed significant convergence problems for higher order DCA calculations when not using momentum quantum numbers. Our DMRG calculation are always initialised with a random state. If a symmetry is not explicitly implemented, it may happen that the starting state of DMRG is located in a part of the Hilbert space that is orthogonal to the ground state. But even if a part of the randomly generated starting state has a non-orthogonal component with respect to the correct ground state, it can happen that DMRG is discarding these parts first few iterations. Both situations prevent DMRG from ever reaching the true ground state. To avoid this, we strongly recommend to use the momentum-space representation of the Hubbard model and implement momentum quantum numbers.

## 6.2 Bath Size

In this section we want to discuss the behaviour of the fitting procedure of the hybridisation and show that only small bath sites are necessary to obtain converged DMFT results with respect to the number of bath sites. If not stated otherwise, presented results are obtained for a system with interaction strength $U = 7t$ and a chemical potential $\mu = -3t$. DMRG was performed with a maximal bond dimension $m = 2000$ and the time evolution with a truncated weight $w = 10^{-9}$. We used the Krylov method for the time evolution until $\tau_c = 4$ and TDVP afterwards until $\tau_{\max} = 100$. The Krylov subspace is considered to be converged if the state $|\psi\rangle(\tau)$ changes by less than $10^{-8}$ when adding an additional Krylov vector. Each calculation is initialised with the hybridisation of the non-interacting system. For DCA calculations we will use the patches defined by Gull et al. shown in Fig. 5.12.

We will focus in this section on DMFT and DCA with four or less patches and discuss the case of eight patches in a later section. The left panel of Fig. 6.1 shows the cost function $\chi$ of the fitting procedure of the hybridisation of the $(0, 0)$ patch for single-site DMFT and multi-site DCA. $\chi$ decays exponentially with the number of bath sites $L_b$ for DMFT as well as for DCA. The cost function approaches a lower bound at a certain bath size, which is approximately around $10^{-8}$. Adding additional sites does not decrease the cost function any further. This is the regime of overfitting, where different optimisations can lead to very similar cost function values but significantly different parameter sets due to the numerous local minima. Typically in this regime, we observe convergence problems of DMFT because the impurity Hamiltonian often changes significantly from iteration to iteration.

When using the same amount of bath sites, we observe better fit results in the case of DCA calculations with more patches than with less. Since for a higher number of patches each patch is getting smaller, the physical quantities like the Green's function or the hybridisation are averaged over smaller areas in the first Brillouin zone. Thus, they include less physics and describe less energy modes. Consequently, a smaller number of effective bath sites is needed to discretise the hybridisation in these patches. This explains why overfitting sets in at different bath sizes for DMFT and DCA and begins at smaller bath sizes for systems with more patches.

We only show results up to $L_b = 7$ for the four-site DCA calculations because the runtimes were too large for $L_b = 8$. While a single iteration of the two-site calculation with $L_b = 12$ takes only two hours, each iteration of the four-site case with $L_b = 8$ is running approximately a day. We believe that this exponential increase in runtimes is caused by the complex Hubbard model interaction. However, the behaviour of the four-site case is qualitatively similar to the two-site case.

The right panel of Fig. 6.1 shows the expectation value of the total filling of the lattice $n$ for DMFT and the DCA calculations. It is obtained by computing and summing up the occupation numbers of all impurity sites and normalising them by the number of patches. We observe very small even-odd oscillations of $n$ with the number of bath sites

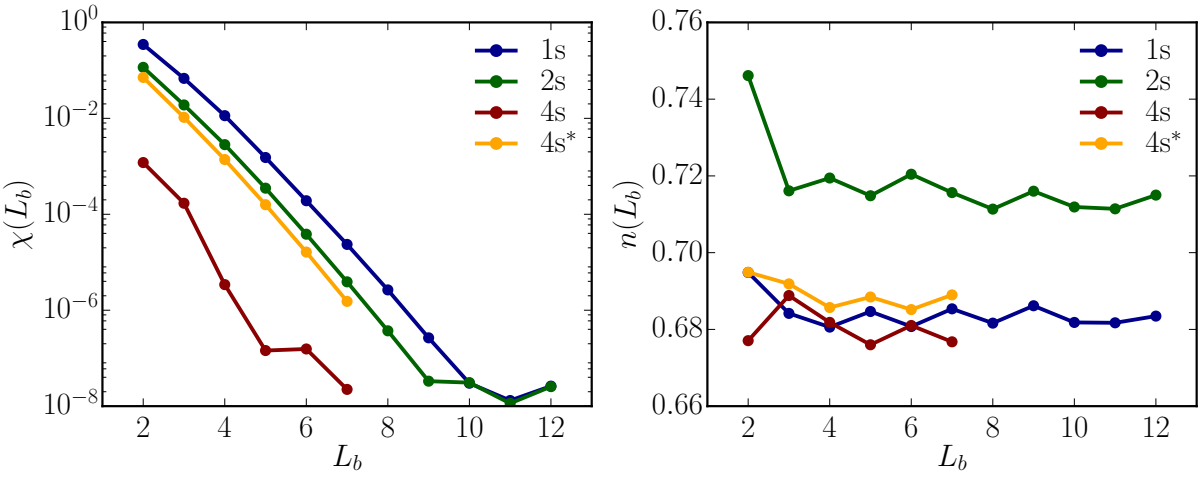


*Figure 6.1: Left panel: Cost function value $\chi$ of the $(0,0)$ patch for different numbers of bath sites $L_b$. We display results for single-site DMFT (1s), two-site DCA (2s) and results obtained with two different four-site patchings (4s and 4s*). $\chi$ decreases exponentially with the number of bath sites. Higher DCA approximations lead to better fit results for the same number of bath sites. In all cases a region of overfitting is reached when the cost function drops to approximately $10^{-8}$. This can not be seen for four-site DCA since we only considered $L_b < 8$ bath sites due to the very long runtimes for bigger bath sizes. Right panel: The converged total filling of the lattice $n$. Small even-odd oscillations can be seen around the converged filling from $L_b = 4$ bath sites on for all cluster sizes. The value of $n$ depends on the number of patches but is located in the same region for all DCA calculations.*

$L_b$ in all cases. Since the Hamiltonian parameters, obtained with the hybridisation fit, vary from iteration to iteration by $10^{-3}$, it is reasonable that occupation values vary on the same scale. This is also the case for calculations with different bath sizes. An even or odd number of bath sites can bias the fit for certain solutions and occupation numbers. However, it is obvious that the filling of the lattice is, in general, already converged for relatively small bath sizes of around four bath sites. This corresponds to cost function values of the order $10^{-3} - 10^{-2}$, which indicates relatively bad fits of the hybridisation. Furthermore, the filling of the lattice is dependent on the number of patches. We will discuss this in more detail when we compare our results with CTQMC.
In Fig. 6.2 the cost function values of all hybridisations in the first and last iteration of single-site DMFT and different multi-site DCA calculations are displayed. In general, the fit results of the later iterations are significantly better. It seems that the non-interacting hybridisation, which is used to initialise DMFT, is a comparable bad choice.
Interestingly, the hybridisations of the distinct patches behave significantly different. Especially the patches located near the $(\pi, \pi)$ patch are, in general, fitted much better than all others when using the same number of bath sites. Since these patches are connected to energetically higher states in the lattice, they are only occupied by a small amount of electrons. This seems to make the interaction with the environment much simpler, which

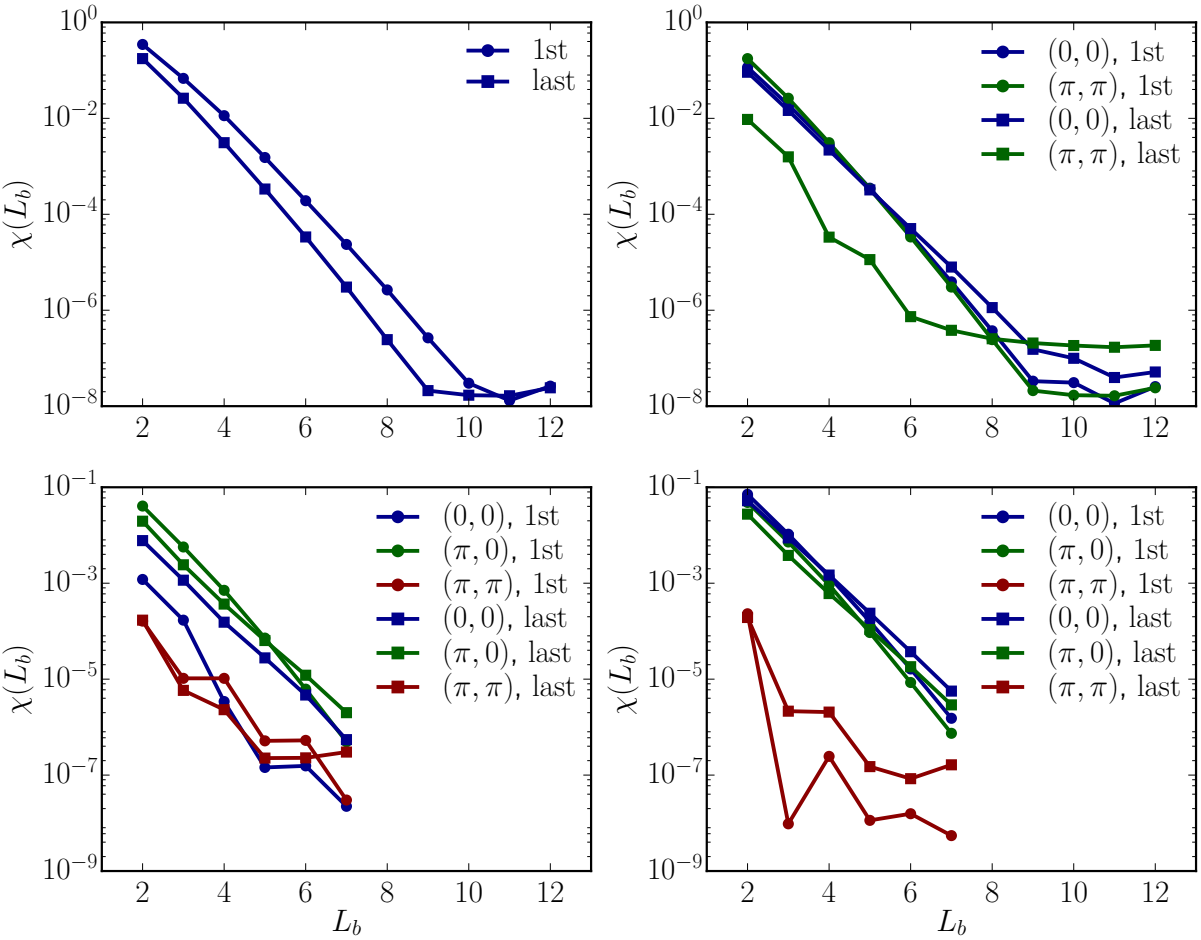


*Figure 6.2: Cost function values of the fits of the hybridisation for all patches in the first (circles) and last iteration (squares) of a single-site DMFT calculation (upper left), two-site DCA calculation (upper right), and four-site DCA calculation with conventional (lower left) and alternative patching (lower right). The qualitative behaviour in all cases is similar. The fit results can differ by up to one order of magnitude between the first and last iteration. In general, the hybridisation of the $(\pi,\pi)$ patch is fitted much better than the other patches for the same number of bath sites.*

is reflected in the small number of bath sites needed for a good description of $\Delta(i\omega_n)$. If only a certain quality of the hybridisation fit is needed, this fact can be used to reduce computation times by attributing different bath sizes to the impurity sites in order to reduce the total system size.

This explanation is supported by the behaviour of the four-site DCA system with alternative patching. The different way of dividing the Brillouin zone changes the filling of the impurity sites and thus the physics the hybridisations have to describe. This clearly changes the behaviour of $\chi(L_b)$, especially for the patch around the $(\pi,\pi)$ point. And indeed, the occupation of the $(\pi,\pi)$ patch is lower for the alternative patching compared

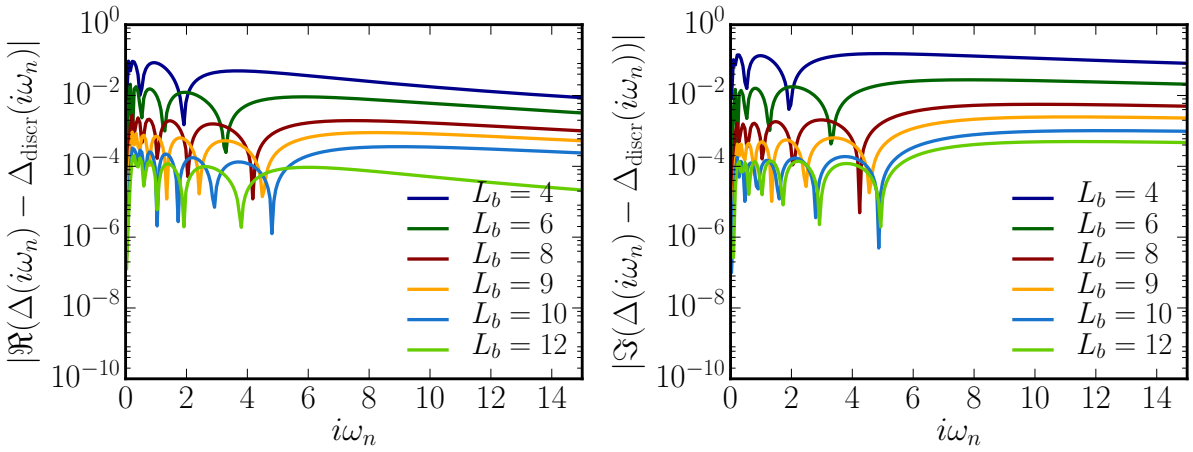


*Figure 6.3: Difference of the real (left) and imaginary (right) part of the hybridisation $\Delta(i\omega_n)$ and its discretisation $\Delta_{discr}(i\omega_n)$ for different numbers of bath sites $L_b$ in the case of single-site DMFT. The hybridisation is fitted better for small frequencies since $\alpha = 1$ in the cost function $\chi$. Because of the limited number of parameters, the fit oscillates around the hybridisation, which can be seen by the kinks in the curves. As already shown in Fig. 6.2, the results for $L_b = 10$ and higher numbers of baths sites are qualitatively similar. This can be seen explicitly for the imaginary part where we either observe no improvements at all or only small ones. Nevertheless, the parameter sets obtained from the fit can differ significantly.*

to the usual one, as can be seen in the following section.
We based our analysis so far only on the cost function values $\chi$. For the sake of completeness, we now want to show the actual differences between a typical hybridisation $\Delta(i\omega_n)$ and its discretised version $\Delta_{\text{discr}}(i\omega_n)$ in Fig. 6.3. Obviously, since we choose $\alpha = 1$ in the cost function (see Eq. (5.3.11)), the fits are in better agreement with the hybridisation for small than for large frequencies. Due to the finite number of parameters and the finite superposition of summands in Eq. (5.3.11), the fits oscillate around $\Delta(i\omega_n)$, which is indicated by the kinks in the plot. These kinks correspond to intersections between the fit and the hybridisation. We see that the real and imaginary parts of the hybridisation are fitted equally well and that the differences between $\Delta(i\omega_n)$ and thew fit are typically of the order $\sqrt{\chi}$.
In agreement to the behaviour of $\chi$, the absolute value of the differences between the hybridisation and its discretised version are staying nearly constant for a high number of bath sites. However, the parameter sets can differ strongly, which can be seen especially well for the results with $L_b = 10$ and $L_b = 12$ where the real parts are remarkably different for the very small difference in the cost function value $\chi$.
To avoid the regime of overfitting and the possible corresponding convergence problems, we choose to use $L_b = 9$ bath sites for single-site DMFT, $L_b = 8$ bath sites for two-site DCA, and $L_b = 5$ for both four-site DCA calculations. With this choice we observe very good fitting results for the first as well as the last iterations of DMFT and DCA. For

all calculations with $\mu = -3$ we observe convergence after six iterations, which results in very fast runtimes ranging from one hour to one day. Of course, this behaviour is strongly influenced by the chemical potential, which not only determines the filling of the lattice and the different patches but is also setting the complexity of the hybridisation, the convergence properties, and whether the system exhibits metallic or insulating behaviour. We will discuss this in more detail in the next sections.
While for single-site and two-site calculations no convergence issues are observed for any choice of $\mu$, for four-site DCA it is strongly recommended to use momentum quantum numbers to achieve convergence over a wide range of values for the chemical potential. Only with the momentum quantum numbers we were able to determine global ground states in each iteration reliably. This is in strong contrast to the single-site and two-site case where global ground states can be found easily and repeatedly even without momentum quantum numbers. Since for higher number of patches the Hamiltonian is getting more complicated and the Hilbert space more fractured into different symmetry sectors, it is comprehensible that DMRG is strongly dependent on the randomly generated starting state if not all symmetries are implemented.

## 6.3 Comparison with CTQMC Results

After we specified the DMFT settings, we can now compare our DMRG+DMFT results with the results from Gull et al.[53] obtained with CTQMC at $\beta t = 20$. This is the check whether our implementation of the model is correct before we focus on regimes where no comparisons are possible as in the case of intermediate interaction strengths. We expect small differences next to the Mott insulating regime due to finite temperature effects but nearly no differences otherwise. We will follow Gull et al. when arguing about the physical behaviour of the Hubbard model and the form of CTQMC or DMRG results.
Fig. 6.4 shows the total filling of the lattice $n$ dependent on the chemical potential $\mu$ for DMFT and DCA with different patches. A filling of $n = 2$ corresponds to doubly occupied lattice sites, $n = 1$ corresponds to half-filling, and $n = 0$ denotes an empty lattice. The CTQMC results show a Mott insulating regime at half-filling with DCA with two or more sites. The spatial correlations taken into account by DCA stabilise the insulating state at interaction strengths smaller than $U = 12t$, which is the onset of the insulating behaviour at half-filling for single-site DMFT[166]. The actual size of the plateau depends not only on the number of patches but also on their form. This can be seen when comparing the results for the different four-site patchings. The two-site, the alternative four-site as well as the eight-site (not displayed), and 16-site DCA (not displayed) all show similar but slightly different sizes of the Mott plateau. We will discuss later why the conventional four-site patching is not able to represent a similar behaviour. Far away from the Mott plateau, both on the hole and electron doped site, all calculations show the same density, and the physical behaviour is well described by single-site DMFT. This indicates no momentum dependence for nearly empty or full systems, which is in

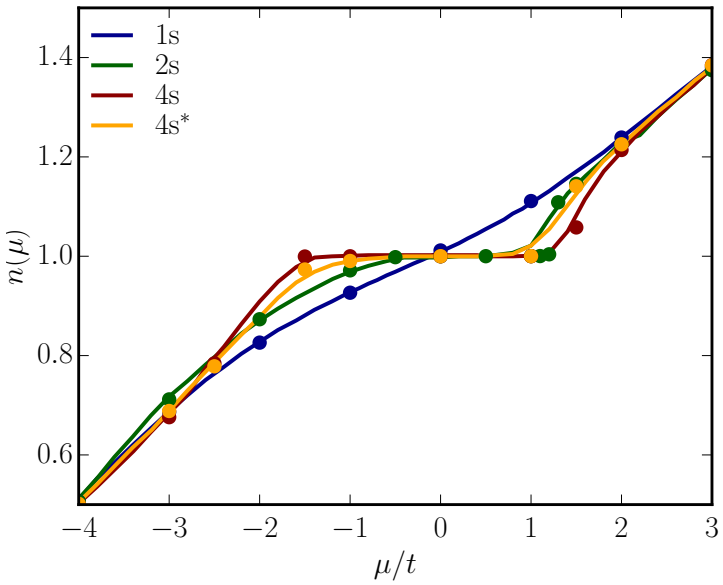


*Figure 6.4: Total electron density n dependent on the chemical potential μ for single-site DMFT and different multi-site DCA calculations. Our DMRG results (dots) are in agreement with the CTQMC results (lines) from Gull et al.[53]. The temperature difference between the two methods explains why DMRG predicts a slightly larger gap in the Mott insulating regime. However, all patch choices show the same behaviour for high electron- and hole-doping and differ close to half-filling dependent on the number of patches.*

agreement with previous studies[9].

Our DMRG results show very good agreement with all CTQMC results. We only see small deviations next to the Mott plateau where DMRG predicts a slightly larger gap. This is reasonable since DMRG produces results at $T = 0$ while the finite temperature in CTQMC causes the onset of metallic behaviour for slightly smaller chemical potentials due to thermal excitations.

Fig. 6.5 and Fig. 6.6 show the partial occupation of the patches $n_k$ as a function of the chemical potential $\mu$ and as a function of the total filling $n$. Our DMRG+DMFT results are, again, in full agreement with the CTQMC results by Gull et al.[53] and show slightly larger gaps in correspondence with the total filling of the lattice. The behaviour of $n_k(n)$ in Fig. 6.6 shows that with the alternative four-site patching the $(\pi, 0)$ sector is incompressible while the other sectors can still be doped. This feature is reproduced for higher cluster DCA calculations with CTQMC and thus can be considered as robust. This physical behaviour is a signature of a sector-selective regime[167], and it is interesting to see that the conventional patching does not exhibit this feature. Gull et al.[53] explain this by the missing possibility to distinguish the nodal and anti-nodal excitations in the conventional patching. The inset of Fig. 6.6 shows clearly that the sector-selective regime is only located on the hole-doped site, which is in agreement with higher cluster CTQMC results.

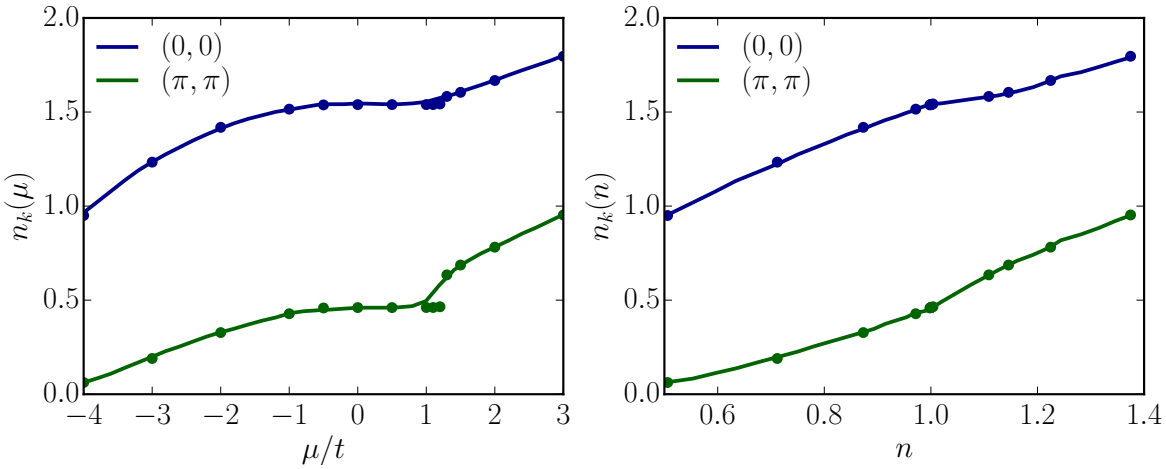


*Figure 6.5: Occupation in the different patches $n_k$ as a function of the chemical potential $\mu$ (left) and the total electron density $n$ (right) for two-site DCA. We observe very good agreement between CTQMC (lines) and DMRG results (dots). Despite the fact that the bands have different fillings, they behave qualitatively similar. The slightly larger gap for DMRG compared to CTQMC observed in Fig. 6.4 can also be seen in the partial occupations.*

While the sector-selective regime is not present in the conventional four-site patching, the region where the $(\pi, 0)$ patch is half-filled is found for both patchings. Gull et al. suggest that the conventional $(\pi, 0)$ patch has to represent the pseudogap behaviour of the $(\pi, 0)$ patch as well as the physics of the gapless nodal quasiparticles located at the Fermi surface. The alternative patching avoids this problem by locating the nodal portion of the Fermi surface in the $(0, 0)$ patch.

Our DMRG+DMFT results are again in excellent agreement with the CTQMC+DMFT results while being computed extraordinarily fast. For the single-site and two-site case we observe convergence in less than ten iterations and runtimes for each iteration of around 15 minutes in the case of single-site DMFT and 40 minutes in the case of two-site DCA while using six cores. Unfortunately, in the four-site calculations the runtime per iteration increases from five to 15 hours. However, convergence is, in general, still observed in less than ten iterations, which results in total runtimes for DMFT of around a day or two with ten cores.

The runtime for the four-site cases can probably be reduced by not using momentum quantum numbers. For the ground state search we observe similar runtimes when using or not using momentum quantum numbers. But for the time evolutions using these additional quantum numbers slows down the computation by roughly a factor of two. However, using these quantum numbers is vital for finding the global ground state reliably, which means they cannot simply be abandoned. Rather, we suggest to determine the global ground state with the help of the momentum quantum numbers. Afterwards, the ground state has to be computed a second time without the quantum numbers in the pre-determined symmetry sector. Unfortunately, this second step can require several

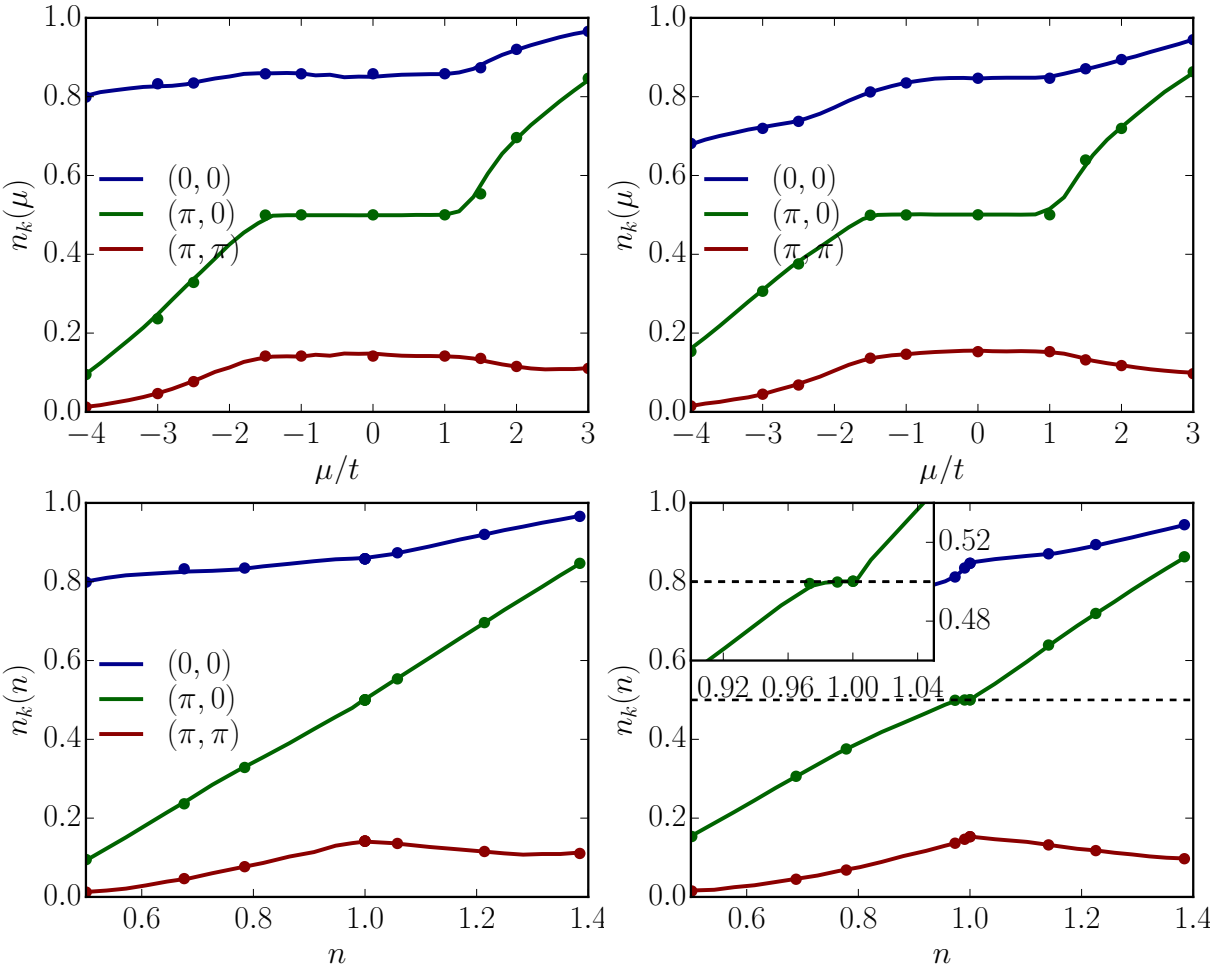


*Figure 6.6: Occupation in the different patches $n_k$ as a function of the chemical potential $\mu$ (upper panels) and the total electron density $n$ (lower panels) for four-site DCA with the conventional (left) and the alternative patching proposed by Gull et al.[53] (right). We observe very good agreement between CTQMC and DMRG results. Most notably, a range of chemical potentials exist where the $(\pi, 0)$ patch is half-filled. The partial occupation $n_k$ as a function of the total density $n$ reveals qualitative differences between the conventional and alternative patching. In the latter, the $(\pi, 0)$ remains at half-filling for a range of densities while the other patches accommodate the electrons. The inset shows the zoomed-in area of the plateau. Using the conventional patching this behaviour is missing.*

attempts due to the previously described convergence problems of the DMRG calculations in multi-site DCA calculations. However, for four-site DCA this should still be a net-win in computation times since a single DMRG run only takes a minute.

We want to mention here that we observed convergence issues for the four-site calculation with standard patching and $\mu = -2$. The issues were neither related to overfitting nor was DMFT oscillating between two solutions. Up to now, we were not able to deduce

what exactly causes the seemingly random behaviour.

## 6.4 DCA with Eight Sites

Several features mentioned in the previous sections, like sector-selective doping and pseudogap behaviour, are only observed for DCA calculations with four or more patches. Since DCA is not a perturbation theory, some features can occur for a certain number of patches and vanish again if the patch number is increased. Thus, it is important to have results for at least eight-site DCA to have an indication if features observed with four patches are robust physical properties of the model or only artefacts due to the DCA description. The development of runtimes from DMFT to multi-site DCA indicates that calculations with eight patches could show dangerously long iteration times mainly caused by very slow time evolutions. A closer investigation shows that we already encounter problems when trying to determine the global ground state. For single-site DMFT with $L_b = 9$, two-site DCA with $L_b = 8$, and both four-site DCA calculations with $L_b = 5$ a bond dimension of $m = 2000$ is enough to ensure very well converged ground state energies with DMRG. But in the case of eight patches with $L_b = 2$ even a bond dimension of $m = 6400$ seems not to be sufficient. The left panel of Fig. 6.7 shows the energy difference $\Delta E = E_m - E_{6400}$ between calculations with different bond dimensions $m$ and a reference calculation with $m = 6400$ states. For eight patches we still observe an energy change of about $10^{-2}$ when increasing the bond dimension from $m = 3200$ to $m = 6400$. This is in strong contrast to single-site and two-site calculations where from $m = 2000$ on, numerically, no differences can be observed. And even in the four-site cases we can only observe small changes below $10^{-7}$ for bond dimensions larger than $m = 2000$. Since $\Delta E(m)$ decays nearly linearly in the semi-logarithmic plot, this indicates that for eight-site DCA at least a bond dimension of $m = 6400$, or an even larger one, is needed to obtain well converged ground state energies.

The sufficiently precise computation of the ground state is very important for the calculation of the Green's function, which is strongly dependent on the ground state energy $E_{GS}$ due to the exponential $e^{-(H-E_{GS})\tau}$. If $E_{GS}$ is not correct by a large margin, the self-energy $\Sigma(i\omega_n) = G_0^{-1}(i\omega_n) - G^{-1}(i\omega_n)$ can behave unphysical or can simply cause convergence problems for DMFT. Because $E_{GS}$ only influences the interacting $G^{-1}(i\omega_n)$, but not the non-interacting Green's function $G_0^{-1}(i\omega_n)$, each imprecision of $E_{GS}$ is directly interpreted by DMFT as an interaction effect. DMFT can exhibit convergence problems since these imprecisions can be different in each iteration.

If symmetries are used during the ground state search, neighbouring symmetry sectors can have ground state energies that lie very close to each other. Dependent on the Hamiltonian parameters, in some models we observed differences between the ground state energies of different sectors of the order of $10^{-3}$. If ground state energies have a large uncertainty due to insufficient bond dimensions, it can happen that a ground state of a wrong symmetry sector is identified as the global ground state. This clearly leads to convergence problems or unphysical behaviour of DMFT.

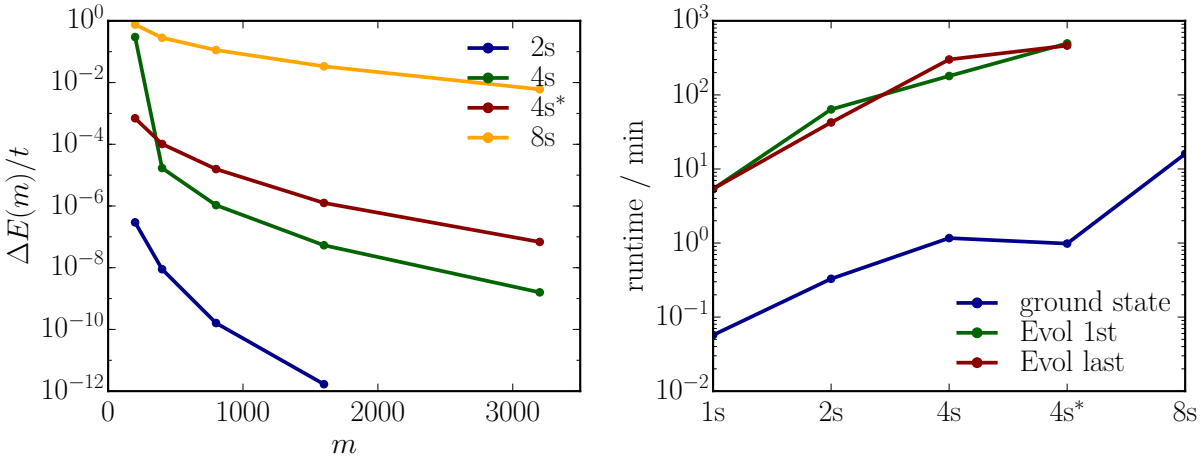


*Figure 6.7: Left panel: Difference* $\Delta E(m) = E_m - E_{6400}$ *between the ground state energy* $E_m$ *obtained with bond dimension* $m$ *and a reference calculation with* $m = 6400$ *for different numbers of patches. For two-site DCA and single-site DMFT, DMRG with a bond dimension of* $m = 2000$ *clearly finds the global ground state up to machine precision (differences around* $10^{-16}$*). For four-site DCA a reasonably good approximation of the ground state can be obtained with* $m = 2000$*. The energy difference to a calculation with* $m = 6400$ *is roughly* $10^{-7}$ *and therefore still small. However, for the eight-site DCA systems the difference between* $m = 2000$ *and* $m = 6400$ *is already* $10^{-2}$*, which definitely will cause problems for DMFT. Right panel: Runtimes for a single ground state search in a single symmetry sector for single-site DMFT and different DCA calculations with* $m = 2000$*. Additionally, the runtime to compute all Green's function components* $G(\tau)$ *in the first and last iteration of DMFT is shown. The numerical effort scales exponentially with the cluster size.*

Further, we also observe a strong dependence of our DMRG results on the initial state used for the ground state search. It is nearly impossible to obtain the same ground state energy in separate calculations with more than two or three digits being equal. Typically, we observe this behaviour if symmetries, which are present in the Hamiltonian, are not implemented in DMRG. So far, we use the $SU(2)$-symmetry of the conserved length of the total spin of the system $||\vec{S}||^2$, the $U(1)$-symmetry of the conserved number of particles $N$, and the $\mathbb{Z}_4 \times \mathbb{Z}_4$-symmetry of the conserved momentum. We doubt that this is the reason for this problem because we cannot find any other symmetries in the model Hamiltonian. It seems that the Hubbard-interaction of eight DCA sites in momentum space (compare Eq. (6.1.12)) is so complicated, that DMRG, in general, has problems to converge to the correct ground state. In fact, the bond dimension of the Hamiltonian itself is $m_{Ham} = 48$, which is quite large compared to typical Hamiltonian dimensions of around ten. This indicates that there are many interactions present.
In most cases, reordering the lattice problem can improve the ground state energies compared to unordered systems with the same bond dimension significantly. In general, this is also the case for this model. However, we do not observe that the reordering improves

the convergence properties. Contrarily, since the optimal order of the lattice is obtained from a DMRG calculation itself, the reordering depends strongly on the convergence of the used DMRG state. Since that is already questionable, the reordering is not very efficient. Moreover, it increases the fluctuations of the obtained ground state energies even more. How to solve these problems is a topic for further research.
Apart from the convergence properties of the ground state search, runtimes are the second biggest problem of eight-site DCA. In the right panel of Fig. 6.7 we compare runtimes for a single ground state calculation as well as for the time needed to compute the complete time evolution of a single DMFT iteration for single-site DMFT and different orders of DCAs. In general, we see that computing the Green's function roughly takes 100-500 times longer than a single DMRG run for all cluster sizes. Unfortunately, for eight-site DCA a single ground state search with $m = 2000$ already runs longer than ten minutes. Putting aside the fact that this bond dimension is probably not large enough, the runtime for the time evolution could increase to one up to three days.
An increase of the bond dimension, which seems utterly necessary, would definitely exceed reasonable computation times for DCA. We also want to emphasise that we only considered the case of $L_b = 2$ bath sites, which is the smallest non-trivial bath size and most probably not enough to describe the hybridisation of this model correctly.
Without significant improvements of the ground state search and time evolution by a better setup of the problem through basis transformations of the Hamiltonian or by a suitable topology change of the MPS, eight-site DCA will not be solvable with DMRG+DMFT.

## 6.5 Intermediate Interaction Strengths

In this last section we want to focus on intermediate interaction strengths. CTQMC has severe problems reaching this regime at low temperatures with large DCA clusters since it is based on an expansion from large or small interaction strengths. From a physical point of view, the region of $U = 9t$ is particularly important since it is believed to be more relevant for systems that exhibit high-temperature superconductivity.
With DMRG as an impurity solver there exist no systematic problems when increasing the interaction strength. It is more important whether an increase of $U$ will increase the entanglement of the system significantly such that calculations will become unfeasible. Fig. 6.8 shows the cumulated runtimes for different numbers of patches and different interaction strengths. We chose chemical potentials $\mu = 2t$, $\mu = 3t$, and $\mu = 4t$ so the filling of the lattice $n$ for the different interactions strengths $U = 7t$, $U = 9t$, and $U = 11t$ is roughly similar (see Fig. 6.9). Thus, we can expect similar physical behaviour of the models and can deduce the influence of $U$ on the runtimes. While for the single-site DMFT calculations we used six cores in parallel, all other calculations were performed with ten cores. For all calculations it can clearly be seen that the choice of $U$ does not influence the runtimes. The small differences in runtimes probably originate from the slightly different fillings. The biggest influence on the runtime of the whole calculation is how many patches are chosen for the system and how they are distributed. It is interesting

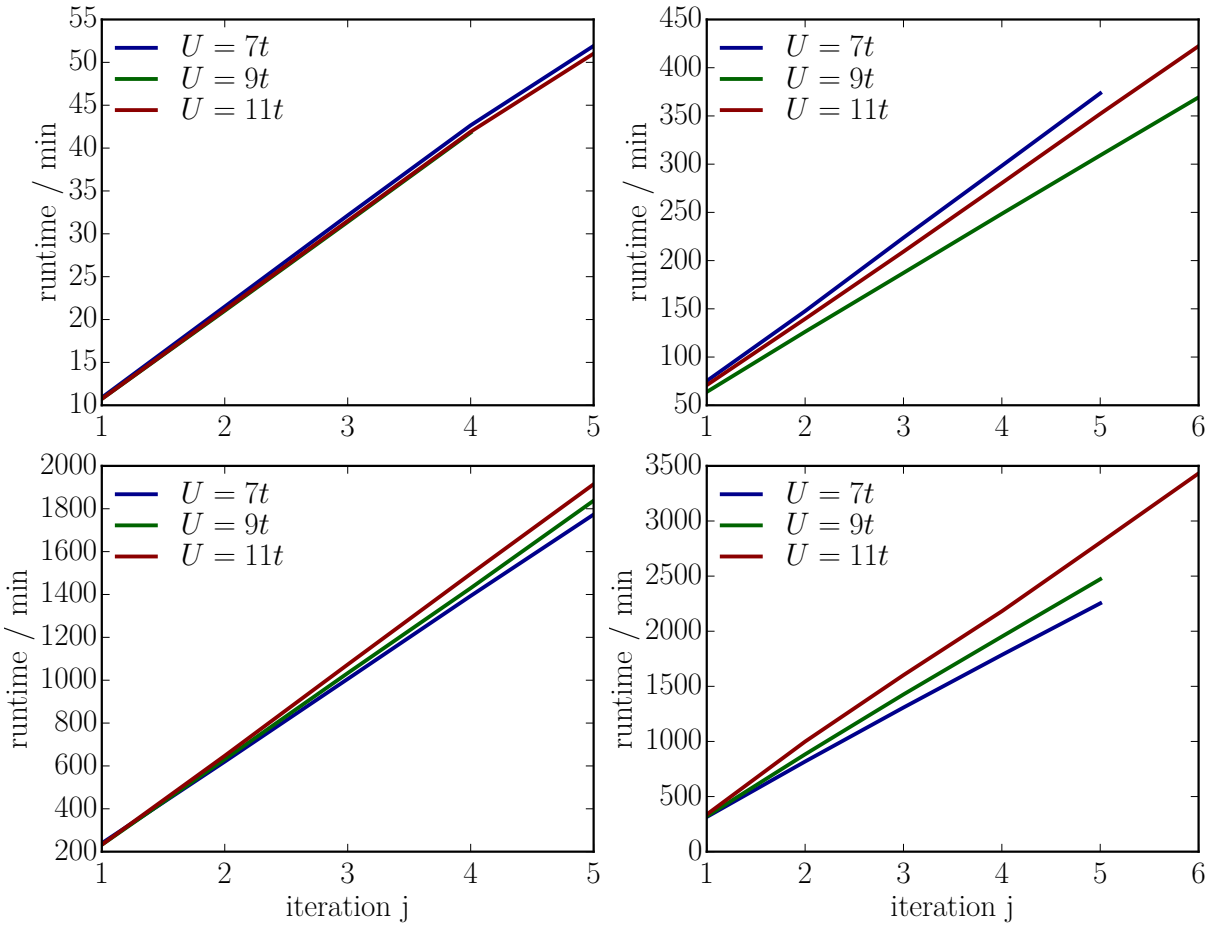


*Figure 6.8: Runtimes cumulated over all DMFT iterations $j$ until convergence for single-site DMFT (upper left), two-site DCA (upper right), four-site DCA with standard patching (lower left) and alternative patching (lower right) for different interaction strengths $U$. We have chosen different chemical potentials $\mu = 2t$, $\mu = 3t$, $\mu = 4t$ for the different interaction strengths $U = 7t$, $U = 9t$, $U = 11t$ such that the filling of the lattice is similar in all cases. Thus, we can expect similar physics and can deduce the influence of $U$ on the runtimes. We see that in all cases the runtimes are quite similar, independently of the interaction strength, and that the number of iterations until convergence is reached is independently of the choice of $U$, too. However, the form and location of the patches influence the runtimes significantly, as the comparison of the different four-site patchings reveals.*

to see that the alternative patching for four-site DCA results in runtimes roughly being 1.5 times longer compared to the standard patching. Also important for the runtime is how many iterations are needed for convergence, which fluctuate at most by a single iteration and seem to be independent of the interaction strength and number of patches, too. Of course, other choices of $\mu$, which correspond to other physical regimes, can change the number of iterations needed for convergence drastically. In the case of four-site DCA with

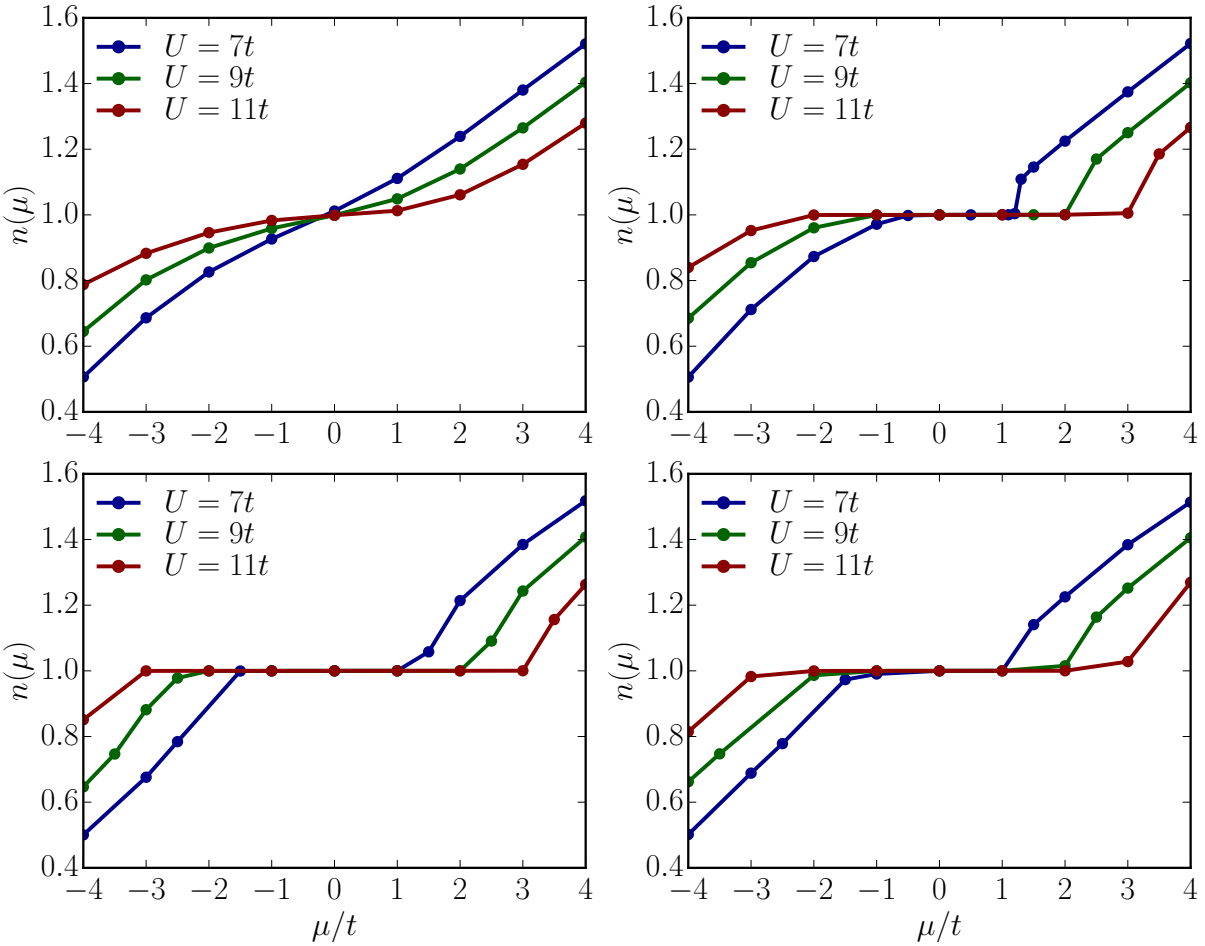


*Figure 6.9: Filling of the lattice $n$ as a function of the chemical potential $\mu$ for different interaction strengths $U$ for single-site DMFT (upper left), two-site DCA (upper right) and four-site DCA with standard (lower left) and alternative patching (lower right). For the single-site case all interaction strengths show a metallic behaviour, but the developing Mott insulator plateau around the half-filled lattice can already be observed. In all DCA calculations the Mott insulating regime is present and grows for larger $U$ both on the hole and the electron-doped site.*

the alternative patching this can lead to runtimes of several days. However, choosing a higher interaction strength does not increase runtimes and numerically requires the same effort as calculations at $U = 7t$, which is quite encouraging for DMRG+DMFT.
Now we can focus on Fig. 6.9, which shows the total filling of the lattice for different interaction strengths and different numbers of patches. In each panel the cluster size is fixed and $U$ is varied. While single-site DMFT obviously is approaching the Mott insulating regime, which sets in at $U = 12t$, in the DCA calculations the Mott insulating regime is already present and grows on the electron-doped as well as on the hole-doped site with an increasing interaction strength.

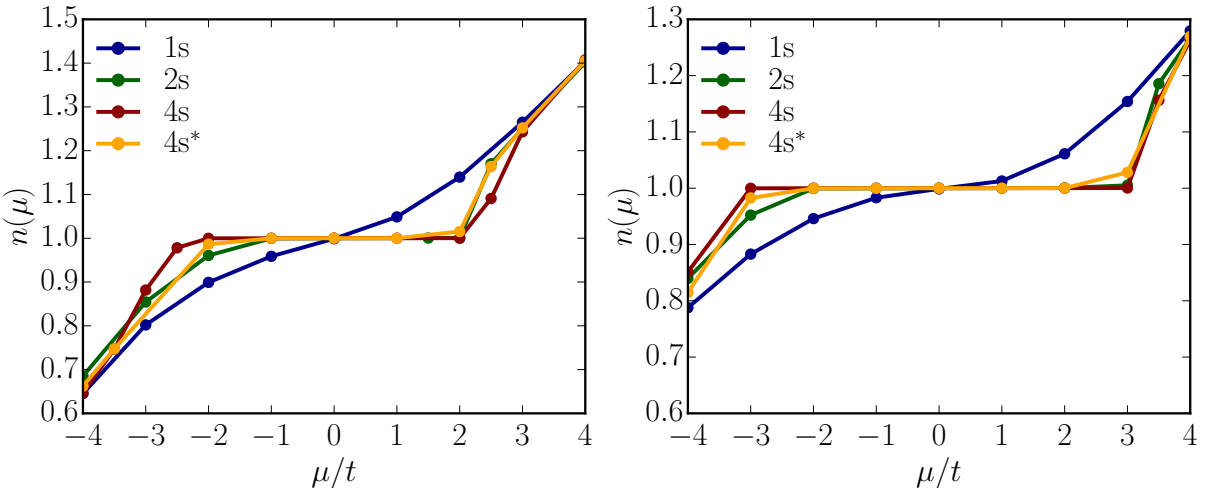


*Figure 6.10: The total filling $n$ dependent on the chemical potential $\mu$ for $U = 9t$ (left) and $U = 11t$ (right) similar to Fig. 6.4 for $U = 7t$. The size of the Mott insulating plateau around half-filling is similar for all multi-site DCA calculations.*

For single-site DMFT and two-site DCA we observe no convergence problems at all. In contrast, in the case of four-site DCA with the conventional patching with $U = 9t$ and $\mu = -3t$, no convergence was possible. This seems to be similar to the $U = 7t$ and $\mu = -2t$ case, which also showed convergence problems and had a similar filling. This suggests that these convergence problems are connected to physical properties in this regime. Further investigation is needed to understand this behaviour and its origin. However, for all other choices convergence was achieved without any problems.
Similar to Fig. 6.4, where CTQMC and DMRG data for $U = 7t$ was shown, Fig. 6.10 compares the lattice filling for $U = 9t$ and $U = 11t$ obtained with different cluster sizes. Thus, it can easily be seen that, similar to $U = 7t$, the DCA calculations agree approximately on the size of the Mott insulating regime. The qualitative behaviour of $n(\mu)$ is the same for all choices of the interaction strength.

## 6.6 Summary

We showed that DMRG+DMFT is able to obtain results at $T = 0$ for the Hubbard model for single-site DMFT, two-site DCA, and four-site DCA. The outcomes are in perfect agreement with the CTQMC results obtained by Gull et al.[53] despite small differences due to finite temperature effects. The total runtime for all calculations is very small and ranges from one hour for single-site DMFT to two days in the case of of four-site DCA, which makes DMRG+DMFT highly competitive with CTQMC.
Furthermore, we showed that the different patches in multi-site DCA not only differ in their physical observables, like the filling of the bands $n_k$, but also show significantly different behaviour during the fitting procedure. The hybridisation of patches that are nearly filled completely or are nearly empty are fitted better than hybridisations of patches that are nearly half-filled, when using the same amount of parameters. In the future, this feature can be used to reduce the numerical effort for multi-site DCA calculations with large clusters by using different bath sizes for different patches. In this context we also discussed overfitting and its influence on convergence properties of DMFT.
While CTQMC is not able to produce results for the Hubbard model with intermediate interaction strengths at sufficiently low temperatures and for high numbers of patches, we were able to show that DMRG+DMFT can easily access this regime. The results obtained in this thesis for intermediate interaction strengths are the first DMFT results for multi-site clusters at $T = 0$. Most notably, they show that runtimes and convergence properties are independent of the interaction strength, which is in strong contrast to the increasing problems CQTMC encounters in this regime.
Unfortunately, with the current implementation it seems that eight-site DCA systems are not treatable with DMRG+DMFT for any kind of interaction strengths. Even the computations of the ground states in the smallest non-trivial system with $L_b = 2$ bath sites are showing convergence problems as well as unreliable und imprecise results, already. At the same time, the runtime of a single DMRG ground state is of the order of ten minutes, which leads to runtimes for a whole DMFT iteration of several days. For these very complex systems it can be worthwhile to use variational ansatzes to determine the optimal basis representation or the most suitable topology of the system. Similar ideas used to reorder systems show a significant effect on runtimes for highly entangled systems. Eight-site DCA calculations are very important in the DCA analysis to evaluate whether properties found in four-site calculations are robust physical features or simply artefacts of the dynamical cluster approximation.
Nevertheless, we showed that DMRG+DMFT can reproduce CTQMC+DMFT results in comparably short times up to four-site DCA and at the same time has access to regimes where CTQMC has severe and systematic problems due to the sign problem. After further progress is made to run eight-site DCA calculations at reasonable times, the low-temperature physics of the Hubbard model with intermediate interaction strengths can immediately be investigated with respect to momentum properties in the context of DMFT.

# Chapter 7

# A Real Material Study: $Sr_2VO_4$

Many transition metal oxides are believed to undergo a Mott metal-insulator transition [168] as chemical composition, temperature or pressure is changed. This is especially important since it is believed that strong electron-electron correlations near these Mott insulating regimes give rise to interesting physical phenomena like high transition-temperature superconductivity, high Curie-temperature magnetism or electric-field driven metal-insulator transitions [11]. Therefore, it is very important, from a theoretical and practical point of view, to understand the physics of the Mott insulating regimes in order to to predict which material compounds exhibit desired correlated electron effects.
We will focus in this chapter on the layered perovskite $Sr_2VO_4$. They belong to the family of compounds $Sr_{n+1}V_nO_{3n+1}$, which share a fixed number of electrons. In the opposite limits for the configuration number $n$ one obtains the material $Sr_2VO_4$ (for $n = 1$), which is experimentally measured to be a small gap correlation-driven insulator [54], and the compound $SrVO_3$ (for $n = \infty$), which is experimentally measured to be a moderately correlated metal [169]. DFT+DMFT calculations based on the Hubbard-Kanamori Hamiltonian though yield metallic solutions in both cases for any reasonable choice of electron-electron interaction strengths.
Single-site DMFT overestimates the true value of the critical interaction for the Mott metal-insulator transition in many effectively two-dimensional materials by about a factor of two [55]. This, for example, also happens for $LaTiO_3$ and $LaVO_3$ [170]. Therefore, *Ab initio* predictions for the early transition metal oxides, in general, are known to be difficult [55].
In 2015, Wolf et al. [129] showed that DMRG as an imaginary time impurity solver for DMFT in the case of a completely degenerate three-band model with the Hubbard-Kanamori Hamiltonian produces very good results compared to CTQMC in very short computation times. In agreement with previous calculations, DMFT produces a metallic solution for small values of the interaction strength $U$ and a Mott insulating phase for higher $U$. Additional calculations with a two-site dynamical cluster approximation result in a Mott metal-insulator transition at much lower interaction strength than with single-site DMFT. Wolf et al. proposed that a similar effect could also be observed in the real

$Sr_2VO_4$ material, which would lead to better agreement between experiment and theory. Since $Sr_2VO_4$ is described by an effective three-band model with Hubbard-Kanamori interaction, a two-site DCA approach results in six impurity sites with a complicated interaction Hamiltonian. At low temperature, these kind of models are problematic for nearly all impurity solvers out of various reasons. Since each impurity comes with its own bath, the system size is too large for ED. Even after recent improvements[18], six impurity sites still provide an insurmountable problem for NRG while for CTQMC the sign problem prevents solutions at low enough temperatures. After the first promising test by Wolf et al., DMRG seems to be the candidate of choice due to its fast performance and quantitative good results compared to CTQMC for three-band models with two-site DCA.
However, the step from a purely theoretical model that has completely degenerate bands and a simply dispersion relation only including nearest-neighbour interaction to a real material study is challenging. The entanglement properties, the behaviour of the model with respect to quantum numbers and convergence properties of DMFT change dramatically if the band degeneracy is partly broken and if an approximation of a real dispersion relation is used. This leads to a significantly higher computational effort than expected from the initial tests made by Wolf et al.. Several of the improvements introduced in this thesis were necessary to obtain results for two-site DCA calculations of $Sr_2VO_4$.
To understand this behaviour we want to discuss the Hubbard-Kanamori Hamiltonian for $Sr_2VO_4$ and the symmetries being present in single-site DMFT and two-site DCA in the beginning of this chapter. Afterwards, we will show results obtained with single-site DMFT for the dependence of the lattice filling on the chemical potential and interaction strength. This allows to identify the onset of Mott-insulating behaviour for $Sr_2VO_4$. Finally, we will present DCA results and show that reintroducing non-local interactions via two-site DCA does not change the critical interaction strength significantly.

## 7.1 The Hubbard-Kanamori Hamiltonian

In this section, we want to discuss the model Hamiltonian used to describe the three-dimensional material $Sr_2VO_4$ in the thermodynamic limit of having an infinitely large lattice. The first thing we notice from DFT calculations is that the material is built up of two dimensional layers that are interacting very weakly with each other. This is also reflected in the band structure being effectively two-dimensional and having no $k_z$-dependence. Thus, we can focus on describing the physics of the two dimensional layers, which will result in a reasonable good description of the three-dimensional compound $Sr_2VO_4$.
Vanadium (denoted with the chemical symbol V) is a transition element with 23 electrons in total. The outermost occupied orbitals of Vanadium are the 4s and 3d orbitals. Since they are only partly occupied, they are the most important ones for defining the electronic properties in every chemical compound. Thus, we only have to consider the two electrons located in the 4s orbital and the three electrons located in the 3d orbitals. In the layered

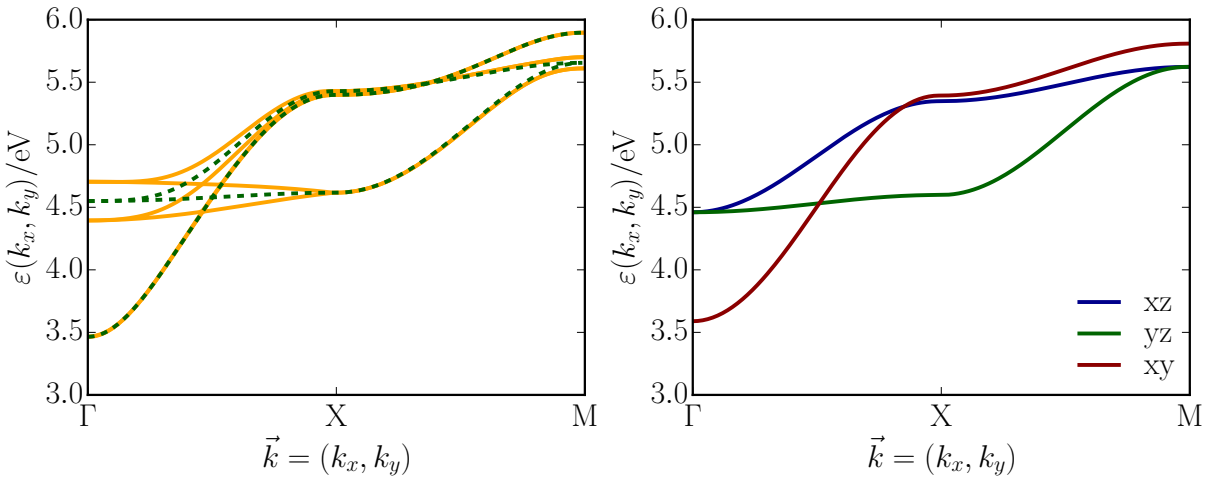


*Figure 7.1: Left panel: Dispersion relation $\varepsilon(k_x, k_y)$ for $Sr_2VO_4$ along the direct path from Γ to X and finally to M in the 1st Brillouin zone obtained from density functional theory calculations (yellow lines)[171]. As described in the text, the interaction between different two-dimensional layers in z-direction is neglected. This reduces the dispersion relation to be essentially $k_z$-independent. Neglecting the very weak coupling between the Strontium atoms will allow to describe the problem with only three-bands. The corresponding band structure is plotted with green dashed lines. Right panel: Dispersion relation obtained when only taking nearest and next-nearest neighbour interaction into account. We see very good agreement with the full dispersion relation, i.e. with the green dashed lines of the left panel. This will also cause the bands xz and yz to be degenerate.*

perovskite $Sr_2VO_4$, Vanadium is forming a chemical compound together with the Oxygen (O) and Strontium atoms (Sr). The oxygen atoms have a very high negativity and will fill their shells with the four electrons of the Strontium atoms and with four electrons from the Vanadium atom. Consequently, only one electron will remain in the five bands of Vanadium. Since in our compound the outer lying orbitals 4s have more overlap with the electron orbitals of the neighbouring atoms, their energy is increased with respect to the inner lying 3d orbitals. Thus, the properties of $Sr_2VO_4$ can be described pretty well by only considering the three energetically lower lying 3d orbitals.
Furthermore, DFT predicts the strength of the coupling terms between the Strontium atoms to be smaller than 0.03eV, which is, compared to the interaction strengths present for $Sr_2VO_4$, very small. Neglecting them reduces the six-band problem to a much simpler three-band problem, which lowers computations times dramatically. This affects the band structure of the model as illustrated in the left panel of Fig. 7.1. Therein, the full band structure of the six-band problem (solid lines) is compared to the band structure that emerges from the decoupled three-band problem (dashed lines) in the first Brillouin zone next to some high symmetry points. The strongest differences can be observed close to the Γ-point but overall the differences are very small or non-existing. Thus, neglecting the coupling between the Strontium atoms still allows to describe the behaviour of $Sr_2VO_4$

reasonably well.
The orbitals of each lattice site have a finite overlap with the orbitals of sites that are nearest neighbours, next-nearest neighbours, or with sites that are located even farther away. Sometimes, finite overlaps can be obtained with twenty or more different lattice sites. These overlaps define the single-particle hopping elements of the lattice model and when Fourier transformed, they give rise to the band structure displayed in Fig. 7.1. The model can be further simplified by only taking into account on-site energies and nearest as well as next-nearest neighbour hopping terms. The resulting band structure for this case is plotted in the right panel of Fig. 7.1 and has very good agreement with the full three-band model. This simplification reduces the numerical effort for DMFT and DCA calculations further while having no significant effect on the physical quantities we will compute.
The actual mathematical form of the single-particle Hamiltonian $\hat{H}_{\text{kin}}$ and the interaction Hamiltonian $\hat{H}_{\text{int}}$ depends on the type of functions that are chosen to describe the orbitals. Because of the geometrical structure of the unit cell of $Sr_2VO_4$, which is slightly distorted, the cubic harmonics reflect the symmetry of the problem best and are well suited to describe the 3d orbitals of $Sr_2VO_4$ in an efficient way. Since the three orbitals of Vanadium are described by the cubic harmonics labeled with xz, yz and xy, we will also label the bands of our lattice problem accordingly. At this point we want to introduce the creation $d_\alpha^\dagger$ and annihilation operators $d_\alpha$ of an electron in orbital $\alpha \in [\text{xz},\ \text{yz},\ \text{xy}]$. By grouping them into vectors $\vec{d} = (d_{\text{xz}}\ d_{\text{yz}}\ d_{\text{xy}})^T$ and $\vec{d}^\dagger = (d_{\text{xz}}^\dagger\ d_{\text{yz}}^\dagger\ d_{\text{xy}}^\dagger)$, the single-particle Hamiltonian can be defined as $\hat{H}_{\text{kin}} = \vec{d}^\dagger H_{\text{kin}} \vec{d}$, with $H_{\text{kin}}$ being a $3 \times 3$ matrix

$$H_{\text{kin}} = \begin{pmatrix} \varepsilon_{\text{xz}}(k_x, k_y) & \sim 0 & 0 \\ \sim 0 & \varepsilon_{\text{yz}}(k_x, k_y) & 0 \\ 0 & 0 & \varepsilon_{\text{xy}}(k_x, k_y) \end{pmatrix}, \tag{7.1.1}$$

and

$$\varepsilon_\alpha(k_x, k_y) = \bar{\varepsilon}_\alpha + 2t_{\alpha,1x}\cos(k_x) + 2t_{\alpha,1y}\cos(k_x) + 4t_{\alpha,2}\cos(k_x)\cos(k_y), \tag{7.1.2}$$

the dispersion relation of band $\alpha$. Because of the spatial structure of the material, the bands xz and yz are degenerate. We neglect the coupling between those two bands, i.e. the off-diagonal terms in $H_{\text{kin}}$ indicated with $\sim 0$, since it is of the order $\mathcal{O}(10^{-3})$eV, which is smaller by at least an order of magnitude than the values for the nearest neighbour hoppings $t_{\text{xz},1x} = t_{\text{yz},1y} = -0.24$eV, $t_{\text{xz},1y} = t_{\text{yz},1x} = -0.05$eV, $t_{\text{xy},1x} = t_{\text{xy},1y} = -0.28$eV and for the next-nearest neighbour hoppings $t_{\text{xz},2} = t_{\text{yz},2} = 0.01$eV, $t_{\text{xy},2} = -0.09$eV. The average energy of the bands is given by $\bar{\varepsilon}_{\text{xz}} = \bar{\varepsilon}_{\text{yz}} = 5.01$eV and $\bar{\varepsilon}_{\text{xy}} = 5.05$eV. All values have been rounded to two digits.
In the case of single-site DMFT, only a single site is taken out of the infinitely large lattice and used as the impurity of an auxiliary problem, which has to be solved self-consistently. Thus, the single-particle Hamiltonian

$$\hat{H}_{\text{sp}} = -\sum_{\alpha,\sigma}(\mu - \bar{\varepsilon}_\alpha)\hat{n}_{\alpha,\sigma}, \tag{7.1.3}$$

simply consists of the on-site energies $\bar{\varepsilon}_\alpha$, which are resulting from the dispersion relation Eq. (7.1.2) and determine the average energy of each orbital. These energies are shifted by the chemical potential $\mu$, which can be used to control the number of electrons in the lattice. $\hat{n}_{\alpha,\sigma} = d^\dagger_{\alpha,\sigma} d_{\alpha,\sigma}$ denotes the occupation number operator for electrons with spin $\sigma$ in orbital $\alpha$.
The interactions in the layered perovskite $Sr_2VO_4$ are well described with the three-band Hubbard-Kanamori model, which is defined as

$$\begin{aligned}\hat{H}_{\text{int}} = &\sum_\alpha U \hat{n}_{\alpha,\uparrow}\hat{n}_{\alpha,\downarrow} + \sum_{\alpha>\beta} [U'\hat{n}_{\alpha,\sigma}\hat{n}_{\beta,-\sigma} + (U'-J)\hat{n}_{\alpha,\sigma}\hat{n}_{\beta,\sigma}] \\ &- \sum_{\alpha\neq\beta} J(d^\dagger_{\alpha,\downarrow} d^\dagger_{\beta,\uparrow} d_{\beta,\downarrow} d_{\alpha,\uparrow} + d^\dagger_{\beta,\uparrow} d^\dagger_{\beta,\downarrow} d_{\alpha,\uparrow} d_{\alpha,\downarrow} + \text{h.c.}),\end{aligned} \tag{7.1.4}$$

where $J$ denotes the interaction strength for the Hund's coupling and pair-hopping terms, $U$ determines the strength of the intra-orbital and $U'$ the strength of the inter-orbital Coulomb interaction. $\alpha$ and $\beta$ are indices running over the three band labels. We will adopt the conventional choice of $U' = U - 2J$, which follows from symmetry considerations for the d-orbitals in free space and also holds, at least for reasonably symmetric situations, for solids[172]. The local state space of each impurity site consists of four states, namely being empty, having a single electron with spin-up or spin-down, or being doubly occupied. The interaction Hamiltonian can be written in a more compact form if we define the total number of particles $\hat{N}$, the total spin $\vec{S}$ and the orbital isospin $\vec{L}_\alpha$

$$\hat{N} = \sum_{\alpha\sigma} \hat{n}_{\alpha\sigma}, \tag{7.1.5}$$

$$\vec{S} = \frac{1}{2} \sum_\alpha \sum_{\sigma\sigma'} d^\dagger_{\alpha\sigma} \vec{\tau}_{\sigma\sigma'} d_{\alpha\sigma'}, \tag{7.1.6}$$

$$\hat{L}_\alpha = i \sum_{\beta,\gamma} \sum_\sigma \epsilon_{\alpha\beta\gamma} d^\dagger_{\beta\sigma} d_{\gamma,\sigma}. \tag{7.1.7}$$

$\epsilon_{\alpha\beta\gamma}$ is denoting the Levi-Civita-symbol and $\vec{\tau}_{\sigma\sigma'}$ the Pauli matrices. With these definitions the Hamiltonian can be rewritten as

$$\hat{H}_{\text{int}} = (U-3J)\frac{\hat{N}(\hat{N}-1)}{2} - 2J\vec{S}^2 - \frac{1}{2}J\vec{L}^2 + \frac{5}{2}J\hat{N}. \tag{7.1.8}$$

The impurity problem is completed by introducing a non-interacting bath describing the rest of the infinitely large lattice that is coupled to the impurity sites. Since no single-particle hopping exists between the impurity sites describing the orbitals, each impurity site is only coupled with its own non-interacting bath

$$\hat{H}_{\text{hyb}} = \sum_{l,\alpha,\sigma} V_{l,\alpha,\sigma} d^\dagger_{\alpha,\sigma} c_{l,\alpha,\sigma} + \text{h.c.}, \tag{7.1.9}$$

$$\hat{H}_{\text{bath}} = \sum_{l,\alpha,\sigma} \epsilon_{l,\alpha,\sigma} c^\dagger_{l,\alpha,\sigma} c_{l,\alpha,\sigma}, \tag{7.1.10}$$

where $c^\dagger_{l,\alpha,\sigma}$ creates a fermion on the bath site $l$ associated with impurity $\alpha$, $V_{l,\alpha,\sigma}$ describes the coupling strength of the bath site $l$ with the corresponding impurity $\alpha$ and $\epsilon_{l,\alpha,\sigma}$ is the on-site energy of the bath site $l$. This is similar to the multi-site DCA calculations of the Hubbard model and is reflected in diagonal hybridisations, self-energies, and Green's functions. As described chapter 5 about DMFT, the on-site energies and coupling elements are obtained via independent fits of the diagonal elements of the hybridisation. The complete impurity Hamiltonian $\hat{H}_{\text{imp}}$, used for all following single-site DMFT calculations, is the sum of all previous Hamiltonian terms

$$\hat{H}_{\text{imp}} = \hat{H}_{\text{int}} + \hat{H}_{\text{sp}} + \hat{H}_{\text{hyb}} + \hat{H}_{\text{bath}}. \tag{7.1.11}$$

This Hamiltonian exhibits several symmetries:

- In Eq. (7.1.4) it is easy to see that $H_{int}$ conserves the total number of particles $N$ since it consists only of density operators $\hat{n}$, pair-hopping, and spin-flip terms. Also $\hat{H}_{\text{hyb}}$ and $\hat{H}_{\text{bath}}$ conserve the total particle number, trivially. This $U(1)$-symmetry is described by the quantum number $N \in \mathbb{N}_0$ with a maximum of two times the lattice sites. The corresponding operator $\hat{N}_{\text{total}}$ measuring $N$ is

  $$\hat{N}_{total} = \sum_{j,\sigma} \hat{n}_{j,\sigma}, \tag{7.1.12}$$

  where $j$ runs over all sites of the impurity problem.

- At the same time, the $z$-component of the total spin $\vec{S}$ is conserved. Hopping terms conserve this quantity clearly. The spin-flip terms in $H_{\text{int}}$ always flip the spin of two particles in different bands in the opposite direction and thus conserving the z-component. We denote the corresponding quantum number to this $U(1)$-symmetry with $S_z \in [-S, S]$, where $S$ is the quantum number denoting the total spin $||\vec{S}||^2 = S(S+1)$. We can measure $S_z$ with

  $$\hat{S}_{z,total} = \frac{1}{2}\sum_j (\hat{n}_{j,\uparrow} - \hat{n}_{j,\downarrow}). \tag{7.1.13}$$

- It can also be shown that the Hubbard-Kanamori Hamiltonian not only conserves the z-component but also the length of the total spin $||\vec{S}||^2$. This corresponds to a $SU(2)$-symmetry described by the quantum number $S = \frac{1}{2}n$ with $n \in \mathbb{N}_0$ via $||\vec{S}||^2 = S(S+1)$. It is preferable to use the $SU(2)$-symmetry rather than the $U(1)$-symmetry because bond dimensions and computation times can be reduced significantly. The total spin operator $\vec{S}^2$ is defined as $\vec{S}^2 = \sum_j \vec{S}_j^2$ with

  $$\vec{S}_j^2 = \frac{1}{2}\sum_{\sigma\sigma'} d^\dagger_{j,\sigma} \vec{\tau}_{\sigma\sigma'} d_{j,\sigma'}, \tag{7.1.14}$$

  as in Eq. (7.1.6) with the difference that now all sites $j$ of the lattice are included.

- Additionally, the total angular momentum $||\vec{L}||^2 = L(L+1)$ with $L \in \mathbb{N}_0$ is conserved by $H_{\text{int}}$. Unfortunately, we cannot use the $SO(3)$-symmetry of the conserved total angular momentum, since it is not defined locally. Note that we need a clearly defined change of all implemented quantum numbers if we apply a single creation or annihilation operator on any site of the lattice independent of the state of the other sites. On top, since the symmetry is not defined locally on the impurity sites, the introduction of bath sites makes an implementation impossible. Electrons can move into the bath and therefore reduce the angular momentum on the impurity sites but at the same time it is not clear how they should increase $L$ on the non-interacting bath sites. We cannot even write down an operator that can measure $||L||^2$ in the whole system.

- A single impurity with its associated bath sites describes a single band of the system. The interaction between the different bands takes place only on the impurity sites via density terms (i.e. the first four terms of Eq. (7.1.4)), pair spin-flip, and two-particle hoppings of $H_{\text{int}}$. There is no single-particle hopping present. Thus, the parity of the number of particles in each band is conserved. In total, this is a $\mathbb{Z}_2 \times \mathbb{Z}_2 \times \mathbb{Z}_2$ symmetry since the parity for each of the three bands has to be fixed with a single quantum number. The operator measuring the parity $\hat{P}_\alpha$ of the band $\alpha$ can be defined as

$$\hat{P}_\alpha = \sum_{j,\sigma} \hat{n}_{j,\sigma} \mod 2, \tag{7.1.15}$$

  with $j$ belonging to the band $\alpha$. A zero indicates an even number while a one indicates an odd number of particles in the band. We will refer to the three combined symmetries as the band parity of the system.

It is highly recommended to use all quantum numbers that can be implemented for the following DMFT calculations, not just to reduce the numerical effort of the computations but also to improve convergence properties of the ground state search. Especially the band symmetry ensures that global ground states can be found reliably. This is similar to the four-site DCA calculations of the Hubbard model, where using the momentum quantum numbers is vital for determining the global ground states in each iteration.
After we discussed the Hamiltonian for DMFT calculations of $Sr_2VO_4$ in detail, we now want to focus on the two-site DCA case. As in chapter 6, we introduce two patches $P_{\vec{K}_i}$ in the first Brillouin zone with representative momentum vectors $\vec{K}_0 = (k_x, k_y) = (0,0)$ and $\vec{K}_1 = (k_x, k_y) = (\pi, \pi)$ for each patch, respectively. The patches are defined as in Fig. 5.12 and are each represented by a single impurity site. Since the Brillouin zone is separated for each band, we end up with six impurity sites. From now on, we will label the impurities with $K, \alpha$, where $\alpha$ denotes the band and $K = 0$ and $K = 1$ the patches $\vec{K} = (0,0)$ and $\vec{K} = (\pi, \pi)$, respectively. We will also denote all operators acting in momentum space with a tilde to make the notation more clear. With the same reasoning

as during the derivation of the Hubbard model Hamiltonian for multi-site DCA, we obtain the single-particle Hamiltonian

$$\hat{H}_{\text{sp}}^{\text{mom}} = -\sum_{K,\alpha,\sigma} (\mu - \bar{\varepsilon}_\alpha + \tilde{t}_{K,\alpha}) \tilde{n}_{K,\alpha,\sigma}, \tag{7.1.16}$$

in momentum space with

$$\tilde{t}_{K,\alpha} = \sum_{\vec{k} \in P_K} \varepsilon_{\vec{k},\alpha}, \tag{7.1.17}$$

denoting the shift of the chemical potential that ensures the correct high-frequency behaviour of the Green's functions. In momentum space the hybridisation is completely diagonal and each impurity site couples only to its own non-interacting bath. Thus, we can write the Hamiltonians describing the non-interacting baths and the coupling between impurity sites and bath sites as

$$\hat{H}_{\text{bath}}^{\text{mom}} = \sum_{l,K,\alpha,\sigma} \epsilon_{l,K,\alpha,\sigma} c^\dagger_{l,K,\alpha,\sigma} c_{l,K,\alpha,\sigma}, \tag{7.1.18}$$

$$\hat{H}_{\text{hyb}}^{\text{mom}} = \sum_{l,K,\alpha,\sigma} V_{l,K,\alpha,\sigma} \tilde{d}^\dagger_{K,\alpha,\sigma} c_{l,K,\alpha,\sigma} + \text{h.c.}. \tag{7.1.19}$$

In the real-space representation of multi-site DCA the usual Hubbard-Kanamori interaction $\hat{H}_{\text{int}}$ is present on each site since the momentum patches are chosen such that they all have the same weight. The momentum-space representation of the interaction Hamiltonian is obtained via a Fourier transform of the impurity sites according to the definitions in Eq. (5.4.12), Eq. (5.4.13) and Tab. 5.2. Written out, the transformations are defined as

$$d^\dagger_{0,\alpha,\sigma} = \frac{1}{\sqrt{2}} (\tilde{d}^\dagger_{0,\alpha,\sigma} + \tilde{d}^\dagger_{1,\alpha,\sigma}), \tag{7.1.20}$$

$$d^\dagger_{1,\alpha,\sigma} = \frac{1}{\sqrt{2}} (\tilde{d}^\dagger_{0,\alpha,\sigma} - \tilde{d}^\dagger_{1,\alpha,\sigma}). \tag{7.1.21}$$

We will not present the exact form of the interaction Hamiltonian in momentum space $\hat{H}_{\text{int}}^{\text{mom}}$ since it will be highly complicated and will not provide any new insights. However, the whole real-space Hamiltonian for two-site DCA is given by the sum

$$\hat{H}_{\text{imp}}^{\text{mom}} = \hat{H}_{\text{int}}^{\text{mom}} + \hat{H}_{\text{sp}}^{\text{mom}} + \hat{H}_{\text{hyb}}^{\text{mom}} + \hat{H}_{\text{bath}}^{\text{mom}}. \tag{7.1.22}$$

As already mentioned, the real-space representation of the interaction Hamiltonian is simply $\hat{H}_{\text{int}}$ acting on both real-space sites

$$\begin{aligned} \hat{H}_{\text{int}}^{\text{real}} = &\sum_{K,\alpha} U \hat{n}_{K,\alpha,\uparrow} \hat{n}_{K,\alpha,\downarrow} + \sum_{K,\alpha>\beta} [(U-2J) \hat{n}_{K,\alpha,\sigma} \hat{n}_{K,\beta,-\sigma} + (U-3J) \hat{n}_{K,\alpha,\sigma} \hat{n}_{K,\beta,\sigma}] \\ &- \sum_{K,\alpha\neq\beta} J (d^\dagger_{K,\alpha,\downarrow} d^\dagger_{K,\beta,\uparrow} d_{K,\beta,\downarrow} d_{K,\alpha,\downarrow} + d^\dagger_{K,\beta,\uparrow} d^\dagger_{K,\beta,\downarrow} d_{K,\alpha,\uparrow} d_{K,\alpha,\downarrow} + \text{h.c.}). \end{aligned} \tag{7.1.23}$$

The single-particle Hamiltonian Fourier transformed into real space features a hopping term between the impurity sites

$$\hat{H}_{\text{sp}}^{\text{real}} = -\sum_{K,\alpha,\sigma} (\mu - \bar{\varepsilon}_\alpha)\hat{n}_{K,\alpha,\sigma} + \sum_{K\neq K',\alpha} t_\alpha d^\dagger_{K,\alpha,\sigma} d_{K',\alpha,\sigma}, \tag{7.1.24}$$

which, as in the case of the Hubbard model, originates from the on-site energy differences of the impurity sites in momentum-space

$$t_\alpha = \frac{1}{2}\left(\tilde{t}_{0,\alpha} - \tilde{t}_{1,\alpha}\right). \tag{7.1.25}$$

The Hamiltonians describing the baths and the coupling between bath sites and impurity sites transformed into real space

$$\hat{H}_{\text{bath}}^{\text{real}} = \sum_{l,K,\alpha,\sigma} \epsilon_{l,K,\alpha,\sigma} c^\dagger_{l,K,\alpha,\sigma} c_{l,K,\alpha,\sigma}, \tag{7.1.26}$$

$$\begin{aligned}\hat{H}_{\text{hyb}}^{\text{real}} &= \sum_{l,\delta,\alpha,\sigma} V_{l,\delta,\alpha,\sigma} \tilde{d}^\dagger_{\delta,\alpha,\sigma} c_{l,\delta,\alpha,\sigma} + \text{h.c.} \\ &= \sum_{l,\alpha,\sigma} \frac{V_{l,1,\alpha,\sigma}}{2}(d^\dagger_{1,\alpha,\sigma} + d^\dagger_{2,\alpha,\sigma}) c_{l,1,\alpha,\sigma} + \sum_{l,\alpha,\sigma} \frac{V_{l,2,\alpha,\sigma}}{2}(d^\dagger_{1,\alpha,\sigma} - d^\dagger_{2,\alpha,\sigma}) c_{l,2,\alpha,\sigma} + \text{h.c.},\end{aligned} \tag{7.1.27}$$

show that each bath site is coupled to both impurity sites of the same band. Summing up all terms, we can write the complete real-space Hamiltonian as

$$\hat{H}_{\text{imp}}^{\text{real}} = \hat{H}_{\text{int}}^{\text{real}} + \hat{H}_{\text{sp}}^{\text{real}} + \hat{H}_{\text{hyb}}^{\text{real}} + \hat{H}_{\text{bath}}^{\text{real}}. \tag{7.1.28}$$

For each DCA calculation it has to be decided whether the momentum- or real-space representation of the Hamiltonian is used. While the computation of the new hybridisation at the end of an iteration is always performed in momentum space, because Green's functions, self-energies, and hybridisations are diagonal in this representation, the ground state search and the computation of $G(t)$ can be done in either one of the two representations. This choice can have dramatic influence on computation times, convergence properties, and usable symmetries.

While the quantum numbers for the total number of particles $N$, the length of total spin $S$, as well as for the band parity can be used in both representations, only in momentum space the $\mathbb{Z}_4 \times \mathbb{Z}_4$-symmetry, which is describing the conserved total momentum of the system, can be implemented. See chapter 6 for a detailed discussion of this symmetry and the reason why it only can be implemented in a momentum-space representation. From DCA calculations of the Hubbard model we know that DMRG can find the global ground state of two-site DCA calculations without using momentum quantum numbers quite reliably when using an artificial tunnelling Hamiltonian that breaks the symmetry. Convergence problems of DMRG only start to occur when the Brillouin zone is separated into more patches (e.g. four or more) and the Hilbert space starts to break up into orthogonal subspaces. In general, this causes also convergence problems of DCA calculations

and should be avoided.
However, it seems that also for two-site DCA calculations of the three-band Hubbard-Kanamori model the momentum quantum numbers are not necessary to determine the global ground state in each DCA iteration reliably. Additionally, we observed that the real-space representation of the Hubbard-Kanamori Hamiltonian exhibits better entanglement properties. Runtimes per iteration can be increased up to a factor of two compared to calculations in momentum space. It is for these these reasons that all results in this chapter for two-site DCA are obtained with the Hamiltonian in real-space representation.

## 7.2 Single-Site DMFT and Two-Site DCA

As for the Hubbard model, we first have to evaluate how many bath sites are needed to obtain reasonable good discretisations of the hybridisations while avoiding overfitting and overlong runtimes. If not stated otherwise, presented results are obtained for a system with interaction strength $U = 6\text{eV}$, Hund's coupling strength $J = 0.7\text{eV}$ and a chemical potential $\mu = 9\text{eV}$. DMRG and DCA are performed with a maximal bond dimension $m = 2000$ and the time evolution with a truncated weight $w = 10^{-9}$. We use TDVP to time evolve the excited states $\psi(\tau)$ until $\tau_{max} = 100$. Each calculation is initialised with the hybridisation of the non-interacting system.
The left panel of Fig. 7.2 shows the cost function values $\chi$ for the degenerate $xz$- and $yz$-band as well as for the $xy$-band. We display results for the first and last iteration of a single-site DMFT calculation. The cost function values decay exponentially with an increasing number of bath sites $L_b$ for both bands and are fitted better in the first than in the last iteration. Out of experience with the Hubbard model, we expect the onset of overfitting when $\chi$ is of the order $10^{-8}$. We expect this to happen for the $xz$-band with $L_b = 7$ or more bath sites and in fact, for all bath sizes larger than $L_b = 6$ we observe convergence problems. It seems that the overfitting in the first iterations prevents DMFT from approaching close enough to the converged solution, where fit results with the same number of bath sites should be worse and no overfitting should be present for $L_b = 7$ and $L_b = 8$ at least. Therefore, starting the calculations with a hybridisation that is closer to the converged solution could allow to obtain results with slightly more bath sites. A typical choice would be a hybridisation obtained from a converged calculation with $L_b = 6$ bath sites and the same $\mu$ or a converged hybridisation for a slightly different chemical potential. However, since the behaviour of $\chi$ is strongly influenced by the choice of $\mu$, we will use $L_b = 5$ bath sites per impurity for all following DMFT calculations to avoid convergence problems. Then, the resulting cost function values in the last iteration before convergence are of the order of $10^{-5}$, which is sufficient for well converged results.
In the case of two-site DCA we are not able to use more than $L_b = 2$ bath sites per impurity because runtimes are increasing too fast. While for $L_b = 2$ computing a single time step is taking about $t = 2\text{min}$, the runtime increases to $t = 30\text{min}$ per time step for $L_b = 3$. We want to mention at this point that it is very useful to reorder DCA systems with respect to the global ground state. Thus, the runtime of the time evolution can be

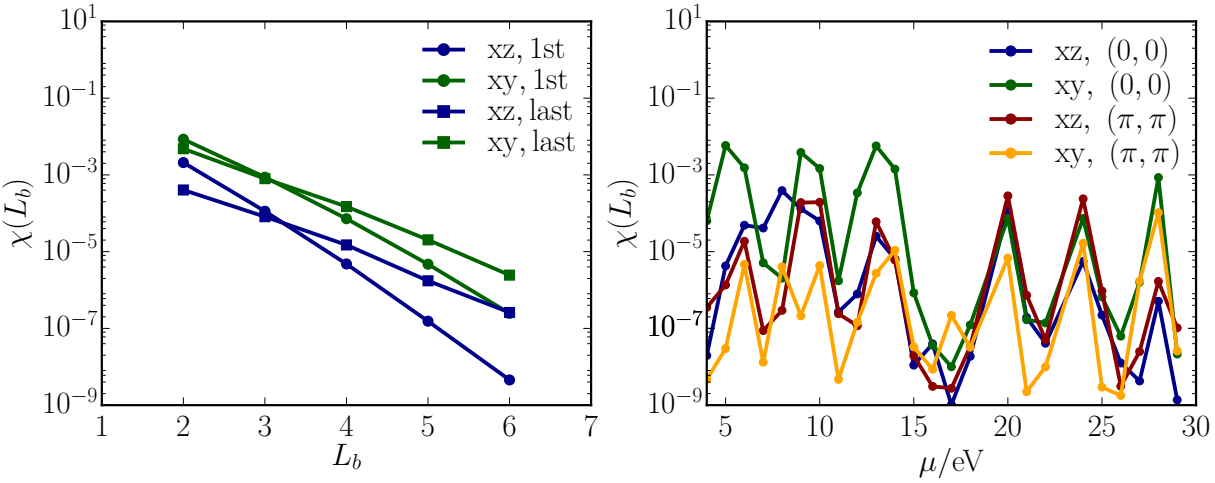


*Figure 7.2: Left panel: Cost function values $\chi$ of the different bands in DMFT in the first (circles) and last (squares) iteration depending on the number of bath sites $L_b$. We observe an exponential decay of $\chi$ in the case of DMFT. While for small bath sizes the cost function value is, in general, smaller in the last than in the first iteration, we observe the opposite behaviour for a large number of bath sites. DMFT calculations with more than six bath sites were not converging due to overfitting. Right panel: Cost function values of different bands and patches in the case of two-site DCA. We display results obtained in the last iteration before convergence for $U = 6t$, $L_b = 2$, and for different choices of $\mu$. The actual size of $\chi$ is varying a lot and depends strongly on the physical behaviour.*

reduced by up to a factor of three. For the cost of calculating the mutual information and computing a new ground state, both together typically taking less than a minute, the runtime of a single iteration of two-site DCA with $L_b = 2$ can be reduced from 15 to five hours. But even with these significant improvements, calculations with $L_b = 3$ bath sites are out of the scope.

The right panel of Fig. 7.2 shows the cost function values of different bands and patches obtained in the last iteration before convergence of two-site DCA calculations with $L_b = 2$ for different choices of $\mu$. First of all, the obtained cost function values vary a lot in a very large range $\chi \in [10^{-2}, 10^{-9}]$. The best values are obtained for chemical potentials where the system is a Mott insulator. This can be seen best in comparison with Fig. 7.4, which we will discuss in more detail later on. In these cases $L_b = 2$ is more than sufficient to obtain very good DCA results. Additionally, very close to these regimes the cost function values are of the order $10^{-5}$, which, by experience, leads to reasonable well converged results with respect to the bath size. The worst cost function values are obtained when the system behaves metallic between the Mott plateaus. In these cases, $\chi$ is of the order $10^{-2}$ to $10^{-3}$, which typically means that larger bath sizes still result in small changes of the Green's functions and physical observables. Since the hybridisations of the $xz$-band, in general, seem to be fitted worse than the ones of the $xy$-band, we suggest to add a single bath site more to the $xz$-band in those regimes. This could be sufficient to obtain

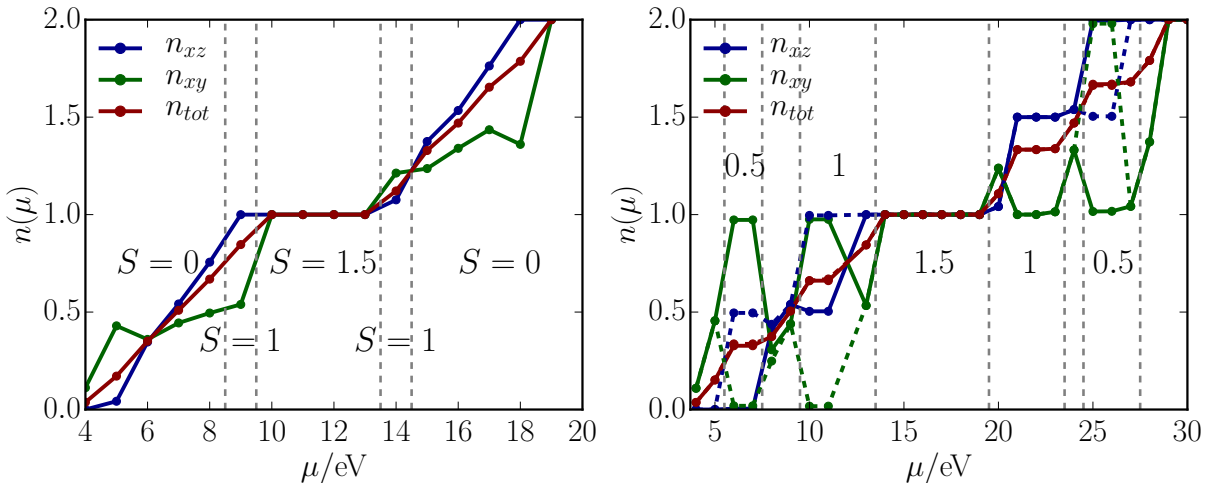


*Figure 7.3: Left panel: Filling of the two degenerate bands $n_1 = n_2$, the third band $n_3$ and the total system $n_{tot}$ dependent on the chemical potential $\mu$ for $U = 4eV$ obtained with single-site DMRG. The system exhibits a half-filled Mott-insulating state for $\mu \in [10, 13]$ and behaves metallic otherwise. The global ground state has different symmetry quantum numbers $S$ over the range of chemical potentials $\mu$. While in the Mott-insulating regime we observe $S = 1.5$, directly next to this regime the quantum number changes to $S = 1$ and afterwards to $S = 0$. Right panel: Same picture as in the left panel but for $U = 6eV$. The system exhibits additional Mott-insulating regimes at $n = 1/3$, $n = 2/3$, $n = 4/3$, and $n = 5/3$ filling. The insulating regimes for $1/3$ and $5/3$ filling are accompanied with the total spin quantum number $S = 0.5$. In the regimes where the spin quantum number is not specified we obtained $S = 0$. We observe oscillating behaviour of DMFT in the regions of $n = 1/3$, $n$=2/3 and $n = 5/3$ filling as well as for $\mu = 8$. In those cases we show both solutions, one with a dashed and the other with a solid line.*

well converged DCA results also for the metallic regimes and it could also prevent the runtimes of two-site DCA calculations from increasing too dramatically. Unfortunately, this was out of the scope of this thesis and should be pursued in further research. Therefore, all DCA results presented in this chapter are obtained with $L_b = 2$ and should, at least around the Mott plateaus, be precise and reliable.

Now, we can focus on the results for single-site DMFT. Fig. 7.3 shows the total filling $n_{tot}$ of the lattice, the filling of the two degenerate bands $n_{xz} = n_{yz}$, and the filling of the third band $n_{xy}$ for different chemical potentials. The left panel shows results for $U = 4$eV where only at half-filling a Mott insulating plateau can be seen. Interestingly, the quantum number for the length of the total spin $||\vec{S}||^2 = S(S+1/2)$ is varying strongly. While we observe $S = 1.5$ when the system is a Mott insulator and $S = 1$ directly next to this regime, for all other choices of $\mu$ the global ground state of the system is located in the $S = 0$ symmetry sector. This can be explained with the form of the Hubbard-Kanamori Hamiltonian, which mimics the Hund's rules known from atomic physics. They state that first the total spin of all electrons in a shell is maximised and afterwards the angular momentum. This is reflected in the Hamiltonian $\hat{H}_{\text{int}}$ by the fact that the energy of the

system is minimised the most by the term $-2J\vec{S}^2$ and by a smaller amount by $-\frac{1}{2}J\vec{L}^2$. Therefore, if possible, the system prefers to align the spins of all electrons on the impurity sites. Consequently, if the three impurity sites are half-filled, this corresponds to a total spin quantum number $S = 1.5$ on the impurity sites. Next to the Mott insulating regime, the non-degenerate band $xy$ is populated first when doping the system with electrons or holes, respectively. The degenerate bands $xz$ and $yz$ are still close to fully occupied, which corresponds to states with two electrons on the impurity sites and thus a spin quantum number $S = 1$. The remaining system, consisting only of non-interacting bath sites, has no preference for any kind of spin alignment and has spin quantum number $S = 0$. Therefore, the spin quantum number of the whole system is determined only by the physics taking place on the impurity sites.
When increasing the interaction strength to $U = 6eV$, additional Mott plateaus form at fillings $n = 1/3$, $n = 2/3$, $n = 4/3$, and $n = 5/3$, which can be seen in the right panel of Fig. 7.3. This is expected to happen for all multi-band Hubbard models at sufficiently large interaction strengths due to the Hubbard-term $U/2 \cdot N(N-1)$ in the Hubbard-Kanamori Hamiltonian (see Eq. (7.1.8)). Since $N = \sum_i n_i$ is the sum of expectation values of the number particles in all bands, there will be Mott plateaus for every integer number of particles. Normalised by the number of bands, Mott plateaus are observed at every fractional filling.
While for $U = 4$eV all calculations converge without having any kind of problems, for $U = 6$eV and some choices of $\mu$ DMFT oscillates between two different solutions. This behaviour occurs only in the Mott insulating regimes with $n = 1/3$, $n = 2/3$, and $n = 5/3$ filling and prevents DMFT from converging. For those cases we show both solutions in Fig. 7.3, one indicated by a dashed and the other by a solid line.
In the Mott insulating regime with $n = 1/3$ filling one solution of DMFT seems to be a state where the non-degenerate $xy$ band is half filled and the degenerate bands are empty. The other solution exhibits degenerate ground states that differ in their band symmetry quantum numbers. In the one case only the impurity corresponding to the $xz$ band, and in the other case only the one corresponding to the $yz$ band, is half-filled while the other impurities are empty. Since the two bands are completely degenerate, both ground states have the same energy. Due to the different quantum numbers, these two states are orthogonal to each other and form a basis for the degenerate ground state space. Any kind of combination of these two states can be the true global ground state realised by the system. We choose to take the symmetric combination of both states as the global ground state for the DMFT calculation as described in chapter 5. With this choice, both bands show the same filling $n = 0.5$, and DMFT oscillates between both described solutions back and forth. The same behaviour is observed for the Mott plateau at $n = 5/3$ filling.
The calculations for the Mott plateau with filling $n = 2/3$ show similar behaviour with the difference that two particles have to be distributed over three bands. One of the DMFT solutions has half-filled, degenerate bands and an empty non-degenerate band. The other solution is a superposition of two degenerate ground states where the non-degenerate band and either the $xz$ or the $yz$ band is half-filled.

Choosing only one of the degenerate ground states, or not using the band symmetry at all and leaving DMRG to determine its own ground state superposition, leads to a seemingly chaotic behaviour of DMFT with no oscillations but also no convergence. Therefore, we assume that using the band symmetry and superposing the degenerate ground states is the correct ansatz, especially since the oscillating behaviour between the two rivalling DMFT solutions seems very robust. Breaking the degeneracy of the $xz$ and $yz$ band by shifting the on-site energies of their impurity sites by $\pm 0.01$eV does not prevent DMFT from oscillating between two solutions. Only with a relatively large shift of $\pm 0.1$eV DMFT converges again. However, this shift is so large that the non-degenerate band $xy$, which had the highest energy before the shift, now has an energy that is located between the energies of the previously degenerate bands. Thus, the whole structure of the problem has changed. In this case, the DMFT solutions show that the band with lowest energy is filled first until it is half-filled. Then, with an increasing chemical potential, the band with next-lowest energy and finally the band with the highest energy is populated until it is half filled.
We changed the bond dimension of the ground state search, the precision for the time evolution, the number of bath sites, we examined mixing iteration results and starting from a nearby converged solution, but none of these approaches changed this behaviour. This suggests that these oscillations are the result of the physics of the model. Contrarily, calculations in the Mott plateau with $n = 4/3$ filling have converged smoothly without showing any kind of convergence problems. This is an indication that the oscillations are not entirely determined by the physics of the model and perhaps are influenced by parameter choices or implementation details. By finding the exact origin of this qualitatively different behaviour, it could be possible to get rid of the oscillations in the other plateaus. This is definitely a topic of further research. However, it is important to note that the total filling of the lattice $n_{tot}$ for both oscillating solutions is very similar and seems to fit well into the global behaviour of $n(\mu)$. Therefore, we assume that these oscillations do not influence the comparison with DCA and the following conclusions significantly.
We now want to focus on the DCA results for $n(\mu)$ shown in Fig. 7.4. We want to emphasise at this point that the two sites of each band in real-space two-site DCA calculations describe sites of the original lattice. Therefore, it is not surprising to find that they are degenerate and have the same occupation numbers. Thus, we show only the total filling $n_{\mathrm{tot}}$ and the filling of the bands $n_{xz}$ and $n_{xy}$ in Fig. 7.4. In both cases, $U = 4$eV and $U = 6$eV, we observe qualitatively similar behaviour compared to the DMFT results. The $U = 4$eV calculations only exhibit a Mott insulating plateau at half-filling and for $U = 6$eV we observe additional Mott insulating regimes for fractional filling. The sizes of the plateaus are very similar. The biggest difference is that the global ground state in all DCA calculations is located in the $S = 0$ sector for all choices of $\mu$. Because of the two-site DCA calculation in real space, the system consists of six impurity sites that can be grouped into two sets of three. On each set the Hubbard-Kanamori Hamiltonian acts independently and aligns the electrons such that the energy is minimised. However, the two sets of electrons can always be aligned in different directions, which corresponds to a

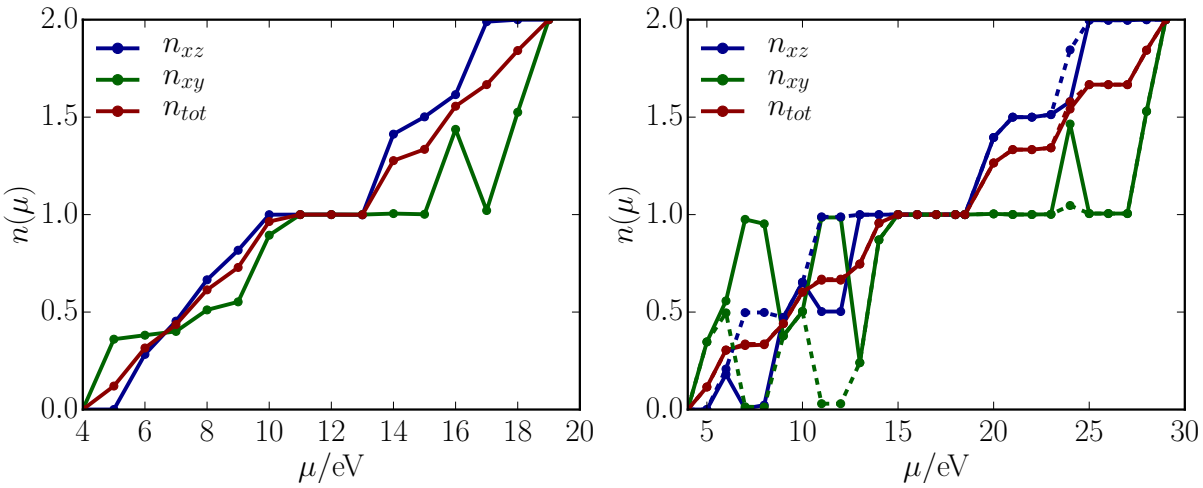


*Figure 7.4: Left panel: Filling of the two degenerate bands $n_1 = n_2$, of the third band $n_3$ and of the total system $n_{tot}$ depending on the chemical potential $\mu$ for $U = 4eV$ obtained with two-site DCA. We only show the occupation of the first site in each band since for two-site DCA in real space both sites of the same band show the same occupation. The system exhibits a single half-filled Mott-insulating state and behaves metallic otherwise. Right panel: Same picture as in the left panel but for $U = 6eV$. The system exhibits additional Mott-insulating regimes at $n = 1/3$, $n = 2/3$, $n = 4/3$, and $n = 5/3$ filling. We observe oscillating behaviour more often than for DMFT but in similar regions. To be precise, DMFT oscillates between two solutions for $\mu \in [6, 7, 8, 9, 11, 12, 24]$. In those cases we show both solutions, one with a dashed and the other with a solid line.*

total spin quantum number $S = 0$. This is energetically favourable because it imposes less constraints on the movement of the electrons than a high spin quantum number would do. This implies that the electrons on neighbouring sites in the infinite lattice are aligned in different directions, similar to an antiferromagnetic order.
In Fig. 7.5 we compare the total filling $n$ obtained with DMFT and DCA for both interaction strengths. For $U = 4$eV we see small differences, which could originate from the very small bath $L_b = 2$ for the DCA calculation. While the fillings obtained with DCA are slightly smaller than the ones obtained with DMFT on the hole-doped site, on the electron-doped site the behaviour is reversed. This can also be seen for the case $U = 6$eV. This is contradicting the observations in the Hubbard model where an increasing interaction strength was shifting the filling more towards the Mott plateau for both doping regimes. However, the differences between the results of the two methods are so small that they could change when using larger bath sizes for DCA.
We suspect that the Mott insulating plateaus are slightly larger for the DCA calculations, but to make a definite statement more data points are needed. The DMFT calculations predict that the Mott plateaus at fractional filling form at an interaction strength $U_c$ between $U = 4$eV and $U = 6$eV. From the current DCA results we can judge that the interaction strength $U_c$ is still located inside of this region. Even if two-site DCA increases

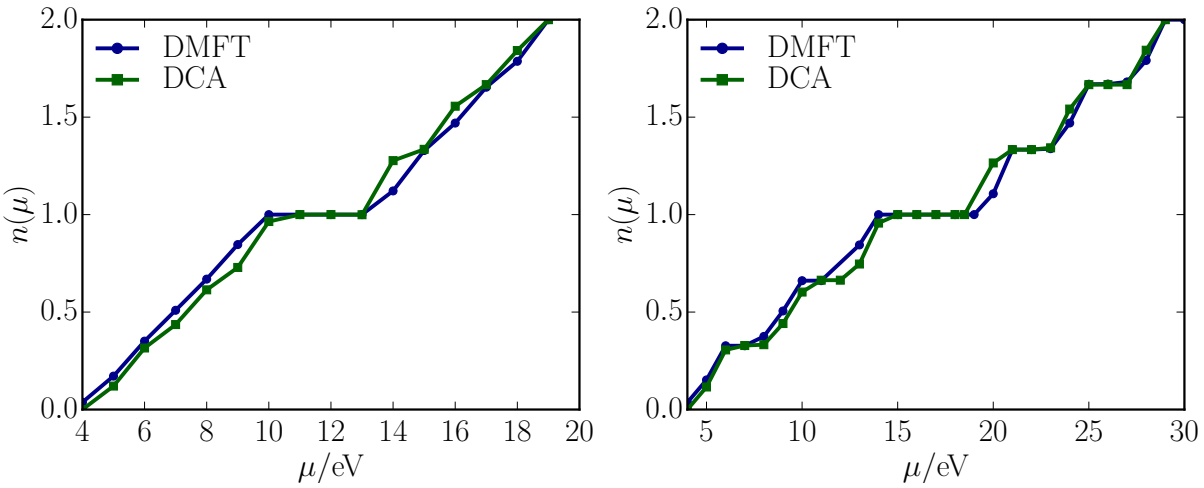


*Figure 7.5: Left panel: Comparison of the total filling obtained with DMFT (blue circles) and DCA (green squares) for $U = 4eV$ (left) and $U = 6eV$ (right). For $U = 4eV$ we see only small differences between the two methods, which could get even smaller when using bigger bath sizes for DCA. For $U = 6eV$ the Mott-insulating phases sets in at slightly larger values of $\mu$ in the case of DCA. It also seems that the Mott plateaus are slightly larger for DCA and that the increase of the filling between the plateaus is steeper.*

the Mott plateaus slightly for $U = 6$eV, the changes are too small to indicate a change of $U_c$ by more than a couple of 0.1eV from DMFT to DCA. Therefore, the difference of nearly a factor of two[170] between the critical interaction strength $U_c$ determined with DMFT and determined in experiments cannot be reduced with DCA. This indicates that the momentum dependence that is neglected in DMFT and partly captured with DCA is not the reason for this discrepancy.
Of course, larger bath sizes can still influence the DCA results and increase the change in $U_c$ but we doubt that the effect will be noteworthy. In the case of the Hubbard model large differences were observed between the qualitative behaviour of two-site and four-site DCA. This could also be true for $Sr_2VO_4$. Thus, DCAs with larger cluster sizes could still lead to the desired change in $U_c$. However, since the differences between single-site DMFT and two-site DCA in the case of the Hubbard model were already much larger than the ones we observe for $Sr_2VO_4$, we assume that the momentum dependence of $Sr_2VO_4$ is quite small. Since we already observe very long runtimes for the two-site DCA calculations with very small bath sizes, right now four-site DCA calculations on three-band models are out of reach for DMRG+DMFT without significant improvements. While a change of the MPS topology to MET or MST should allow to calculate two-site DCA with larger bath sites, it is questionable if these changes are sufficient to make four-site DCA calculations feasible.

## 7.3 Summary

In this chapter we discussed the real material $Sr_2VO_4$, which can be described by a three-band model with lattice filling $n = 1/3$ and a Hubbard-Kanamori interaction. While experiments show that this material is a small gap correlation-driven insulator [54], DMFT calculations predict metallic behaviour for any reasonable choice of interaction strengths [55]. When using DMRG+DMFT, we obtain a Mott-insulating plateau at half filling for the interaction strengths $U = 4$eV and $U = 6$eV, but additional Mott insulating site plateaus of significant size only for $U = 6$eV. Thus, the critical interaction strength $U_c$ defining the Mott metal-insulating transition for $Sr_2VO_4$ is located between those two interaction strengths.

Previously, Wolf at al. showed that using two-site DCA on an artificial, completely degenerate three band model can lower the critical interaction strength significantly [17]. This was impressive since up to that point three-band models were not accessible in the context two-site DCA with any kind of impurity solver at low temperatures. They suggested that reintroducing non-local interactions via DCA could also lower $U_c$ for real materials like $Sr_2VO_4$. However, we observed that introducing a real band structure and lifting the degeneracy of the three bands partly increases the complexity of these three-band models dramatically compared to the benchmark calculations made by Wolf et al.. Only by introducing additional symmetries, improving time evolutions, and reordering the MPS systems, we were able to obtain results with DMFT and DCA on the imaginary axis at temperature $T = 0$. With these improvements we were able to show that two-site DCA and single-site DMFT results only differ slightly, and that the critical interaction strength $U_c$, which defines the onset of Mott insulating behaviour for $Sr_2VO_4$, is either not lowered at all or only changed by a couple of 0.1eV. Therefore, missing non-local interactions in single-site DMFT do not explain the differences between theory and experiment.

However, we want to emphasise that these results are obtained with very small bath sizes $L_b = 2$. Thus, they still can change slightly with larger system sizes. Unfortunately, already for these relatively small impurity systems the runtime of one DCA iteration is close to a day, which results in runtimes of a couple of days up to a week until convergence is achieved. This is relatively fast considering that no other impurity solver can produce results for this model at $T = 0$. Adding a single bath site more per impurity increases the runtime up to 20 days per iteration, which is too large for any reasonable calculation. However, $Sr_2VO_4$ shows a similar behaviour as we observed in the Hubbard model. For a good fit of the hybridisations the necessary number of bath sites per impurity decreases when separating the Brillouin zone into more patches. While the effect in the Hubbard model decreases the bath sizes by one site per impurity when doubling the number of patches, the effect in the three-band model seems to be stronger. We showed that especially in or very close to Mott insulating regimes $L_b = 2$ bath sites are completely sufficient to obtain very good hybridisation fits. This is promising for further studies on multi-band problems with multi-site DCA since it could partly counter the exponential growth of computation times we observed.

# Chapter 8

# Spin-Orbit coupling: $Sr_2RuO_4$

In this chapter we want to discuss the perovskite oxide compound $Sr_2RuO_4$. $Sr_2RuO_4$ has attracted attention[173] since it was shown to exhibit non-conventional superconductivity[174] in 1994. It has been of interest both to experimentalist[175,176] and theorists[177,178] due to its nearly perfect Fermi liquid behaviour[179], its characteristics of a Hund's metal[12] and its superconducting ground state. Of special interest is the interplay between of spin-orbit coupling (SOC) and electronic correlations. SOC has significant influence on the topography of the Fermi surface[56,180], leads to a mixed orbital character of the individual fermi surface sheets and was shown to lead to an effective correlation-enhancement of the spin-orbit coupling by approximately a factor of two[56,181].
More precisely, while the influence of SOC is well understood for weakly correlated metals[182], Mott insulators[183], and heavy-fermion compounds[184], the situation for intermediate interaction strengths is less clear. Ruthenate is a notable example of this regime. Several physical properties are well described by $Sr_2RuO_4$ being a Hund's metal, which indicates that SOC plays no important role for this material. But it cannot be neglected since the SOC interaction strength $\lambda \approx -0.11\text{eV}$ is comparable to the Hund's coupling $J = 0.4\text{eV}$[185] and much larger than low-energy scales like the Fermi-liquid temperature $T_{FL}$ or spin-degrees of freedom. Accordingly, angle-resolved photoemission spectroscopy experiments[186] and DMFT[56] calculations emphasise the influence of SOC. Therefore, understanding the explicit nature of SOC and its influence on the physics of correlated metals is still an interesting field of research.
Beside the physical importance of this material and despite the fact that $Sr_2RuO_4$ was studied extensively with DFT+DMFT since 2000[177], methodologically $Sr_2RuO_4$ is especially interesting for us. Up to now DMFT, combined with any impurity solver, cannot access the Fermi-liquid regime if SOC is present: Spin-orbit coupling creates single-particle hopping between different bands and therefore off-diagonal components in hybridisations, self-energies, and Green's functions. For CTQMC this results into a severe sign problem at low temperatures[56,181]. In the case where DMRG or ED are used as impurity solvers for DMFT, this requires fitting matrix-valued functions to setup the impurity Hamiltonians. To our knowledge, there are no efficient schemes to do this.
In this chapter we tackle the problem and first discuss the influence of SOC on our

DMRG+DMFT scheme. Important effects are the breaking of the $SU(2)$-symmetry of the conserved length of the total spin of the system as well as the occurrence of matrix-valued physical quantities. In this context we will introduce a suitable basis to minimise the negative influences of those changes on the DMFT calculation and discuss how to fit matrix-valued hybridisations effectively. To check the quality of DMRG as an impurity solver and the correct parameter options for this model, we will first compare CTQMC and DMRG results without SOC. We end the chapter by discussing our results obtained with SOC at temperature $T = 0$, which confirm frequency independence in the off-diagonal components of the self-energy for small frequencies, and an effective correlation-enhancement of SOC by about a factor two.

## 8.1 The Hamiltonian

$Sr_2RuO_4$ is described by an effective three-band model with the Hubbard-Kanamori Hamiltonian:

$$\hat{H}_{\text{int}} = -\sum_{\alpha,\sigma}(\mu - \bar{\varepsilon}_\alpha)\hat{n}_{\alpha,\sigma} + (U - 3J)\frac{\hat{N}(\hat{N}-1)}{2} - 2J\vec{\hat{S}}^2 - \frac{1}{2}J\vec{\hat{L}}^2 + \frac{5}{2}J\hat{N}, \tag{8.1.1}$$

as introduced for $Sr_2VO_4$ in chapter 7. Similar to $Sr_2VO_4$, we can restrict ourselves to consider only the three 3d orbitals from the Ruthenium atom. The Hamiltonian can be written in second quantisation by choosing or example the cubic harmonics as a basis set. With this choice the operators are defined as

$$\hat{N} = \sum_{\alpha\sigma}\hat{n}_{\alpha\sigma}, \tag{8.1.2}$$

$$\vec{S} = \frac{1}{2}\sum_{\alpha}\sum_{\sigma\sigma'} d^\dagger_{\alpha\sigma}\vec{\tau}_{\sigma\sigma'}d_{\alpha\sigma'}, \quad \text{and} \tag{8.1.3}$$

$$\hat{L}_\alpha = i\sum_{\sigma}\sum_{\beta,\gamma=1}^{3}\epsilon_{\alpha\beta\gamma}d^\dagger_{\beta\sigma}d_{\gamma,\sigma}. \tag{8.1.4}$$

Here, $\vec{\tau}$ are the Pauli matrices, $d^\dagger_{\alpha,\sigma}$ and $d_{\alpha,\sigma}$ creation and annihilation operators for the three relevant orbitals indicated with $\alpha \in \{123\}$ and spin $\sigma$, and $\varepsilon_{\alpha\beta\gamma}$ the Levi-Civita tensor with the convention $\varepsilon_{1,2,3} = 1$. The three relevant orbitals correspond to the cubic harmonics labeled with $\alpha \in \{yz, xz, xy\}$.
The spin-orbit coupling of $Sr_2RuO_4$ is described by

$$\hat{H}_{\text{SOC}} = \lambda\hat{\vec{s}}_i \cdot \hat{\vec{L}}_i, \tag{8.1.5}$$

where the spin $\hat{\vec{s}}_i$ of each electron couples first with its own angular momentum $\hat{\vec{L}}_i$ with strength $\lambda$. To express the SOC-term in the basis of the cubic harmonics, we switch

from summing over all electrons on the impurity sites, to summing over all orbitals and introduce the corresponding single-particle states $|\phi_{\beta,\sigma}\rangle$. Thus, we can write $\hat{H}_{\mathrm{SOC}}$ as

$$\hat{H}_{\mathrm{SOC}} = \hat{\vec{s}} \cdot \hat{\vec{L}} = \sum_{\sigma,\sigma'} \sum_{\alpha,\beta,\gamma} \langle \phi_{\gamma,\sigma'} | \hat{s}_\alpha \hat{L}_\alpha | \phi_{\beta,\sigma} \rangle \ |\phi_{\gamma,\sigma'}\rangle\langle\phi_{\beta,\sigma}|. \tag{8.1.6}$$

After inserting $\mathbb{1} = \sum_{\delta,\sigma''} |\phi_{\delta,\sigma''}\rangle\langle\phi_{\delta,\sigma''}|$ between the operators und using the definitions from Eq. (8.1.2) we can deduce

$$\begin{aligned}
\hat{\vec{s}} \cdot \hat{\vec{L}} &= \sum_{\sigma,\sigma',\sigma''} \sum_{\alpha,\beta,\gamma,\delta} \langle \phi_{\gamma,\sigma'} | \hat{s}_\alpha | \phi_{\delta,\sigma''} \rangle \langle \phi_{\delta,\sigma''} | \hat{L}_\alpha | \phi_{\beta,\sigma} \rangle \ |\phi_{\gamma,\sigma'}\rangle\langle\phi_{\beta,\sigma}| \\
&= \frac{1}{2} \sum_{\sigma,\sigma',\sigma''} \sum_{\alpha,\beta,\gamma,\delta} \tau^{(\alpha)}_{\sigma',\sigma''} \delta_{\gamma,\delta} i \varepsilon_{\alpha,\delta,\beta} \delta_{\sigma'',\sigma} \ |\phi_{\gamma,\sigma'}\rangle\langle\phi_{\beta,\sigma}| \\
&= \frac{i}{2} \sum_{\sigma,\sigma'} \sum_{\alpha,\beta,\gamma} \tau^{(\alpha)}_{\sigma',\sigma} \varepsilon_{\alpha,\gamma,\beta} \ |\phi_{\gamma,\sigma'}\rangle\langle\phi_{\beta,\sigma}| \\
&= \frac{i}{2} \sum_{\alpha} \tau^{(\alpha)}_{\sigma,\sigma'} \varepsilon_{\alpha,\beta,\gamma} \ d^\dagger_{\beta,\sigma} d_{\gamma,\sigma'}.
\end{aligned} \tag{8.1.7}$$

In the last line we relabelled $\gamma \leftrightarrow \beta$, replaced the vectors $|\phi_{\gamma,\sigma'}\rangle$ and $\langle\phi_{\beta,\sigma}|$ with their corresponding annihilation and creation operators, and followed the convention that all indices occurring twice have to be summed over.
The spin-orbit term in this basis has the following disadvantages:

- Obviously the SOC flips the spin of an electron and thus breaks the $U(1)$-symmetry of the conserved $z$-component of the total spin and the $SU(2)$-symmetry of the conserved length of the total spin $||\vec{S}||^2$. This will increase computation times because less symmetry quantum numbers can be used, and will also cause all quantities to be spin-dependent.
  Thus, we have to compute the full $6 \times 6$ single-particle Green's function $\boldsymbol{G}$. This is in contrast to the case of $Sr_2VO_4$, where we could compute only the spin-up components and assumed similarity to the spin-down components.

- The SOC is a single-particle hopping term between the orbitals, which can be seen in Eq. (8.1.7). Written in matrix form

  $$\hat{H}_{\mathrm{SOC}} = \vec{d}^\dagger H_{\mathrm{SOC}} \vec{d}, \tag{8.1.8}$$

  where we order the orbitals like $\vec{d} = \begin{pmatrix} d_{xy,\uparrow} & d_{xy,\downarrow} & d_{yz,\uparrow} & d_{yz,\downarrow} & d_{xz,\uparrow} & d_{xz,\downarrow} \end{pmatrix}^T$, and the spin-orbit interaction term takes the form

  $$H_{\mathrm{SOC}} = \begin{pmatrix} 0 & 0 & 0 & -\frac{\lambda}{2} & 0 & -\frac{i\lambda}{2} \\ 0 & 0 & \frac{\lambda}{2} & 0 & -\frac{i\lambda}{2} & 0 \\ 0 & \frac{\lambda}{2} & 0 & 0 & \frac{i\lambda}{2} & 0 \\ -\frac{\lambda}{2} & 0 & 0 & 0 & 0 & -\frac{i\lambda}{2} \\ 0 & \frac{i\lambda}{2} & -\frac{i\lambda}{2} & 0 & 0 & 0 \\ \frac{i\lambda}{2} & 0 & 0 & \frac{i\lambda}{2} & 0 & 0 \end{pmatrix}. \tag{8.1.9}$$

Consequently, the SOC generates non-zero off-diagonal terms in the non-interacting single-particle Green's function, the interacting single-particle Green's function, the hybridisation, and the self-energy. In fact, in all these cases, exactly the same components as in the SOC term are non-zero.
The main consequence of off-diagonal terms is that the fitting procedure is dramatically complicated. Instead of fitting decoupled diagonal elements, a matrix-valued function has to be fitted. This is a complex and not well understood problem that we will discuss in detail in section 8.3. Additionally, the self-consistency equations and the computation of the hybridisation of the next DMFT iteration have to be evaluated for the whole matrix-valued quantities and can not be parallelised over the diagonal elements as before. However, the numerical effort of the latter is negligible compared to the fitting procedure of the hybridisation.

- The single-particle coupling between the orbitals together with the spin-flip introduces additional entanglement between the orbitals and the corresponding bath sites, especially since the interaction between the orbitals is now also present on a single-particle level. This will increase the computation time of the time evolution significantly.

To define the model completely a dispersion relation describing the single-particle behaviour is needed, which we obtained from a DFT calculation with the TRIQS[187] toolkit based on the WIEN2k package[188]. In Fig. 8.1 the band structure of $Sr_2RuO_4$ with (right) and without (left) spin-orbit coupling is displayed. It is clear that only three bands are relevant for the low-energy physics due to their vicinity to the Fermi surface. In the next step maximally localised Wannier functions are generated out of the band structure, which roughly match the form of the $xy$, $xz$ and $yz$ orbitals of the cubic harmonics. By Fourier transforming the overlaps of the orbitals of different lattice sites, one can compute a dispersion relation for the three relevant bands, which is plotted as red lines in Fig. 8.1. The agreement between the DFT band structure and the computed dispersion relation for the three-band model is perfect for the three relevant bands.
Now the interaction Hamiltonian can be combined with the environment, as in the previous cases

$$\begin{aligned} \hat{H} &= \hat{H}_{\text{int}} + \hat{H}_{\text{SOC}} + \hat{H}_{\text{hyb}} + \hat{H}_{\text{bath}}, \\ \hat{H}_{\text{hyb}} &= \sum_{l,\alpha,\beta,\sigma,\sigma'} V_{l,\alpha,\beta,\sigma,\sigma'} d^{\dagger}_{\beta,\sigma'} c_{l,\alpha,\sigma} + \text{h.c.}, \quad \text{and} \\ \hat{H}_{\text{bath}} &= \sum_{l,\alpha,\sigma} \epsilon_{l,\alpha,\sigma} c^{\dagger}_{l,\alpha,\sigma} c_{l,\alpha,\sigma}. \end{aligned} \tag{8.1.10}$$

As before $\epsilon_{l,\alpha,\sigma}$ denotes the on-site energy of the $l$-th bath sites associated with the impurity site $\alpha$ with spin $\sigma$. Since the Hamiltonian describing the spin-orbit coupling is complex, we also consider complex single-particle hopping elements $V_{l,\alpha,\beta,\sigma,\sigma'}$ between an impurity $\beta$ with spin $\sigma'$ and the bath site $l$ associated with impurity $\alpha$ with spin $\sigma$. As in the case of the real-space DCA of the Hubbard model, bath sites can couple with multiple

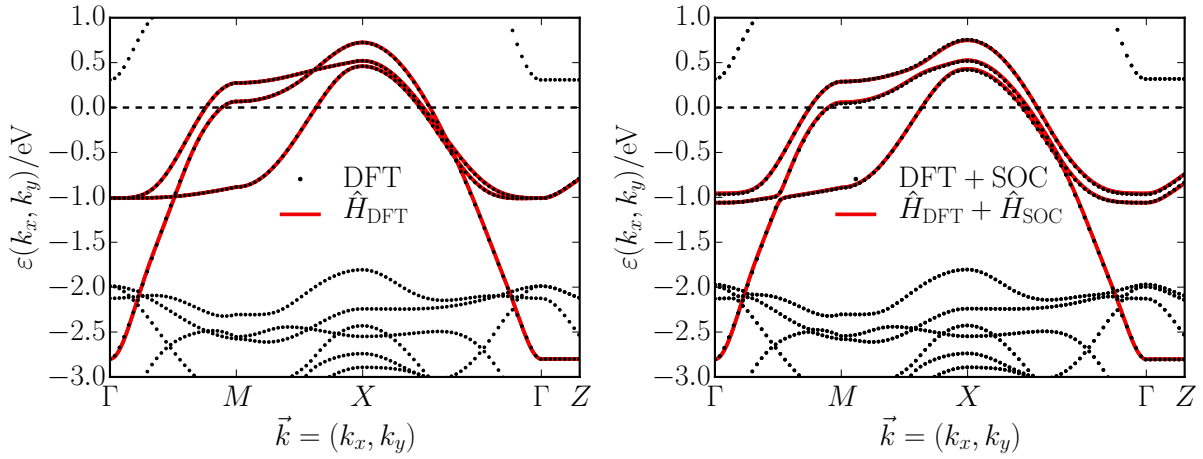


*Figure 8.1: Band structure of* $Sr_2RuO_4$ *obtained with DFT without (left) and with (right) spin-orbit coupling. Only three bands are important for the low-energy physics since they are the only bands intersecting the Fermi surface* $\varepsilon_k = 0$*. The red lines are representing the dispersion relation used in the impurity model. It is obtained by generating maximally localised Wannier functions out of the DFT band structure. As they match the form of the cubic harmonics orbitals, the can be used to calculate the overlaps between different overlaps. Fourier transforming the results generates an effective dispersion relation. The agreement in both cases is very good.*

impurity sites due to the off-diagonal elements of the hybridisation.
All calculations for $Sr_2RuO_4$ are performed with an interaction strength $U = 2.3$eV, a Hund's coupling $J = 0.4$eV and, if spin-orbit coupling is considered, with an SOC strength $\lambda = -0.11$eV.
With the completely defined Hamiltonian and dispersion relation in hand the DMFT calculations can in principle be started. But it is worthwhile to discuss the representation of the model in the basis of the cubic harmonics in more detail first.

## 8.2 Basis Transformation

We already mentioned some of the negative consequences of the SOC term on the DMFT calculation. In this and the next section we want to show how to diminish some of those consequences. Basically, we will show that for this model it is convenient to switch to the common eigenbasis of the total angular momentum $\hat{\vec{J}}^2$, its z-component $\hat{J}_z$, $\hat{\vec{L}}^2$, and $\hat{\vec{S}}^2$. We will call this basis the $J$-basis for the rest of this chapter. In the $J$-basis we can rewrite the SOC with the help of

$$\begin{aligned}
\hat{\vec{J}}^2 &= (\hat{\vec{s}} + \hat{\vec{L}})^2 \\
&= \hat{\vec{s}}^2 + \hat{\vec{L}}^2 + \hat{\vec{s}}\hat{\vec{L}} + \hat{\vec{L}}\hat{\vec{s}} \\
&= \hat{\vec{s}}^2 + \hat{\vec{L}}^2 + \hat{s}_x\hat{L}_x + \hat{s}_y\hat{L}_y + \hat{s}_z\hat{L}_z + \hat{L}_x\hat{s}_x + \hat{L}_y\hat{s}_y + \hat{L}_z\hat{s}_z \\
&= \hat{\vec{s}}^2 + \hat{\vec{L}}^2 + 2\hat{L}_z\hat{s}_z + \hat{L}_+\hat{s}_- + \hat{s}_+\hat{L}_- \\
&= \hat{\vec{s}}^2 + \hat{\vec{L}}^2 + 2\hat{\vec{s}}\hat{\vec{L}},
\end{aligned} \tag{8.2.1}$$

where working in the common eigenbasis of $\hat{\vec{S}}^2$, $\hat{\vec{L}}^2$ and $\hat{J}_z = \hat{L}_z + \hat{s}_z$ allows us to commute the operators $\hat{\vec{L}}$ and $\hat{\vec{S}}$ and also $\hat{L}_z$ and $\hat{s}_z$. Rearranging the equation results in

$$\hat{\vec{s}}\hat{\vec{L}} = \frac{1}{2}(\hat{\vec{J}}^2 - \hat{\vec{L}}^2 - \hat{\vec{S}}^2), \tag{8.2.2}$$

which shows that the SOC is diagonal in the $J$-basis. To investigate whether the $J$-basis is better suited to describe $Sr_2RuO_4$, we need to study the whole Hamiltonian in the new basis. Thus, we need to derive the transformation $\boldsymbol{T}$ from the basis of the cubic harmonics to the $J$-basis.
The best way to do this is to decompose the transformation $\boldsymbol{T}$ into

$$\mathbf{T} = \mathbf{T}_{Y_1^m \to J}\mathbf{T}^{-1}_{Y_1^m \to X_{1c}}, \tag{8.2.3}$$

i.e. a transformation $\mathbf{T}^{-1}_{Y_l^m \to X_{lc}}$ from the cubic harmonics $X_{lc}$ to the spherical harmonics $Y_l^m$ and a transformation $\mathbf{T}_{Y_l^m \to J}$ from there to the $J$-basis, defined via Clebsch-Gordan coefficients.
For $Sr_2RuO_4$ the same argumentation is valid as for $Sr_2VO_4$ (see chapter 7), i.e. the three orbitals, which are described by the Hubbard-Kanamori Hamiltonian, belong to the five $d$-orbitals with angular momentum quantum number $l = 2$. The $d_{z^2}$ and the $d_{x^2-y^2}$ orbitals have a much higher energy in compounds like $Sr_2VO_4$ and $Ru_2VO_4$ because of their vicinity to the oxygen atoms and thus are typically neglected. Unfortunately, in the naive approach the transformation $\boldsymbol{T}$ has to include all five orbitals of $X_{2c}$, which corresponds to ten states due to the spin-degrees of freedom. Since all states of $X_{2c}$ are coupled in the $J$-basis, none of the basis states can be neglected. Instead of having to consider six states in the $X_{2c}$ basis, we would have to consider ten states in the $J$-basis.

However, the trick is to find a transformation that is valid on the subspace of the three relevant orbitals in the basis of the cubic harmonics, which would lead to only six states in the $J$-basis. To find this transformation, we first define the transformation $\mathbf{T}_{Y_2^m \to X_{2c}}$ from the spherical harmonics $Y_2^m$ to the cubic harmonics $X_{2c}$ with angular momentum quantum number $l = 2$. $m$ denotes the quantum number for the z-component of the angular momentum and goes from $l$ to $-l$ in integer steps. Thus, the transformation is given by

$$\begin{pmatrix} d_{z^2} \\ d_{xy} \\ d_{yz} \\ d_{xz} \\ d_{x^2-y^2} \end{pmatrix} = \underbrace{\begin{pmatrix} 0 & 0 & 1 & 0 & 0 \\ \frac{i}{\sqrt{2}} & 0 & 0 & 0 & \frac{-i}{\sqrt{2}} \\ 0 & \frac{i}{\sqrt{2}} & 0 & \frac{i}{\sqrt{2}} & 0 \\ 0 & \frac{1}{\sqrt{2}} & 0 & \frac{-1}{\sqrt{2}} & 0 \\ \frac{1}{\sqrt{2}} & 0 & 0 & 0 & \frac{1}{\sqrt{2}} \end{pmatrix}}_{\equiv \mathbf{T}_{Y_2^m \to X_{2c}}} \begin{pmatrix} Y_2^{-2} \\ Y_2^{-1} \\ Y_2^0 \\ Y_2^1 \\ Y_2^2 \end{pmatrix}, \tag{8.2.4}$$

and the transformation for $l = 1$ from $Y_1^m$ to $X_{1c}$ by

$$\begin{pmatrix} p_z \\ p_x \\ p_y \end{pmatrix} = \underbrace{\begin{pmatrix} 0 & 1 & 0 \\ \frac{1}{\sqrt{2}} & 0 & \frac{-1}{\sqrt{2}} \\ \frac{i}{\sqrt{2}} & 0 & \frac{i}{\sqrt{2}} \end{pmatrix}}_{\equiv \mathbf{T}_{Y_1^m \to X_{1c}}} \begin{pmatrix} Y_1^{-1} \\ Y_1^0 \\ Y_1^1 \end{pmatrix}. \tag{8.2.5}$$

Comparing the components of the angular momentum operators in the basis of the cubic harmonics for $l = 2$

$$L_x^{Y_2^m} = \mathbf{T}_{Y_2^m \to X_{2c}} \begin{pmatrix} 0 & 1 & 0 & 0 & 0 \\ 1 & 0 & \sqrt{\frac{3}{2}} & 0 & 0 \\ 0 & \sqrt{\frac{3}{2}} & 0 & \sqrt{\frac{3}{2}} & 0 \\ 0 & 0 & \sqrt{\frac{3}{2}} & 0 & 1 \\ 0 & 0 & 0 & 1 & 0 \end{pmatrix} \mathbf{T}^{-1}_{Y_2^m \to X_{2c}} = \begin{pmatrix} 0 & 0 & -i\sqrt{3} & 0 & 0 \\ 0 & 0 & 0 & i & 0 \\ i\sqrt{3} & 0 & 0 & 0 & i \\ 0 & -i & 0 & 0 & 0 \\ 0 & 0 & -i & 0 & 0 \end{pmatrix}, \tag{8.2.6}$$

$$L_y^{Y_2^m} = \mathbf{T}_{Y_2^m \to X_{2c}} \begin{pmatrix} 0 & i & 0 & 0 & 0 \\ -i & 0 & i\sqrt{\frac{3}{2}} & 0 & 0 \\ 0 & i\sqrt{\frac{3}{2}} & 0 & i\sqrt{\frac{3}{2}} & 0 \\ 0 & 0 & i\sqrt{\frac{3}{2}} & 0 & i \\ 0 & 0 & 0 & -i & 0 \end{pmatrix} \mathbf{T}^{-1}_{Y_2^m \to X_{2c}} = \begin{pmatrix} 0 & 0 & 0 & -i\sqrt{3} & 0 \\ 0 & 0 & i & 0 & 0 \\ 0 & -i & 0 & 0 & 0 \\ i\sqrt{3} & 0 & 0 & 0 & -i \\ 0 & 0 & 0 & i & 0 \end{pmatrix}, \tag{8.2.7}$$

$$L_z^{Y_2^m} = \mathbf{T}_{Y_2^m \to X_{2c}} \begin{pmatrix} -2 & 0 & 0 & 0 & 0 \\ 0 & -1 & 0 & 0 & 0 \\ 0 & 0 & 0 & 0 & 0 \\ 0 & 0 & 0 & 1 & 0 \\ 0 & 0 & 0 & 0 & 2 \end{pmatrix} \mathbf{T}^{-1}_{Y_2^m \to X_{2c}} = \begin{pmatrix} 0 & 0 & 0 & 0 & 0 \\ 0 & 0 & 0 & 0 & -2i \\ 0 & 0 & 0 & -i & 0 \\ 0 & 0 & i & 0 & 0 \\ 0 & 2i & 0 & 0 & 0 \end{pmatrix}, \tag{8.2.8}$$

with the operators for $l = 1$

$$L_x^{Y_1^m} = \mathbf{T}_{Y_1^m \to X_{1c}} \begin{pmatrix} 0 & \frac{1}{\sqrt{2}} & 0 \\ \frac{1}{\sqrt{2}} & 0 & \frac{1}{\sqrt{2}} \\ 0 & \frac{1}{\sqrt{2}} & 0 \end{pmatrix} \mathbf{T}_{Y_1^m \to X_{1c}} = \begin{pmatrix} 0 & 0 & -i \\ 0 & 0 & 0 \\ i & 0 & 0 \end{pmatrix}, \tag{8.2.9}$$

$$L_y^{Y_1^m} = \mathbf{T}_{Y_1^m \to X_{1c}} \begin{pmatrix} 0 & \frac{i}{\sqrt{2}} & 0 \\ \frac{-i}{\sqrt{2}} & 0 & \frac{i}{\sqrt{2}} \\ 0 & \frac{-i}{\sqrt{2}} & 0 \end{pmatrix} \mathbf{T}_{Y_1^m \to X_{1c}} = \begin{pmatrix} 0 & -i & 0 \\ i & 0 & 0 \\ 0 & 0 & 0 \end{pmatrix}, \tag{8.2.10}$$

$$L_z^{Y_1^m} = \mathbf{T}_{Y_1^m \to X_{1c}} \begin{pmatrix} -1 & 0 & 0 \\ 0 & 0 & 0 \\ 0 & 0 & 1 \end{pmatrix} \mathbf{T}_{Y_1^m \to X_{1c}} = \begin{pmatrix} 0 & 0 & 0 \\ 0 & 0 & i \\ 0 & -i & 0 \end{pmatrix}, \tag{8.2.11}$$

it can be seen that in the relevant subspace for $Sr_2RuO_4$ (the cubic harmonics basis set $X_{2c}$ without the elements $d_{z^2}$ and $d_{x^2-y^2}$) the angular momentum operators are the same up to a minus sign. Therefore, if we restrict ourselves to the subspace of the relevant three orbitals, the operators can be transformed with $-\mathbf{T}_{Y_1^m \to X_{1c}}$ according to a fictitious angular momentum $l = 1$ with an additional minus sign.
The transformation from the spherical harmonics to the $J$-basis can be derived via Clebsch-Gordan coefficients

$$\begin{pmatrix} q_{\frac{3}{2}} \\ q_{\frac{1}{2}} \\ q_{-\frac{1}{2}} \\ q_{-\frac{3}{2}} \\ d_{\frac{1}{2}} \\ d_{-\frac{1}{2}} \end{pmatrix} = \underbrace{\begin{pmatrix} 0 & 0 & 0 & 0 & 1 & 0 \\ 0 & 0 & \sqrt{\frac{2}{3}} & 0 & 0 & \frac{1}{\sqrt{3}} \\ \frac{1}{\sqrt{3}} & 0 & 0 & \sqrt{\frac{2}{3}} & 0 & 0 \\ 0 & 1 & 0 & 0 & 0 & 0 \\ 0 & 0 & \frac{-1}{\sqrt{3}} & 0 & 0 & \sqrt{\frac{2}{3}} \\ -\sqrt{\frac{2}{3}} & 0 & 0 & \frac{1}{\sqrt{3}} & 0 & 0 \end{pmatrix}}_{\equiv \mathbf{T}_{Y_1^m \to J}} \begin{pmatrix} Y_{2,\uparrow}^{-1} \\ Y_{2,\downarrow}^{-1} \\ Y_{2,\uparrow}^{0} \\ Y_{2,\downarrow}^{0} \\ Y_{2,\uparrow}^{1} \\ Y_{2,\downarrow}^{1} \end{pmatrix}. \tag{8.2.12}$$

With quantum numbers $l = 1$ and $s = 1/2$ for each single-particle state in $Y_1^m$, the $J$-basis has quantum numbers $j = l + s = 3/2$ (described by operators $q$) and $j = l - s = 1/2$ (described by the operators $d$) with corresponding $j_z$ values running from $j$ to $-j$ in integer steps. Combining the transformations from $X_{1c}$ to $Y_1^m$ and to the $J$-basis, we

obtain the complete transformation

$$\begin{pmatrix} q_{\frac{3}{2}} \\ q_{\frac{1}{2}} \\ q_{\frac{-1}{2}} \\ q_{\frac{-3}{2}} \\ d_{\frac{1}{2}} \\ d_{\frac{-1}{2}} \end{pmatrix} = \underbrace{\begin{pmatrix} 0 & 0 & \frac{-1}{\sqrt{2}} & 0 & \frac{-i}{\sqrt{2}} & 0 \\ \sqrt{\frac{2}{3}} & 0 & 0 & \frac{-1}{\sqrt{6}} & 0 & \frac{-i}{\sqrt{6}} \\ 0 & \sqrt{\frac{2}{3}} & \frac{1}{\sqrt{6}} & 0 & \frac{-i}{\sqrt{6}} & 0 \\ 0 & 0 & 0 & \frac{1}{\sqrt{2}} & 0 & \frac{-i}{\sqrt{2}} \\ \frac{-1}{\sqrt{3}} & 0 & 0 & \frac{-1}{\sqrt{3}} & 0 & \frac{-i}{\sqrt{3}} \\ 0 & \frac{1}{\sqrt{3}} & \frac{-1}{\sqrt{3}} & 0 & \frac{i}{\sqrt{3}} & 0 \end{pmatrix}}_{\equiv \mathbf{T} = \mathbf{T}_{Y_1^m \to J} \mathbf{T}^{-1}_{Y_1^m \to X_{1c}}} \begin{pmatrix} d_{xy,\uparrow} \\ d_{xy,\downarrow} \\ d_{yz,\uparrow} \\ d_{yz,\downarrow} \\ d_{xz,\uparrow} \\ d_{xz,\downarrow} \end{pmatrix}. \tag{8.2.13}$$

After we derived the transformation to the $J$-basis, we want to mention some advantages this representation offers. First, it can be shown that the SOC is a diagonal matrix in the new basis either by transforming the SOC term $\hat{H}_{\text{SOC}}$ from Eq. (8.1.9) to the $J$-basis with $\boldsymbol{T}$ or by evaluating Eq. (8.2.2) directly in the $J$-basis with the eigenvalues $J = 3/2$, $j_z = 1/2$, $L = 1$ and $S = 1/2$

$$\left(\vec{s}\vec{L}\right)^J = \begin{pmatrix} \frac{1}{2} & 0 & 0 & 0 & 0 & 0 \\ 0 & \frac{1}{2} & 0 & 0 & 0 & 0 \\ 0 & 0 & \frac{1}{2} & 0 & 0 & 0 \\ 0 & 0 & 0 & \frac{1}{2} & 0 & 0 \\ 0 & 0 & 0 & 0 & -1 & 0 \\ 0 & 0 & 0 & 0 & 0 & -1 \end{pmatrix}. \tag{8.2.14}$$

Since the SOC interaction strength for $Sr_2RuO_4$ ($\lambda = -0.11$eV) is comparatively small compared to the on-site energies of the orbitals $\bar{\varepsilon} \approx -5$, the spin-orbit coupling will, in general, not generate much entanglement. Unfortunately, the pair-hopping and pair spin-flip terms in the Hubbard-Kanamori Hamiltonian will consist of two-particle hopping terms between all impurity sites due to the structure of the transformation. The only constraint is that the $z$-component $J_z$ of the total angular momentum is conserved. Nevertheless, the Hubbard-Kanamori Hamiltonian consist of around a hundred terms in the $J$-basis and will create strong entanglement between the impurity sites independently of the spin-orbit coupling strength $\lambda$. Especially for higher values of $\lambda$ this is an advantage compared to the form of the impurity Hamiltonian in the basis of the cubic harmonics where stronger SOC leads to stronger single-particle interaction and therefore entanglement between the different bands.
Second, the interaction Hamiltonian in the $J$-basis is completely real. Thus, we can also assume that the Hamiltonian of the non-interacting bath and the coupling between bath and impurity sites is described by real parameters. This simplifies the fitting procedure of the hybridisation significantly. Finally, if the three bands of the model are completely degenerate, the single-particle term in $\hat{H}_{\text{int}}$ is proportional to a unit matrix and will keep its form under the transformation with $\boldsymbol{T}$. In this case, there exists no single-particle hopping between the impurity sites in the $J$-basis, leading to completely diagonal single-particle

Green's functions, self-energies, and hybridisations. This means that in the $J$-basis the computation and discretisation of the diagonal hybridisation is separated into the six bands, as in the case of the Hubbard model and $Sr_2VO_4$. The Hamiltonian in the $J$-basis for this case conserves the total number of particles described by an $U(1)$-symmetry and the $z$-component of the total angular momentum $\vec{J}$, which is another $U(1)$-symmetry.
However, the single-particle on-site energies of the impurity sites are not entirely degenerate for $Sr_2RuO_4$ since $\bar{\varepsilon}_{xy} \neq \bar{\varepsilon}_{yz} = \bar{\varepsilon}_{xz}$. Thus, transformed into the $J$-basis the first term of Eq. (8.1.1) takes on the form

$$\boldsymbol{\mu}^J = \boldsymbol{T} \begin{pmatrix} \bar{\varepsilon}_{xy}-\mu & 0 & 0 & 0 & 0 & 0 \\ 0 & \bar{\varepsilon}_{xy}-\mu & 0 & 0 & 0 & 0 \\ 0 & 0 & \bar{\varepsilon}_{yz}-\mu & 0 & 0 & 0 \\ 0 & 0 & 0 & \bar{\varepsilon}_{yz}-\mu & 0 & 0 \\ 0 & 0 & 0 & 0 & \bar{\varepsilon}_{xz}-\mu & 0 \\ 0 & 0 & 0 & 0 & 0 & \bar{\varepsilon}_{xz}-\mu \end{pmatrix} \boldsymbol{T}^{-1} \tag{8.2.15}$$

$$= \begin{pmatrix} a & 0 & 0 & 0 & 0 & 0 \\ 0 & b & 0 & 0 & d & 0 \\ 0 & 0 & b & 0 & 0 & -d \\ 0 & 0 & 0 & a & 0 & 0 \\ 0 & d & 0 & 0 & c & 0 \\ 0 & 0 & -d & 0 & 0 & c \end{pmatrix}. \tag{8.2.16}$$

From (8.2.16) one can see, that the single-particle hopping connects only impurity sites with the same quantum number $J_z$. Therefore the $U(1)$-symmetry of the $z$-component of $\vec{J}$ is still conserved.
In summary, in both the cubic harmonics and the $J$-basis the hybridisations, Green's functions, and self-energies of $Sr_2RuO_4$ have non-zero off-diagonal components. But the advantage of the $J$-basis is that there are only four instead of twelve non-zero components, and two $U(1)$-symmetries can be used instead of only a single one. Additionally, the form of the physical quantities is more symmetric, which can be used to reduce the amount of computations and the Hamiltonian is completely real. Out of those reasons we use the $J$-basis for $Sr_2RuO_4$ calculations.

## 8.3 Fitting of Matrix-Valued Hybridisations

As described in section 5 the usual form of the hybridisation,

$$\boldsymbol{\Delta}(z) = \sum_k \frac{\vec{V}_k^\dagger \vec{V}_k}{(z-\epsilon_k)}, \tag{8.3.1}$$

is also valid for matrix-valued hybridisations if the vector of hopping elements from bath site $k$ to each of the $N_{imp}$ impurities is defined as $\vec{V}_k = (V_{1k}\ V_{2k}\ \ldots\ V_{N_{imp}k})$ with $\vec{V}_k^\dagger$

being the transposed and complex conjugated vector of $\vec{V}_k$. For $Sr_2RuO_4$, the number of impurity sites is $N_k = 6$. Trying to fit the $6 \times 6$ matrix directly will result in unbearable computation times and in fits with relatively bad accuracy because of the high amount of parameters and bad convergence properties of the gradient descent methods due to numerous local minima. For example, if we consider three bath sites per impurity, we have in total 18 bath sites. This amounts into 18 parameters describing the on-site energies and $18 \cdot 6 = 98$ parameters describing the possible hopping elements. Because the SOC term in the Hamiltonian is complex, the hopping elements of the hybridisation should be considered to be complex too. In total there are 194 parameters to fit if real and imaginary part of the hopping elements are described by independent real numbers. This is a dramatic increase of parameters compared to the other models where typically six to 18 parameters are considered per fit.
However, as in the other models it is possible to decouple the problem into independent fits of parts of the hybridisation matrix. This reduces the number of parameters significantly and allows for better parallelisation. Fig. 8.2 shows a typical hybridisation for $Sr_2RuO_4$ in the basis of the cubic harmonics. It can be seen that the hybridisation couples the impurities 1, 4 and 6 and independently of them the impurities 2, 3 and 5. This means in the case of SOC we can decompose the problem into the fit of two $3 \times 3$ matrices. This will reduce the number of parameters in a single fit from 194 to 63 in our example. Because of the non-linearity of the problem this reduction will reduce the numerical effort significantly.
As can be seen in Fig. 8.3, the hybridisation has a better structure after switching to the $J$-basis. The form of the hybridisation allows to decouple the $6 \times 6$-matrix into two scalar functions and two $2 \times 2$-matrices. These sub-matrices can be fitted independently. Additionally, since the Hamiltonian in this basis is real, we can assume that the hybridisation can be described by real parameters only. Thus, in our example of three bath sites per impurity the $2 \times 2$-matrices can be fitted by 18 parameters. This is comparable to the amount of parameters in the other models we discussed in this thesis and where the fitting procedure poses no problems.
It is also noteworthy that the off-diagonals components of the hybridisation are one order of magnitude smaller in the basis of the cubic harmonics while they are only smaller by a factor of two in the $J$-basis. This can not be seen in the plots since we rescaled the components to improve the quality of the figure. Since the fitting procedure tries to minimise the distance between the fit and the original hybridisation, the quality of the results is better if all occurring quantities in the cost function $\chi$ are of the same order of magnitude. Else, the gradient descent method will focus on the components that are the largest because there even small deviations lead to big changes in $\chi$.
The symmetry between the components of the hybridisation in the $J$-basis seen in Fig. 8.3 is reflected in the parameters. While the fit of the components $\mathbf{\Delta}_{1,1}$ and $\mathbf{\Delta}_{4,4}$ results in the same parameters, the fit of the two $2 \times 2$ matrices produces on-site energies and hopping elements that differ by a minus sign. This can be used to reduce the numerical effort for the fitting procedure and at the same time increase the the quality of the results

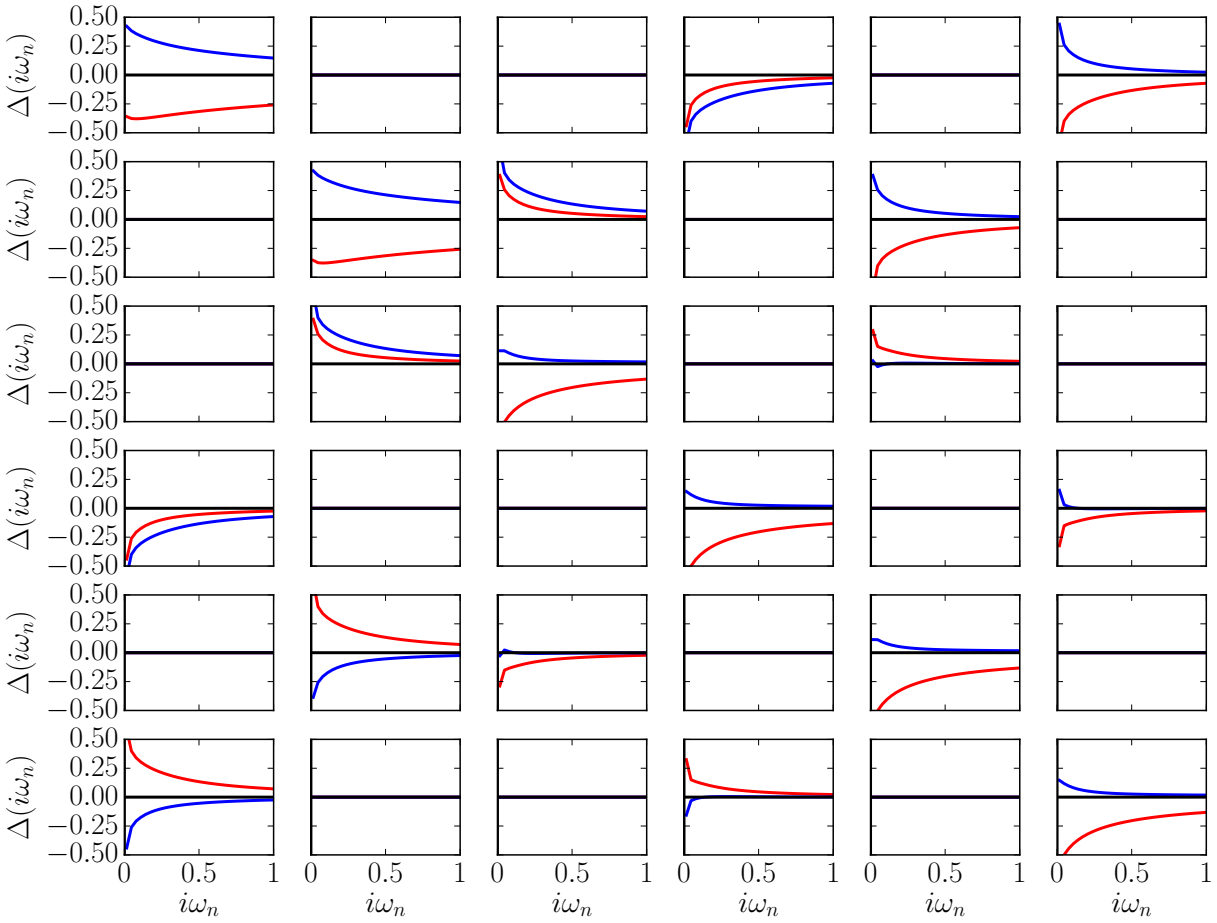


*Figure 8.2: Real (red lines) and imaginary (blue lines) parts of the components of the hybridisation* $\mathbf{\Delta}$ *in the basis of the cubic harmonics. The first two rows correspond to the spin-up and spin-down orbitals of the* $xy$*-band, the second and third to the orbitals of the* $yz$*-band and the last two to the orbitals of the* $xz$*-band. The columns are ordered in the same way. The off-diagonal components are smaller by a factor of ten compared to the diagonal elements. They are rescaled to the same order of magnitude to improve the quality of the plot. The matrix decouples into two independent* $3 \times 3$*-matrices consisting of the impurities* 1*,* 4 *and* 6 *and the impurities* 2*,* 3 *and* 5*. The hybridisation was obtained after convergence of the DMFT calculation.*

significantly. Note, this feature is up to now not implemented in our code and thus results displayed in this chapter are obtained without exploiting this symmetry. Nevertheless, it can be seen in the data that this symmetry is reproduced by our method to a very high degree.

Compared to the fitting procedure described in section 5.3.1 we only alter the method in one point when fitting matrix-valued functions. To improve the quality of the results we first fit only the diagonal elements of the hybridisation $\mathbf{\Delta}$ independently of each other and combine those results into a parameter set used as the starting point for the matrix fit. Since the off-diagonal components are small compared to the diagonal elements, it

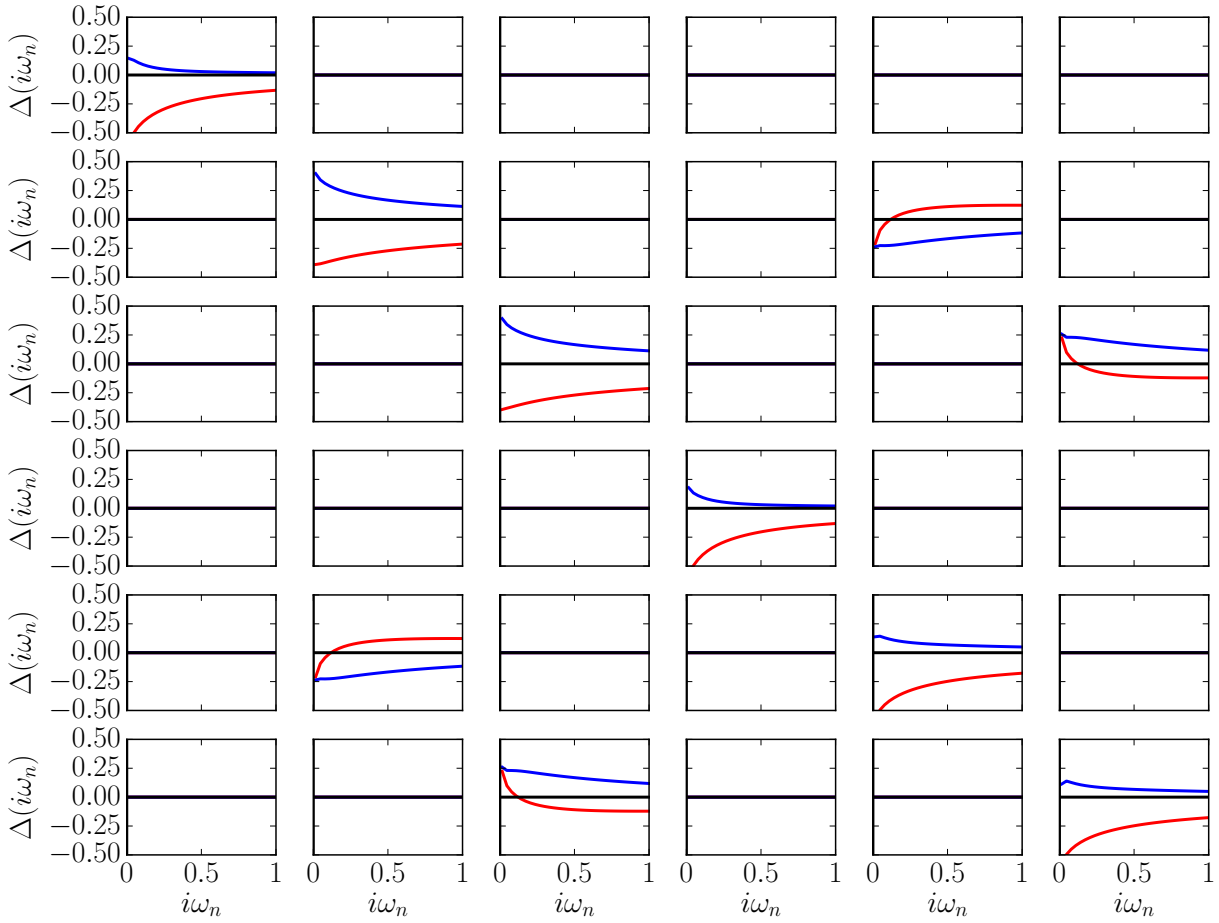


*Figure 8.3: Real (red lines) and imaginary (blue lines) parts of the components of the hybridisation* $\mathbf{\Delta}$ *in the J-basis. The first four rows correspond to the states with* $J = 3/2$ *and the last two to the states with* $J = 1/2$*, with descending* $J_z$ *quantum number respectively. The columns are ordered in the same way. The off-diagonal components are smaller by a factor of two compared to the diagonal elements. They are rescaled to improve the quality of the plot. The number of off-diagonal components is reduced significantly in his basis, namely from twelve to four. Additionally, they display a symmetry* $\mathbf{\Delta}_{25} = \mathbf{\Delta}_{52}$ *and* $\mathbf{\Delta}_{36} = -\mathbf{\Delta}_{63}$*. This symmetry is also reflected in the fitting parameters and can be exploited to reduce the numerical effort and improve the quality of the fitting results. The matrix decouples into two independent* $2 \times 2$*-matrices and two degenerate scalar functions. This allows to reduce the amount of parameters even further. The hybridisation was obtained after convergence of the DMFT calculation.*

seems reasonable that the resulting parameters are quite similar to the purely diagonal case. Good results could be obtained by performing 20 independent calculations, each consisting of fits of the diagonal elements with 100 iterations and followed by fits of the matrix-valued hybridisation with 50 iterations.

We end the description of the fitting procedure with a comparison of the fit results obtained with the three different ansatzes described in this section and with $L_b = 3$ bath

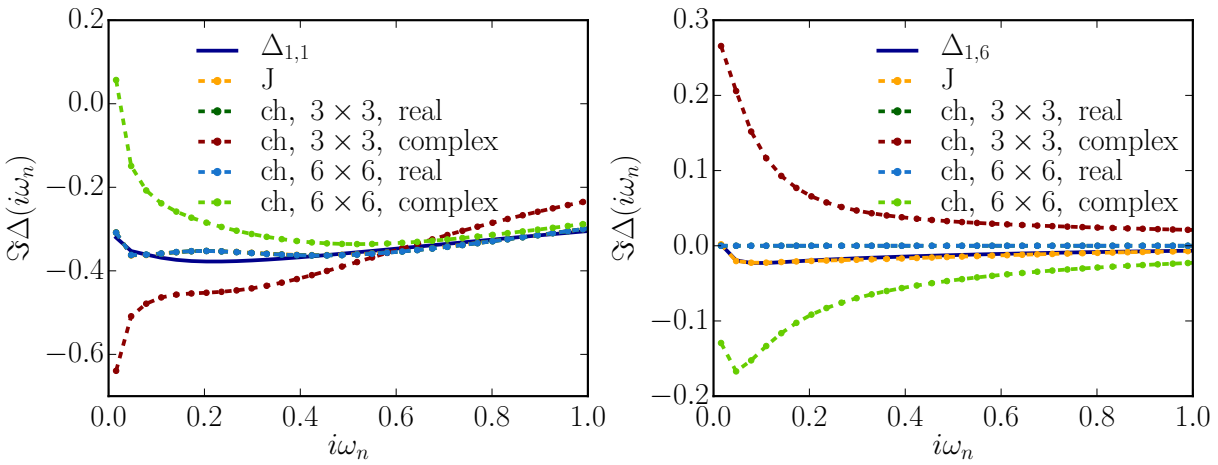


*Figure 8.4: Fit results obtained either in the $J$-basis or in the basis of the cubic harmonics with three bath sites per impurity for a diagonal (left) and an off-diagonal element of the hybridisation (right) in the basis of the cubic harmonics. For the fits in the basis of the cubic harmonics we distinguish between fitting the whole $6 \times 6$ matrix with complex and with real parameters. We also show results obtained by separating the problem into two $3 \times 3$ matrices and using either real or complex parameters. For the diagonal element we obtain similar good results for the fit in the $J$-basis and the two fits with real parameters, which are lying on top of each other. The results with the complex parameters are significantly off. For the off-diagonal component we again observe very good agreement with the fit in the $J$-basis. The real-parameter fit in the basis of the cubic harmonics produces curves nearly identical to zero and the complex results are again significantly off.*

sites. In Fig. 8.4 the results are displayed in the basis of the cubic harmonics. For the sake of completeness we perform fits in the basis of the cubic harmonics with complex as well as with real parameters. We only display a representative example of a diagonal and on off-diagonal element of $\mathbf{\Delta}$ and its fits to allow for more detailed plots. First of all we note that the fit in the $J$-basis, rotated back to the basis of the cubic harmonics, is the only result being in good agreement with $\mathbf{\Delta}$. While the fits in the basis of the cubic harmonics with real parameters give the same results for the diagonal elements they fail to describe the off-diagonal components because they are nearly identical to zero. The fit with the complex parameters results in non-zero off-diagonal elements but differs significantly from the hybridisation for the diagonal, as well as for the off-diagonal elements.
The complex fits are probably stuck in one of the numerous local minima due to the large amount of parameters while the real parameter fits are simply not able to reproduce all non-zeros off-diagonal elements. However, not only do we obtain better results with the fit in the $J$-basis, we are also considerably faster with this approach. The fit in the $J$-basis is 2.4 times faster compared to the fit of the decoupled $3 \times 3$ matrices with real parameters, 15 times faster compared to the fit with complex parameters, 11 times faster compared to the fit of the whole $6 \times 6$ matrix with real parameters, and 160 times faster

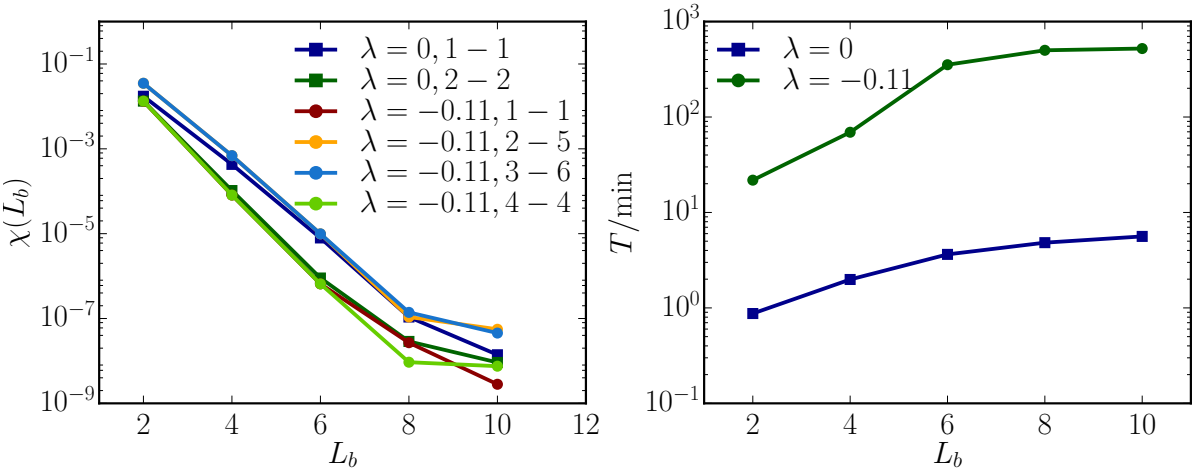


*Figure 8.5: Left panel: Cost function values $\chi$ of the fits of the hybridisation $\mathbf{\Delta}$ in the first DMFT calculation for different numbers of bath sites $L_b$. Squares indicate results for the fits of the scalar-valued hybridisations in the case of no spin-orbit coupling ($\lambda = 0eV$). In this case the hybridisation is a diagonal $3 \times 3$-matrix with $\mathbf{\Delta}_{11} \neq \mathbf{\Delta}_{22} = \mathbf{\Delta}_{33}$. The component $\mathbf{\Delta}_{ij}$ is denoted by $i-j$ in the legend. Circles denote results for the calculations with SOC ($\lambda = -0.11eV$), where the hybridisation can be fitted completely with two scalar functions $\mathbf{\Delta}_{11}$ and $\mathbf{\Delta}_{44}$ and two $2 \times 2$ matrix-valued functions. The latter are denoted with $2-5$ and $3-6$ in the plot. Right panel: Corresponding runtimes $T$ in minutes for both cases. The runtimes are increased by one up to two orders of magnitude if SOC is present. This fact is caused by the loss of symmetries and the additional off-diagonal components.*

compared to the fit of the whole $6 \times 6$ with complex parameters.
Concluding, the fitting procedure is better behaved, scales significantly better and gives better results in the $J$-basis than in the basis of the cubic harmonics. This strengthens our decision to perform all DMFT calculations with SOC in the $J$-basis.

## 8.4 Comparison between DMFT and CTQMC without SOC

We shortly want to mention some implementation related details of our DMFT computations before we now focus on the discussion of the obtained results. If not stated otherwise, all ground state search calculations are performed with a maximal bond dimension $m = 2000$. The time evolution is computed with the Krylov method up to $\tau_c = 4\mathrm{eV}^{-1}$ and afterwards with TDVP up to a maximal time $\tau_{\max} = 100$. We use a truncated weight $w = 10^{-9}$. The MPS used in the case without SOC are normal Hubbard sites with a local dimension of four, describing spin-down and spin-up electrons. In the case with SOC, the spin-degeneracy is lifted, which forces us to use separate sites for spin-up and spin-down

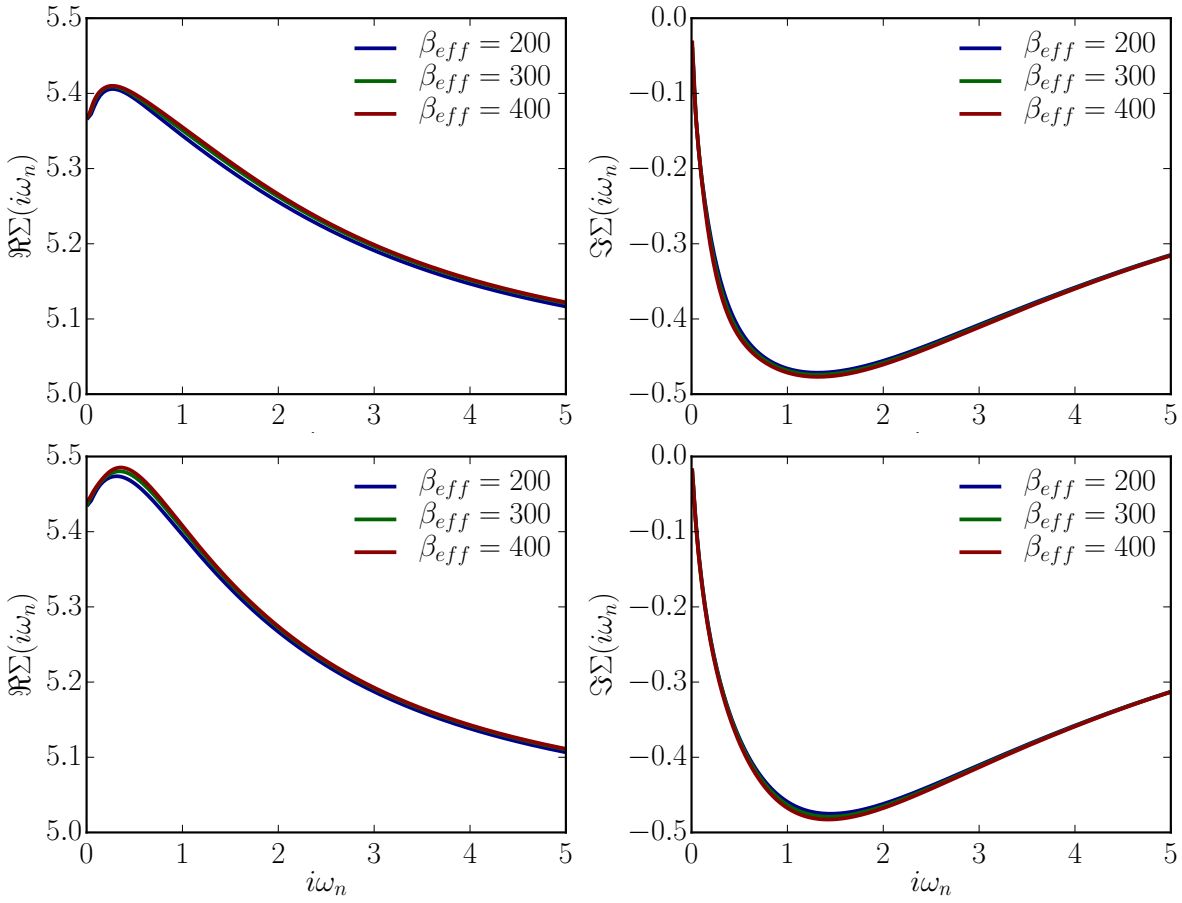


*Figure 8.6: Upper panels: Real (left) and imaginary (right) part of the converged self-energy for the xy band in the case $\lambda = 0eV$. The results are obtained by calculations that use different grid points defined by Matsubara frequencies $i\omega_n = (2n+1)\pi/\beta$. As described in chapter 5, the choice of the grid points changes the lower limit of the fitting interval of the hybridisation. This influences the Hamiltonian parameters and the resolution of the low-energy behaviour. Obviously, DMFT for this model and with these parameters is quite robust under changes of the grid points and results in similar self-energies. Lower panels: The same plot for the degenerate yz band. The data is obtained with $L_b = 4$ bath sites.*

particles with two local states describing a filled or an empty site, respectively. $Sr_2RuO_4$ is described by a Hubbard interaction strength $U = 2.3$eV, a Hund's coupling strength $J = 0.4$eV and a spin-orbit coupling strength $\lambda = 0.11$eV.
Before we focus on the DMFT calculations with spin-orbit coupling, we first want to compare our DMRG with CTQMC results obtained for $Sr_2RuO_4$ without SOC. This is interesting because it is the first comparison for imaginary-time DMRG as an impurity solver for a real material computation. Furthermore, it is the first time we use TRIQS to

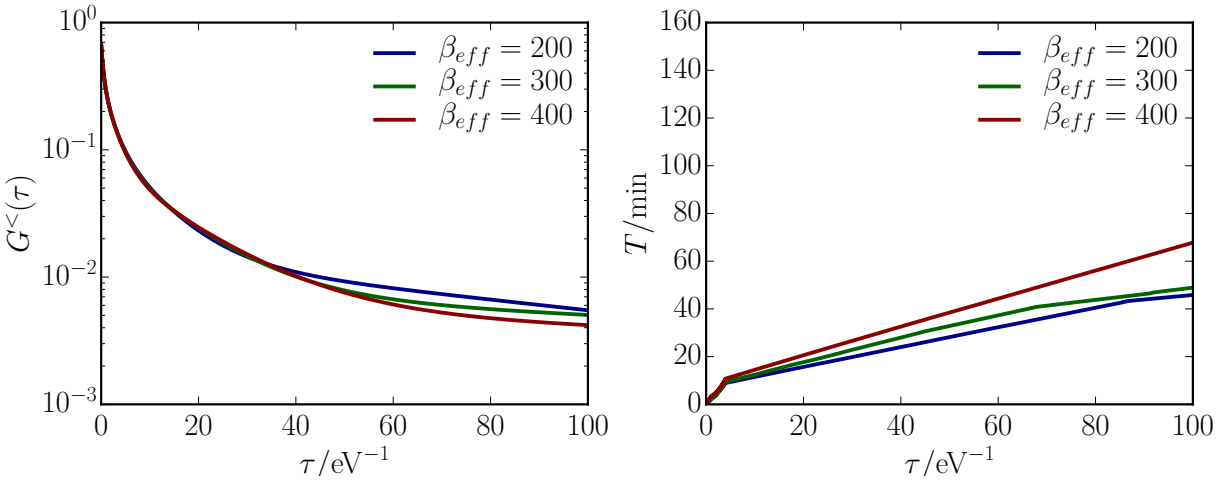


*Figure 8.7: Left panel: Time-dependent lesser Green's function $G^<(\tau)$ of the $yz$-band for different artificial temperatures $\beta_{eff}$ in the last iteration before convergence. Albeit the DMFT calculations give rise to the same self-energies, the $G^<(\tau)$ behave differently. The different choices of $\beta_{eff}$ change the lower bound of the fitting interval of the hybridisation, which effects merely the low-energy spectrum. Consequently, we see the biggest differences for large times. While the results for $\beta_{eff} = 200$ show linear behaviour from $\tau = 50$ on and the results for $\beta_{eff} = 300$ from $\tau = 80$ on, the lesser Green's function for $\beta_{eff} = 400$ either just started to decay linearly or still changes the decay rate slightly. Right panel: Corresponding runtimes $T$ to compute the lesser Green's functions from the left panel. We see a small increase of runtimes for larger $\beta_{eff}$. At $\tau_c = 4$ the Krylov evolution is replaced by TDVP, which can be seen clearly by the change of the slope. At the kinks around $\tau = 70$ and $\tau = 90$ the number of cores for the time evolution is increased. Up to those points all calculations are performed with the same number of cores.*

perform all DMFT related steps such as determining the dispersion relation from a DFT calculation, calculating the new hybridisation for the next iteration from the consistency equation, or computing the chemical potential from the self-energy such that the system exhibits the desired filling of $n = 4$ particles. In this context we also want to investigate the influence of the artificial temperature $\beta_{\mathrm{eff}}$, which we use to set up the discrete grid points for our continuous Green's functions, hybridisations and self-energies.
In Fig. 8.5 we compare cost function values and runtimes of the fitting procedure for $Sr_2RuO_4$ with and without spin-orbit coupling. At this point we only want to focus on the left panel and the fact that we obtain very good fitting results with $L_b = 8$ bath sites for both, the degenerate $yz$- as well as the $xy$-band. For more bath sites we see the onset of overfitting, which correspond to unreliable fit results and possible convergence problems. Accordingly, we choose $L_b = 8$ bath sites for all $Sr_2RuO_4$ calculations without SOC.
As described in chapter 5, the choice of the grid points used for describing physical quantities like the self-energy, the hybridisation, or the Green's function determines the resolution of the underlying physics in the model. Using higher values of $\beta_{\mathrm{eff}}$ shifts the

lower bound of the fitting interval of the hybridisation closer to zero. This forces the fit to emulate the low-energy physics more accurately, which can allow DMFT to resolve low-energy structures in the Green's function and hybridisation.
In Fig. 8.6 we display the converged self-energies for different choices of $\beta_{\text{eff}}$. We only observe very small differences and that the low-energy behaviour has not changed noteworthy. However, the increase of $\beta_{\text{eff}}$ comes not without cost. The on-site energies of the bath sites $\epsilon_k$ are typically pushed to smaller values if the lower bound of the fitting interval is lowered. In general, the $\epsilon_k$ set the smallest energy scale in the impurity Hamiltonian, which in turn strongly influences the long-time behaviour of the greater and lesser Green's functions. In Fig. 8.7 we show the Green's functions $G(\tau)$ corresponding to the self energies in Fig. 8.6 and the runtimes of the time evolutions needed to compute them. It can be seen clearly that the linear decay of $G(\tau)$ for large times sets in at later times for higher $\beta_{\text{eff}}$. Consequently, it is not surprising that DMFT with $\beta_{\text{eff}} = 400$ converges only after the maximal time up to which the time evolution is performed is increased from $\tau_{\max} = 100\text{eV}^{-1}$ to $\tau_{\max} = 300\text{eV}^{-1}$. This allows $G(\tau)$ to decay linearly sufficiently long for the linear prediction to produce correct results. Of course, this increases the runtime significantly. Additionally, each single time step of the time evolution takes longer if the artificial temperature is increased, which can be seen in the right panel of Fig. 8.7. Concluding, an increase of $\beta_{\text{eff}}$ increases computation times significantly and does not necessarily produces qualitatively different results. Since for $Sr_2RuO_4$ we cannot see any qualitative and only minor quantitative changes in the converged results, we will stick with $\beta_{\text{eff}} = 200$ for the following DMFT calculations.
After we have clarified the convergence of DMFT with respect to the number of bath sites and the artificial temperature $\beta_{\text{eff}}$, we can focus on the comparison between DMRG and CTQMC results. In Fig. 8.8 we show the converged Matsubara self-energy $\boldsymbol{\Sigma}(i\omega_n)$ obtained with CTQMC at temperature $\beta = 200$ and with DMRG at temperature $T = 0$. Overall, we observe very good agreement on the whole Matsubara axis with slightly bigger deviations for higher frequencies. For small frequencies, even after zooming-in, we see that both methods are in agreement. The very small differences are probably due to finite temperature effects.
We want to emphasise that is necessary to compute very dense grid points for $\boldsymbol{G}(\tau)$, at least for small times, so that the high-frequency behaviour of all physical functions is correct and in agreement with CTQMC. We ensure this by computing the time evolutions as described in chapter 5 with the Krylov method until $\tau_{\text{c}} = 4\text{eV}^{-1}$ and afterwards with TDVP. Effectively, we use a step size of $\delta\tau = 0.0005\text{eV}^{-1}$ for times $\tau < \tau_c$ and $\delta\tau = 0.1\text{eV}^{-1}$ for times $\tau > \tau_c$. The remaining differences between DMRG and CTQMC for higher frequencies may be reduced further by increasing $\tau_c$ or computing more dense values for $\boldsymbol{G}(\tau)$.
The drawback of using Krylov is a significant increase of numerical demands and the total runtime. In most of the calculations the time evolution with Krylov until $\tau_c = 4\text{eV}^{-1}$ is responsible for 33 percent of the runtime of the whole time evolution. The small frequency behaviour is not influenced by the choice of $\tau_c$ nor by moderate changes of the time step

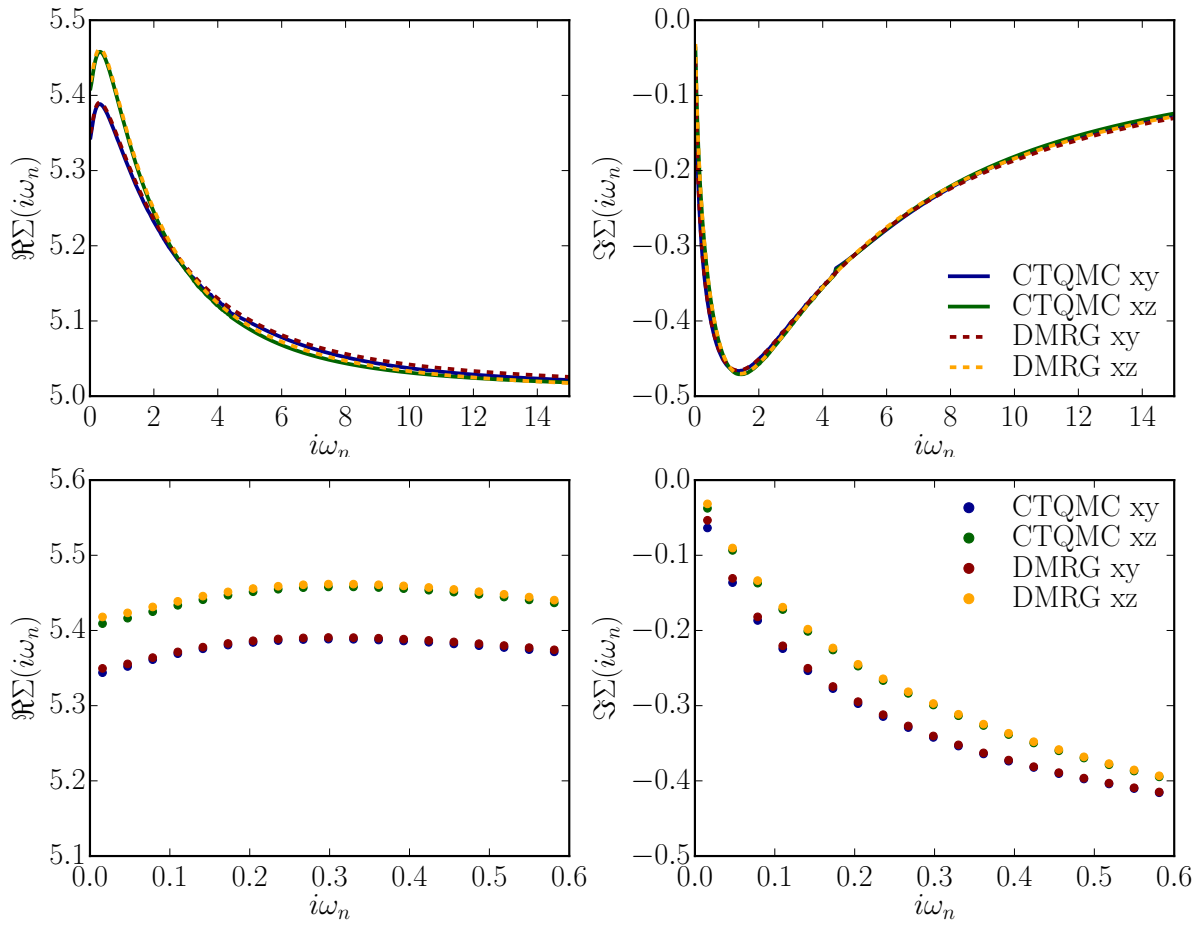


*Figure 8.8: Upper panels: Real (left) and imaginary (right) part of the converged Matsubara self-energy obtained with CTQMC and DMRG for the bands xy and xz in the case of no SOC. Lower panels: The same plot zoomed-in for small frequencies. The agreement between CTQMC and DMRG is extraordinary good. Small differences are probably due to temperature effects since CTQMC was running at temperature $\beta = 200$ and DMRG at $T = 0$.*

size. Consequently, the convergence of DMFT is independent of these parameters since it is only checked on the interval $\omega_n \in [0, 6]$. Therefore, we propose to converge DMFT while only using TDVP. After convergence an additional iteration is performed with the Krylov+TDVP approach. This guarantees the correct high-frequency behaviour of the Green's function and self-energies while keeping runtimes comparably low.

## 8.5 The Influence of Spin-Orbit Coupling

In this section we will focus on $Sr_2RuO_4$ with SOC and corresponding interaction strength $\lambda = -0.11$eV. In Fig. 8.5 we compare typical cost function values (left panel) and runtimes (right panel) for $Sr_2RuO_4$ with and without spin-orbit coupling. We observe that the scalar-valued components of the hybridisation are fitted slightly better in the presence of spin-orbit coupling then without, and that the matrix-valued elements are fitted slightly worse. This can partially be explained with the form of the cost function

$$\chi = \sum_n \omega_n^{-\alpha} ||\mathbf{\Delta}(i\omega_n) - \mathbf{\Delta}_{discr}(i\omega_n)||^2. \tag{8.5.1}$$

When using the Frobenius norm, the cost function for matrix-valued functions with dimension $n \times n$ consists of $n^2$ summands while a scalar fit only consists of one term. Thus, the value of $\chi$ is higher for a matrix-fit than for a scalar fit even if both fits have the same quality. Of course that can be countered by an appropriate pre-factor, which we have not included yet. Furthermore, fitting a matrix is obviously harder than fitting a scalar-function. If the components of the matrix have different orders of magnitude, fitting procedures tent to focus on the components with the largest amplitude, which can result in suboptimal fits. This can be countered by rescaling the smaller contributions in the cost function accordingly. However, up to now the fit results are so good that this approach does not seem necessary. We also assume that components of the matrix-values hybridisations with a higher amplitude are, in general, more important for the behaviour of the model. Consequently, they should have more weight in the cost function.
Similar to the case without SOC, overfitting sets in roughly at $L_b = 9$ bath sites. Unfortunately, the runtimes of the time evolutions with SOC increase so fast that a single DMFT iteration with $L_b = 4$ bath sites already take two days. The cost function values in this case are around $10^{-4}$, which is sufficient for our calculations but not optimal. However, due to the strong increase of runtimes we have to perform all following calculations including SOC with $L_b = 4$ bath sites.
The right panel Fig. 8.5 shows the runtimes of the fitting procedures in both cases, with and without SOC. First, it can be observed that the runtimes increase by up to two orders of magnitude when introducing spin-orbit coupling. Second, increasing the number of bath sites has only a small effect on the runtime in the case that no SOC is present but lead to a significant increase if spin-orbit coupling is there. This can be explained by the fact that a $6 \times 6$ instead of a $3 \times 3$ matrix has to be fitted because the spin-symmetry is gone. If off-diagonal components exist the scaling of the number of parameters is unfavourable. While in the case without SOC we have to consider two fits with $2 \cdot L_b$ parameters, in the case with SOC we have two fits of scalar functions with $2 \cdot L_b$ and two fits of matrix-valued functions with $6 \cdot L_b$ parameters. The scaling of the latter is the reason for the dramatic increase of the runtimes. The runtimes can be reduced by at least a factor of two by using the symmetries of the parameters as described in the previous section.
We now focus on the comparison between the converged self-energies with and without

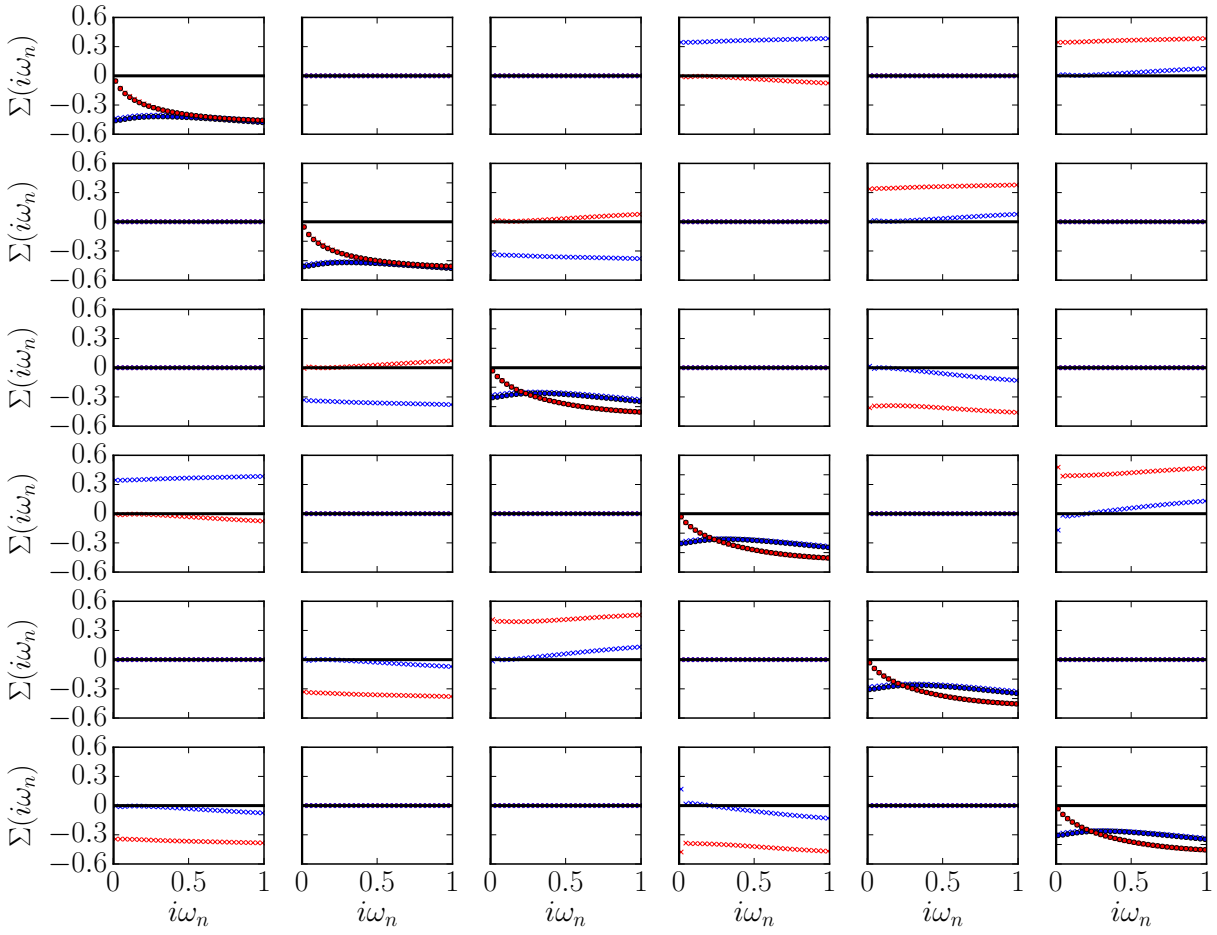


*Figure 8.9: Real (red lines) and imaginary (blue lines) parts of the components of the converged self-energy* $\mathbf{\Sigma}$ *in the basis of the cubic harmonics with SOC (crosses) and without (circles). The off-diagonal components are again smaller by a factor of ten compared to the diagonal elements and are rescaled with this factor. The real part of the self-energy on the diagonal is shifted by the on-site energy of the corresponding impurity site (*$\sim 5eV$*) to have both the real and imaginary part on the same scale. The agreement of the results obtained with and without spin-orbit coupling on the diagonal are extraordinary good. The off-diagonal components of the self-energy stay approximately constant in the displayed region of small frequencies. This is according to our expectations.*

spin-orbit coupling displayed in Fig. 8.9. The diagonal elements of the self-energy in both cases agree perfectly. The real part of the self-energy on the diagonals is shifted to smaller values by the corresponding on-site energy of the impurity to ensure a compact and detailed figure. The off-diagonal elements are multiplied by a factor of ten such that all pictures have the same scale. They display a symmetry that reflects the form of the

spin-orbit coupling Eq. (8.1.9) when we break up the symmetry of the components slightly

$$H_{\mathrm{SOC}} = \begin{pmatrix} 0 & 0 & 0 & -\frac{\lambda_{xy}}{2} & 0 & -\frac{i\lambda_{xy}}{2} \\ 0 & 0 & \frac{\lambda_{xy}}{2} & 0 & -\frac{i\lambda_{xy}}{2} & 0 \\ 0 & \frac{\lambda_{xy}}{2} & 0 & 0 & \frac{i\lambda_z}{2} & 0 \\ -\frac{\lambda_{xy}}{2} & 0 & 0 & 0 & 0 & -\frac{i\lambda_z}{2} \\ 0 & \frac{i\lambda_{xy}}{2} & -\frac{i\lambda_z}{2} & 0 & 0 & 0 \\ \frac{i\lambda_{xy}}{2} & 0 & 0 & \frac{i\lambda_z}{2} & 0 & 0 \end{pmatrix}. \tag{8.5.2}$$

$\lambda_{xy}$ and $\lambda_{xy}$ describe different couplings which we set to be similar $\lambda_{xy} = \lambda_z = \lambda$ for $Sr_2RuO_4$. We also observe that the off-diagonal elements are nearly frequency-independent for small frequencies. Thus, they can be considered as additional single-particle terms that can be added to the existing ones[56]. Since they correspond directly to the single-particle terms of the SOC with the same symmetry this leads to an effective correlation-enhanced SOC

$$\tilde{\lambda}_{xy} = \lambda + 2\Re\Sigma_{xy\uparrow,xz\downarrow}(i\omega_n) \approx 0.18\mathrm{eV}, \quad \text{and} \tag{8.5.3}$$

$$\tilde{\lambda}_z = \lambda + 2\Re\Sigma_{xz\uparrow,yz\uparrow}(i\omega_n) \approx 0.17\mathrm{eV}, \tag{8.5.4}$$

which is roughly enhanced by a factor of two compared to the bare SOC. Thus, our results are in agreement with CTQMC calculations at higher temperature with simplified models[56,181].

In some off-diagonal components we observe that the first Matsubara frequency is shifted significantly compared to the other frequencies. This originates from the relatively small number of bath sites $L_b = 4$ used in our calculations, which results in oscillating fit functions $\mathbf{\Delta}_{\mathrm{discr}}$. Unfortunately, the calculation with $L_b = 4$ already takes two days per iteration, and adding one bath site more per impurity increases the runtime to three up to four days. Considering the 20 iterations needed for convergence, it was not feasible to start another calculation at the end of this thesis.

## 8.6 Conclusion

We were able to show that DMRG+DMFT produces very good results for the three-band model of the real material $Sr_2RuO_4$ without SOC at zero temperature, which are in agreement with CTQMC results. For the calculations with spin-orbit coupling, we introduced a transformation from the basis of the cubic harmonics to the common eigenbasis of the total angular momentum $\vec{J}$, its $z$-component, the angular momentum $\vec{L}$, and the total spin $\vec{S}$. We showed that the fit of the $6 \times 6$ matrix describing the hybridisation decouples into the fit of two scalar functions and two $2 \times 2$ matrices in this new eigenbasis. Additionally, while the Hubbard-Kanamori Hamiltonian in the basis if the cubic harmonics is complex because of the SOC term, in the new basis the Hamiltonian is complete real again. Both advantages together are necessary to obtain very good fit results at relatively

short runtimes.
This allowed us to converge DMRG+DMFT calculations for $Sr_2RuO_4$ successfully with SOC and without any simplifications of the underlying model. Up to now a three-band model at low temperatures with spin-orbit coupling was not solvable with any kind of impurity solver. However, our results are in agreement with previously obtained results of CTQMC calculations of simplified models[56,181]. The off-diagonal parts of the self-energy are nearly constant for small frequencies and can be understand as a correlation-enhanced increase of the SOC by a factor slightly smaller than two.
The runtimes for DMRG+DMFT with SOC are roughly two days per iteration. Those runtimes can still be reduced by exploiting the symmetries in the model. Not only the degeneracy of the components in the hybridisation can be used to improve the fitting procedure but also the degeneracy of the Green's function components can be used to reduce the number of necessary time evolutions. With those tricks alone a reduction of runtimes by a factor of two is possible. Additionally, we recommend to investigate the influence of reordering on the performance. Since the model consist of 6 impurities with multiple interactions between the different bath sites considerable speed-ups are possible. With those improvements it should be possible to increase the number of bath sites per impurity and to improve the quality of the DMFT results.
For further research it is interesting to see which properties influence the structure of the off-diagonal components of the self-energy. By changing the filling of the lattice or the strength of the Hund's coupling $J$ it can be investigated which role the Hund's metal physics play and how robust observed features are under model changes. This can help to understand the origin of the self-energy behaviour with respect to SOC.
Furthermore, it is interesting to investigate the behaviour of $Sr_2RuO_4$ under compressive or tensile strain, which is supposed to influence superconductivity[189]. This can be achieved by changing the dispersion relation obtained from a previous DFT calculation. Should the degeneracy of the $xy$- and $yz$-band get lifted in this new setup, it is interesting to see whether the $J$-basis is still offering better performance compared to the basis of the cubic harmonics. In summarise, our methodological progress opens the possibility of investigating a wide range of questions regarding SOC and $Sr_2RuO_4$ that were not accessible before.

# Chapter 9

# Conclusion

In the beginning of this thesis, the idea to use DMRG as an impurity solver for DMFT on the imaginary-frequency axis was brand-new. Initial studies were performed on a complicated but still not realistic three-band model and showed impressive performance and high quality results on the imaginary axis that were in perfect agreement with results obtained with other solvers such as CTQMC. As it has been shown in this thesis, the step from describing an artificial system to describing a real material is more challenging than originally suspected. Thus, we introduced several improvements to DMRG ranging from methodological advancements for time evolution methods like Krylov to ideas originating from other fields such as restructuring the MPS lattice system. In addition, our implementation of several quantum numbers describing symmetries, so far considered as not being important in the Hubbard and Hubbard-Kanamori model, were key elements for ensuring convergence of DMFT in several cases. With all these improvements we were able to access systems and parameter regimes with DMRG +DMFT that are still out of reach for other solvers.

In the case of the Hubbard model we were able to produce results for intermediate interactions strengths and up to four cluster sites with DCA at moderate computation times. We showed that the numerical effort stays constant for systems with the same filling but different interaction strengths, which is impressive since CTQMC encounters more and more numerical problems when moving towards this regime. We also showed that increasing the number of patches for DCA decreases the number of bath sites needed for a good fit of the hybridisations. This partly counters the exponential growth of entanglement that we observe when considering larger cluster sizes in the context of DCA. Nevertheless, eight-site DCA calculations with DMRG are not possible so far due to the large runtimes we already encounter when searching for the global ground state.

To extend the analysis of the Hubbard model to DCA calculations with more than four patches, we suggest to minimise the entanglement of the impurity systems significantly by using other topologies for the lattice systems. Our work shows that large cluster systems suffer on two contradicting demands. The Hubbard interaction in momentum space generates strong entanglement between the different impurity sites. Therefore, it is preferable to locate these sites close together. The drawback is that this locates bath

sites far away from their associated impurity sites, which generates artificial long-range interactions. Additionally, higher order DCA calculations of the Hubbard model produce many patches that are degenerate. The bath sites associated to these degenerate impurity sites are very strongly entangled with each other. Thus, it is preferable to locate the bath sites close to the impurity sites for large cluster calculations. A different topology could fulfil both requirements and reduce runtimes significantly. A better initial setup of the DMRG ground state search based on ideas originating from quantum chemistry [21] should also lower the runtimes for global ground state searches noteworthy and is worth pursuing. It could also be interesting to investigate how the Green's functions of different patches change when the cluster sizes or the patching itself is altered. This can be used to find better starting hybridisations for the calculations and could lower the number of necessary iterations until convergence is reached. These ideas will be especially useful when the runtime of a single iteration increases significantly.

In the case of the layered perovskite $Sr_2VO_4$, we produced the first two-site DCA results of a realistic three-band model at zero temperature. Similarly to the Hubbard model, we observed that the amount of bath parameters needed for a good fit of the hybridisations is significantly smaller for the two-site DCA than for the single-site DMFT calculations. Therefore, albeit only calculations with two bath sites were possible in the two-site DCA case, we are sure that the results are reliable with respect the bath size. We observe that single-site DMFT and two-site DCA give similar results for the critical interaction strength that marks the onset of the Mott insulating behaviour of $Sr_2VO_4$. Thus, in contrast to expectations, the difference between experiment and theory is not reduced by partially reintroducing non-local interactions and the momentum-dependence of Green's functions.

The results obtained for the two-site DCA calculations can still be improved by introducing different bath sizes for different impurity sites. Some of the patches are fitted already with a very high quality while some are fitted more poorly for some choices of the chemical potential. The reliability of the results can be improved by only increasing the number of bath sites for those patches while keeping the runtimes relatively small. Nonetheless, we will expect only small changes of our results. This gives rise to the question whether a four-site DCA calculation supports our result that the onset of Mott insulating behaviour of $Sr_2VO_4$ is not changed significantly by introducing momentum-dependent self-energies and Green's function. Since significant differences between two-site and four-site DCA results in the case of the Hubbard-model can be observed, it is reasonable to suspect a similar behaviour for $Sr_2VO_4$. Unfortunately, a four-site DCA calculation of a three-band model would involve 12 impurity sites. Based on the runtimes of our calculations in the Hubbard model and for $Sr_2VO_4$, we believe that these four-site DCA calculations are only possible after further improvements of DMRG+DMFT. From our perspective, most promising are ansatzes involving a better topology structure of the impurity problem such as MSTs or METs which we discussed at the end of chapter 3.

The second real material we discussed was the perovskite oxide compound $Sr_2RuO_4$. It is described by a three-band model with Hubbard-Kanamori interaction and an addi-

tional term that describes spin-orbit coupling. This term breaks the spin symmetry of the impurity system and couples different orbitals with each other. While the former increases computation times, the second introduces off-diagonal components in self-energies Green's functions and hybridisations. The latter poses a not well-considered mathematical problem of fitting a matrix-valued function. We show that by introducing a suitable basis, the problem of fitting the matrix-valued hybridisation becomes much simpler. In this basis we reliably obtain reasonably good results for the matrix fit, which are much better than the ones obtained in original basis. Additionally, the calculations are much faster due to the better structure of the matrix. With this approach we were able to show that the diagonal elements of the converged self-energy of the system with and without the spin-orbit coupling term are in perfect agreement. The off-diagonal elements are nearly frequency-independent for small frequencies and can be interpreted as correlation-enhanced spin-orbit coupling of a factor slightly smaller than two. These results are in agreement with expectations based on simplified models. However, up to now no results existed for the Hubbard-Kanamori model with spin-orbit coupling without any kind of approximations.

For further research it is interesting to change the interaction strengths, the material filling and the dispersion relation. This could help to further understand the influence of SOC and whether its behaviour is robust or simply extraordinary in the case of $Sr_2RuO_4$. It is also interesting to see whether our ansatz of transforming the Hamiltonian into the eigenbasis of the angular momentum operator is still helpful when the degeneracy of the $xy$- and $yz$-band is lifted. Since we solved the material without making any kind of assumptions specific to $Sr_2RuO_4$, these studies should pose no problems.

Concluding, we improved the DMRG+DMFT method in many areas to an extent that we were able to access regimes and problems that were not solvable with any other impurity solver up to now. However, albeit we already implemented several improvements with great success, many ideas we mentioned in this thesis are very promising and have not been implemented so far and should be further exploited to tackle new materials and more complex configurations. In this regard, we also want to mention the PhD thesis of Alex Wolf[190] where many other ideas are presented that we have not pursued so far. Particularly promising are ideas found in quantum chemistry and are based on entanglement analyses. In this field, DMRG calculation of highly complex and strongly entangled Hamiltonians with up to 50 sites are performed while in this thesis we started to encounter problems for systems with around 24 sites. The difference suggest that there are still significant improvements possible. With all the progress we made during the last years, we are confident that DMRG has established itself already now as a trustworthy and promising impurity solver for multi-band and larger-cluster DMFT problems. Following some of the more encouraging ideas, it could be possible in near future to calculate three-band problems with four-site DCA or systems with more bands and two-site DCA. These are important steps forward, to tackle, for example, pnictide superconductors, which are believed to be described by five-band models and at least two momentum patches. These kind of models are so far out of reach with any other impurity solver.

# Acknowledgements

This work would not have been achieved without the support and influence of several people. In particular, I want to thank the following

- Ulrich Schollwöck from the LMU Munich for the opportunity to work on this PhD, his mentoring and support. Several of the ideas developed in this thesis originate from his questions, comments and suggestions. I also want to thank him for trusting me to give his lectures when he was ill or indisposed and his support in all the small things that occur during and especially in the end of an PhD.

- Dieter Vollhardt from the University of Augsburg for examining this thesis.

- Andrew Millis from the Columbia University of New York for his invaluable insights on real materials and more specifically on our projects regarding the Vanadates and the Hubbard model. I also want to thank him for hosting me several times in New York at the Columbia University, the annual conferences of the Many Electron Problem of the Simons Foundation and the Flatiron Institute.

- Claudius Hubig, now at the Max-Planck-Institut für Quantenoptik in Munich, for numerous things: the impressive DMRG toolkit he programmed and maintains and which is the fundament of this thesis; the countless situations where he helped me with programming and compiling C++ code for the toolkit and other IT related problems; the very helpful discussions about physics; and the small things he did by adapting the toolkit to my very special DMFT needs.

- Manuel Zingl from the Flatiron Institute in New York for his wonderful support, unlimited patience and the delightful and enlightening discussions in the context of the ruthenate project.

- Ara Go for her very useful insights regarding DMFT and the spin-orbit coupling in particular. Without her suggestions the Ruthenate project would not have been so successful in such a short time.

- Alex Wolf for the foundation of this PhD, the discussions about DMFT and useful tips for further research that set some tracks of this thesis.

- Cordula Weber for not only being an impressive help regarding all administrative issues in our group but also for her being a great support, cheering me up on several occasions and for just being there to talk to.

- Ralph Simmler, Klaus Steinberger, Daniela Aldea, Ralph Heuer and Veronika Finsterwalder for making sure that our computers and cluster were working.

- Inés de Vega for being the best office mate one can wish for during a PhD. She not only encouraged and supported me on uncountable times, made fun with and of me, discussed with me about physics, philosophy, politics and society but also corrected all introductions of this thesis. Overall, she influenced my personal development during this PhD the most.

- Katharine Stadler, Frauke Schwarz, Benedikt Bruognolo and other residents of the fourth floor for very nice discussions regarding physics and other topics.

- Jennifer Kennes for doing the incredible job of correcting 100 pages of this PhD. I doubt I can ever repay this.

- Sara Milosevic for all the fun I had with here during the last five years in and outside of the university. She also did an impressive job in correcting two chapters.

- Dante Kennes, Antonia Prantl and Andrew Hayward for correcting chapters of the PhD.

- All my friends here in Munich. They made this city a second home for me and were a constant source of happiness, which was definitely necessary during the last years. In particular, I want to thank Sarah Brei for her essential support during the last years. Without her this thesis would probably not exist.

- Leonie Tief for supporting me during the last months. The time when every PhD student despairs the most, is the time where support is most needed and the hardest to give. She did a wonderful job.

- Ute Linden, Ernst Reiner Linden, and Sven Classen for their constant support and believe that I will master every challenge and finish this PhD successfully. Only due to them I have achieved so much.

# List of Figures

# List of Tables

# Bibliography


[1] S. Okamoto and A. J. Millis, *Electronic reconstruction at an interface between a Mott insulator and a band insulator*, Nature **428**, 630 (2004).

[2] A. J. Millis and D. G. Schlom, *Electron-hole liquids in transition-metal oxide heterostructures*, Phys. Rev. B **82**, 073101 (2010).

[3] E. Assmann, P. Blaha, R. Laskowski, K. Held, S. Okamoto and G. Sangiovanni, *Oxide Heterostructures for Efficient Solar Cells*, Phys. Rev. Lett. **110**, 078701 (2013).

[4] S. Graser, P. J. Hirschfeld, T. Kopp, R. Gutser, B. M. Andersen and J. Mannhart, *How grain boundaries limit supercurrents in high-temperature superconductors*, Nature Physics **6**, 609 (2010).

[5] F. A. Wolf, S. Graser, F. Loder and T. Kopp, *Supercurrent through Grain Boundaries of Cuprate Superconductors in the Presence of Strong Correlations*, Phys. Rev. Lett. **108**, 117002 (2012).

[6] J. P. F. LeBlanc, A. E. Antipov, F. Becca, I. W. Bulik, G. K.-L. Chan, C.-M. Chung, Y. Deng, M. Ferrero, T. M. Henderson, C. A. Jiménez-Hoyos, E. Kozik, X.-W. Liu *et al.*, *Solutions of the Two Dimensional Hubbard Model: Benchmarks and Results from a Wide Range of Numerical Algorithms*, Phys. Rev. X **5**, 041041 (2015).

[7] T. Valla, A. V. Fedorov, P. D. Johnson, B. O. Wells, S. L. Hulbert, Q. Li, G. D. Gu and N. Koshizuka, *Evidence for Quantum Critical Behavior in the Optimally Doped Cuprate* $Bi_2Sr_2CaCu_2O_{8+\delta}$, Science **285**(5436), 2110 (1999).

[8] A. G. Loeser, Z.-X. Shen, D. S. Dessau, D. S. Marshall, C. H. Park, P. Fournier and A. Kapitulnik, *Excitation Gap in the Normal State of Underdoped* $Bi_2Sr_2CaCu_2O_{8+\delta}$, Science **273**(5273), 325 (1996).

[9] O. Parcollet, G. Biroli and G. Kotliar, *Cluster Dynamical Mean Field Analysis of the Mott Transition*, Phys. Rev. Lett. 92 **92**, 226402 (2004).

[10] A. Comanac, L. de' Medici, M. Capone and A. J. Millis, *Optical conductivity and the correlation strength of high-temperature copper-oxide superconductors*, Nature Physics **4**, 287 (2008).

[11] M. Imada, A. Fujimori and Y. Tokura, *Metal-insulator transitions*, Rev. Mod. Phys. **70**(4), 1039 (1998).

[12] J. Mravlje, M. Aichhorn, T. Miyake, K. Haule, G. Kotliar and A. Georges, *Coherence-Incoherence Crossover and the Mass-Renormalization Puzzles in $Sr_2RuO_4$*, Phys. Rev. Lett. **106**, 096401 (2011).

[13] S. R. White, *Density matrix formulation for quantum renormalization groups*, Phys. Rev. Lett. **69**(19), 2863 (1992).

[14] M. Caffarel and W. Krauth, *Exact diagonalization approach to correlated fermions in infinite dimensions: Mott transition and superconductivity*, Phys. Rev. Lett. **72**(10), 1545 (1994).

[15] A. N. Rubtsov, V. V. Savkin and A. I. Lichtenstein, *Continuous-time quantum Monte Carlo method for fermions*, Phys. Rev. B **72**(3), 035122 (2005).

[16] G. Knizia and G. K.-L. Chan, *Density matrix embedding: A simple alternative to dynamical mean-field theory*, Phys. Rev. Lett. **109**, 186404 (2012).

[17] F. A. Wolf, J. A. Justiniano, I. P. McCulloch and U. Schollwöck, *Spectral functions and time evolution from the Chebyshev recursion*, Phys. Rev. B **91**, 115144 (2015).

[18] K. M. Stadler, A. Weichselbaum, Z. P. Yin, J. von Delft and G. Kotliar, *DMFT+NRG study of spin-orbital separation in a three-band Hund's metal*, Phys. Rev. Lett. **115**, 136401 (2015).

[19] G. . V. Evenbly, *Tensor Network States and Geometry*, J Stat Phys **145**(4), 891 (2011).

[20] D. Zgid and G. K.-L. Chan, *Dynamical mean-field theory from a quantum chemical perspective*, The Journal of Chemical Physics **134**(9), 094115 (2010).

[21] S. Szalay and O. Legeza, *Tensor product methods and entanglement optimization for ab initio quantum chemistry*, Int. J. Quant. Chem. **115**, 1342 (2015).

[22] G. Carleo and M. Troyer, *Solving the Quantum Many-Body Problem with Artificial Neural Networks*, Science **355**(6325), 602 (2017).

[23] X. Gao and L.-M. Duan, *Efficient representation of quantum many-body states with deep neural networks*, Nature Communications **8**(1), 662 (2017).

[24] J. Greitemann, K. Liu and L. Pollet, *Probing Hidden Spin Order with Interpretable Machine Learning*, arXiv (2018).

[25] H. Shen, J. Liu and L. Fu, *Self-learning Monte Carlo with deep neural networks*, Phys. Rev. B **97**, 205140 (2018).

[26] C. Gross and I. Bloch, *Quantum simulations with ultracold atoms in optical lattices*, Science **357**(6355), 995 (2017).

[27] H. Lin and J. Gubernatis, *Exact Diagonalization Methods for Quantum Systems*, Computers in Physics **7**, 400 (1993).

[28] N. Gubernatis, J. amd Kawashima and P. Werner, *Quantum Monte Carlo Methods: Algorithms for Lattice Models*, Cambridge University Press (2016).

[29] W. Metzner and D. Vollhardt, *Correlated Lattice Fermions in $d = \infty$ Dimensions*, Physical Review Letters **62**(3), 324 (1989).

[30] A. Georges and G. Kotliar, *Hubbard model in infinite dimensions*, Phys. Rev. B **45**(12), 6479 (1992).

[31] A. Georges, G. Kotliar, W. Krauth and M. J. Rozenberg, *Dynamical mean-field theory of strongly correlated fermion systems and the limit of infinite dimensions*, Rev. Mod. Phys. **68**(1), 13 (1996).

[32] T. Maier, M. Jarrell, T. Pruschke and M. Hettler, *Quantum cluster theories*, Rev. Mod. Phys. **77**(3), 1027 (2005).

[33] G. Kotliar, S. Savrasov, K. Haule, V. Oudovenko, O. Parcollet and C. Marianetti, *Electronic structure calculations with dynamical mean-field theory*, Reviews of Modern Physics **78**(3), 865 (2006).

[34] E. Gull, A. J. Millis, A. I. Lichtenstein, A. N. Rubtsov, M. Troyer and P. Werner, *Continuous-time Monte Carlo methods for quantum impurity models*, Rev. Mod. Phys. **83**(2), 349 (2011).

[35] K. G. Wilson, *The renormalization group: Critical phenomena and the Kondo problem*, Rev. Mod. Phys. **47**(4), 773 (1975).

[36] D. J. García, K. Hallberg and M. J. Rozenberg, *Dynamical Mean Field Theory with the Density Matrix Renormalization Group*, Phys. Rev. Lett. **93**(24), 246403 (2004).

[37] D. Zgid, E. Gull and G. K.-L. Chan, *Truncated Configuration Interaction expansions as solvers for correlated quantum impurity models and dynamical mean field theory*, Phys. Rev. B **86**, 165128 (2012).

[38] Y. Lu, M. Höppner, O. Gunnarsson and M. W. Haverkort, *Efficient real-frequency solver for dynamical mean-field theory*, Phys. Rev. B **90**(8), 085102 (2014).

[39] S. Nishimoto and E. Jeckelmann, *Density-matrix renormalization group approach to quantum impurity problems*, J. Phys.: Condens. Matter **16**(4), 613 (2004).

[40] D. Bauernfeind, M. Zingl, R. Triebl, M. Aichhorn and H. G. Evertz, *Fork Tensor-Product States: Efficient Multiorbital Real-Time DMFT Solver*, Physical Review X **7**, 031013 (2017).

[41] R. J. Baxter, *Dimers on a Rectangular Lattice*, Journal of Mathematical Physics **9**(4), 650 (1968).

[42] I. V. Oseledets, *Tensor-Train Decomposition*, SIAM J. Sci. Comput. **33**(5), 2295 (2011).

[43] U. Schollwöck, *The density-matrix renormalization group in the age of matrix product states*, Annals of Physics **326**, 96 (2011).

[44] N. Nakatani and G. K.-L. Chan, *Efficient tree tensor network states (ttns) for quantum chemistry: Generalizations of the density matrix renormalization group algorithm*, The Journal of Chemical Physics **138**, 134113 (2013).

[45] G. Vidal, *Efficient Simulation of One-Dimensional Quantum Many-Body Systems*, Phys. Rev. Lett. **93**, 040502 (2004).

[46] J. Haegeman, C. Lubich, I. Oseledets, B. Vandereycken and F. Verstraete, *Unifying time evolution and optimization with matrix product states*, Phys. Rev. B **94**, 165116 (2016).

[47] Y. Saad, *Iterative Methods for Sparse Linear Systems*, Society for Industrial and Applied Mathematics, 2nd edn. (2003).

[48] A. Macridin, M. Jarrell, T. Maier, P. R. C. Kent and E. DAzevedo, *Pseudogap and Antiferromagnetic Correlations in the Hubbard Model*, Phys. Rev. Lett. **97**, 036401 (2006).

[49] C. Berthod, T. Giamarchi, S. Biermann and A. Georges, *Breakup of the Fermi Surface Near the Mott Transition in Low-Dimensional Systems*, Phys. Rev. Lett. **97**, 136401 (2006).

[50] M. Ferrero, P. S. Cornaglia, L. De Leo, O. Parcollet, G. Kotliar and A. Georges, *Pseudogap opening and formation of Fermi arcs as an orbital-selective Mott transition in momentum space*, Physical Review B **80**(6), 064501 (2009).

[51] P. Werner, E. Gull and A. J. Millis, *Metal-Insulator phase diagram and orbital selectivity in 3-orbital models with rotationally invariant Hund coupling*, Phys. Rev. B **79**, 115119 (2009).

[52] P. W. Anderson, *The Theory of Superconductivity in the High-$T_c$ Cuprate Superconductors*, Princeton University Press (1997).

[53] E. Gull, M. Ferrero, O. Parcollet, A. Georges and A. J. Millis, *Momentum-space anisotropy and pseudogaps: A comparative cluster dynamical mean-fieldanalysis of the doping-driven metal-insulator transition in the two-dimensional Hubbard model*, Phys. Rev. B **82**, 155101 (2010).

[54] J. Matsuno, Y. Okimoto, M. Kawasaki and Y. Tokura, *Variation of the Electronic Structure in Systematically Synthesized $Sr_2MO_4$ ( M = Ti , V, Cr, Mn, and Co)*, Physical Review Letters **95**(17), 176404 (2005).

[55] H. Chen, H. Park, A. J. Millis and C. A. Marianetti, *Charge transfer across transition metal oxide interfaces: emergent conductance and new electronic structure*, Phys. Rev. B **90**, 245138 (2014).

[56] G. Zhang, E. Gorelov, E. Sarvestani and E. Pavarini, *Fermi Surface of $Sr_2RuO_4$: Spin-Orbit and Anisotropic Coulomb Interaction Effects*, Phys. Rev. Lett. **116**, 106402 (2016).

[57] C. Hubig, *Symmetry-Protected Tensor Networks*, Ph.D. thesis, Ludwig-Maximilians-Universität München (2017).

[58] R. J. Baxter, *Variational approximations for square lattice models in statistical mechanics*, Journal of Statistical Physics **19**(5), 461 (1978).

[59] I. Affleck, T. Kennedy, E. H. Lieb and H. Tasaki, *Rigorous results on valence-bond ground states in antiferromagnets*, Phys. Rev. Lett. **59**, 799 (1987).

[60] M. Fannes, B. Nachtergaele and R. F. Werner, *Finitely correlated states on quantum spin chains*, Communications in Mathematical Physics **144**(3), 443 (1992).

[61] A. Klümper, A. Schadschneider and J. Zittartz, *Matrix Product Ground States for One-Dimensional Spin-1 Quantum Antiferromagnets*, EPL (Europhysics Letters) **24**(4), 293 (1993).

[62] A. Kolezhuk, R. Roth and U. Schollwöck, *First Order Transition in the Frustrated Antiferromagnetic Heisenberg $S = 1$ Quantum Spin Chain*, Phys. Rev. Lett. **77**, 5142 (1996).

[63] A. K. Kolezhuk, H.-J. Mikeska and S. Yamamoto, *Matrix-product-states approach to Heisenberg ferrimagnetic spin chains*, Phys. Rev. B **55**, R3336 (1997).

[64] S. Östlund and S. Rommer, *Thermodynamic Limit of Density Matrix Renormalization*, Phys. Rev. Lett. **75**, 3537 (1995).

[65] J. Dukelsky, M. A. Martin-Delgado, T. Nishino and G. Sierra, *Equivalence of the variational matrix product method and the density matrix renormalization group applied to spin chains*, EPL (Europhysics Letters) **43**(4), 457 (1998).

[66] F. Verstraete and J. I. Cirac, *Renormalization algorithms for Quantum-Many Body Systems in two and higher dimensions*, ArXiv pp. cond–mat/0407066 (2004).

[67] F. Verstraete and J. I. Cirac, *Matrix product states represent ground states faithfully*, Phys. Rev. B **73**(9), 094423 (2006).

[68] S. R. White and A. E. Feiguin, *Real time evolution using the density matrix renormalization group*, Phys. Rev. Lett. **93**, 076401 (2004).

[69] M. C. Bañuls, M. B. Hastings, F. Verstraete and J. I. Cirac, *Matrix Product States for Dynamical Simulation of Infinite Chains*, Phys. Rev. Lett. **102**, 240603 (2009).

[70] P. Pippan, S. R. White and H. G. Evertz, *Efficient matrix-product state method for periodic boundary conditions*, Phys. Rev. B **81**, 081103 (2010).

[71] G. Vidal, *Entanglement Renormalization*, Physical Review Letters **99**(22), 220405 (2007).

[72] F. Verstraete and J. I. Cirac, *Continuous Matrix Product States for Quantum Fields*, Phys. Rev. Lett. **104**, 190405 (2010).

[73] J. Eisert, M. Cramer and M. B. Plenio, *Area laws for the entanglement entropy*, Rev. Mod. Phys. **82**, 277 (2010).

[74] E. Stoudenmire and S. R. White, *Studying Two-Dimensional Systems with the Density Matrix Renormalization Group*, Annual Review of Condensed Matter Physics **3**(1), 111 (2012).

[75] P. Corboz, *Variational optimization with infinite projected entangled-pair states*, Phys. Rev. B **94**, 035133 (2016).

[76] J. Jordan, R. Orús, G. Vidal, F. Verstraete and J. I. Cirac, *Classical Simulation of Infinite-Size Quantum Lattice Systems in Two Spatial Dimensions*, Phys. Rev. Lett. **101**, 250602 (2008).

[77] M. Srednicki, *Entropy and area*, Phys. Rev. Lett. **71**, 666 (1993).

[78] I. Peschel, M. Kaulke and O. Legeza, *Density-matrix spectra for integrable models*, Ann. Phys. (Leipzig) **8**, 153 (1999).

[79] M.-C. Chung and I. Peschel, *Density-matrix spectra of solvable fermionic systems*, Phys. Rev. B (2001).

[80] E. M. Stoudenmire and S. R. White, *Minimally entangled typical thermal state algorithms*, New J. Phys **12**, 055026 (2010).

[81] U. Schollwöck, *The density-matrix renormalization group*, Rev. Mod. Phys. **77**(1), 259 (2005).

[82] K. A. Hallberg, *Density matrix algorithm for the calculation of dynamical properties of low dimensional systems*, Phys. Rev. B **52**, 9827 (1995).

[83] T. D. Kühner and S. R. White, *Dynamical correlation functions using the density matrix renormalization group*, Phys. Rev. B **60**(1), 335 (1999).

[84] E. Jeckelmann, *Dynamical density-matrix renormalization-group method*, Phys. Rev. B **66**, 045114 (2002).

[85] I. McCulloch, *Collective Phenomena in Strongly Correlated Systems*, Ph.D. thesis, Canberra (2001).

[86] I. P. McCulloch, *From density-matrix renormalization group to matrix product states*, Journal of Statistical Mechanics: Theory and Experiment **2007**(10), P10014 (2007).

[87] A. Weichselbaum, *Non-abelian symmetries in tensor networks: A quantum symmetry space approach*, Annals of Physics **327**(12), 2972 (2012).

[88] O. Legeza and J. Sólyom, *Optimizing the density-matrix renormalization group method using quantum information entropy*, Phys. Rev. B **68**, 195116 (2003).

[89] G. Barcza, O. Legeza, K. H. Marti and M. Reiher, *Quantum-information analysis of electronic states of different molecular structures*, Phys. Rev. A **83**, 012508 (2011).

[90] V. Murg, F. Verstraete, O. Legeza and M. Noack, *Simulating strongly correlated quantum systems with tree tensor networks*, Phys. Rev. B **82**, 205105 (2010).

[91] M. G. and R. M., *Construction of environment states in quantum-chemical density-matrix renormalization group calculations.*, J. Chem. Phys. **124**(3), 034103 (2006).

[92] J. L. Lagrange, *Mécanique Analytique*, Ve Courcier (1811).

[93] C. Hubig, I. P. McCulloch, U. Schollwöck and F. A. Wolf, *Strictly Single-Site DMRG Algorithm with Subspace Expansion*, Phys. Rev. B **91**, 155115 (2015).

[94] S. V. Dolgov and D. V. Savostyanov, *Alternating minimal energy methods for linear systems in higher dimensions. Part I: SPD systems*, SIAM J. Sci. Comput. **36**, A2248 (2014).

[95] M. S. D. Kressner and B. Vandereycken, *Low-rank tensor completion by Riemannian optimization*, BIT Num. Math. **54**, 447 (2014).

[96] E. B. J. Atkins and B. Hendrickson, *A spectral algorithm for seriation and the consecutive ones problem*, SIAM Journal on Computing **28**, 297 (1998).

[97] P. Corboz and G. Vidal, *Fermionic multiscale entanglement renormalization ansatz*, Phys. Rev. B **80**, 165129 (2009).

[98] S. N. Sivanandam and S. N. Deepa, *Introduction to Genetic Algorithm*, Springer Verlag (2010).

[99] A. J. Daley, C. Kollath, U. Schollwöck and G. Vidal, *Time-dependent density-matrix renormalization-group using adaptive effective Hilbert spaces*, J. Stat. Mech.: Theor. Exp. p. P04005 (2004).

[100] J. Haegeman, B. Pirvu, D. J. Weir, J. I. Cirac, T. J. Osborne, H. Verschelde and F. Verstraete, *Variational matrix product ansatz for dispersion relations*, Phys. Rev. B **85**, 100408 (2012).

[101] J. García-Ripoll, *Time evolution of Matrix Product States*, New J. Phys. **8**, 305 (2006).

[102] A. E. Feiguin and S. R. White, *Time-step targeting methods for real-time dynamics using the density matrix renormalization group*, Phys. Rev. B **72**, 020404 (2005).

[103] A. Holzner, A. Weichselbaum, I. P. McCulloch, U. Schollwöck and J. von Delft, *Chebyshev matrix product state approach for spectral functions*, Phys. Rev. B **83**(19), 195115 (2011).

[104] J. C. Halimeh, F. Kolley and I. P. McCulloch, *Chebyshev matrix product state approach for time evolution*, Phys. Rev. B **92**, 115130 (2015).

[105] P. E. Dargel, A. Wöllert, A. Honecker, I. P. McCulloch, U. Schollwöck and T. Pruschke, *Lanczos algorithm with matrix product states for dynamical correlation functions*, Phys. Rev. B **85**(20), 205119 (2012).

[106] M. Wall and L. D. Carr, *Out of equilibrium dynamics with Matrix Product States*, New J. Phys. **14**, 125015 (2012).

[107] T. Barthel, U. Schollwöck and S. R. White, *Spectral functions in one-dimensional quantum systems at finite temperature using the density matrix renormalization group*, Phys. Rev. B **79**, 245101 (2009).

[108] M. P. Zaletel, R. S. K. Mong, C. Karrasch, J. E. Moore and F. Pollmann, *Time-evolving a matrix product state with long-ranged interactions*, Phys. Rev. B **91**, 165112 (2014).

[109] R. Pereira, S. White and I. Affleck, *Exact Edge Singularities and Dynamical Correlations in Spin-1/2 Chains*, Physical Review Letters **100**(2), 027206 (2008).

[110] M. Capone, L. de' Medici and A. Georges, *Solving the dynamical mean-field theory at very low temperatures using the Lanczos exact diagonalization*, Phys. Rev. B **76**(24), 245116 (2007).

[111] A. Liebsch, *Correlated Dirac Fermions on the Honeycomb Lattice studied within Cluster Dynamical Mean Field Theory*, Phy. Rev. B **83**, 035113 (2011).

[112] P. Hohenberg and W. Kohn, *Inhomogeneous Electron Gas*, Phys. Rev. **136**, B864 (1964).

[113] S. Lundqvist and N. H. March, eds., *Theory of the Inhomogeneous Electron Gas*, Springer US (1983).

[114] R. O. Jones and O. Gunnarsson, *The density functional formalism, its applications and prospects*, Rev. Mod. Phys. **61**, 689 (1989).

[115] S. Wouters, C. A. Jiménez-Hoyos, Q. Sun and G. K.-L. Chan, *A Practical Guide to Density Matrix Embedding Theory in Quantum Chemistry*, J. Chem. Theory Comput. **12**(8), 2706 (2016).

[116] G. Baym and L. P. Kadanoff, *Conservation Laws and Correlation Functions*, Phys. Rev. **124**, 287 (1961).

[117] G. Baym, *Self-Consistent Approximations in Many-Body Systems*, Phys. Rev. **127**, 1391 (1962).

[118] P. Werner, A. Comanac, L. de' Medici, M. Troyer and A. J. Millis, *A continuous-time solver for quantum impurity models*, Phys. Rev. Lett. **97**, 076405 (2006).

[119] M. Troyer and U.-J. Wiese, *Computational Complexity and Fundamental Limitations to Fermionic Quantum Monte Carlo Simulations*, Phys. Rev. Lett. **94**, 170201 (2005).

[120] R. Bulla, A. C. Hewson and T. Pruschke, *Numerical renormalization group calculations for the self-energy of the impurity Anderson model*, Journal of Physics: Condensed Matter **10**(37), 8365 (1998).

[121] R. Bulla, *Zero Temperature Metal-Insulator Transition in the Infinite-Dimensional Hubbard Model*, Phys. Rev. Lett. **83**(1), 136 (1999).

[122] T. Pruschke and R. Bulla, *Hunds coupling and the metal-insulator transition in the two-band Hubbard model*, Eur. Phys. J. B **44**(2), 217 (2005).

[123] R. Žitko and T. Pruschke, *Energy resolution and discretization artifacts in the numerical renormalization group*, Phys. Rev. B **79**, 085106 (2009).

[124] C. Lanczos, *An Iteration Method for the Solution of the Eigenvalue Problem of Linear Differential and Integral Operators*, Journal of Research of the National Bureau of Standards **45**, 2133 (1950).

[125] A. Liebsch and H. Ishida, *Temperature and bath size in exact diagonalization dynamical mean field theory*, J. Phys.: Condens. Matter **24**(5), 053201 (2012).

[126] A. Go and A. Millis, *Adaptively truncated Hilbert space based impurity solver for dynamical mean-field theory*, Physical Review B **96**, 085139 (2017).

[127] M. Karski, C. Raas and G. S. Uhrig, *Electron spectra close to a metal-to-insulator transition*, Phys. Rev. B **72**, 113110 (2005).

[128] M. Ganahl, M. Aichhorn, P. Thunström, K. Held, H. G. Evertz and F. Verstraete, *Efficient DMFT impurity solver using real-time dynamics with Matrix Product States*, Phys. Rev. B **92**, 155132 (2014).

[129] F. A. Wolf, A. Go, I. P. McCulloch, A. J. Millis and U. Schollwöck, *Imaginary-time matrix product state impurity solver for dynamical mean-field theory*, Phys. Rev. X **5**, 041032 (2015).

[130] R. Bulla, T. Pruschke and A. C. Hewson, *Anderson impurity in pseudo-gap Fermi systems*, J. Phys.: Condens. Matter **9**(47), 10463 (1997).

[131] R. Žitko, *Adaptive logarithmic discretization for numerical renormalization group methods*, Computer Physics Communications **180**(8), 1271 (2009).

[132] I. de Vega, U. Schollwöck and F. A. Wolf, *Discretizing the spectral representation of a continuous quantum bath*, Phys. Rev. B **92**, 155126 (2015).

[133] Python documentation for the basinhopping method, *https://docs.scipy.org/doc/scipy/reference/generated/scipy.optimize.basinhopping.html*.

[134] Python documentation for different minimisation methods, *https://docs.scipy.org/doc/scipy/reference/generated/scipy.optimize.minimize.html*.

[135] M. J. D. Powell, *An efficient method for finding the minimum of a function of several variables without calculating derivatives*, The Computer Journal **7**(2), 155 (1964).

[136] J. Nocedal and S. Wright, *Numerical Optimization*, Springer-Verlag New York (2006).

[137] A. Lewis and M. Overton, *Nonsmooth optimization via quasi-Newton methods*, Mathematical Programming **141**(2), 135 (2012).

[138] N. Metropolis, A. W. Rosenbluth, M. N. Rosenbluth and A. H. Teller, *Equation of State Calculations by Fast Computing Machines*, The Journal of Chemical Physics **21**, 1087 (2004).

[139] J. Kennedy and R. Eberhart, *Particle swarm optimization*, Proceedings of ICNN'95 - International Conference on Neural Networks **4**, 1942 (1995).

[140] H. Aoki, N. Tsuji, M. Eckstein, M. Kollar, T. Oka and P. Werner, *Nonequilibrium dynamical mean-field theory and its applications*, Rev. Mod. Phys. **86**(2), 779 (2014).

[141] R. M. Martin, *Electronic Structure: Basic Theory and Practical Methods*, Cambridge UniversityPress (2004).

[142] J. Kohanoff, *Electronic structure calculations for solids and molecules: Theory and computational methods*, Cambridge University Press (2006).

[143] L. Lin and C. Young, *Elliptic Preconditioner for Accelerating the Self-Consistent Field Iteration in Kohn-Sham Density Functional Theory*, SIAM Journal on Scientific Computing **35**(5), 277 (2013).

[144] C. G. Broyden, *A class of methods for solving nonlinear simultaneous equations*, Math. Comp. **19**, 577 (1965).

[145] R. Žitko, *Convergence acceleration and stabilization of dynamical mean-field theory calculations*, Phys. Rev. B **80**, 125125 (2009).

[146] D. Vanderbilt and S. G. Louie, *Total energies of diamond (111) surface reconstructions by a linear combination of atomic orbitals method*, Phys. Rev. B **30**, 6118 (1984).

[147] D. D. Johnson, *Modified Broyden's method for accelerating convergence in self-consistent calculations*, Phys. Rev. B **38**, 12807 (1988).

[148] G. P. Srivastava, *Broyden's method for self-consistent field convergence acceleration*, J. Phys. A (1984).

[149] A. Baran, A. Bulgac, M. M. Forbes, G. Hagen, W. Nazarewicz, N. Schunck and M. V. Stoitsov, *Broyden's method in nuclear structure calculations*, Phys. Rev. C **78**, 014318 (2008).

[150] P. Pulay, *Convergence acceleration of iterative sequences. the case of scf iteration*, Chem. Phys. Lett. **73**(2), 393 (1980).

[151] D. G. Anderson, *Iterative Procedures for Nonlinear Integral Equations*, J. Assoc. Comput. Mach. **12**(4), 547 (1965).

[152] M. J. J. Gubernatis, *Bayesian inference and the analytic continuation of imaginary-time quantum Monte Carlo data*, Physics Reports **269**(3), 133 (1996).

[153] R. Levy, J. LeBlanc and E. Gull, *Implementation of the maximum entropy method for analytic continuation*, Computer Physics Communications **215**, 149 (2017).

[154] G. J. Baker and P. Graves-Morris, *Padé Approximants*, Cambridge University Press (1996).

[155] K. S. D. Beach, R. J. Gooding and F. Marsiglio, *A reliable Padé analytical continuation method based on a high accuracy symbolic computation algorithm*, Phys. Rev. B **61**, 5147 (2000).

[156] M. Potthoff, *Self-energy-functional approach: Analytical results and the Mott-Hubbard transition*, Eur. Phys. J. B **36**, 335 (2003).

[157] S. Okamoto, A. J. Millis, H. Monien and A. Fuhrmann, *Fictive impurity models: An alternative formulation of the cluster dynamical mean-field method*, Phys. Rev. B **68**, 195121 (2003).

[158] W. F. Brinkman and T. M. Rice, *Application of Gutzwiller's Variational Method to the Metal-Insulator Transition*, Phys. Rev. B **2**, 4302 (1970).

[159] Z. M. Yusof, B. O. Wells, T. Valla, A. V. Fedorov, P. D. Johnson, C. K. Q. Li, S. Jianand and D. G. Hinks, *Quasiparticle Liquid in the Highly Overdoped* $Bi_2Sr_2CaCu_2O_{8+\delta}$, Phys. Rev. Lett. **88**, 167006 (2002).

[160] M. Grilli, B. G. Kotliar, and A. J. Millis, *Mean-field theories of cuprate superconductors: A systematic analysis*, Phys. Rev. B **42**, 329 (1990).

[161] X.-G. Wen and P. A. Lee, *Theory of Underdoped Cuprates*, Phys. Rev. Lett. **76**, 503 (1996).

[162] B. Kyung, V. Hankevych, A.-M. Daré, and A.-M. S. Tremblay, *Pseudogap and Spin Fluctuations in the Normal State of the Electron-Doped Cuprates*, Phys. Rev. Lett. **93**(14), 147004 (2004).

[163] C. Castellani, C. D. Castro, and M. Grilli, *Singular Quasiparticle Scattering in the Proximity of Charge Instabilities*, Phys. Rev. Lett. **75**, 4650 (1995).

[164] C. Huscroft, M. Jarrell, T. Maier, S. Moukouri and A. N. Tahvildarzadeh, *Pseudogaps in the 2D Hubbard Model*, Phys. Rev. Lett. **86**(1), 139 (2001).

[165] M. Ferrero, P. S. Cornaglia, L. De Leo, O. Parcollet, G. Kotliar and A. Georges, *Valence bond dynamical mean-field theory of doped Mott insulators with nodal/antinodal differentiation*, EPL (Europhysics Letters) **85**(5), 57009 (2009).

[166] M. Civelli, M. Capone, S. S. Kancharla, O. Parcollet and G. Kotliar, *Dynamical Breakup of the Fermi Surface in a Doped Mott Insulator*, Phys. Rev. Lett. **95**, 106402 (2005).

[167] P. Werner, E. Gull, O. Parcollet and A. J. Millis, *Momentum-selective metal-insulator transition in the two-dimensional Hubbard model: An 8-site dynamical cluster approximation study*, Phys. Rev. B **80**, 045120 (2009).

[168] N. F. Mott and R. Peierls, *Discussion of the paper by de Boer and Verwey*, Proceedings of the Physical Society **49**(4S), 72 (1937).

[169] M. Onoda, H. Ohta and H. Nagasawa, *Metallic properties of perovskite oxide $SrVO_3$*, Solid State Communications **79**(4), 281 (1991).

[170] H. T. Dang and A. J. Millis, *Theory of ferromagnetism in vanadium-oxide based perovskites*, Phys. Rev. B **87**, 155127 (2013).

[171] *Private communication with Andrew Millis.*

[172] A. Georges, L. de' Medici and J. Mravlje, *Strong electronic correlations from Hund's coupling*, Annual Reviews of Condensed Matter Physics **4**, 137 (2012).

[173] A. P. Mackenzie and Y. Maeno, *The superconductivity of $Sr_2RuO_4$ and the physics of spin-triplet pairing*, Rev. Mod. Phys. **75**, 657 (2003).

[174] Y. Maeno, H. Hashimoto, K. Yoshida, S. Nishizaki, T. Fujita, J. G. Bednorz and F. Lichtenberg, *Superconductivity in a layered perovskite without copper*, Nature **372**, 532 (1994).

[175] A. P. Mackenzie, S. R. Julian, G. G. Lonzarich, Y. Maeno and T. Fujita, *Comment on "Extended Van Hove Singularity in a Noncuprate Layered Superconductor $Sr_2RuO_4$"*, Phys. Rev. Lett. **78**, 2271 (1997).

[176] S. Liu, H. Weng, D. Mou, W. Zhang, Q. Wu, J. He, G. Liu, L. Zhao, H. Liu, X. Jia, Y. Peng, S. He *et al.*, *Fermi surface sheet-dependent band splitting in $Sr_2RuO_4$ revealed by high-resolution angle-resolved photoemission spectroscopy*, Phys. Rev. B **86**, 165112 (2012).

[177] A. Liebsch and A. Lichtenstein, *Photoemission Quasiparticle Spectra of $Sr_2RuO_4$*, Phys. Rev. Lett. **84**, 1591 (2000).

[178] E. Pavarini and I. I. Mazin, *First-principles study of spin-orbit effects and NMR in* $Sr_2RuO_4$, Phys. Rev. B **74**, 035115 (2006).

[179] D. Stricker, J. Mravlje, C. Berthod, R. Fittipaldi, A. Vecchione, A. Georges and D. van der Marel, *Optical Response of $Sr_2RuO_4$ Reveals Universal Fermi-Liquid Scaling and Quasiparticles Beyond Landau Theory*, Phys. Rev. Lett. **113**, 087404 (2014).

[180] M. W. Haverkort, I. S. Elfimov, L. H. Tjeng, G. A. Sawatzky and A. Damascelli, *Strong Spin-Orbit Coupling Effects on the Fermi Surface of $Sr_2RuO_4$ and $Sr_2RhO_4$*, Phys. Rev. Lett. **101**, 026406 (2008).

[181] M. Kim, J. Mravlje, M. Ferrero, O. Parcollet and A. Georges, *Spin-Orbit Coupling and Electronic Correlations in $Sr_2RuO_4$*, Phys. Rev. Lett. **120**, 126401 (2018).

[182] M. Z. Hasan and C. L. Kane, *Colloquium: Topological insulators*, Rev. Mod. Phys. **82**, 3045 (2010).

[183] D. I. Khomskii, *Transition Metal Compounds*, Cambridge University Press (2014).

[184] G. R. Stewart, *Heavy-fermion systems*, Rev. Mod. Phys. **56**, 755 (1984).

[185] D. Sutter, C. G. Fatuzzo, S. Moser, M. Kim, R. Fittipaldi, A. Vecchione, V. Granata, Y. Sassa, F. Cossalter, G. Gatti, M. Grioni, H. M. Rønnow *et al.*, *Hallmarks of Hunds coupling in the Mott insulator $Ca_2RuO_4$*, Nature Communications **8**, 15176 (2017).

[186] H. Iwasawa, Y. Yoshida, I. Hase, S. Koikegami, H. Hayashi, J. Jiang, K. Shimada, H. Namatame, M. Taniguchi and Y. Aiura, *Interplay among Coulomb Interaction, Spin-Orbit Interaction, and Multiple Electron-Boson Interactions in $Sr_2RuO_4$*, Phys. Rev. Lett. **105**, 226406 (2010).

[187] Homepage of the TRIQS package, *https://triqs.github.io/triqs/master/*.

[188] Homepage of the WIEN2K package, *http://susi.theochem.tuwien.ac.at*.

[189] C. W. Hicks, D. O. Brodsky, E. A. Yelland, A. S. Gibbs, J. A. N. Bruin, M. E. Barber, S. D. Edkins, K. Nishimura, S. Yonezawa, Y. Maeno and A. P. Mackenzie, *Strong Increase of Tc of $Sr_2RuO_4$ Under Both Tensile and Compressive Strain*, Science **344**(6181), 283 (2014).

[190] F. A. Wolf, *Tensor networks for dynamical mean-field theory*, Ph.D. thesis, LMU Munich (2015).